DESIGN, MANUFACTURE, AND IMPLEMENTATION OF 3D-PRINTED TISSUE ENGINEERING SCAFFOLDS USED WITH STROMAL VASCULAR CELLS FOR CRANIOFACIAL BONE REGENERATION

by

ETHAN LYTLE NYBERG

A dissertation submitted to The Johns Hopkins University in conformity with the requirements for the degree of Doctor of Philosophy

Baltimore, Maryland
July 2019

ABSTRACT

Craniofacial bone defects have poor outcomes under current treatments: implants become infected, loosen, and displace; bone grafts resorb and weaken over time; and there are no satisfactory pediatric options. To improve outcomes, this thesis develops a novel osteoinductive biomaterial, the methods to 3D-print the biomaterial, and the tools to design of that 3D-printed scaffold for the mechanical loads of the craniofacial skeleton. Further, it combines the scaffold with key regenerative agents – autologous stem cells – to facilitate boney regeneration in the implanted scaffold. The feasibility of the scaffold and cells approach is tested by implementation in preclinical models and assessment of bone and vascular outcomes. **Aim 1:** To create an osteoinductive biomaterial, trabecular bone was decellularized, cryo-milled, and mixed with polycaprolactone. This thermoplastic material mixture was then 3D-printed and demonstrated osteoinductive effects on cells. **Aim 2:** As regenerative autologous cells, the stromal vascular fraction of adipose tissue was isolated in a point-of-care manner and timeframe and the stem cell yield, surface markers, *in vitro* and *in vivo* regenerative potential for vascular and bone tissue was demonstrated. **Aim 3:** Then the means to design 3D-print the biomaterial with controlled tissue engineering properties – pore size and porosity – at human craniofacial scales and for human physiologic loads was developed and tested. **Aim 4:** Finally, the biomaterial, cells, and design and manufacturing were implemented in a patient-specific, large-animal, preclinical model of zygomatic arch regeneration in swine. Implant design and manufacture was successfully validated, and the implanted scaffolds and cells showed a substantial bone regenerating response compared to untreated controls.

THESIS COMMITTEE

Warren L. Grayson, PhD (*primary advisor, reader*)

Associate Professor, Department of Biomedical Engineering

Johns Hopkins University School of Medicine

Dara L. Kraitchman, VMD, PhD (*committee chair*)

Professor, Russell H Morgan Department of Radiology and Radiological Science

Johns Hopkins University School of Medicine

Hai-Quan Mao, PhD

Professor, Department of Materials Science and Engineering

Johns Hopkins University Whiting School of Engineering

James K. Guest, PhD

Associate Professor, Department of Civil Engineering

Johns Hopkins University Whiting School of Engineering

Michael Grant, MD, PhD (*reader*)

Professor, Department of Surgery and Ophthalmology

University of Maryland School of Medicine

Amir H. Dorafshar, MBChB

Professor, Department of Surgery

Rush Medical College

To my Family:
Grandad, for his support, inspiration, and encouragement,
Grandmommy, for never-ending supply of steak and life advice,
Mom, for never having expectations and sending food,
Dad, for exemplary work ethic, and
my Sisters, for never-ending amusement and comedic relief.

ACKNOWLEDGEMENTS

A great many people helped me survive this scholastic maelstrom, but I can never thank my family enough. Mom and Dad, for all their teaching, support, and nagging. Mom for the constant packages of cookies and bratwursts. Dad for his proof-reading and helpful discussions. Granddad and Grandmommy, for their endless support, encouragement, and pride. And my sisters, Hannah, Bethany, and Virginia, who never really understood what I was doing but sent innumerable encouraging notes and post-cards.

My advisors and mentors have been key to my intellectual development and in providing the opportunity and resources flex that intellect. In particular, Shayn Peirce-Cottler passed on the joy of the pursuit of knowledge and prepared me for graduate studies, and Warren Grayson imparted an unending doggedness during that chase throughout the course of this PhD. The large animal preclinical studies in the dissertation would have been infeasible without the aid and expertise of Michael Grant in designing and performing the surgeries. Finally, much of my benchtop attitude is due to Cynthia Huang, my very first research mentor, who modelled a powerful can-do approach to science and engineering wet-lab research.

There are some things money cannot buy, and one of those things that was essential to this work is fresh human adipose tissue. I am immeasurably grateful to the multitude of human patients that generously donated their adipose tissue and cells for this research. In particular, thank you to the cancer-surviving patients for kindness and grace when, at 5am, I mumbled and nervously asked for this tissue donation, amidst the final stages of your own recovery.

This work is heavily rooted in the biologic testing of the technology, which would be impossible without the many research animals used in the dissertation and the field. Those animals were a cost of doing this research, and they contributed in success and failure to the meaningfulness and impact of this thesis.

TABLE OF CONTENTS

LIST OF TABLES

LIST OF FIGURES

LIST OF ABBREVIATIONS

3D	Three Dimensional
ABS	Acrylonitrile Butadiene Styrene
AM	Additive Manufacturing
ASCs	Adipose-derived Stomal/stem Cells
BMP-2	Bone Morphogenic Protein-2
BMPs	Bone Morphogenetic Proteins
bMSCs	Bone Marrow Stem Cells
BO	Bio-Oss
BrdU	bromodeoxyuridine
BTE	Bone Tissue Engineering
CBCT	Cone Beam Computed Tomography
CM	Control Media
CMF	Craniomaxillofacial
CNC	Computer Numerical Control
CS	Chondroitin Sulphate
CT	Computed Tomography
DAPI	4'-6-diamidino-2-phenylindole
DCB	Decellularized Bone Matrix
DICOM	Digital Imaging and Communications in Medicine
DMEM	Dulbecco's Modified Eagle Medium
DNA	Deoxyribonucleic Acid

EBM-2	Endothelial Basal Medium-2
ECM	Extracellular Matrix
ECs	Endothelial Cells
EDTA	Ethylenediaminetetraacetic Acid
FBS	Fetal Bovine Serum
FDA	Food and Drug Administration
FDM	Fused Deposition Modeling
FGF	Fibroblastic Growth Factor
GAGs	Glycosaminoglycans
GFs	Growth Factors
HA	Hydroxyapatite
HIF	Hypoxia Induced Factor
HU	Hounsfield Units
IGF	Insulin-like Growth Factor
LbL	Layer-by-layer
MMPs	Matrix Metalloproteinases
MRI	Magnetic Resonance Imaging
MSCs	Mesenchymal Stem Cells
OM	Osteogenic Media
P/S	Penicillin / Streptomycin
PBS	Phosphate Buffered Saline
PCL	Polycaprolactone
PCs	Pericytes

PDGF-BB	Platelet-Derived Growth Factor BB
PDMS	Polydimethylsiloxane
PEEK	Polyetheretherketone
PEG	Polyethylene Glycol
PEI	Polyetherimide
PEO	Polyethylene Oxide (same as PEG)
PEs	Polyelectrolytes
PLA	Polylactide or Polylactic Acid
PLGA	Poly(lactic-co-glycolic) Acid
PMMA	Polymethyl Methacrylate
PVA	Poly-vinyl Alcohol
qRT-PCR	real-time polymerase chain reaction
RBC	Red Blood Cell
rhBMP-2	Recombinant Human BMP-2
SBF	Simulated Body Fluid
SEM	Scanning Electron Microscopy
SIMP	Simplified Isotropic Material with Penalization
SLA	Stereolithography
SLS	Selective Laser Sintering
STL	Stereolithography or Standard Triangle Language or Standard Tessellation Language
SVF	Stromal Vascular Fraction
TCP	Tri-calcium Phosphate

TGF-B	Transforming Growth Factor Beta
TNF	Tumor Necrosis Factor
VEGF	Vascular Endothelial Growth Factor
VSP	Virtual Surgery Planning
αSMA	Alpha Smooth Muscle Actin

CHAPTER 1
INTRODUCTION: REGENERATING CRANIOMAXILLOFACIAL BONE
WITH TISSUE ENGINEERED BONE SCAFFOLDS

There is a high incidence – over 200,000 annually[1] – of craniomaxillofacial skeleton reconstructions in the US every year, and those reconstructions suffer from poor healing outcomes, treatments that create donor-site morbidities, or infection. A regenerative medicine treatment could address those complications and improve outcomes of craniofacial reconstructions. However, the inherent complexity of regenerative materials and designs, compounded due to the scale, shape, and mechanical function of the craniofacial skeleton has been a barrier to such treatments. This thesis works to overcome those complexities and improve craniofacial outcomes by developing a regenerative implant treatment. By producing tissue engineered scaffolds through 3D-printing of bone material, a regenerating defect could be vascularized to fight infection, integrated with the surrounding bone, and eventually become indistinguishable from surrounding bone; thus, poor healing outcomes, co-morbidities, and rates of infection could be reduced. This chapter establishes (i) the context and function of the CMF skeleton, (ii) the common pathologies and treatments of CMF bones, (iii) the potential of regenerative medicine to improve treatments of CMF boney defects, and (iv) outlines the organization of the dissertation.

Form and Function of Craniofacial Bones

First, the craniofacial skeleton provides an important set of mechanical functions: it enables respiration, mastication, communication, and it is the primary

protection of the central nervous system. The airway begins in the mouth and nose and connects with the sinus system as well as continuing down the trachea. The bones surrounding the nose, and lining the sinus are thin and precisely defined to allow for respiration and mucosal production. Mastication is due to the motion of the mandible, which pulls against the zygomaxillofacial complex, the temple, and the frontal bone, and the reaction forces of that movement on the maxilla.

Second, the CMF skeleton has important functions in communication. Facial expression is fully dependent on the craniofacial skeleton and communication *via* facial expression is one of mammals' first conscious skills[2]. Facial recognition is one of the first skills infants use—within minutes of birth. Facial identity is not only crucial to communication, but it is foundational to self-identity[3]. The CMF skeleton is also crucial for speech and verbal communication.

Embryologically, the bones of the face (mandible, maxilla, and zygoma) are outgrowths of pharyngeal arches and develop *via* intramembranous growth until skeletal maturity. This developmental process differs from that of the bones of the neurocranium, which begin with intramembranous ossification, and join together at sutures that maintain growth during development *via* fibrous (non-endochondral) edge ossification[4]. Importantly, these processes are distinct from the endochondral formation and growth of long bones throughout the remainder of the body. Further, the process of fracture healing in cranial bones is different, with a delayed osteoblastic response[5].

Geometrically, CMF bones are thin (<2cm) and encompass a narrow marrow cavity or air sinus—resulting in even thinner wall structures. The facial bones have jutting prominences, while the cranial bones form a reinforced sphere

around the brain. Orbital bones are exceptionally thin (on the order of a few millimeters) and facilitate the movement, position, and protection of the orbit. Facial bones are thinner and weaker than the cranial bones, and a more common source of fracture and morbidity while the cranial bones are more often injured during operations to access or treatments of malignancies in the central nervous system.

Pathologies of Craniofacial Bones

Craniofacial skeletal defects commonly arise from trauma, congenital malformation, or cancerous re-sectioning (**Figure 1-1**). Trauma, such as gunshot wounds[6], blast injuries, or motor vehicle accidents[7] can severely fracture the craniofacial bones and render the fragments non-viable. Non-viable fragments are removed to prevent necrotic masses, resulting in a void in the skeleton. These injuries often involve multiple bones and soft tissues. Compared to congenital or resection injuries, these involve a healthy, skeletally-mature population.
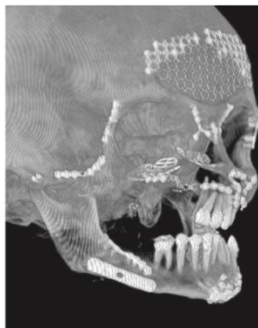
High-velocity motor vehicle collision Maxillary defect
Rodriguez 2006, Plastic and Reconstructive Surgery

Hemifacial Microsomia
Santamaria 2008, Plastic and Reconstructive Surgery

Goldenhar Syndrome
Canter 2008, J Craniofacial Surgery
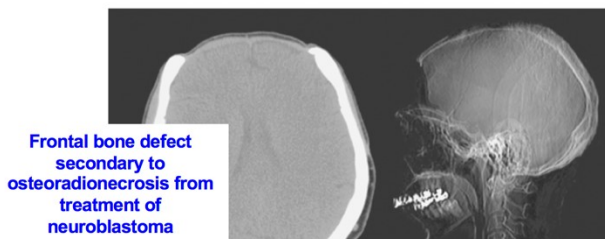
Frontal bone defect secondary to osteoradionecrosis from treatment of neuroblastoma
Chacon-Moya 2009, Cir Ciruj
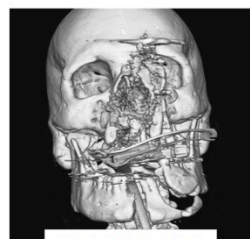
Facial Gunshot
Pereira 2012, Ann Plast Surg
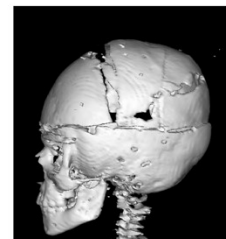
Saethre-Chotzen Craniosyntosis

Figure 1-1 Examples of CMF Pathologies.

Congenital malformations such as Goldenhar syndrome[8,9] and hemifacial microsomia[10,11] present early in life (0 – 6 months). They typically involve malformation (as absence or undergrowth) of the mandible, the temporomandibular joint, or the maxilla. Additionally, there are cases of premature synostosis of the sutures, resulting in a misshapen cranial vault. These disorders can be grouped together because of the large volumes of bone that must be corrected as well as the dynamic nature of the pediatric craniofacial skeleton. Disorders of cleft palate also present with malformation of the craniofacial skeleton. However, cleft palate can be treated with soft tissue reconstruction.

Defects also arise as a secondary morbidity such as resection due to cancer[12], radio-osteonecrosis[13], or through the failure of a previous craniofacial implant. These defects are often massive (>50 cm^2) and occur in an elderly or otherwise infirm population that may have reduced healing or integration capacity.

While bone is a self-healing organ, defects of large sizes are slow or impossible to heal, result in functional failings of the CMF skeleton, and can cause disfigurement and associated psychosocial pathologies[14]. Many researchers in the field characterize defects in animal studies as 'critical sized' or non-healing in the life of the animals. In human treatment, such a concept is very poorly tested, as nearly all defects are treated with a packed granule/cement or implant. Generally, it is used to refer to defects that are >6cm in width. Reconstructive surgery is the primary treatment for these defects. In the US, there are 200,000 craniomaxillofacial reconstructions a year, at a cost of $610M[1].

Shortcomings of Standard-of-care Interventions
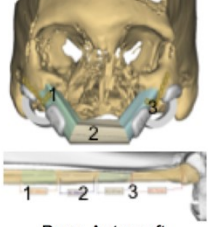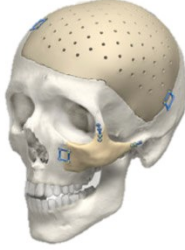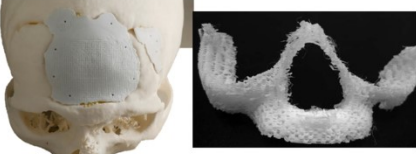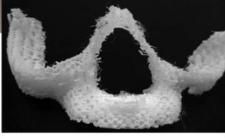
These anatomically complex reconstructions are treated with bone grafts and implants, each with disadvantages (**Figure 1-2**). Filling the defect with bone or a solid implant maybe replace the shape and rigidity of the deficient bone, but such treatments do not restore multifaceted biology activity of the original native bone.

Solid implants suffer from infection rates of 8-20%[15] due to poor vascularization (thereby not enough blood supply of immune cells to clear infections) and soft tissue thinning on the surface of the implant (the soft tissue cannot integrate with implants and detaches and thins as a result). Implant materials, such as titanium, can be stiffer than bone and cause stress shielding from the surrounding bone, resulting in the adjacent bone weakening and the implant loosening or dislodgement.

Autologous bone grafts are the gold standard treatment because they can become vascularized and have a small degree of integration with the surrounding hard and soft tissue, and they fill the defect with living bone. With autologous bone grafts, there is initially a high degree of implanted viable bone, at the cost of anatomic shape. However, these grafts necessarily cause donor site morbidity and experience high rates of resorption[16].

Allograft bone implants were initially unable to meet demand, but they have increased in supply over the last decade as bone banks have become established[17]. While allograft is still true bone material (collagen and mineral) like autografts, allografts are acellular, less bioactive, and have high resorption rates compared to autologous bone grafts. While precise surgical planning has improved

the speed and cosmetic outcome of bone grafting operations, bone grafts remain

the most expensive and time-consuming treatment option[18].

Figure 1-2 Different Craniofacial Bone Therapies

> Each of the current standards of treatment have different advantages
> and disadvantages. A. Bone autograft from the fibia to the maxilla, with
> 3D-printed cutting guide and fixation hardware. B. Patient-specific PEEK
> manufactured with a casting process. C. Ceramics made through a high-
> temperature sintering or baking process. D. 3D-printed tissue
> engineering scaffold.

Plastic implants are the common alternative to bone grafts. The leading

material, polyetheretherketone (PEEK), can be manufactured to match exact

anatomic shape (e.g. patient-specific products from Stryker and Synthes).

However, plastic implants suffer from moderate rates of infection and displacement

or extrusion[15]. These patient-specific implants are the cutting-edge in implant

technology, but they are often not appropriate for pediatric cases as the craniofacial skeleton is continuing to grow and the implants do not grow with the patient. There are no satisfactory pediatric options[19,20].

More recently, solid implants of hydroxyapatite (HA) ceramics and bioglasses have been developed for patient-specific use. While their mineral nature supports osteoconduction and bone integration, these implants are typically brittle and non-resorbable[21].

3D-printed thermoplastics, such as polycaprolactone (PCL), can be manufactured in a patient-specific manner and have a high porosity that is appropriate to bone tissue ingrowth and regeneration through the bulk of the implant. Osteopore (PCL Scaffold Bone Void Filler, Singapore) has a 3D-printed implant line (non-patient specific) which has FDA approval, with the important caveat that the implant must not be load bearing. However, the porous and plastic properties of these grafts result in mechanical weakness and plastics are generally bioinert.

Promise of Regenerative Interventions for Bones

Regenerative approaches differ from classical implants and grafts by intending to fully replace the missing tissue and thereby restore the function of the bone, whereas implants aim to fill the defect with bone-like material that falls short of fully recapitulating the bone. Even bone grafts—which can fill the void with viable living tissue—have a poor rate of integration and do not properly remodel according to the implant location.

Tissue engineering is classically defined as a combination of cells and biomaterials to manufacture a replacement tissue[22]. These replacement tissues

can be designed to fully integrate with the surrounding tissue, and work with the host ingrowth to endogenously replace the tissue, finishing with the eventual degradation of the implant and regeneration of the native tissue. Bone is a promising target of tissue engineering because healing of most bone injuries occurs naturally throughout many stages of life.

Thorough vascularization is a hallmark of a healing tissue, and both fully heathy or regenerated bone has an intricate and pervasive vascular network. The vascular response is critical for the bone growth and remodeling process as well as for providing the immune response to fight off infection. The avascular nature of implants and allografts, and the poorly vascularized nature of allografts might be a major source of their poor outcomes.

Outcomes of large CMF bone defects would be improved by a regenerative treatment. Regenerative medicine treatments will be highly vascularized and able to resist infection, eventually being composed entirely of living bone that will not be extruded by the body. However, no regenerative medicine treatments for large CMF bone defects currently exist. This shortcoming is primarily due to the complex design requirements of such an approach. Early treatments have had problems that include implanted cell death, a lack of cell permanency, and weak biomaterials that degrade asynchronously with regeneration. While biodegradation is needed to eventually create the space for a total regenerative response it weakens the primary stability of the implant (**Figure 1-3**).
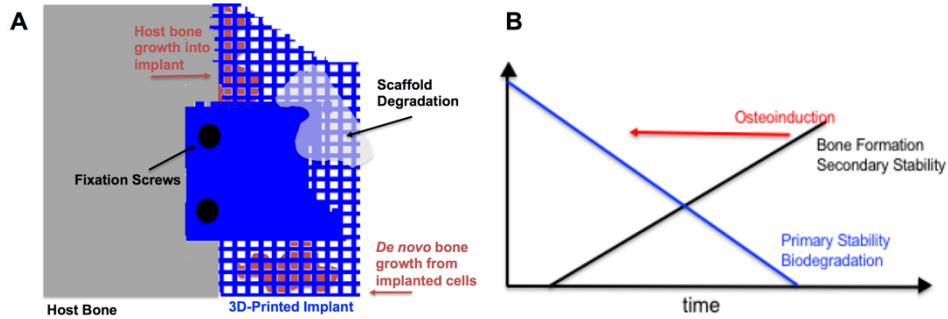
Figure 1-3 The Effect of Osteoinduction and Biodegradation on Implant Stability
   A. Primary implant stability degrades over time due to the biodegradation of the implant and the parts used to fixate it in place. This degradation needs to be matched with increases in stability from the boney regeneration into and throughout the implant (secondary stability). The combination of these stabilities cannot drop below the level of the forces acting on the implant.
   B. Schematic of primary and secondary stability in the context of scaffold degradation and bone growth into and throughout the scaffold. Osteoinduction would increase the rate of formation of secondary stability.

Tissue Engineering Approaches to Regenerate Bone

Bone tissue engineering combines cells and a rigid scaffold together to recreate the mechanics and biology of bone—collagen fibrils mineralized with apatite crystals, assembled into porous bone trabeculae, where the porous space is lined and filled with bone cells and blood vessels. Often, this re-creation is achieved through the additional combination osteoinductive agents (such as growth factors PDGF-BB or BMP-2) (**Figure 1-4**).
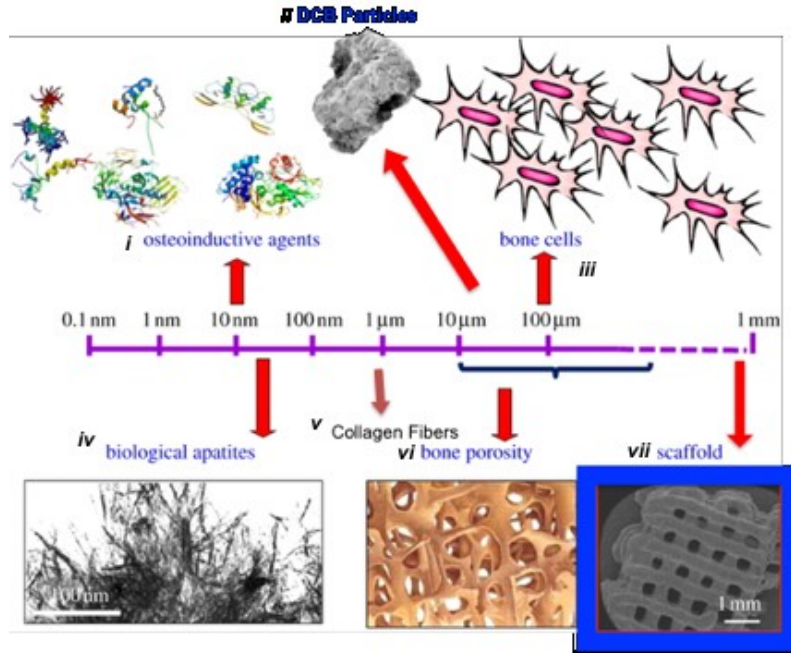
Figure 1-4 Scale of Bone Tissue Engineering Components
The different materials used throughout this dissertation are many different scales, but all interact with the key regenerative agent: the cells. i. Osteoinductive agents such as GFs and small molecules. ii. DCB particles. iii. Bone forming cells. iv. Biological apatites form on the extracellular matrix – collagen fibers. v. Collagen fibers are deposited by the implanted cells. vi. Bone has a natural porosity on the scale of 50-100μm pores and trabeculae. vii. 3D-printed scaffolds are much larger, and contain struts and pores on the scale of millimeters.

Regenerative bone scaffolds necessarily must be cellular, as cells are a vital part of the remodeling and vascular features of bones. However, cell and blood vessel growth into large implants is unreasonably slow. Osteoconduction is a process where the bone edge of the host grows into the implant (7-70μm/hr for osteoblasts)[23]. The scale of defects and therefore scaffolds is much larger (>6cm), resulting in months to a year for osteoblasts to migrate to the bulk of the scaffold. Placing cells (that can form bone and vascular tissue structures) throughout the scaffold, is therefore an indispensable feature of the scaffolds. Further, the scaffold should have signals (osteoinductive, angiogenic) in the component materials directing the implanted cells to form the desired bone and vascular tissues.

ASCs have been used as an autologous bone cell alternative throughout the bone tissue engineering (BTE) literature because they can be induced to create a strong mineral deposition in vitro over the course of as few as 10 days, without the morbidity or pain of harvest. Their manner of deposition is similar to osteoblasts, with caveats for *in vitro* vs *in vivo* scale and complexity. This timescale applied to volumetric defects is similar to the bone callus formation that occurs in fracture healing. Finally, these cells have been used in a large number of clinical trials and have been shown to be generally safe[24] (non-immunogenic, non-tumorigenic).

The rigid scaffolds, if acting as a load-bearing implant, are made up of struts of material with a network of pores throughout for the cells to invade and fill with tissue. Firm fixation with the adjacent host bone is required for the connection of host and graft tissue – even millimeter scale motion will prevent tissue from joining across the implant-host border. The material itself must be highly biocompatible and biodegradable. Often, engineers include an osteoinductive factor with the material to increase the bone forming potential of the implant.

Cost reductions in 3D-printing has enabled many researchers to use this manufacturing process to create regenerative implants that match the geometric shape of the bone, or that have a characteristic porous interior. 3D-printing technology has the potential to enable the manufacture of the material phase of tissue engineered bone scaffolds at human scale, and in a highly patient-specific manner. While there are a number of different 3D-printing (additive manufacturing) systems, fused deposition is commonly used for bone scaffolds because it does not require alterations or additives to deposit solid material (like light/resin

crosslinking 3D-printing systems) nor does it require high temperatures (like selective laser sintering systems) that discourage the inclusion of bioactive factors, which are sensitive to temperature.

There are three common methods to drive the extrusion from a fused deposition print head: pneumatic pressure, filament flow, and screw extrusion. The first parts of this dissertation use a pneumatic pressure system because it affords small batch manufacturing with minimum volumes as low to 5mL, which enables the rapid testing of different materials. The latter parts of the dissertation used a filament driven system, because that enables the larger scale manufacture of scaffolds up to the size of a whole skull (**Figure 1-5**).
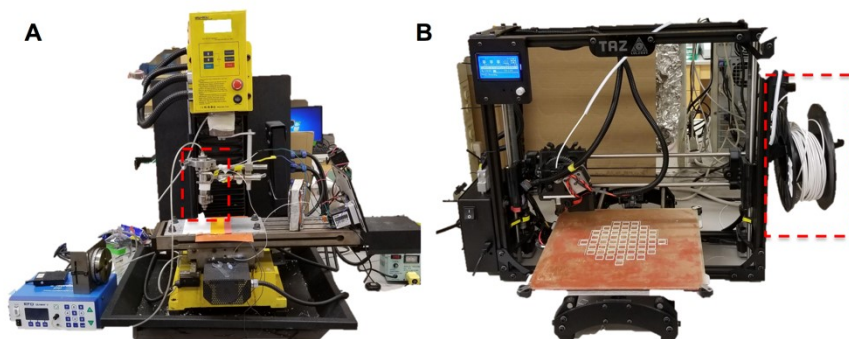
Figure 1-5 3D-Printing Systems Used in the Dissertation
      A. The pneumatic deposition system was advantageous for small batch testing but was limited in scale <1cm and continually clogged.
      B. Filament driven system has fewer printing complications but requires separate filament manufacturing.
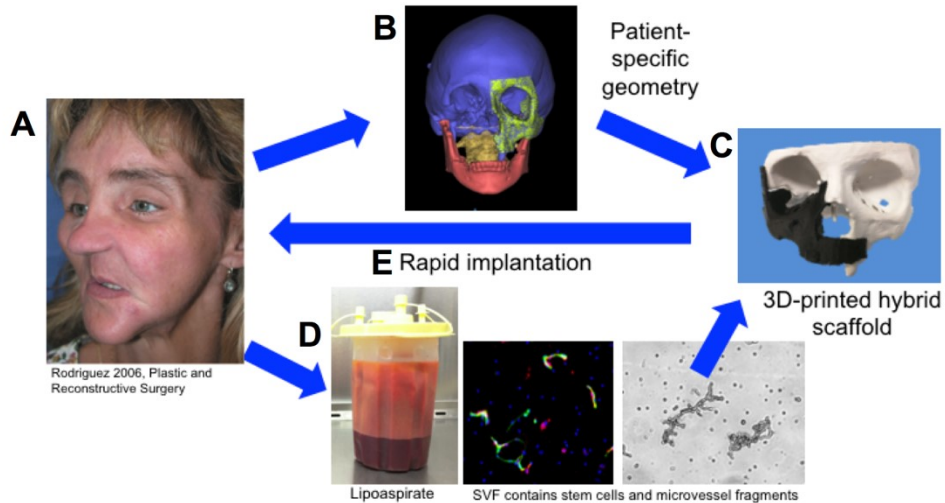
Figure 1-6 Overview of Proposed Intervention
- A. Patient with severe midface osteotomy following cancer resectioning.
- B. CT provides patient-specific anatomy, and normative anatomy can be reflected (green) across the midline of the face to create the shape of the implant.
- C. The implant can be manufactured with FDM 3D-printing
- D. Stem and endothelial cells can be isolated from the patient's own adipose lipoaspirate.
- E. Cells loaded into the scaffold and acutely implanted back into the patient in a single surgical session.

Dissertation Goals

This dissertation builds directly upon and integrates the work of two previous doctoral researchers in the Grayson Lab: Daphne Hutton-Hosmane and Ben Hung. Daphne developed methods to regenerate vascularized bone from adipose-derived stromal/stem cells[25,26]. These methods are key to facilitate rapid, cell-driven regeneration of boney tissues. Importantly, she demonstrated that a single cell source – ASCs – could develop into both blood vessels and mineralizing matrix. In part, this work seeks to further the application of these cells to blood vessel and bone formation, and it works to do so in a clinically relevant iteration of the cells—the uncultured stromal vascular fraction cells.

Ben pioneered the idea of incorporating bone extracellular matrix in 3D-printed scaffolds to create an implant with bone-forming bioactivity[27]. While his system had promising *in vitro* osteoinductivity, manufacturing was practically infeasible. An enduring bone-forming signal throughout the implant is crucial for implanted stem cells or surrounding endogenous progenitors to fully regenerate the bone. This dissertation improves the manufacturing of such scaffolds, and fully characterizes the scaffolds in the context of other clinical technologies. Further, it develops an open and replicable method of designing 3D-printed tissue engineered scaffolds. Together, the scaffold and cells represent a powerful technology to affect bone regeneration.

In addition to furthering and integrating these two technologies, the personal goal of this dissertation is to translate those technologies to a human-scale intervention and acute clinical context, from small-scale *in vitro* and murine platforms (**Figure 1-6**). Herein, studies break new ground in the design, manufacturing, and implementation of implants of human scale and quality, and the effect thereof combined with acutely grafted SVF cells on regeneration of craniofacial bones.

Organization of the Dissertation

The dissertation is grouped into five parts: (1) background, (2) biomaterial, (3) cells, (4) scaling design and manufacturing, and (5) clinical feasibility and translation. Part 1 develops the background in 3D-printing and bone tissue engineering.

Chapter 2. 3D-printing technology is a powerful tool for manufacturing the shapes of the craniofacial skeleton. This chapter reviews the different ways the

technology can be used to manufacture products that aid in the reconstruction, repair, or regeneration of craniofacial bone.

Chapter 3. Growth factors and extracellular matrix cues are key tools for tissue engineers as they provide instructive cues for cells to develop certain types of tissue. This chapter reviews the growth factors that are important for bone tissue formation and the different methods of using them.

Part 2 characterizes the 3D-printed biomaterial and the resulting scaffolds for bioactivity and osteoinductivity.

Chapter 4. Decellularized bone particles are the key bone forming signal in this dissertation. This chapter considers the materials and the methods of preparing particles polycaprolactone, as well as the process of 3D-printing them in combination. Further, it evaluates the different methods used to assess these scaffolds.

Chapter 5. Scaffolds containing DCB are compared with other clinically used bone-forming ceramics in their manufacturability, material properties, osteoinductivity, and *in vivo* behavior in mice. It finds that the scaffolds prepared with particles containing extracellular derived particles have increased osteoinductivity *in vitro*, and equivalent bone formation in murine cranial defects.

Part 3 concerns the cells (both SVF and ASCs) used to accelerate up the growth of bone tissue.

Chapter 6. New blood vessels are hallmarks of regeneration and are essential to supply oxygen and nutrients to the bulk of the implant. This chapter looks at the ability of ASCs to undergo vasculogenesis and form blood vessels through *in vitro* pseudo implant conditions and *in vivo* implantation in the

15

subcutaneous space. It finds that the cells form blood vessels and are more likely to survive harsh implant conditions if they are able to assemble for a period of four days.

Chapter 7. Clinical implementation requires cells that are available intraoperatively and in large quantities. This chapter compares such a cell source—SVF—to the common cultured form of cells—ASCs—to determine their relative osteogenic and vasculogenic potential. It uses a high number of donors to demonstrate that the trend of regenerative potential eclipses donor-to-donor variability. It finds that SVF is an appropriate cell source for our scaffold system.

Part 4 focuses on designing and manufacturing 3D-printed craniofacial scaffolds at human scale and with a mechanical integrity that can endure the loads of the implant condition.

Chapter 8. Inherently, porous PCL-DCB scaffolds deform easily and are mechanically inferior to bone. This weakness stems from the soft plastic character of PCL, and the thin strands of material that result from 3D-printing. Patterning areas of human-sized craniofacial scaffolds with stiffer regions to increase the mechanical strength without sacrificing overall porosity might alleviate this short-coming. This chapter develops optimization software to find optimal patterns of stiff regions and porous regions throughout the implant in response to the exact anatomic shape, surgical fixation, and physiologic loading. Using this software tool results in designs that are superior generic homogenously patterned implants.

Chapter 9. The ability to 3D-print scaffolds with different pore sizes, porosities, and mechanics throughout the shape is lacking in the field, despite being within the capabilities of most 3D-printing systems. This chapter develops a

versatile MATLAB approach to control the manufacture of scaffolds with many different porous regions. Characterization of those different regions and the quality of the transitions between them finds a range of different porous or stiff patterns that can be faithfully manufactured. Importantly, this approach can be combined with the designs in chapter 8 to manufacture functionally heterogeneous implants.

Part 5 tests the different technologies developed in parts two, three, and four at human scales, and comments on the challenges of implementing them in clinical use.

Chapter 10. Bone regeneration at a human scale remains a challenge for the field of bone tissue engineering. This chapter takes the biomaterial and cells from parts two and three and tests them in a novel porcine—human scale—model of craniofacial bone regeneration.

Chapter 11. Actual translation of these technologies into clinical use will require the clearing of different hurdles in the technical, clinical, and regulatory dimensions of craniofacial care. Challenges and future perspectives are considered for the proposed scaffold system and for the field of craniofacial regenerative medicine as a whole.

CHAPTER 2[§]
3D-PRINTING FOR CRANIOFACIAL RECONSTRUCTION,
REPAIR, AND REGENERATION

Summary

The treatment of craniofacial defects can present many challenges due to the variety of tissue-specific requirements and the complexity of anatomical structures in that region. 3D-printing technologies provide clinicians, engineers and scientists with the ability to create patient-specific solutions for craniofacial defects. Currently, there are three key strategies that utilize these technologies to restore both appearance and function to patients: rehabilitation, reconstruction and regeneration. In rehabilitation, 3D-printing can be used to create prostheses to replace or cover damaged tissues. Reconstruction, through plastic surgery, can also leverage 3D-printing technologies to create custom cutting guides, fixation devices, practice models and implanted medical devices to improve patient outcomes. Regeneration of tissue attempts to replace defects with biological materials. 3D-printing can be used to create either scaffolds or living, cellular constructs to signal tissue-forming cells to regenerate defect regions. By integrating these three approaches, 3D-printing technologies afford the opportunity to develop personalized treatment plans and design-driven manufacturing solutions to improve aesthetic and functional outcomes for patients with craniofacial defects.

Introduction

Craniofacial defects arise as a direct result of trauma, oncological resection, or congenital differences. They cause soft tissue or bone deficits, or a combination of both leading to non-healing composite tissue wounds. Defects in the craniofacial region in particular are difficult to treat because of the emphasis on positive aesthetic outcomes and the number of tissue types (bone, cartilage, muscle, and skin) and structures (auricle, orbit, nose, oral cavity) in close proximity. The current options for reconstructive surgery to treat these defects include grafts, local tissue rearrangement which fills defects with adjacent healthy tissue, microsurgical tissue transfer whereby one area of the body is transferred with its blood supply to another area[7,28], and vascularized composite allotransplantation whereby a portion of the body containing skin, muscle and/or bone is transplanted from one patient to another[29]. However, the major challenges with using traditional reconstructive surgery to treat large craniofacial defects are donor-site morbidity and procuring sufficient donor tissue with the same properties, including skin color, quantity and contour of bone, and quantity and quality of subcutaneous tissues, as the surrounding recipient tissue to restore normal anatomic structure and primary organ functions.

The challenge of integrating the various tissues of the face while maintaining or improving aesthetics motivates collaboration between the fields of prosthetic rehabilitation, craniofacial reconstruction, and regenerative medicine.

Prosthetic Rehabilitation refers to the use of custom-made facial prosthetics to restore normal facial appearance (**Figure 2-1A**).

Reconstruction of the craniofacial region can be performed using a variety of plastic surgery techniques to replace structures and is aided by the precise manufacture of cutting guides, fixation devices, practice models and implanted medical devices (e.g. **Figure 2-1B**).

Regeneration aims to stimulate regrowth of damaged or malformed craniofacial tissues using stem cells and biologically active scaffold materials. (**Figure 2-1C**). For a particular defect, these approaches may be employed individually or in conjunction with one another. However, a common thread is the need for patient-specific treatments that fit a particular defect site to achieve both aesthetic cosmesis and functional replacement. As such, 3D-printing techniques that can create highly complex craniofacial geometries with high fidelity are well-suited for addressing particular needs.

Figure 2-1. Examples of Rehabilitation, Reconstruction, and Regeneration. (**A**) Custom PDMS midfacial and ocular prosthesis. (**B**) Cutting and placement guides for auricular autogenous reconstruction. (**C**) 3D-printed maxilla, porous PCL scaffold.

Table 2-1. Summary of 3D-printing technologies used for treating craniofacial deformities

Treatment Type	3D printing Applications	Printing Methods	Qualities of Printed Material
Prosthetic Rehabilitation (Improve patient aesthetics)	□ Molds for casting duplicates □ Printed prostheses □ Surgical guides □ Auricle, orbit, and nose rehabilitation	□ Inkjet □ FDM	□ Lightweight □ Non-degradable □ Rigid or flexible □ Anatomical shape of the missing tissue □ Ultra-high resolution for molds or prostheses □ Color stability for prostheses
Reconstruction (Tissue grafting)	□ Surgical positioning and cutting guides □ Custom metal implants □ Bone reconstruction	□ FDM, □ Stereolithography □ Laser sintering □ Direct-ink writing	□ Rigid □ Non-degradable □ Biologically inert
Tissue Regeneration (Recapitulate native tissue structure and function)	□ Scaffold generation □ Cellular constructs □ Bone, cartilage, skin, muscle □ Composite craniofacial tissues	**Acellular:** □ SLS □ FDM	□ Degradable □ Porous □ Bioactive □ Tissue-like stiffness □ Anatomical shape of healthy tissues
		Bioprinting: □ Inkjet □ Extrusion □ Laser-assisted □ Stereolithography	□ Degradable □ Bioactive □ Biomimetic 3D-spatial organization of cells

Anatomical geometries can be captured using medical imaging such as computed tomography (CT), magnetic resonance imaging (MRI), or light scanning and then 3D-modeled digitally to create useful 3D-printed products. The particular method of 3D-printing affects the print outcome and may be selected based on the particular applications (**Table 2-1**). The primary methods for 3D-printing include fused deposition manufacturing (FDM), stereolithography (SLA), selective laser sintering (SLS), inkjet printing, inkjet bioprinting, extrusion bioprinting, and laser assisted bioprinting, which have been reviewed extensively[30,31]. Briefly, in FDM, molten material is extruded layer-by-layer onto a bed; once the material cools and solidifies, it serves as the foundation for the layer above it. While this method is easily applied to many materials – any material that can be melted and extruded – it requires support structures for printing overhangs. SLA uses a laser to solidify photocurable liquid polymers in a layer-by-layer fashion.[30] In contrast, SLS creates structures by sintering a powder bed layer-by-layer. The powder that is not sintered therefore serves as the support structure. A variation of this method, inkjet writing, also uses a powder bed, but uses a chemical binder instead of a laser to bind the particles together. The similarly named, inkjet bioprinting, uses acoustic, thermal, or electromagnetic forces to eject hydrogel droplets, which could contain cells or biological molecules, onto a platform in an additive fashion, onto a clean print bed or a binding solution.[30] Extrusion bioprinting is similar to inkjet printing, but uses pumps, screws, or pneumatic systems to extrude cell slurries with viscosities too high for inkjet printing. Finally, laser-assisted bioprinting consists of a laser source, a glass "ribbon" covered with a layer of cells in hydrogel solution, and a receiving

22

substrate. The laser vaporizes a small portion of the hydrogel solution, which forms a bubble that can then fall as a droplet onto the platform below[30].

In this review, we examine how recent developments in 3D-printing enable more effective personalized treatment of complex craniofacial defects. We highlight advances in 3D-printing as applied to prosthetic rehabilitation, surgical reconstruction, and tissue regeneration for non-healing defects in the craniofacial region and identify avenues for further research.

3D-Printing for Prosthetic Rehabilitation

Recapitulation of patient specific coloring, texture, stiffness, and shape for prostheses is currently a labor-intensive process, which could be streamlined using 3D-printing. Prosthetic rehabilitation may be used in cases where successful surgical reconstruction is not a viable option due to factors such as poor prognosis, co-morbidities, compromised healing due to poor vascularization[32], and patient refusal of further surgical interventions[33]. Further, the economic burden and treatment time for prosthetic rehabilitation is lower than that of surgical reconstruction[34]. Typical sites for craniofacial prosthetic rehabilitation include oral, orbital, nasal, and auricular regions[35,36]. Prosthetic rehabilitation can also serve as an interim strategy during the period of treatment planning for a later surgical reconstruction[37]. Besides providing an aesthetic solution to covering an affected area, prosthetic devices are considered medically necessary due to the functional benefits they offer to warm incoming air, maintain humidity of moisture filled cavities, protect fragile tissue, modulate speech, and provide support for corrective eyeglasses.

Treatment of craniofacial defects with prostheses traditionally involves the creation of a custom made device generally made of polydimethylsiloxane (PDMS) to replace missing tissue and cover underlying tissue[35,36]. The workflow for creating these devices has gone relatively unchanged since the 1970's. However, the use of advanced 3D imaging techniques (including surface laser scanning and stereo photogrammetry) combined with 3D-printing is changing what was once a traditionally based workflow to include several facets achieved through digitally analogous methods (**Figure 2-2**). Only one study to date has reported a clinically viable workflow for directly 3D-printing these devices[38]. It is still limited, however, as it does not result in a fully colorized prosthesis with physical properties similar to the PDMS devices typically made by traditional methods. An alternate approach has been to 3D-print a negative multiple-piece mold that can be used for casting the final PDMS prosthesis. Advanced digital technologies and additive manufacturing techniques can thus be leveraged in craniofacial cases to increase the quality of outcomes for prosthetic rehabilitation. Future development of methods to directly print fully colorized PDMS prosthetics could significantly improve manufacture time and costs for craniofacial prostheses. A number of companies are developing technologies to directly print PDMS[39–41] and new techniques to precisely color complex and soft constructs (such computational hydrographic printing[42]) offer exciting methods to fully recapitulate the appearance of the prosthetic.
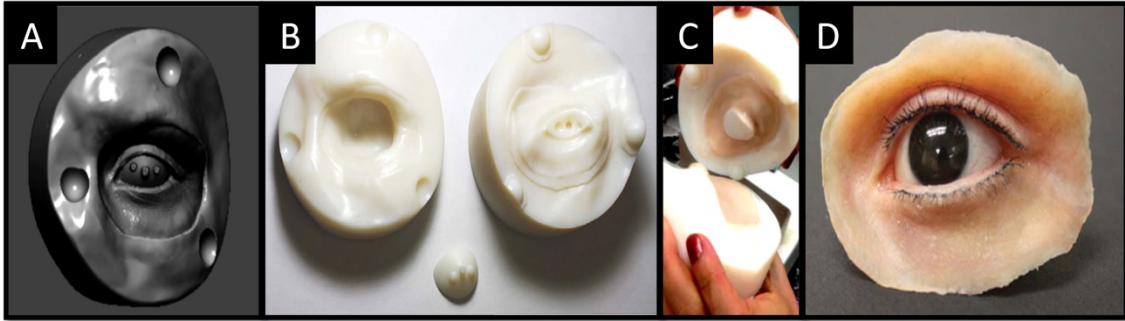
Figure 2-2. Example prosthetic design process.
(**A**) Orbital mold 3D model obtained through a fully digital workflow. (**B, C**) Resulting 3D-printed 3-piece mold that can be used for casting PDMS prosthesis. **(D)** The final PDMS prosthesis can be colored and provide satisfactory cosmesis. Photos used with author's permission. (Perry, R. The Development of an Orbital Prosthesis Workflow Using Advanced Digital Technologies, A thesis submitted to Johns Hopkins University in conformity with the requirements for the degree of Master of Arts, Baltimore, Maryland October, 2015)

3D-Printing for Surgical Reconstruction

3D modeling and manufacturing tools can provide aid in the personalized, surgical reconstruction of complex craniofacial defects by precisely cutting tissues according to preoperative plans, decreasing the total time and cost of surgery, and planning the shape of alloplastic and metal materials. Furthermore, such tools have helped to improve precise shaping and positioning of the newly incorporated tissues and improved the cosmetic and functional outcome of reconstructive operations[43] and are useful for patient education[44]. Tools that are used transiently in the reconstruction process, such as placement or cutting guides, are produced using FDM or SLA out of sterile and bioinert materials such as acrylonitrile butadiene styrene (ABS), poly(methylmethacrylate) (PMMA), or polypropylene[45]. Implanted products additionally require long-term biocompatibility and mechanical strength and are often laser sintered from titanium or bioglass. Both types of products are often accurate to the millimeter scale.

VSP and Guides

Advances in 3D imaging and manipulation of the resulting datasets have enabled surgeons to plan surgeries using computer models of the patient, virtually moving bones and other tissue to assess different approaches, options, and outcomes (**Figure 2-3**). This virtual surgery planning, together with rapid physical modeling of the defects and custom cutting and positioning guides, has vastly improved preoperative planning techniques compared to more traditional approaches, and has significantly aided the surgeon in his or her approach to complex craniofacial reconstruction[46,47]. 3D modeling and virtual planning aids intraoperative precision and efficiency of the surgery to match the preoperative design. Models of the defect site and the transferred bone segments can be manufactured to practice positioning, fixation, and evaluate aesthetic outcomes[48]. Such planning segues easily into precise, custom cutting and placement guides, increasing cosmesis and reducing ischemia and total surgery time. Consider the clinical standard for reconstruction of mandibular bone, the free fibular flap[49]: the fibula and the defect site are first scanned using CT (**Figure 2-3A**), then cuts are made in the fibula to adequately position the grafted bone into the defect site (**Figure 2-3C**). To aid in the precision of harvesting and repositioning the pieces of fibula, cutting and placement guides are designed and rapidly manufactured, often through FDM (**Figure 2-3D**). Finally, custom surgical guides have been essential in enabling the advent of facial transplants—in addition to the planning and guide fabrication, 3D-printing is essential in preparing an exact fit for the donated face[50].
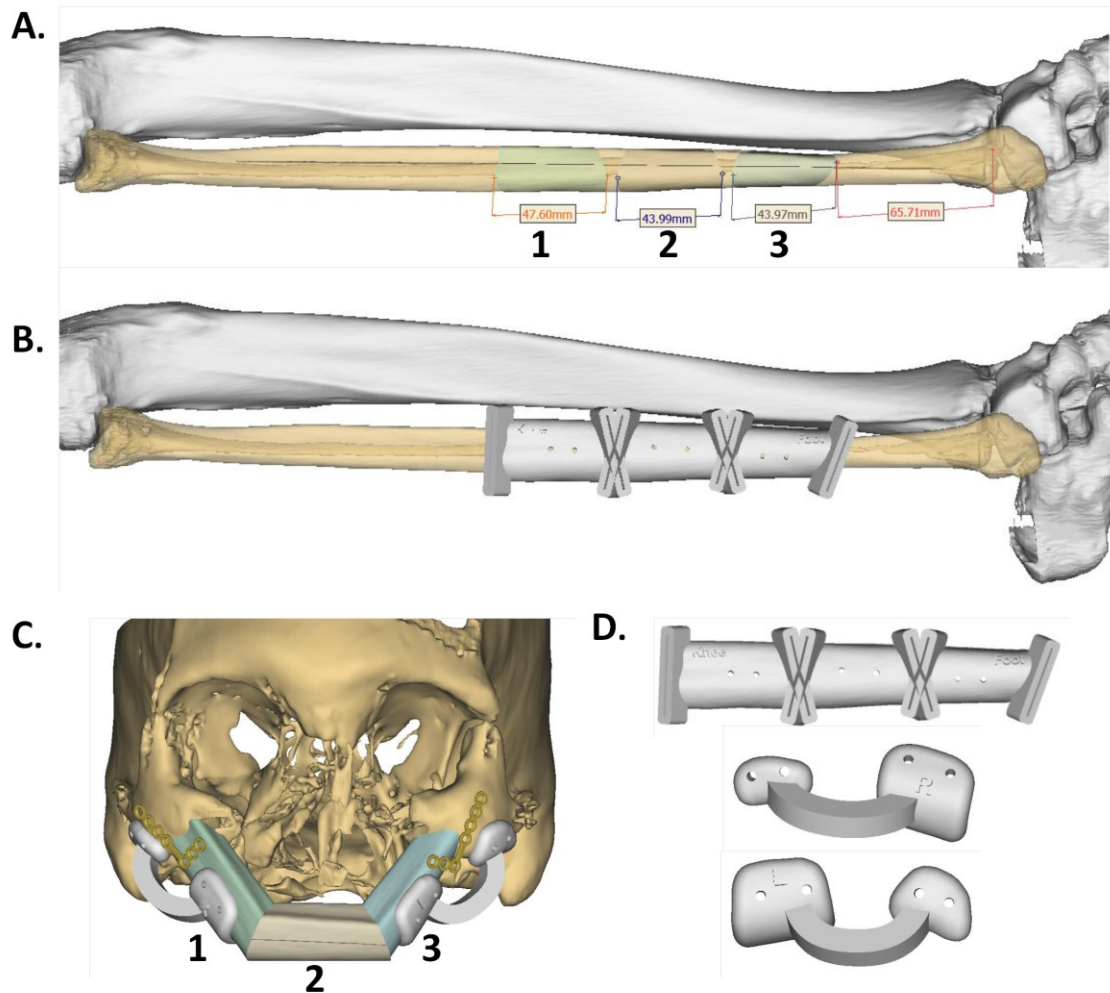
Figure 2-3. Virtual Surgery Plan and 3D-printing Cutting and Placement Guides. From the Synthes Pro Plan. (**A**) Pre-operative CT Scan of the right fibula. Graft pieces are labeled beginning 6.6 cm from the distal end of the fibula. (**B**) Planned cutting guide superimposed over the fibula. (**C**) Planned fibular flaps in the context of the remaining zygoma, using the positioning guides and exact graft pieces. (**D**) 3D-printed parts delivered to the surgeon include an anatomic guide, the fibula cutting guide, and positioning guides.

Pre-fitting Implants

Rapid prototyped models of the defect, or the predicted defect, are also used to pre-bend generic off-the-shelf implants such as reconstruction plates and titanium meshes to fit the specific anatomy of the patient. Such precise and methodical pre-bending can result in improved functional and aesthetic outcomes[12], decreased subjectivity[51], and reduced surgery and ischemia time[47]. Stereolithographic models of the defect site have also been used to mold PMMA to fashion an alloplastic bone-graft alternative[52]. In addition, 3D-printing models of ideal and patient-specific anatomy produced by mirroring a normal contralateral side has been used to press fit a composite titanium and porous polyethylene implant, and then guide the surgical placement in order to reconstruct the orbital floor after facial trauma[53]. These methods allow for the customization of patient implants without significantly changing the manufacturing process of the device, which is a major regulatory and production hurdle.

Materials for Patient Specific Implants

Non-resorbable implants can be designed and manufactured specific to individual patients and can used in lieu of autologous tissue[54]. Many materials including metals, bioglasses, and bio-inert plastics can be used in a number of manufacturing processes and maintain biocompatibility over time. For example polyetheretherketone (PEEK) has strong biocompatibility, mechanical strength, and radiographic translucency and can be 3D fabricated into patient specific implants through laser sintering or Computer Numerical Control (CNC) machining[55]. In addition, patient-specific titanium mesh can be manufactured via direct metal laser sintering to hold grafted bone in place and re-create contours

and structures of the facial bone[56]. Bioglasses (such as S53P4, 6P53B, and 13-93) have been widely used in craniofacial surgery as a bone graft substitute due to their biocompatibility, strong mechanical strength, and osteoconductivity[57,58]. Bioglass structures can be manufactured by mixing glass particles into a solution, cold-printing in a layer-by-layer fashion, and then dehydrating at high temperatures to sinter the glass particles together and remove the solution[59,60]. Others have reported formulations of bioglass (such as 13-93 which has the composition $53SiO_2$, $6Na_2O$, $12K_2O$, $5MgO$, $20CaO$, $4P_2O_5$; wt.%) which can be laser sintered into anatomic shapes[61]. Hydroxyapatite (the main component of bone) implants, via a resin carrier, can be produced through SLA and have been used to reconstruct large (>20 cm^2) defects with resolutions less than 0.4mm [62]. Finally, in 2012 a titanium mandible was laser sintered and implanted into an 83-year-old patient. The patient was able to speak and swallow the same day, and exhibited excellent restoration of facial aesthetics[63]. While titanium is the industry standard in orthopedic implants, the cost of materials, unknown long-term efficacy, and manufacturing remain limiting. There is particular concern of implant exposure and infection over time as there is often only a thin layer of soft tissue covering the implant.

As the intersection of 3D imaging, manipulation, design, and manufacturing develops further, these tools for surgeons will broaden from individual case studies to common practice. The past decade of developing these tools apace with the maturation of 3D technology will likely revolutionize surgical standards, just as 3D-printing has revolutionized transradial prostheses[64,65]. Increased efficiency and accuracy provided by these tools will be driving factors of their widespread

adoption while regulatory, biocompatibility, and reimbursement challenges remain[66]. Innovation stimulated and facilitated by these 3D technologies will also continue, leading to techniques as impressive as the recent total face and jaw transplants[29,50].
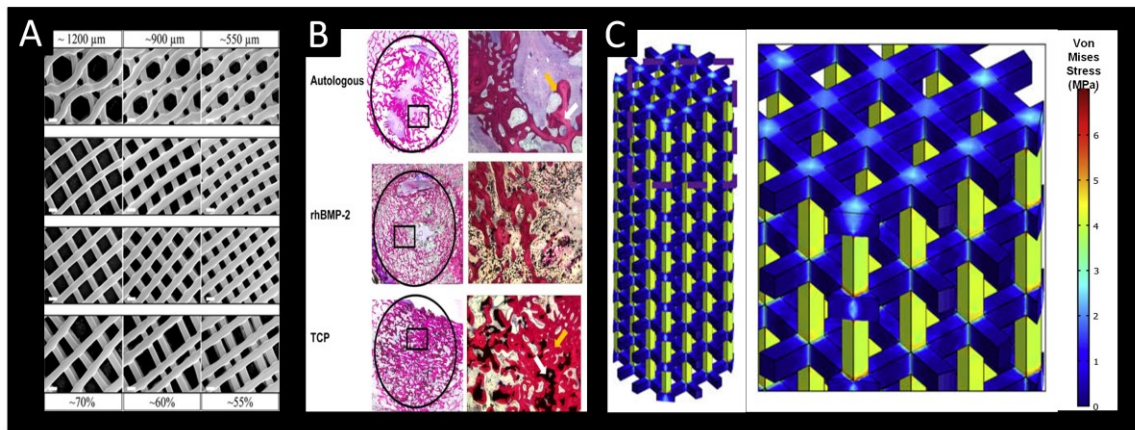
Figure 2-4. Features of 3D-printed scaffolds for regeneration.
(**A**) The scaffold should have appropriate micro-architecture, encompassing pore size and porosity. Using direct ink writing of a ceramic powder in a viscoelastic solution, different well-defined pore geometries were manufactured and visualized under scanning electron microscopy. Scale bars represent 500 μm. Adapted from [67]. (**B**) Cells residing within the scaffold should be signaled appropriately to regenerate tissue. Sintered tricalcium phosphate scaffolds were implanted in critically sized iliac defects in sheep. Bone formation by resident cells, denoted by the red stain, is evident when compared against other osteoinductive materials (bone morphogenetic protein and autologous bone graft). Adapted from [68]. (**C**) The mechanical properties of the scaffold must be appropriate for the tissue being regenerated. Selective laser sintering of polycaprolactone was used to fabricate a porous cylinder, which was tested mechanically to result in a stiffness of 15 MPa, within the range of trabecular bone. Adapted from [69].

3D Printing for Craniofacial Bone Regeneration

The goal of a 3D-printed construct for regeneration is to fill the defect with biological tissue. To accomplish this, an appropriately shaped construct can be produced that is populated uniformly with tissue-forming cells that are signaled to regenerate tissue. This can be accomplished in two ways: printing of acellular scaffolds that can be populated with cells prior to implantation or the printing of living, cellular constructs, termed '*bioprinting*'.

Acellular Printing

Several key parameters should be considered and optimized for scaffold development: (1) macro-geometry (**Figure 2-1C**), (2) micro-architecture, (3) bioactivity, and (4) mechanical properties (**Figure 2-4**). The strengths and weaknesses of these currently investigated printing approaches to achieving the four considerations outlined above are discussed below.

Incorporating micro-architecture, which encompasses pore geometry and pore size, is critical for uniform cell distribution and cell migration into the scaffold; interconnected pores can improve integration of regenerated tissue with native tissue.[70] For bone tissue engineering *in vivo,* higher porosity has been correlated with increased bone ingrowth into scaffolds.[71] Designing pore architecture results in higher pore connectivity and uniform cell distribution compared to random architecture resulting from salt-leaching methods, despite similar porosity, pore size, and surface area[72]. Pore size and interconnectivity also improves nutrient diffusion into and waste diffusion out of scaffolds.[73] Scaffold vascularization, a critical component of tissue survival, has been shown to increase with increasing pore size; pore sizes between 160-270 μm resulted in extensive vessel formation

in both mathematical and experimental models[74,75]. Osteoblast proliferation and migration through collagen-glycosaminoglycan scaffolds also depends on pore size, with larger pores around 300 μm resulting in higher cell numbers throughout the scaffold[76]. In the context of 3D-printing, some methods are better suited to creating defined pores. For instance, FDM relies on rapid cooling of an extruded molten material, resulting in well-defined scaffold struts and well-defined pores[77]. In contrast, chemical binding-based approaches rely on dispensing a liquid binder onto a powder substrate and result in pore sizes less than 100 μm due to binder flow[78].

The scaffold should also provide biological signals to resident cells to form tissue. For bone, the most widely used strategy is incorporation of mineral phases in scaffolds for osteoinductivity[79]; similar strategies have been investigated with 3D-printed scaffolds. For example, a phosphoric acid binder was used to bind calcium phosphate together, creating a mineralized structure that can house cells[78]. Another method used polycaprolactone (PCL) with incorporated tricalcium phosphate particles in FDM[80]. In addition, incorporation of bioactive molecules, such as bone morphogenetic proteins (BMPs), have been investigated; however, given most 3D-printing methods rely on high temperatures, up to 1300 °C for sintering methods[81], use of growth factors in 3D-printing remains a challenge. Chemical binding methods have the distinct advantage of printing at room temperature, creating potential for application of the method to growth factor incorporation, though careful choice of binder is required to prevent pH-related damage. A second approach is to load growth factors onto a scaffold post-printing, which circumvents these issues but adds another step to scaffold manufacturing.

Finally, in the replacement of craniofacial bone, the scaffold must provide structural support for both resident cells and for transduction of mechanical forces through the craniofacial skeleton. Target scaffold stiffness depends on anatomical location, with the elastic modulus of human trabecular bone within the mandibular condyle ranging between 120-450 MPa or within the mandible from midline to ramus ranging from 112-910 MPa.[82] Many current 3D-printed scaffolds have achieved stiffness within the 10-100 MPa range[78,82–84]. Testing mechanical properties of polymeric scaffolds under physiological conditions is crucial as groups have shown changes in compressive moduli at different temperatures and in aqueous media.[84] It should be noted that increased porosity leads to lower mechanical properties – a study using sintered PCL reported that the stiffness of printed porous scaffolds was around 15 MPa, compared to 300 MPa for a solid PCL piece[85]. As such, the importance of porosity for cellular ingrowth and proliferation must be balanced against the importance of structural scaffold properties for mechanical support and force transduction.

The importance of these four criteria is clearly demonstrated in the clinical regeneration of soft and osseous tissue holding the left mandibular cuspid in place[86]. Using the patient's CT scan the exact macroscopic geometry of the scaffold was determined. The scaffold was printed using SLS of PCL containing 4% hydroxyapatite for osteoinductivity. In addition, the scaffold was designed to release platelet-derived growth factor BB (PDGF-BB), a factor known to support vascularization and mineralization[87,88], in a burst manner from pre-formed channels. Due to the high printing temperatures associated with sintering, the scaffold was first printed without growth factor and immersed in PDGF-BB solution

for 15 minutes after printing. The use of PCL as the main biomaterial was justified from a mechanics standpoint: the stiffness of PCL scaffolds manufactured using SLS has been reported to be ~15 to 300 MPa, depending on porosity[85], values that fall within the reported range for human trabecular bone.

The scaffold porosity or micro-architecture was not reported, though the lack of interconnected pores was noted as a limitation of the approach. The implantation of the scaffold was successful – the image-based geometry fit the defect well – and the printed channels for growth factor release successfully dispensed PDGF-BB in a burst manner[86]. As a shortcoming, the patient presented with scaffold exposure and wound failure past 13 months post-implantation. Upon removal of the scaffold, histological analysis indicated a preponderance of connective tissue formation and little bone regeneration, suggesting the lack of internal micro-architecture prevented the infiltration of regenerative and vascular cells and therefore precluded regeneration. Combined with the slow-degrading properties of PCL, the authors concluded that the scaffold's low porosity served to block tissue regeneration. As such, while the macro-geometry and mechanical properties were appropriate (over the 13-month period, the scaffold did not fail mechanically despite being in a region of load), the lack of micro-architecture inhibited the bioactive and regenerative properties of the scaffold.

This example of the clinical application of 3D-printing scaffolds for craniofacial regeneration highlights strengths and necessary improvements. The combination of image-based extraction of craniofacial geometry and the ability to 3D-print shapes with high fidelity resulted in a scaffold tailored to the specific defect. The ability to incorporate bioactive factors into the printed scaffold was also

demonstrated. Finally, the choice of PCL as a printable biomaterial illustrated the ability to print mechanically appropriate scaffolds for load-bearing craniofacial regions. In addition to the group featured in this case study, other groups have commercialized FDA-approved PCL scaffolds fabricated by FDM[89].

A relatively underexplored area of 3D-printed scaffolds involves printing biological and mechanical gradients. For example, printing scaffolds with hydroxyapatite gradients could improve bone formation with exterior areas having more mineral to encourage growth of compact bone and interior areas having more diffuse mineral to mimic trabecular bone. While printing with growth factors has been a challenge due to printing conditions for many techniques surpassing biological pH and temperatures at which these molecules are stable, several groups have printed bioactive ceramics or extracellular matrix (ECM)[27,90]. The incorporation of ECM enhanced scaffold bioactivity, but high ECM concentrations decreased scaffold mechanics. Printing extracellular matrix proteins in 3D spatial gradients has been achieved by using mask-based SLA to stimulate assembly of genetically engineered photoactive proteins, though this was used as a surface modification for tissue culture rather than an implantable 3D construct[91]. Another group used inkjet printing to create gradients of laminin and used their materials to study cell alignment[92].

Printing mechanical gradients by varying pore structure and size could also assist with building tissue that mimics native function, particularly in the bone example. One group has recently demonstrated that gradient pore sizes created by FDM can slightly improve both chondrogenesis[93] and osteogenesis[94], although they did not investigate different geometries. By designing scaffold pore sizes and

35

geometries based on biological mechanical requirements, these improvements may be further enhanced.

Bioprinting

Bioprinting differs from the traditional tissue engineering approach of seeding cells onto preformed scaffolds by depositing cell and scaffold simultaneously, forming a predesigned structure[95]. Bioprinting is the computer-aided deposition of living cells into 3D patterns. It is currently performed with micron-scaled precision[31]. As cell viability must be maintained during the printing process, the methods used for bioprinting differ from those used for traditional 3D-printing. Important parameters of 3D-bioprinting scaffolds include (1) cell positioning, (2) bioink selection, and (3) mechanical strength. In many cases, the type of bioink used and the required resolution dictates the optimal printing technique for a particular application.

Bioprinting offers a key advantage over the traditional approach of seeding cells into 3D-printed scaffolds: digitally designing layer-by-layer deposition of cells to precisely regulate 3D cell distribution. This is advantageous when designing vascularized soft tissue, as adequate nutrient and oxygen supplies are necessary during tissue regeneration[96]. For example, Kolesky et al. developed a bioprinter that could print up to four cell types simultaneously and created complex 3D patterns of fluorescently labeled human dermal fibroblasts and human umbilical vein endothelial cells[97]. However, there are also several challenges associated with cellular printing.

Another disadvantage of bioprinting compared to acellular printing is that the mechanical strength of bioinks is typically lower than thermoplastic polymers.

36

Originally, the majority of bioinks were natural hydrogel polymers, particularly alginate and fibrin, which when printed have compressive moduli of approximately 5 kPa[98]. Human bone and cartilage typically have moduli of about 10-20 GPa and 700 kPa, respectively[99]. In order to print tissues having similar load-bearing capacities to native bone and cartilage, PEG-based hydrogels have been printed with compressive moduli between 300-350 kPa[100]. Another method used to improve mechanical strength is integrating acellular and cellular bioprinting. Merceron et al. used a combination of FDM and extrusion bioprinting to print two thermoplastic polymers along with C2C12 and NIH/3T3 cells to create a 3D-printed muscle-tendon unit[101] and Kang et al. integrated FDM and extrusion bioprinting to print vascularized bone, muscle, and cartilage[102]. Printing hybrid scaffolds with cellular and acellular components may be one way to improve mechanical strength of bioprinted scaffolds. These limitations are some of the reasons that bioprinting has not yet been used to regenerate craniofacial tissues in human patients.

Of the tissues necessary for craniofacial reconstruction, skin bioprinting is the nearest towards clinical translation, with studies conducted *in vivo* using mice and pigs. One study of note compared bioprinted scaffolds to a commercially available engineered skin graft (Apligraf)[103]. A current limitation of engineered skin grafts such as Apligraf is that they lack microvasculature to maintain cell viability over time and instead rely upon diffusion to transport oxygen and nutrients to cells. Bioprinting can overcome this limitation by precisely patterning microvascular structures for skin grafts. Bioprinted scaffolds were trilayered with the top layer composed of collagen and printed keratinocytes, the middle layer composed of fibrin and endothelial cells, and the bottom composed of collagen and fibroblasts.

37

Apligraf is a bi-layered material cast with two collagen layers: one containing dermal fibroblasts and the other containing keratinocytes[104]. The group found that wound contraction, which if excessive can be a marker for joint contraction, malfunction, and poor aesthetic outcomes decreased in the bioprinted scaffolds compared to Apligraf and no treatment, which were statistically similar. Additionally, the mice with printed grafts healed between 14-16 days, whereas those with no grafts or with Apligraf healed within 21 and over 28 days, respectively. Histologically, the printed groups showed microvessel formation by implanted human endothelial cells in the printed scaffolds. Macroscopic images of skin regeneration in Apligraf and bioprinted groups can be seen in **Figure 2-5A-F**. Patterning endothelial cells to form lumenized microvessels to improve graft viability could allow for scale up in terms of graft thickness and area by reducing oxygen and nutrient diffusion limitations. Binder *et al*[105] have developed a promising *in situ* bioprintier for skin, but initial preclinical tests in pigs demonstrated unsatisfactory healing outcomes in wound closure rates, which the authors suggested was due to an insufficient cell density (2.0×10^5 cells/cm^2). While the bioprinted materials have improved skin wound healing in terms of decreasing wound contraction and healing time *in vivo* is a promising advance for skin bioprinting, but such methods are still inferior or comparable to cell spraying techniques[105].

Bioprinting of bone has also moved forward, with some preliminary bioprinting studies conducted *in vivo*. Of particular import is a pilot study conducted by Keriquel *et al.* that investigated the use of laser assisted bioprinting to manufacture hydroxyapatite scaffolds directly into a calvarial defects in mice, as

seen in **Figure 2-5G, H**[106]. When bone formation was measured by X-ray micro-tomography at the group observed considerable variation in bone formation between individual mice and did not provide quantitative data for bone ingrowth. Though these results are preliminary, they do show that bioprinting *in vivo* is possible and may have potential for clinical use with the proper bioink and cell source.

The precise patterning of biological molecules and cells through bioprinting may be useful in creating tissues with complex spatial orientations. Though the field is young, promising results have been achieved for skin and bone engineering *in vivo.* Studies have investigated cartilage[107], muscle[101], and adipose[108] tissue engineering using bioprinting, though these have not yet advanced to *in vivo* studies. The expensive specialized equipment necessary to use bioprinting technologies and the added regulatory burden of incorporating cells into a biomaterial, acellular printing may be the preferred regenerative method for treating craniofacial defects. Bioprinting could be further improved by widening the selection of available bioinks, decreasing print time, increasing print resolution, and moving more studies towards *in vivo* models.
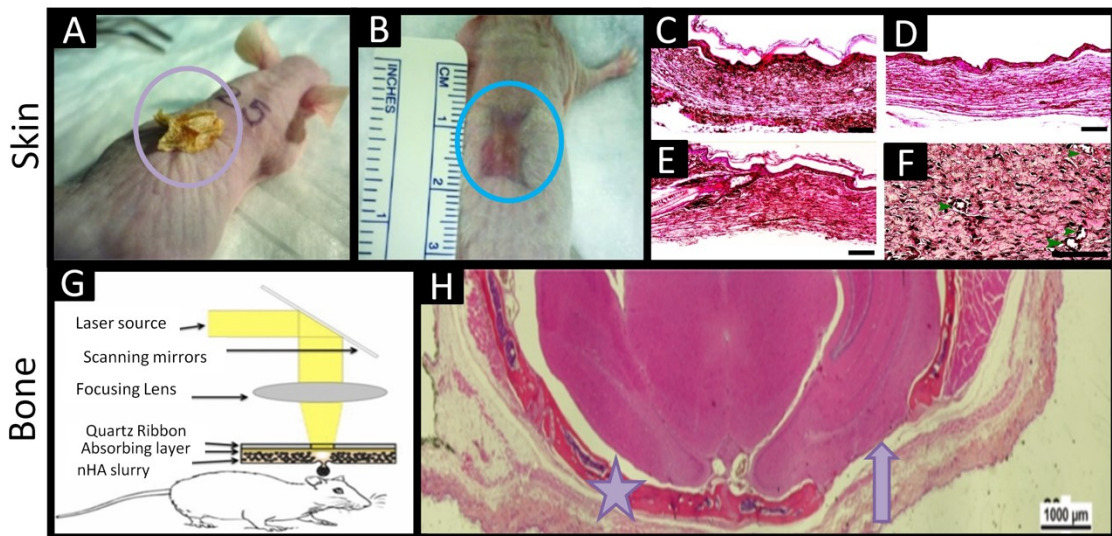
Figure 2-5. Bioprinting for engineering skin and bone tissues.

Full thickness dermal wounds after 4 weeks of healing with (**A**) Apligraf applied, denoted by the yellow circle and (**B**) 3D-bioprinted skin applied denoted by the blue circle. Severe wound contraction and scaffold drying took place in the Apligraf scaffold compared to the bio-printed scaffold with microvessels. **C-E.** H&E stains of (**C**) Apligraf, (**D**) no treatment, and (**E**) 3D-bioprinted skin scaffold. (**F**) A higher magnification image of 2 weeks of healing following application of 3D bioprinted skin. Adapted from [103]. (**G**) Schematic of laser-assisted bioprinting directly into mouse calvarial defect. nHA slurry refers to a nano-hydroxyapatite suspended in a glycerol solution for printing. (**H**) H&E stain 3 months after calvarial defects were made. Bone healing observed in the area where the 3D bio-printed scaffold was applied (denoted by the star) and no bone healing in the no scaffold control (denoted by the arrow). G and H adapted from [106].

Conclusion

Craniofacial deformities, when they arise, are particularly debilitating as they impact emotional, psychosocial, and functional well-being of the affected individual. They are difficult to treat due to the geometrical requirements and multiplicity of tissue types that are impacted. However, recent advances in 3D-printing technologies hold tremendous promise for advancing treatment options available to patients. The requirements of 3D-printed products differ depending on the size and severity of the defects, which together with patient-specific factors determine whether the primary treatment modality is prosthetic rehabilitation, surgical reconstruction, or regeneration. For rehabilitation, the use of 3D-printing technologies to either directly create PDMS prosthetics or print molds has the potential to significantly streamline the associated workflows for this process. The prostheses are flexible, non-degradable, and need to incorporate patient-specific skin tones. They differ considerably from 3D-printed guides or alloplastic implants used in reconstructive surgeries. Perhaps the most transformative applications, of 3D-printing lie in the realm of tissue regeneration. This area remains relatively nascent to date and significant research efforts are being dedicated to its continue rapid advancements that include the development of biodegradable scaffolds as well as bioinks used for printing live cells. The successful implementation of these technologies clinically will expand the treatment options available to patients.

CHAPTER 3[**]
GROWTH FACTOR ELUTING SCAFFOLDS
FOR BONE TISSUE ENGINEERING

Summary

Growth factors are essential orchestrators of the normal bone fracture healing response. For non-union defects, delivery of exogenous growth factors to the injured site significantly improves healing outcomes. However, current clinical methods for scaffold-based growth factor delivery are fairly rudimentary and there is a need for greater spatial and temporal regulation to increase their *in vivo* efficacy. Various approaches used to provide spatiotemporal control of growth factor delivery from bone tissue engineering scaffolds include physical entrapment, chemical binding, surface modifications, biomineralization, micro- and nano-particle encapsulation, and genetically engineered cells. Here, we provide a brief review of these technologies, describing the fundamental mechanisms used to regulate release kinetics. Examples of their use in pre-clinical studies are discussed, and their capacities to provide tunable, growth factor delivery are compared. These advanced scaffold systems have the potential to provide safer, more effective therapies for bone regeneration than the systems currently employed in the clinic.

[**] Adapted from Nyberg, E., Holmes, C., Witham, T., & Grayson, W. L. (2016). Growth Factor-eluting Technologies for Bone Tissue Engineering. *Drug Delivery and Translational Research*, *6*(2), 184-194.

Introduction

Skeletal injuries from trauma, tumors, infections, and degenerative diseases often require a significant intervention, such as bone grafting, to facilitate healing. While 1.6 million bone grafting procedures are performed per year in the United States, the current gold standard – autologous bone grafts – is expensive, inefficient, causes donor site morbidity, and is limited in supply and size[109]. Therefore, there remains a critical need for effective alternatives to bone grafts.

Growth factors are key components in the regenerative process leading to scarless bone regeneration. A complex spatiotemporal cytokine cascade orchestrates healing following bone fracture[110]. Inflammatory cytokines cause an invasion by lymphocytes, plasma cells, macrophages, and osteoclasts. Invading macrophages clean up necrotic centers in the graft and release tumor necrosis factor (TNF), which drives increased osteoclast activity. Osteoclasts resorb fractured bone matrix, releasing incorporated insulin-like growth factor (IGF) and bone morphogenetic proteins (BMPs), and these cause osteoblastic differentiation of progenitor cells[111,112]. Neovascularization of the fracture site occurs early in this process as endothelial cells begin sprouting angiogenesis in response to vascular endothelial growth factor (VEGF) and low oxygen tensions in the graft[113]. Endothelial cells are the primary source of BMPs within the fracture site driving osteogenesis of osteoblasts. Osteoid production by those osteoblasts begins on the outside of the fracture, creating a callus and mechanically integrating the bone[114]. Platelet-derived growth factor (PDGF), transforming growth factor-β (TGF-β), and fibroblastic growth factor (FGF) released from plasma cells, macrophages, and osteoblasts support cellular proliferation and

differentiation[112,115,116]. Finally, remodeling into organized continuous bone progresses over several months according to Wolff's law.

Several of the key growth factors identified above as having critical roles during normal healing (**Table 3-1**) have been utilized in various clinical approaches to treat bony non-unions. The timing of therapeutic growth factor delivery is crucial to optimize tissue induction while minimizing adverse or inhibitory effects. However, growth factors have short half-lives and rapid clearance rates *in vivo*, particularly when delivered systemically[117,118]. Bone tissue engineering (BTE) scaffolds have been used as a feasible treatment methodology to provide temporary mechanical support for cellular ingrowth and to actively guide tissue organization. Additionally, 3D scaffolds can localize and control the temporal delivery of protein growth factors and/or genes required for optimal *in situ* bone development and/or repair. The incorporation of growth factors into scaffolds has considerable potential to enhance healing outcomes. Here, we review growth factor eluting technologies that can be employed to produce such scaffolds.

Table 3-1. Clinically Applied Growth Factors for BTE

Factor	Action	References
Bone Morphogenetic Proteins (BMP)	Bone induction	119–125
Vascular Endothelial Growth Factor (VEGF)	Angiogenesis	126–130
Platelet Derived Growth Factor (PDGF)	Cell proliferation and recruitment and vascularization	115,131,132
Fibroblast Growth Factor (FGF)	Angiogenesis, proliferation and osteogenic differentiation	116,133–136
Insulin-like Growth Factor (IGF)	Osteogenic Differentiation	111,137–140
Transforming Growth Factor Beta (TGF-β)	Osteogenic, Chondrogenic differentiation	112,138,141

Growth Factor Incorporation Strategies

A wide variety of factors – ranging from scaffold material and architecture, to the dosing and release kinetics of the incorporated growth factors – must be optimized in designing an inductive scaffold-based delivery system for BTE applications. The scaffold should exhibit suitable mechanical properties and a biodegradation rate that enables both controlled growth factor delivery and integration with host tissue. These scaffold properties are determined by the materials employed and the processing and biofactor incorporation strategies utilized. Decades of research into drug delivery materials have yielded a broad array of naturally- and synthetically-derived, biodegradable materials which can be employed to produce 3D scaffolds of varying architectures (reviewed in[142–144]).

Controlling growth factor dosage and release kinetics is key to optimizing tissue induction while avoiding adverse or inhibitory effects[145–147]. Currently, the growth factor dosage ranges being used are quite broad and clinical applications typically employ supraphysiological concentrations. Although some of this dosage variation is due to differences in the animal models utilized, there remain many questions regarding optimal target doses and release kinetics. In a study comparing burst release from collagen sponges (100% over 2 days) to polyurethane scaffolds with slow (~20% over 19 days) or fast (60% over 9 days) release of BMP-2 (all systems loaded with 2 µg), fast-releasing scaffolds showed the greatest *in vivo* bone formation (45 mm^3) in a rat femoral critical-sized defect model after 4 weeks, followed by the burst-release collagen scaffold (30 mm^3) and the slow release scaffold (10 mm^3)[148]. This suggests that an initial burst release

followed by a slow sustained release might be best means of delivering BMP-2 for bone formation.

However, the optimal therapeutic dosage and timing of release will depend heavily on the individual growth factor(s) and the particular application. One has to account for factors such as the anatomical location, size, and nature (e.g. trauma vs. tumor re-sectioning) of the bone defect, the extent of vascularization in the surrounding tissue environment, conjunctive therapies (e.g. chemotherapy or the use of metal supports), and the health of the surrounding tissues. For example, in comparing quick and slow release of BMP-2 for induction of bone formation in orthotopic and ectopic sites in dogs, Geuze et al found that while ectopic groups formed more bone in response to quick BMP-2 release, bone formation in the orthotopic site was independent of the release profile[146]. Furthermore, some growth factors are non-effective at low doses, require co-delivery of a second agent to be effective, or are harmful to cells with prolonged exposure. For example, high doses and/or prolonged exposure to BMP-2 in anterior cervical spine fusion cases has resulted in high rates (23%) of adverse effects in patients[149,150], while failure to shut down TGF-β in reparative processes can lead to a number of fibrotic diseases[151]. Finally, indefinite release is not required; rather growth factor delivery need only be maintained – at most – until the defect has healed, which potentiates bone repair technologies to transient gene therapy techniques[144–146].

In native tissues, growth factors are typically encrypted within the ECM where they are protected from enzymatic and hydrolytic degradation. Once they are released from these encrypted sites, the half-life of growth factors in vivo is short – on the order of several minutes – due to enzymatic degradation, chemical

and physical deactivation, and degradation processes such as hydrolysis, oxidation, isomerization, and aggregation[152,153]. Therefore, one of the most critical challenges in scaffold-based growth factor delivery is maintaining native protein conformation and bioactivity throughout scaffold loading and for the duration of in vivo release[154]. The architectural design, processing and storage of scaffold materials and the protein loading strategies must all be optimized to ensure delivery of functional growth factor for the duration of in vivo release. For example, Madurantakam and colleagues demonstrated that exposure of BMP to organic electrospinning solvents during growth factor loading affected its tertiary and quaternary protein conformation and impaired its bioactivity. In contrast using a 50% dilution in an aqueous buffer retained the bioactivity of the incorporated BMP[155]. Similarly, degradation products of scaffold carrier polymers, such as polyesters, can increase local acidity and lead to protein denaturation or degradation, while secondary protein-polymer interactions can trigger protein mis-folding and aggregation[156]. Efforts have also been made to prevent enzymatic degradation of growth factors by tailoring scaffold pore- size to reduce protease penetration into scaffold[153]. Employing a more biomimetic approach, heparin-binding is commonly used to maintain and enhance BMP presentation and bioactivity and increases the half-life of BMP in culture medium 20-fold[157–159].

To date, a variety of methods have been explored to incorporate drugs, protein growth factors, and DNA into 3D polymeric and composite scaffold systems and control their delivery. These approaches encompass bulk incorporation strategies and surface modification techniques, with the current trend moving

towards hybrid approaches to produce tissue engineering systems capable of multi-agent delivery and/or stimuli-responsive release (**Figure 3-1; Table 3-2**).
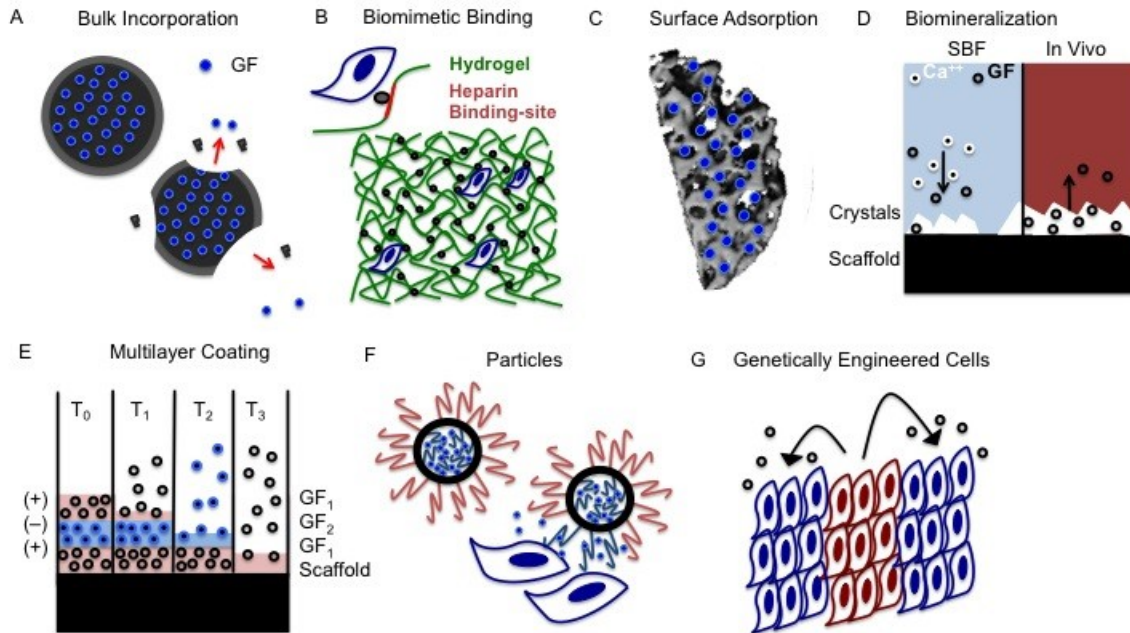
Figure 3-1. Methods of growth factor delivery
> **(A)** Bulk incorporation of GFs (blue) released with degradation of the bulk (black) material   **(B)** Hydrogels (green) can be modified for increased biomimetic affinity (red) to increase binding of GFs (black dots) and natural presentation to cells (blue)   **(C)** Growth factors (blue dots) can directly adsorb to the scaffold surface (grey) without specific chemical modification   **(D)** Biomineralization traps GFs (black dots) in the crystal formation (mediated by Ca^{++} in white) in simulated body fluid (SBF), and released as the crystals degrade *in vivo*   **(E)** Multilayer coating can facilitate multiagent (GF1 = black dots / GF2 = blue dots) delivery and staggered release of GFs over time (**F**) Nano and microparticles can deliver GFs (blue dots) to cells (blue) and can be functionalized with adhesion molecules (red) (**G**) Cells can be genetically engineered (red) to secrete GFs (black dots) to surrounding cells (blue)

Table 3-2. Advantages and Disadvantages of different drug eluting technologies

Method	Advantages	Disadvantages	References
Bulk Incorporation	Highly tunable	Processing may affect GF, Burst Release	160–168
Biomimetic Binding	Increased capacity and prolonged release	Complex loading	136,157,169–175
Surface Adsorption	Simple loading	Poor capacity and release kinetics	176,177
Multilayer Coating	Temporal release, multi-agent	Processing may affect GF	178–185
Particles	High payloads, release control, multi-agent	Complex loading	124,135,186–188
Genetically Engineered Cells	Enduring, bioactive delivery	Regulatory and safety concerns	141,189–193
Biomineralization	Increased osteoconductivity, biomimetic	Requires cell-mediated material degradation	23,194–200

Physical Entrapment Strategies

One of the simplest approaches to producing inductive tissue engineering systems is bulk incorporation, whereby the biofactors to be delivered are blended directly into hydrogels or within solid scaffold polymers and physically entrapped. Protein and/or DNA release kinetics from these bulk incorporation systems is typically characterized by an initial burst followed by slower release that is controlled by the diffusion and degradation rate of the matrix, which are in turn dependent on such properties as matrix, porosity, swelling behavior, polymer cross-linking density, and polymer chemistry (i.e. molecular weight, hydrophobicity/hydrophilicity, charge density). Loading efficiencies within bulk incorporation systems are generally high and are determined by factors including polymer and biofactor interactions, solubility, and concentration ratios, as well as the types of cross-linking interactions and processing times and temperatures employed. These parameters can be specifically tuned (within limits) for various localized, controlled release applications via careful design of polymer composition and scaffold processing techniques.

Solid Scaffold Polymer Blending

In solid polymer or composite scaffolds, biofactors can be directly blended with core polymers via formation of polymer-solvent and biomolecule-water emulsions and subsequent freeze-drying[160], or via gas foaming[161], which eliminates the need for organic solvents that can potentially denature or degrade proteins. For example, super-critical CO_2 processing was used to incorporate rhBMP-2 within PLA scaffolds (96 μg BMP-2) yielding systems, which released low amounts (674 ng over the first 48 hours, followed by 100 ng/mL per 72 hr) over a

period of at least 24 days. Although less than 5% of the initially loaded BMP-2 appeared to be released cumulatively, subcutaneous implantation in a rat model resulted in bone formation at 6 weeks (~12 mm^3) and persisted until at least 26 weeks[162,163]. Growth factors can also be directly incorporated within the strands of electrospun fiber-based scaffolds via blending prior to electrospinning, emulsion electrospinning, or coaxial electrospinning (reviewed in [201]). Srouji and colleagues used coaxial electrospinning to produce scaffolds composed of core-shell fibers with an inner rhBMP-2/PEO core and outer PCL/PEG shell. They found that the degree of porosity of the outer shell determined the BMP-2 release rate, and that slower-releasing scaffolds (which released 12 – 15% of the loaded BMP-2 in 27 days, with 5% released in the first 4 h) resulted in greater *in vivo* bone formation in a rat cranial defect model (80% coverage vs. 55% at 8 weeks), than faster-releasing scaffolds (76% in 27 days, with ~67% released in the first 4 h) [164]. BMP-2 has also been successfully incorporated into a variety of electrospun scaffold architectures composed of natural and synthetic polymers, including silk, PCL, PLLA, and PLGA, as well as polymer-ceramic composite fibers which integrated hydroxyapatite nanoparticles[164–168]. These direct blending strategies are limited in the scaffold architectures that can be produced, and generally display initial diffusive burst-release. Care must be also taken to ensure that processing conditions for the scaffolds do not reduce the bioactivity of the incorporated growth factors.

Hydrogel Encapsulation

Hydrogel encapsulation of drugs and biomolecules is one of the simplest and most popular strategies for producing 3D controlled delivery systems for tissue

engineering. Direct physical entrapment of proteins, drugs and DNA within hydrogels can be achieved via blending with matrix polymers prior to chemical or physical cross-linking. One of the key advantages to using hydrogels for controlled growth factor delivery is the wide array of stimuli-responsive polymeric hydrogels, which can be employed to produce on-demand release systems. However, hydrogel systems are severely limited in the scaffold architectures and mechanical properties that can be produced and are thus often used in hybrid strategies where they are infused into other scaffold structures. Furthermore, the hydrogel cross-linking strategy employed in growth factor encapsulation must be chosen so as to minimize any chemical or physical modifications of protein structure (e.g oxidation reactions, photo-degradation, or cross-linking with polymer chains).

A variety of "smart" hydrogel systems have been developed that respond to changes in temperature, pH, mechanical forces, electromagnetic fields, irradiation, ultrasound, or the presence or absence of certain solutes by dramatically altering properties such as their swelling behavior, network structure or degradation rate (reviewed in[202]). Similarly, biochemically-responsive hydrogels, which incorporate enzymatically-cleavable peptide linkage or cross-linking groups, such as matrix metalloproteinases (MMPs), result in cell-based enzymatic degradation and release of encapsulated growth factors. Holloway and colleagues developed such MMP-sensitive, cell-degradable hyaluronic acid hydrogels for BMP-2 encapsulation (100 ng BMP-2) and demonstrated that faster degrading gels (100% mass degradation and BMP-2 release in 6 days in the presence of collagenase *in vitro*) resulted in improved bone formation in a rat cranial defect model compared to slower degrading gels (100% degradation and release in 10 days)[203].

Chemical and Affinity Binding Strategies

Protein growth factors can also be covalently bound or linked via biomimetic interactions to the polymers that make up the hydrogel matrix in order to more precisely control their loading, distribution, presentation, stability, and delivery. Such chemical and affinity binding strategies generally reduce burst release and prolong growth factor delivery. However, care must be taken in designing the linkage strategy so that growth factor bioactivity is preserved.

Covalent Binding

A variety of covalent binding strategies can be employed to attach protein growth factors to matrix polymers thus enabling on-demand biofactor release. Such linkage strategies can be designed such that release is mediated either by hydrolysis, reduction reactions, or enzymatic degradation of the covalent bonds. For example, BMP-derived peptides functionalized with azide groups were covalently conjugated to PEG-based hydrogels via click chemistry and the resulting system was found to induce osteogenic differentiation of bone marrow stromal cells *in vitro*[204]. In designing such covalent protein-binding systems, however, one must ensure that the linkage process does not affect the biological activity of the proteins by blocking active sites or causing denaturation, and that those growth factors which require cellular internalization for proper function are bound via cleavable linkage strategies.

Biomimetic Binding Interactions

In strategies which mimic the natural interactions between proteins and glycosaminoglycans (GAGs) within the extracellular matrix (ECM), electrostatic and affinity interactions can be employed to aid in hydrogel growth factor loading.

In addition to retaining and delivering the growth factor over a longer period of time, one of the key advantages to utilizing such biomimetic strategies is that ECM- and GAG-bound growth factors are maintained in a more bioactive form than when diffusively released or presented via covalent tethering strategies[136,169]. Thus ECM-binding might allow for the use of more physiologically relevant quantities of growth factors rather than the currently employed supra-physiological concentrations.

Modification of hydrogel polymers with GAGs, such as heparin, which has been shown to bind protein growth factors, including BMP-2, FGF, and TGF-β [170,171], can increase growth factor loading, and prolong growth factor release, as well as protect encapsulated proteins from thermal degradation and proteolysis. Jeon and colleagues developed heparin-modified PLGA scaffolds which demonstrated ~99% BMP-2 loading efficiency and prolonged *in vitro* release over at least 14 days (19% day 1, steady rate until day 14) compared to similar unmodified PLGA scaffolds which demonstrated burst release (~100% over 4 hours). These heparin-modified scaffolds subsequently demonstrated 9-fold higher bone formation at 8 weeks compared to unmodified BMP-loaded scaffolds (both loaded with 1 µg BMP-2) in an ectopic bone formation rat hind-limb muscle model[157] In stark contrast, Bhakta *et al* found that hyaluronan-based hydrogels modified with heparin and loaded with BMP-2 (5 µg) resulted in less *in vivo* bone formation in a similar rat hind-limb muscle model than unmodified BMP-loaded hydrogels, and theorized that it was due to a lack of early burst release (~14 % during day 1 and a total release of ~ 68% vs. ~26% release on day 1 and a total release of ~84%)[172]. These disparate results utilizing different core scaffolds (i.e.

PLGA solid scaffolds vs. hyaluronan hydrogels) but the same growth factor imply that growth factor dosage and release kinetics alone may not dictate successful *in vivo* bone formation, but that scaffold architecture, porosity, and mechanical properties likely play key roles.

Another widespread biomimetic strategy for controlling biofactor delivery from hydrogels involves the incorporation of ECM peptide sequences. For example, Hubbell *et al* mimicked the blood clot microenvironment that forms after skeletal fractures by replicating fibronectin subdomains and attaching them to fibrin gels, thus resulting in improved retention of growth factors, such as PDGF, FGF-2 and TGF-β, over time and improved bone healing outcomes[173,174]. Similarly, Hamilton and colleagues screened a phage-display library of peptide sequences to identify BMP-2 binding peptide sequences that they then incorporated within injectable collagen matrices along with BMP-2, resulting in more than 10-fold higher BMP-2 loading, and increased bone formation and maturity *in vivo* in a rat ectopic bone formation model, compared to collagen matrices containing only BMP-2[175].

Surface Modification Strategies

In contrast to bulk incorporate strategies, surface modification techniques enable growth factor incorporation while preserving underlying scaffold architecture and properties. While surface modification strategies generally result in lower levels of growth factor incorporation, they enable delivery from a much wider variety of scaffolds and implant systems and materials, particularly those with increased mechanical strength. Techniques used to functionalize biomaterial surfaces with proteins, peptides, drugs and/or DNA, include simple surface

adsorption; "grafting-to" and "grafting-from" strategies; incorporation within electrostatic layer-by-layer films; and biomineralization.

Surface Adsorption

Simple surface absorption of biofactors onto scaffolds via dipping or incubation is one of the most commonly utilized techniques to produce localized delivery systems. Biofactor adsorption onto biomaterial surfaces is governed by a combination of non-specific physical forces, such as electrostatic interactions, van der Waals forces, hydrophobic/hydrophilic interactions and hydrogen-bonding interactions, which in turn are determined by a complex interplay of factors including the species and concentrations of biomolecules present in the incubation/dipping solution, the temperature, pH and ionic strength of the solution, and material surface properties such as topography, chemistry, charge, and wettability[176]. BMP surface adsorption onto various polymeric and composite scaffold systems, particularly collagen-based matrices, has been widely investigated, with varying strategies utilized to maximize the amount of adsorbed BMPs, such as increasing incubation time, altering the pH and ionic concentration of the solution, and introducing charged functional groups to the scaffold surface[177]. Non-specific surface adsorption onto scaffold surfaces typically results in low levels of biofactor loading and poor control of release kinetics. Better control of biofactor release from scaffold surfaces, meanwhile, is more easily achieved via surface immobilization methods.

Surface Immobilization

Direct immobilization of proteins and gene delivery vectors to scaffold surfaces, via covalent cross-linking or strategies involving antibody/antigen- or

biotin/avidin- binding, has been widely studied [205,206].   In the case of covalent surface immobilization, chemically- or physically-based methods are often employed to introduce reactive functional groups onto scaffold surfaces in order to activate them for subsequent grafting. Once a scaffold surface has been chemically functionalized, via partial surface hydrolysis, oxidation, aminolysis or plasma treatment, various reactions targeting primary amines and carboxylic acids can be utilized to immobilize protein growth factors, such as BMPs. Such surface conjugation of growth factors tends to increase protein loading and stability and prolong release compared to surface adsorption strategies. For example, when BMP-2 was immobilized onto the surface of aminolysed PCL scaffolds via sulfosuccinimidyl 4-(N-maleimidomethyl)cyclohexane-1-carboxylate (sulfo-SMCC) crosslinking, the resulting scaffolds demonstrated increased loading efficiency (~38.5 vs. ~9%), slower release (7% vs. 27% over 15 days) and increased in vitro osteogenic differentiation of bone marrow stromal cells, compared to similar PCL scaffolds with surface-absorbed BMP-2[207]. As in the case of covalent linkage of bio-factors within bulk hydrogels, covalent surface immobilization strategies must be sure to preserve protein confirmation and bioactivity and enable the release of growth factors which require cellular internalization for function.

Polyelectrolyte Multilayer Film Coating

Deposition of polyelectrolyte multilayer films has been widely investigated for surface-based controlled release of drugs, bioactive proteins, and plasmid DNA (reviewed in [178]). A simple and versatile technique developed by Decher and colleagues[179] electrostatic layer-by-layer (LbL) deposition involves the sequential surface adsorption of alternating layers of oppositely charged polyelectrolytes

(PEs) on nearly any charged substrate surface. Careful selection of the polyelectrolytes used and the layer architecture and chemistry employed enables both the tailoring of release kinetics and sequential delivery of several different proteins and/or genes[180,181]. LbL films can be composed from a wide variety of synthetic and natural polymers, and bioactive proteins, DNA and gene delivery vectors can be incorporated within PE multilayers without any need for covalent attachment[182] and can maintain a structure close to their native conformation. The deposition of PE multilayers onto 3D scaffolds has enabled scaffold-based delivery of both genes and proteins[183–185]. For example, 3D printed β-tricalcium phosphate/polycaprolactone scaffolds coated with LbL films consisting of a poly (β-aminoester) ("poly 2"), chondroitin sulphate (CS), and BMP-2, resulted in a system that successfully induced in vivo bone formation when implanted intramuscularly in rats[184]. Meanwhile, Hammond *et al* developed LbL nanolayer coatings of BMP-2 and PDGF on PLGA membranes and found that low-dose dual delivery resulted in better outcomes (healing rate, bone volume, mechanical properties, and histology) in a rat calvaria defect model than BMP-2 delivery alone (at both 200 ng and 2 μg doses of BMP-2)[208].

Biomineralization

Inspired by the *in vivo* process by which bone apatite crystals are formed, surface biomineralization methods can be utilized to incorporate protein growth factors on scaffold surfaces, while simultaneously improving osteoconductivity (reviewed in [194]). Surface biomineralization techniques involve immersing a material in simulated body fluid (SBF), which leads to formation of a calcium phosphate surface phase similar to that found in native bone[195]. Biomimetic

mineralization has been used extensively to form coatings on orthopedic and dental implants, as well as on polymeric and composite tissue engineering scaffolds, resulting in enhanced osteogenic activity, and/or bone formation both *in vitro* and *in vivo*[196–199]. More importantly, biomineralization has been used to incorporate bioactive growth factors, such as bone morphogenetic proteins (BMPs), within the formed surface coatings, thus further enhancing bone formation and tissue integration[23,200].

Nanoparticles and macroparticles

Polymeric nano and microparticles can be loaded with GFs via internal encapsulation, bulk mixing, or surface attachment. Such particles can then be integrated into 3D scaffold systems via the bulk and surface-based incorporation strategies already discussed. For example, Yu *et al* developed hydroxyapatite microspheres (3-5 μm diameter), which incorporated BMP-2 and VEGF by means of a layered mineral coating. By varying layer thickness release kinetics could be tailored, with sustained release profiles of over 50 days possible[186]. Microparticles can also utilize heparin-growth factor binding, as demonstrated by Xu *et al* who altered the heparin content in hyaluronic acid hydrogel particles (~1.1 μm in diameter, pore size ~24 nm) and obtained a tunable BMP-2 release system that demonstrated a constant dosage over two weeks and a near zero-order release profile, which induced highly efficient chondrogenesis of MSCs[187]. Beyond engineering to control release and cellular uptake rates[124,135], these small particles can be employed to enable multi-factor and/or sequential delivery, as well as spatially patterned release, thus enabling the growth of both bone and blood vessels[188].

60

Multi-Agent Delivery

Natural bone development and repair involve the precise temporal and spatial orchestration of a variety of signaling cascades and cell types. Thus, current trends in scaffold-based protein and gene delivery are extending beyond controlling dosage and release kinetics to encompass multi-agent delivery and spatially controlled release. Many groups have created concentration gradients of growth factors within hydrogels using a variety of methods (reviewed in ref[209]), with the most common being utilization of a gradient maker which mixes two or more types of hydrogel precursor solutions (with/without the growth factor) and then subsequently cross-links them[210,211]. Meanwhile zonal protein delivery was demonstrated employing a scaffold composed of microspheres loaded with either VEGF or PDGF in an *in vivo* angiogenesis model, with VEGF delivery from one scaffold area resulting in formation of small blood vessels while sequentially delivery of first VEGF and then PDGF in another scaffold zone led to fewer but larger and more mature vessels[212].

Many studies have highlighted the importance of multi-agent delivery in enhancing bone tissue formation and vascularization within tissue engineering scaffolds. For example, dual release of low doses of BMP-2 and TGF- β3 proteins from hydrogels seeded with bone marrow stromal cells (BMSCs) induced bone formation when implanted subcutaneously in mice, while supra-physiological concentrations of either factor alone did not induce significant bone formation[213]. Meanwhile, porous PLGA scaffolds delivering both VEGF protein and poly-ethyleneimine (PEI)-condensed BMP-4 plasmid and seeded with BMSCs induced greater bone formation in critical size rat cranial defects compared to delivery of

any other combination of these factors[214]. Similarly, dual delivery of covalently incorporated BMP and osteopontin-derived peptides within hydrogels enhanced in vitro bone marrow stromal cell mineralization, osteogenic differentiation and vasculogenic differentiation[215]. Finally, Yilgor *et al* affixed PLGA nanoparticles with release profiles of 20 days and PHBV nanoparticles with release profiles of 40 days to the surface of chitosan scaffolds to enable the sequential delivery of emulsified BMP-2 and BMP-7, resulting in increased alkaline phosphatase activity and mineralization of scaffold-seeded rat BMSCs[124,216]. In multi-agent delivery systems, the timing of growth factor release can be of even more importance, as the temporal regulation of the influx of each growth factor into the defect site can be critical to enhancing the sequential steps of bone healing.

Cells as Drug Eluting Systems

As cells naturally secrete GFs, osteogenic progenitor cells can be pre-seeded within scaffolds to provide an inherently bioactive supply of GFs to a defect site. Adipose-derived stem cells and mesenchymal stem cells naturally secrete relevant GFs for bone healing in response to cues from the microenvironment—such as hypoxia or ischemia—and cease secretion once bone is healed. These cells can also be genetically engineered *ex vivo* to maintain an increased secretion profile of a specific GF through a variety of gene delivery strategies, including transfection via nucleofection, and viral and non-viral delivery vectors[141,189–191] (reviewed in detail, specficially for BMP gene transfection, by Wilson *et al*[217]). Such cell-based therapies are limited by the tendency of the implanted cells to migrate away from the defect site or be cleared by the host.

Alternatively, inductive tissue engineering scaffolds can be utilized for material-based *in situ* gene delivery. Naked plasmid DNA or DNA complexed with viral, lipid-based, or polymeric delivery vectors can be integrated within 3D scaffolds using the bulk- and surface-based incorporation strategies discussed previously. A variety of scaffold-based gene delivery systems have been investigated for bone tissue engineering. For example, Elangovan *et al* developed collagen sponge scaffolds with surface immobilized PEI-plasmid DNA complexes [encoding PDGF-BB] which demonstrated impressive healing over 4 weeks, recovering 50% of lost bone volume (14-fold greater than empty control and 44-fold greater than a control scaffold) in a rat cranial defect model[192]. Using a liposomal vector in a collagen gel, Park *et al* delivered the BMP-2 gene to peri-implant bone defects (defect 10 mm diameter, 7mm depth) in a pig model. BMP-2 producing cells were present in increased number (compared to controls) at 1 week, and they remained at 4 weeks. Bone matrix formation was accelerated in BMP-2 treated groups at week 1, and resulted in increased osseointegration and bone regeneration[193].

Conclusion

Effective regenerative outcomes for large non-union bone defects relies on appropriate scaffold properties coupled with optimized patterns of cell and growth factor delivery. Indeed, the controlled delivery of osteoinductive and angiogenic factors that act in concert to orchestrate the formation of bone tissues remains a major engineering goal. Currently, delivery of BMPs to non-union defect sites via collagen sponge carriers is the clinical standard for growth factor eluting scaffold technologies. Although generally successful in promoting fusion, the poor control over release kinetics and the supraphysiological BMP concentrations required to induce sufficient bone formation lead to a number of complications and adverse effects – particularly in the craniofacial area – that include heterotopic bone formation, edema, seroma, and even cancer[218,219]. The emerging technologies described above can facilitate greater spatiotemporal control of growth factor(s) released at a bony defect site leading to safer, more effective scaffolds for use in bone regeneration.

CHAPTER 4[††]
MATERIALS AND METHODOLOGY FOR 3D-PRINTING DE-CELLULARIZED BONE AND POLYCAPROLACTONE SCAFFOLDS

Summary

This chapter examines the central methods and materials used in this dissertation. Each of the technical chapters have detailed method sections, but the key systems and materials forming the foundation of the work in this dissertation merit an in-depth consideration and explanation, particularly as they are often inherited or experiential expertise and were not discovered as aims of the research. First, it describes the materials: decellularized bone and polycaprolactone. Second, it examines the 3D-printing system used for the small-scale development and testing of the biomaterial. Third, the cell system and choice of *in vitro* biochemical assessments are discussed. Finally, the murine *in vivo* preclinical model and some results of studies using that model are explored. Overall, this chapter sets the starting point for translating this scaffold system from mouse to human scale.

[††] Parts adapted from Rindone, A. N., Nyberg, E., & Grayson, W. L. (2017). 3D-Printing composite polycaprolactone-decellularized bone matrix scaffolds for bone tissue engineering applications.

Introduction

At the outset of developing this technology system at Johns Hopkins, the Grayson Lab wanted to develop a bone replacement that would be patient-specific and regenerative. The research team arrived at a tissue engineering scaffold approach[220,221]: the combination of a biomaterial that could be 3D-printed into the needed anatomic shape and stem cells that could affect regeneration within the 3D-printed shape (**Figure 4-1**).

Polycaprolactone was chosen as the biomaterial. While PCL is bioinert, it had a low melting temperature which would enable 3D-printing. Further, PCL was widely approved by regulatory agencies in a number of other implants, lowering the burden of translation to the clinic. Finally, PCL degrades in aqueous environments, and could slowly erode as bone regenerates within the construct— enabling a full volume regenerative effect. Other 3D-printed polymers suffer from disadvantages such as acidic degradation by-products, much higher melt temperatures, or a lack of degradation.
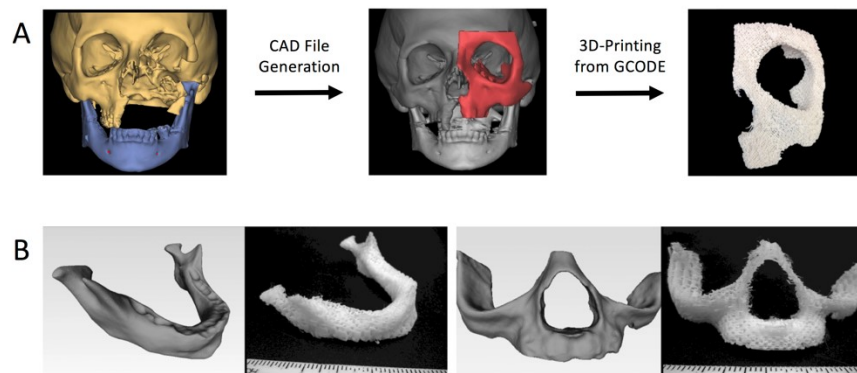
Figure 4-1 3D-printing of patient-specific bone TE scaffolds.
(**A**) Workflow of 3D-printing process. The patient's CT scan is used to create an STL file for the graft that precisely fits into the defect site (2). This STL file is then converted into GCODE and 3D-printed into a customized TE scaffold (3). (**B**) Examples of porous, biodegradable PCL scaffolds that were 3D-printed based upon the specific geometry of the mandible (left) and maxilla (right).

The lab was able to 3D-print these scaffolds and fill them with stem cells, and, *in vitro*, fill them with mineralized tissue using a cocktail of media signals to induce mineral deposition[26]. However, *in vivo*, the signals from the media would no longer be present to direct the stem cells, so the team began looking for ways to modify the system to present bone-forming cues to the stem cells after implantation.

Concurrently in 2013, colleagues down the hall at the Elisseeff lab did a series of experiments with de-cellularized extracellular matrix of different tissues[222]. Uniquely, they used a cryo-milling process to render the tissue to particle size instead of using a digestive enzyme or dissolving solution. When they looked at the resulting bone particles, they found they specifically induced stem cells to deposit boney mineral.
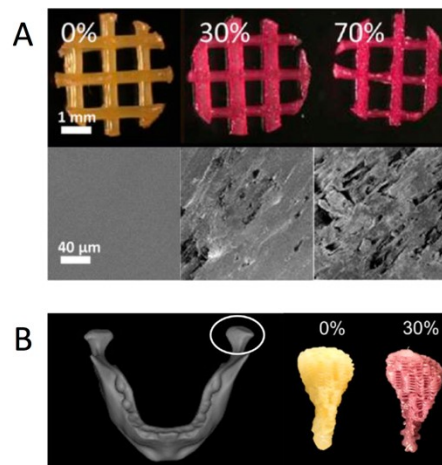
Figure 4-2. 3D-printed, porous DCB:PCL scaffolds.
> (**A**) Two-layer PCL scaffolds with various weight percentages of DCB. The Alizarin red stain (top row) increases with the amount of DCB in the scaffold, demonstrating that the scaffolds have higher mineral content. Surface roughness also increases with the amount of DCB in the scaffold, as shown by the SEM images (bottom row). (**B**) 3D-printed PCL and PCL:DCB scaffolds for the human temporomandibular joint condyle. Alizarin Red staining demonstrates that DCB particles are dispersed throughout the DCB:PCL scaffold.

Around the time that I joined the lab in 2014, Ben Hung had the idea of 3D-printing these bone particles directly with the PCL (**Figure 4-2**, **4-3**), so that the osteoinductive signals of the particles would provide bone-specific bioactivity to the otherwise inert scaffolds[27]. He successfully did so, and demonstrated that the resulting scaffolds had increase surface roughness and cell attachment. Further, the stem cells seeded on the scaffold had increased amounts of mineral deposition, had higher expression of bone-related genes, and caused increased amounts of bone formation *in vivo*.

This chapter details these materials and methods, their advantages and limitations. The specifics of ASC isolation characterization, and function are not addressed here, but in chapter 7. The 3D-printing methods described in this chapter were used for the work in chapters 5, 6, and 7—however the 3D-printing in chapters 9, 10, 11, and 12 uses methods developed and described in chapter 9.
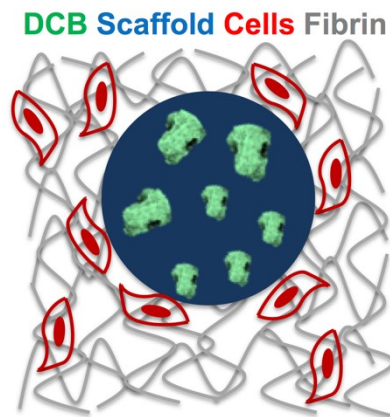
Figure 4-3 Schematic of Scaffold System
A cross-section view 3D-printed strut (blue) containing DCB particles. The strut is surrounded by cells (red) encapsulated within a fibrin hydrogel (grey).

Decellularized Bone Matrix

Bone has been used as a bioactive biomaterial since 1668, as auto and allografts[223,224]. Urist, in the 1960s, isolated the growth factors present in bone that are the putative source of the bone forming signals in bone grafts[119,225]. These BMPs have been used in several bone healing products since then, with some significant adverse events[149] and with structural abnormalities[226]. Additionally, decellularized, demineralized bone has been used as a void filling, non-load bearing biomaterial. Smaller particles of bone have also been used as a more structural filler[227,228].

Decellularization of bone removes the antigen and immunogenic signals from cells that cause problems with human allografts and xenografts. After decellularization, the bone retains its trabecular architecture, and highly ordered osteon structure—hydroxyapatite crystals woven in collagen 1, and encased in non-collagenous proteins that guided the assembly of the shape and prevent the crystals from degrading. Decellularized bone is remarkably stable *in vivo*, undergoing surface resorption *via* osteoclasts over a period of years. While allografts and autografts of bone can integrate with the skeleton at the grafting site, they do not generally reform into the bones they are replacing or undergo systematic remodeling.

Cryo-milling to reduce the size of bone into particles increases the surface area of the material, exposes the interior portions of the trabeculae, which might enable the offloading of non-collagenous proteins, hydroxyapatite crystals, and ions. The resulting DCB particles consist of inorganic hydroxyapatite mineral and organic matrix components, including collagen, glycosaminoglycans, and growth

factors[229,230]. The biochemical composition and micro- and nano-structure of DCB promotes stem cell attachment, proliferation, and differentiation into bone cells[230,231]. When added to 3D-printed PCL scaffolds, DCB significantly enhances *in vitro* adipose-derived stem cell (ASC) osteogenesis, even in the absence of other osteogenic factors[27,232].

Bone Harvesting

Bovine calf knees are obtained from a nearby butcher and either used fresh or stored frozen at -20°C or -80°C. If frozen, calf knees are thawed overnight at 4°C, and then brought knees to room temperature 1 hour before harvesting. The femur is separated from the tibia by cutting the tissue around the knee socket. After separating the joint, the muscle, ligaments, and other connective tissues are cut away from the knee. Connective tissue will interfere with the bone sawing process, so it is essential to remove as much of it as possible. Using a band saw suitable for cutting bone (i.e. Mar-Med Inc. Bone Band Saw; Cleveland, OH), bone is cut into approximately 1 cm^3 pieces. Any cortical bone (present in the diaphysis) or cartilage (present on joint surface and in growth plates) is discarded. Bone pieces are decellularized directly or stored at 20°C.
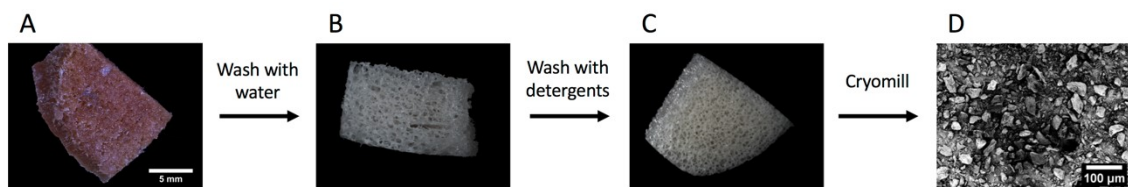
Figure 4-3. Obtaining bone particles for 3D-printing.
Stereoscope images of bone after (**A**) sawing, (**B**) washing with water, (**C**) and decellularizing/lyophilizing. (**D**) Scanning electron micrograph of <40 um bone particles after cryomilling. Scale bars for stereoscope and scanning electron microscope images are 5 mm and 100 µm, respectively.

Bone Decellularization

Bone pieces are washed with a high-pressure water faucet to clear out the bone marrow (**Figure 4-3**). The bone pieces have an off-white color after washing is complete. The bone pieces are then washed with a series of detergent solutions at 2-3 times the bone volume, at 250rpm:

1. 0.1% EDTA in 1x PBS without Ca^{2+}, room temperature, 1 hour
2. 0.1% EDTA, 10 mM Tris buffer in 1x PBS without Ca^{2+}, 4°C for at least 12 hours.
3. PBS for 1 hour at room temperature.
4. 0.5% SDS, 10 mM Tris buffer in 1x PBS without Ca^{2+}, room temperate, 24 hours.
5. 3x PBS for 1 hour, room temperature
6. Twice with 50 units/mL DNAse I, Grade II (Sigma Aldrich) and 1 unit/mL RNAse in 0.1% EDTA, 10 mM Tris buffer in 1x PBS without Ca^{2+}, then PBS for 1 hour, at room temperature

The washed bone pieces are frozen at -20°C for at least 4 hours to prepare for lyophilization, and then the bone pieces are lyophilized overnight to prepare for cryo-milling.

Cryo-Milling

The bone pieces and impactor are loaded into medium or large-sized grinding vials, such that they are able to move freely. The grinding vial is loaded into the cryo-mill (6875 Freezer/Mill with mid or large polyvial set and large vial opener, SPEX SamplePrep; Metuchen, NJ) according the manufacturer's instructions.

The cryo-mill is filled with liquid N_2 until it is ~75-80% full, then slowly closed, and powered on. The cryo-mill is run three times with the following setting: Cycles: 15, Pre-cool: 3 min, Run: 1 min, Cool: 3 min, Rate: 10 CPS. The cryo-mill is monitored every 15 minutes to ensure the liquid nitrogen is not below the level of the vial. At the conclusion of cryo-milling, the vial is opened in a sterile

environment, transferred to 50mL conical tubes, and the particles are stored at -20°C. This cold, dry storage prevents the degradation of the collagenous and non-collagenous proteins in the particles.
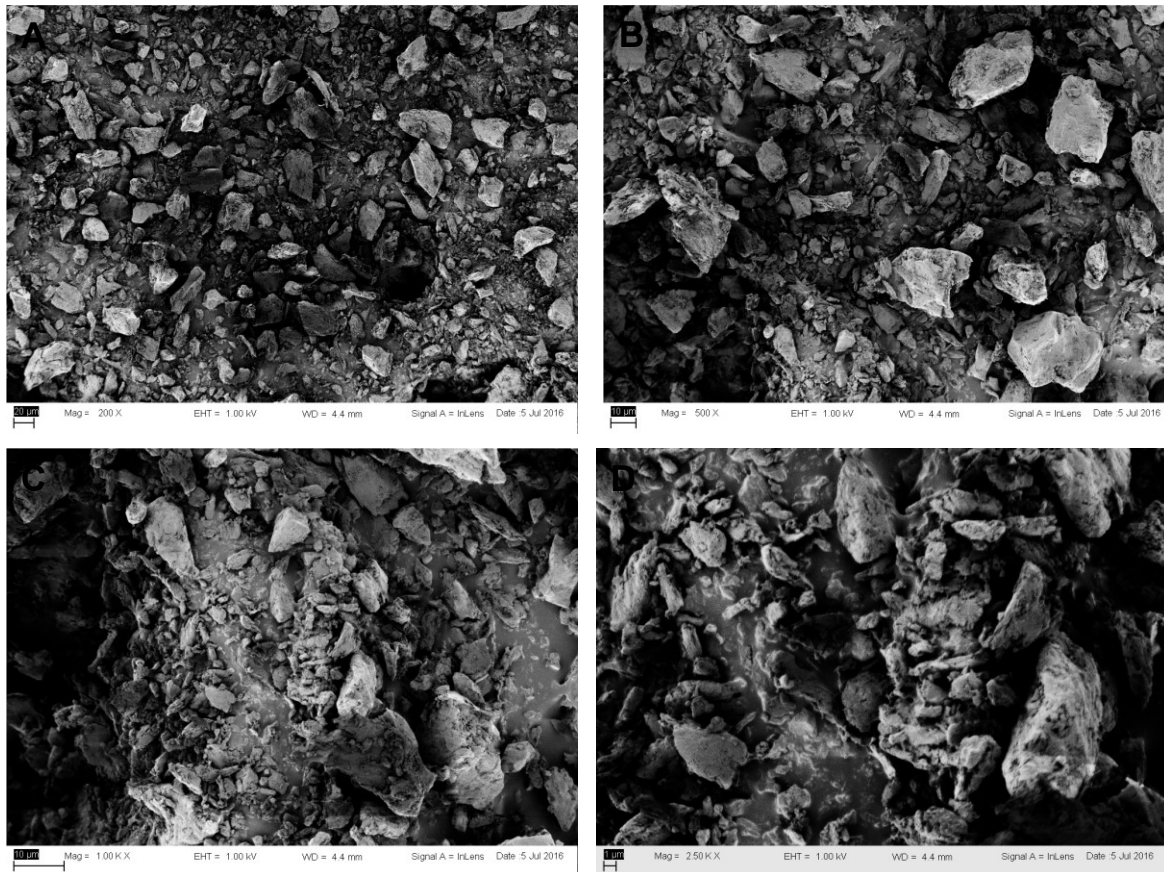
Figure 4-4 DCB Particles Across a Range of Sizes
    SEM images of DCB particles that were passed through a 40µm filter. A = 200x, B = 500x, C = 1000x, D = 2500x.

Particle Size Separation and Characterization

SEM of the particles shows they vary across a wide range of sizes: there are a number of them in the nanoparticle range as well as the micrometer range (**Figure 4-4**). Particles greater than 40um are separated using a sieve shaker, as they might aggregate and clog the 3D-printer. The range of sizes is broad due to the fine nature of bone trabeculae (average thickness) and the random pulverization process. We have found that increasing the amount of cryo-milling

(repeating the 15-cycle loop greater than three times) reduces the fraction of large particles present after cryo-milling. Because the range of particle sizes is so great, further characterization would be best done through separation of particles into different ranges (<10nm, <100nm, <1um, and <100um) by using sieves and characterizing these smaller ranges with tools for visualizing nanoparticles and microparticles.

Polycaprolactone

One of the most widely studied materials is polycaprolactone (PCL), a thermoplastic, aliphatic polyester[233,234]. Polycaprolactone is common in a number of implanted medical devices: Monocryl sutures[235], Capronor, and SynBiosys. Many people also know it as InstaMorph plastic, which can be heated to a putty in a microwave or boiling water, molded to shape, and then sets at room temperature into a hard plastic.

PCL is a desirable material for bone tissue engineering because it is biocompatible (bioinert), has mechanical properties similar to trabecular bone, and has a slower biodegradation rate than other thermoplastics[236,237]. Because it degrades in a hydrolytic manner[238–240], dry storage of PCL and PCL-products is essential to preventing pre-mature degradation. Moreover, the material properties of PCL, such as its low melting temperature and good melt viscosity, allow PCL to be readily fabricated with 3D-printing[26,241]. However, there are complications with other thermal properties, as PCL offloads heat and solidifies much at much lower rates than other thermopolymers, such as ABS or PLGA or PVA[241,242].

PCL is a long starch, and forms micelles as it crystalizes into spherulites. It nucleates on itself or on any small dopants within the mixture. The mechanical

74

property of the polymer stems from the strand entanglement between the different spherulites, which depends on the cooling rate and the molecular weight of the polymer.

Because of the inert, hydrophobic nature of PCL, it has to be treated with a weak acid, sodium hydroxide 3M, for 20 minutes before using it with cells. This treatment accelerates the surface degradation and reduces the hydrophobicity of the construct. This treatment is key to preventing bubbles in porous constructs and creates a wicking effect when seeding scaffolds with hydrogels. To further enable cell attachment, PCL can also be treated with a serum wash, which allows proteins to coat the surface and support more rapid cell attachment.

3D-Printed Scaffolds

The 3D-printing fabrication process involves the generation of a computer aided design (CAD) file that defines the overall geometry and pore design of the scaffold. This CAD file is then converted into a G-code that is uploaded into the 3D-printer. The scaffold material is printed layer-by-layer onto a bed according to the instructions in the G-code. Once the scaffold is printed, post-processing steps such as removal of support material, sintering, or surface modification may be performed to attain desired scaffold geometry and properties.

Mixing DCB with the PCL polymer adds bioactivity to the resulting construct, and that construct can be created using fused deposition modeling to deposit small, molten fibers of the mixed material in specific patters. Fused deposition is advantages to other additive manufacturing systems because it creates less waste material, does not require a high energy or high temperature laser, and has

75

become low cost. The interlayer fusion from the deposited molten fibers into the previously deposited and solidified fibers creates a mechanically rigid construct.

The resulting quality of the print can be affected by a number of manufacturing miscoordinations. (1) The speed of the extruding head and the rate of material extrusion might be mis-matched. While the settings can be calibrated beforehand, variability in the extruding method (such as the pneumatic pressure or material resistance) can cause in-print variability. Additionally, for filament-based FDM systems, any variation in the diameter of the filament directly creates variability in extrusion flow rate. This error results in over or under deposition and is realized by the thinning or thickening of the deposited fibers beyond the effect of die-swell.

(2) The molten-solid transition can take a long time, especially for PCL, and is controlled by matching the melt temperature and the cooling fans. If the extruder head moves away before the recently deposited fiber has solidified, it can draw the fiber away from the deposited location, deforming the shape of the scaffold and creating trailing drawn strand along the travel path. Additionally, when the fiber deposition path crosses space without underlying material (creating a strut or bridge-like structure), gravity will draw molten material downwards, creating a bowing artifact in the print.
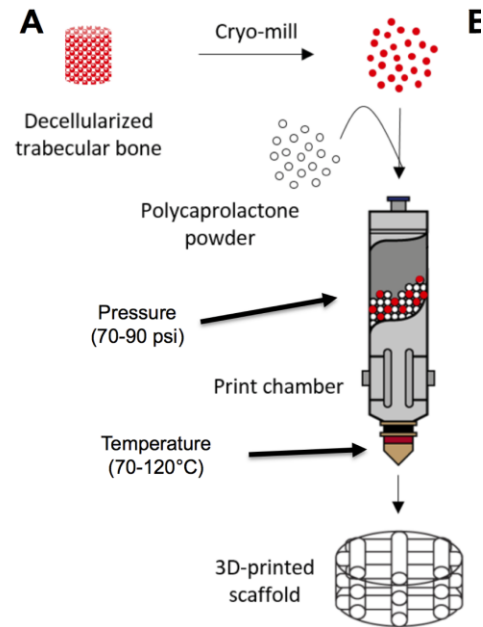
Figure 4-5. Schematic of Scaffold Manufacturing and In Vitro System
DCB and PCL are mixed and placed into the print chamber, where they are melted and then subject to pressure. The pressure drives the molten mixture outwards to create fibers which form the 3D-printed scaffold.

3D-Printing Manufacturing Tools and Materials

The pneumatic-driving fused deposition system (**Figure 4-5**) used for the studies in chapters 5, 6, and 7 was built on an XYZ Positioning Arm (Syil X4 CNC Mill, Syil America, Coos Bay, OR). A stainless-steel extrusion / thermal chamber was attached to the end of the arm and had an adaptor for tubing (Nordson EFD 5225K711). This tubing connected to a pressure regulator (Ultimus V, Nordson EFD, Providence, RI), which was in turn attached to an air compressor (30 – 130 PSI).

The chamber was heated at the base by a heating element (Type K thermocouple, Watlow), and the heat was controlled by a PID controller (Series CV Temperature Controller, Watlow). The material was loaded into the chamber, molten, and extruded through an extrusion nozzle (460µm diameter, Nordson EFD

#322018) onto a heated print surface (Flexible Heater Rectangular 115V 270W, Rapid Industrial Supply connected to a Variable Voltage Regulator 4098 Variac Transformer TDGC-0.5KM, Circuit Specialists).

Design of Scaffolds

Scaffold were designed as thin, two-layer sheets which could be easily punched or cut into sizes appropriate for *in vitro* and murine studies. To create the CAD design, TinkerCAD (www.tinkercad.com) was used to design a box object 3cm x 3cm x 0.782mm. The CAD file was then loaded into slic3r (www.slic3r.com) where it was sliced with the following settings: layer height: 0.46mm, nozzle diameter: 0.46mm, fill density: 40%, fill pattern: rectangular, perimeters: 0, horizontal shells: 0. By setting the perimeters and shells to 0, the only part of the print was the infill struts. At the thin height of the cad file, there was only room for two layers of infill, which generated a crosshatch pattern. Post-hoc measurements revealed that the resulting pores were 800um. The resulting GCODE file was loaded onto the Mach 3 software used to control the mill machine.

3D-Printing

The material mixture was loaded the print chamber and set to melt temperature (80°C) for 30 min using the PID controller and the heating element. The heated bed was set to 50-65°C. The arm position was calibrated such that the origin of the coordinate system matched the front left corner of the heated bed. The extrusion rate was calculated by performing a test extrusion for 1 min. The length of the extruded material was measured and used to calculate mm/min extrusion rate.

The GCODE was modified with the measured extrusion rate by opening the GCODE file in a text editor and replacing the "F###" in the GCODE with the calculated rate "F###." For instance, if the rate is 100 mm/min, a value of "F100" was placed wherever an F value appears in the GCODE. The print was then launched from the software and monitored for any inconsistencies, such as clogging or a change in extrusion rate. After print completion, the scaffold was allowed to cool for 20 min before removal from the print surface. Scaffolds were stored in desiccating conditions at room temperature or at -20C. Prior to use for cell culture or implantation, scaffolds are washed with 3M NaOH for 20min, 3x PBS for 20min, and sterilized in 70% EtOH overnight. The sterile scaffolds are washed with sterile PBS 3x 20min, and finally incubated in serum-containing media for a minimum of 1h.
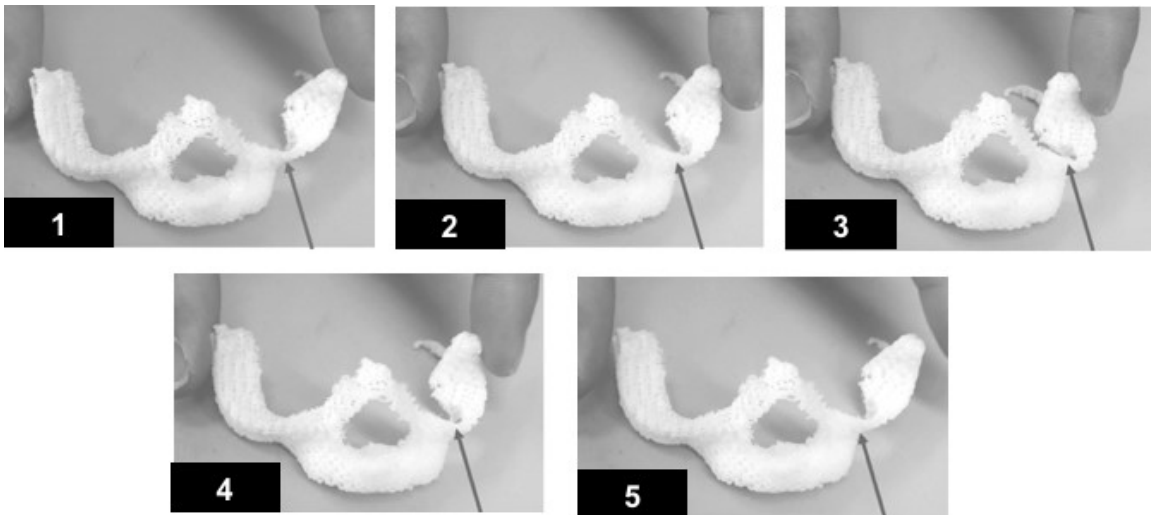
Figure 4-6 Time-lapse of 3D-printed PCL Implant Bending
Light force causes the implant to significantly deform at thin part (Arrow).

Mechanical Analysis

Mechanical function of bone implants is critical, so that the implant does not break or displace under the incident forces. To measure mechanics, large cubic scaffolds (1 cm^3) were printed for mechanical testing. Solid and porous scaffolds were printed to measure both the effective modulus of the porous structure and the base compressive modulus of the material. Samples were tested on a compressive testing machine with a 50 kN load cell at a strain rate of 4 mm/min. The compressive modulus of solid PCL is approximately 120 MPa[232,236]. Porous scaffolds typically have a lower modulus that is proportional to the reduction in the load-bearing cross-sectional area by the porous space.

While the mechanical properties of porous PCL prints are appropriate for trabecular bone, PCL prints of large anatomic shapes deform under handling due to thin, highly porous portions (**Figure 4-6**).

Assessing DCB Content in 3D-printed Scaffold

As the bioactive signal in the 3D-printed scaffolds, it is important to validate that the DCB is present throughout the scaffold at the level intended, evenly spatially distributed, and without clumping. Using Raman spectroscopy, the phosphate and collagen portions of the DCB can be detected. Raman spectroscopy is limited by the penetrating power of the incident light, indicating the DCB is present near or on the surface of the printed fibers. With scanning electron microscopy, the particles present on the surface of the visualized (**Figure 4-7 A&B**). In chapter 5, we can see that the particles are preferentially distributed towards the center of the deposited fibers rather than at the surface.

Serendipitously, the DCB particles fluoresce under blue light into the green channel, which enables the visualization of large particles throughout the 2-layer scaffolds (**Figure 4-7D**). CT scans show the average mineral density of these scaffolds, around 220mg HA/cc, which is approximately one third that of native bone, and corresponds well to a 30:70 mixture of DCB and PCL. uCT at 8nm reveals individual DCB particles throughout the scaffold, similar to the images obtained using fluorescent light (**Figure 4-7C**). Finally, scaffolds can be incubated in a weak acid (0.5M HCl) to dissolve the calcium in the scaffold which can then be measured with the calcium assay described in this chapter. 4mm diameter two-layer scaffolds generally contain 100ug of calcium.

Cellular Activity and Assessment

Because the lab worked with ASCs and intended to use ASCs or SVF in the eventual therapy, ASCs were the natural choice of cell type to assess the bioactivity of the scaffolds *in vitro*. Additionally, previous work in the lab compared ASCs with bone marrow derived cells and found them to be similar for tissue engineering bone, especially when treated with PDGF[243]. As a cell that could be induced, ASCs are most similar to fibroblasts, and generally require a significant intervention of dexamethasone to differentiation into osteoblasts. Other cells used to study bone formation—such as osteosarcoma cell lines or primary periosteal cells—might react differently to the scaffold material.
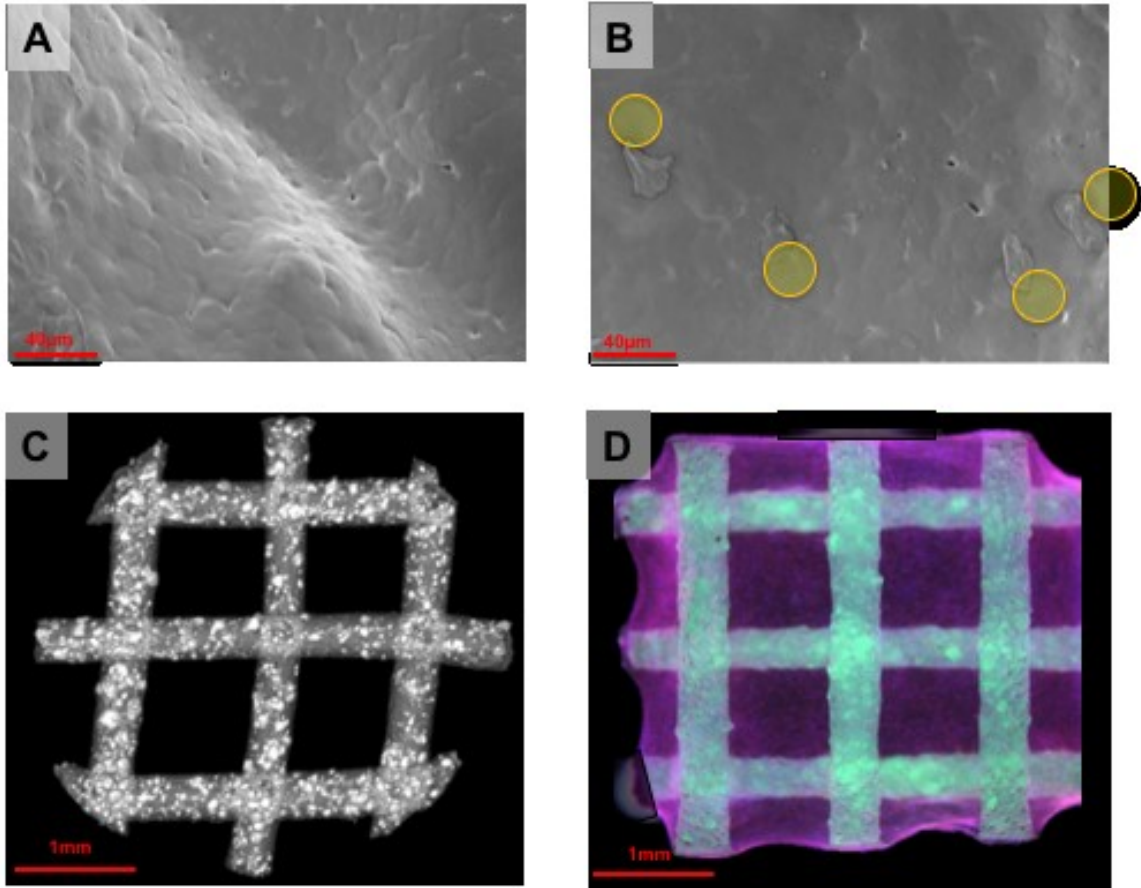
Figure 4-7 Confirming DCB Presence in 3D-Printed Scaffolds.
(A) SEM of the surface of pure PCL scaffold (B) SEM of the surface of a scaffold containing DCB particles (yellow circles). (C) μCT of scaffold with DCB particles in white. (D) Fluorescent image of PCL-DCB scaffold with fibrin hydrogel. DCB particles are green, the gel is purple.

Additionally, it is important to understand that primary or early passage ASCs from human donors have donor-to-donor and isolation-to-isolation variability. This variability might cause variations in the measured calcium deposition response, proliferation, and differentiation. In this dissertation, all of the SVF and ASC samples used have responded to the DCB:PCL material with increased calcium deposition and bone gene expression, albeit at different magnitudes.

The mineral deposition by ASCs *in vitro* is dissimilar to that observed in normal bone growth or fracture healing. The calcium and DNA assays used do not

differentiate between the structured (ordered hydroxyapatite crystals) mineral deposition of bone and the calcium precipitation process that can spontaneously occur from media containing serum[244]. However, the gene expression of the cells can be observed and used to determine they are expressing bone-related genes, which supports the idea that the cells in the scaffold are differentiating into osteoblast-like cells and depositing boney matrix.

Finally, the cells are encapsulated in a fibrinogen-thrombin hydrogel system. The majority of the cells are suspended in the hydrogel and have no physical contact with the 3D-printed scaffold and do not directly sense its mechanics, surface roughness, or bone content. Instead, they are more likely to respond to the vasculogenic cues of the fibrin fibers. However, as cells remodel and pull on the fibrin fibers, it tends to tear apart and compress onto the struts (seen *in vitro* at days 7-14 in ASCs, and earlier in SVF). A different process might occur *in vivo* as imaging of murine cranial scaffolds has revealed tight banding of capillary structures perpendicularly along the scaffold struts.

Cell Culture and Hydrogel Encapsulation

ASCs isolated from lipoaspirate were grown in standard culture conditions using expansion medium: 10% fetal bovine serum, (Atlanta Biological), 1% penicillin-streptomycin, and 1 ng/mL FGF-2 (Peprotech) in high-glucose DMEM with sodium pyruvate (Gibco). FGF-2 encourages cell proliferation and was added to growth medium just before feeding the cells because the protein degrades rapidly in solution. During differentiation, osteogenic medium was used: 10% fetal bovine serum, 1% penicillin-streptomycin, 10 mM β-glycerophosphate (Sigma Aldrich), and 50 μm ascorbic acid (Sigma Aldrich) in low-glucose DMEM with

sodium pyruvate (Gibco). The phosphate provides the available ion supply for mineral growth, and the ascorbic acid provides the biomass for collagen 1 generation. Ascorbic acid was added to the media at the time of feeding because it precipitates out of solution.

Cells were generally seeded into scaffolds in a fibrin gel at a concentration of 20 x 10^6 cells/mL. This concentration is used because the resulting hydrogel has cells not more than one cell width from other cells enabling the rapid establishment of cell-cell contact. Studies of vascularization of the scaffolds showed that higher concentrations of cells led to increased vascular outcomes[245,246]. Finally, more cells in a scaffold generally leads to more mineral deposition.

The hydrogel was prepared as follows. For the fibrinogen solution: 10 mg/mL of fibrinogen (Sigma Aldrich) in PBS without Ca^{2+}, sterile filtered. Thrombin solution: 10 units/mL of thrombin (Sigma Aldrich) in PBS with Ca^{2+}, sterile filtered.

Just before scaffold seeding, scaffolds were prepared by drying them on a sterile KimWipe and placing them in a well plate (**N.B.** Coating the well plates with a thin layer of 2% sterile agarose (~500 μL in 24 well plate) prevents the outgrowth of ASCs onto the well-plate as the scaffolds are cultured).

A cell pellet of ASCs was prepared with the desired number of cells and resuspended in the fibrinogen solution. Aliquots of the cell-fibrinogen solution were prepared and kept on ice. Each aliquot contained enough solution for casting one to four gels. For 4mm, two-layer scaffolds, 12uL was used to seed the scaffold. At the time of casting, thrombin solution is added to the aliquot at a ratio of 1:4. The solutions were rapidly mixed and pipetted into the scaffolds—from the addition of

the thrombin gelation is observed in 20-30 seconds. Scaffolds were incubated in a cell culture incubator for 30 min to allow the fibrin to completely crosslink. Warm osteogenic medium was added to each well and thereafter scaffolds were fed 3 times per week with osteogenic medium for 3-4 weeks to allow for bone regeneration to occur.

Biochemical Assessment of Mineralization and Differentiation

Biochemical assays can be used to examine the mineral deposition in the scaffold construct, and the behavior of the cells in the construct over time. In osteogenic media conditions, cells have the available resources (phosphate ions, calcium ions, ascorbic acid) to deposit mineralized extracellular matrix. The tools in this section were used to look at the scaffold *en bloc*

Alizarin red staining is used to visually see calcium deposited in the matrix of the scaffold. Alizarin red S, an anthraquinone dye, binds to calcium. A solution of 40 mM Alizarin Red S (Sigma Aldrich) is prepared in dH_2O. Enough Alizarin Red stain is used to immerse the entire scaffold. The scaffolds are incubated at room temperature for 10-20 minutes. After washing with dH_2O extensively, the stained scaffold can be imaged. Fibrin hydrogels without any mineral deposition can retain the stain through a number of washes (10-15 washes), so including a control scaffold to ensure enough washes were used to remove non-specific staining. This stain gives a spatial indication of calcium deposition, and we always observe that the entirety of the gel region in osteogenic treated scaffolds was uniformly stained (**Figure 7-4**). Although not used here, the stained samples can be dissolved, and the amount of stain can be measured fluorescently to determine the amount of The scaffolds are robustly vascularized in the cranial defect environment (**Figure 4-10**),

due to their thin nature (<1mm) and the highly vascularized dura and dermal layers sandwiching the implant. We observe this vascularization in gross dissection and in intravital imaging[248]. calcium in the construct.

The number of cells in the scaffold is determined through a DNA assay to quantify the amount of double stranded DNA Quant-iT PicoGreen dsDNA Assay Kit, Invitrogen). The whole scaffold is transferred to lysing solution immediately after the end of the culture period and lysed for 10min. Samples are then incubated at 50°C for 15-16 hours to denature the DNA. The PicoGreen DNA Assay is performed according to manufacturer's instructions to determine the concentration of DNA in each scaffold. By using a day 0 sample with a known concentration of cells, the proliferation and number of cells in the scaffolds can be assessed.

Ca^{2+} was quantified with a calcium (CPC) LiquiColor Test (Stanbio Laboratory; Boerne, TX). Deposited mineral was solubilized with a weak acid (0.5 M HCl). Sufficient volume of the acid must be used to overcome the solubility limit of calcium ions, generally 50-100x. Samples were incubated in the acid on a shaker at 4°C overnight. The calcium quantification assay was performed according to manufacturer's instructions. Scaffolds containing DCB will create a background calcium signal which must be measured and deducted from measurements of deposited scaffolds.

One of the key metrics in this thesis is the measure of calcium deposited per cell. Normalized Ca^{2+}/DNA ratios for scaffolds is found by dividing the mass of Ca^{2+} by the mass of DNA, as determined during DNA quantification.

Beyond bone formation *in vivo*, the most convincing *in vitro* data is the protein expression of the cells. The expression is assessed with isolated mRNA,

which was used to produce cDNA. cDNA was subject to real-time polymerase chain reaction (RT-PCR) for osteogenic genes *Col1a1*, *Runx2*, osteopontin, osteocalcin, and osteonectin. Collagen 1 is the major extracellular matrix component of bone, although it is also expressed in other tissue types. Runx2 is a controlling transcription factor and is considered a master regulator of osteoblast differentiation. Osteocalcin, osteopontin, and osteonectin have extracellular roles in nucleating hydroxyapatite crystals, controlling crystal growth, and preventing the degradation of those formed crystals[247].

Then primers for genes of interest are used to amplify those proteins and measure their presence relative to housekeeping gene. For bone differentiation, the most stably expressed gene throughout the differentiation of the cells is β-actin. Because the scaffolds are seeded with an unpurified cell population, the results can be somewhat noisy—not all the cells are differentiating or are doing so at the same time. Timepoints early in the culture process are especially noisy (but when runx2 is most expressed), but at later timepoints (14 and 21 days post-induction) the noise is reduced as a number of cells have differentiation and are stably expressing mineralization genes such as collagen 1 and osteopontin.

For analysis, the delta-delta Ct method was used in which β-actin served as the housekeeping gene, and gene expression was normalized to that of cells cultured in PCL scaffolds under control conditions at Day 21, or undifferentiated SVF cells before exposure to tissue culture plastic or cow serum. This normalizes the measured gene expression to the number of cells present in the sample, as well as the baseline expression of that gene in uninduced or differentiated cells.

The fold change of the proteins can vary between 10 to 1000-fold depending on the normalizing sample.

Critical-Sized Mouse Cranial Defects

Because of the thin nature of the 3D-printed, two-layer scaffolds, they were ideal implants for cranial bone defects in the parietal bones of mice. These defects were created using a 4mm-diameter circular saw. Mice were always male, 6-8 weeks of age (young adult) and either wild-type (C57/BL6) or nude immunocompromised (*fox1n1-null*). Immunocompromised mice had a mutation which prevented the maturation of T-cells, so they would not reject human cell implants.
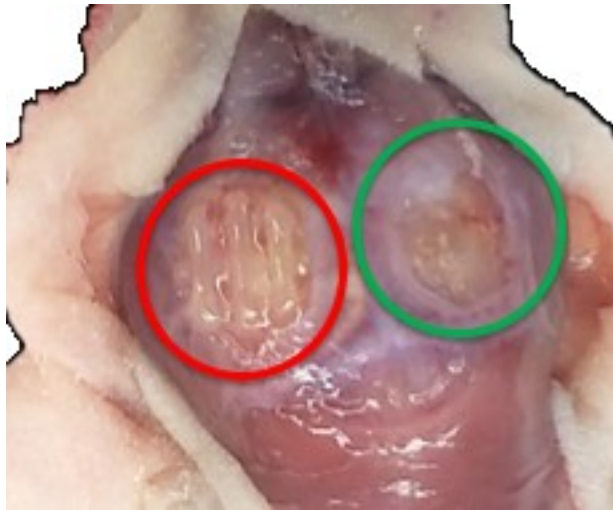
Figure 4-8 Surgical Outcomes for Murine Cranial Implants
Red: PCL-DCB implant fills the defect and is well integrated with the surrounding bone. Green: an empty control defect does not heal over 12 weeks.

3D-printed scaffolds were 816μm thick and were press-fit into the surrounding bone that was 100-200μm thick (**Figure 4-8**). The scaffolds have a 40% infill setting, but from a top-down 2D-view, the scaffold covers 80% of the defect area. Overall, the scaffold provides structured porous areas across the

defect area for bone regeneration. The scaffold is not thick enough to have diffusion limitations leading to cell necrosis, and both the dura and the overlying skin are highly vascularized and rapidly vascularize the implant. Generally, scaffolds are press-fit into the defect and then the cell-fibrinogen-thrombin mixture is pipetted into the scaffold *in situ*, filling the entire defect and helping to hold the scaffold in place. Pre-seeded scaffolds suffer disruption to the gel during the implantation process, and are kept in media containing serum prior to implantation, which is impossible to fully wash out of the scaffold and can cause unwanted or complicated effects *in vivo*.

In numerous studies, I have found untreated, PCL alone, and PCL with ASCs defects to be non-healing, which establishes the critical size of this defect. However, when I treated the defects with the infuse acellular collagen sponge (INFUSE, Medtronic) with 2µg of BMP2, the defect fully regenerated, demonstrating that it is possible to regenerate bone at this site (**Figure 4-9**).
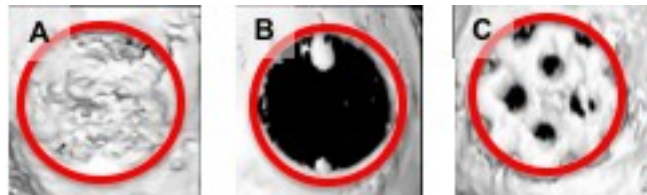
Figure 4-9 Outcomes of Positive and Negative Murine Cranial Treatments
In 4mm-diameter cranial defects at 12-weeks, BMP-2 treatment completely filled the defect with bone (A), while the untreated, empty defect remained unhealed (B). A DCB-PCL scaffold (C) filled the defect and conducted bone formation across the surface of the scaffold.

Over the course of using PCL or PCL-DCB scaffolds in over a hundred mice, I have never observed inflammation, swelling, or excessive fibrosis in this cranial defect, intramuscular site, or subcutaneous site. This serves to confirm the bio-inert nature of the material and that the 3D-printing process and resulting scaffold structure does not negatively impact that property.
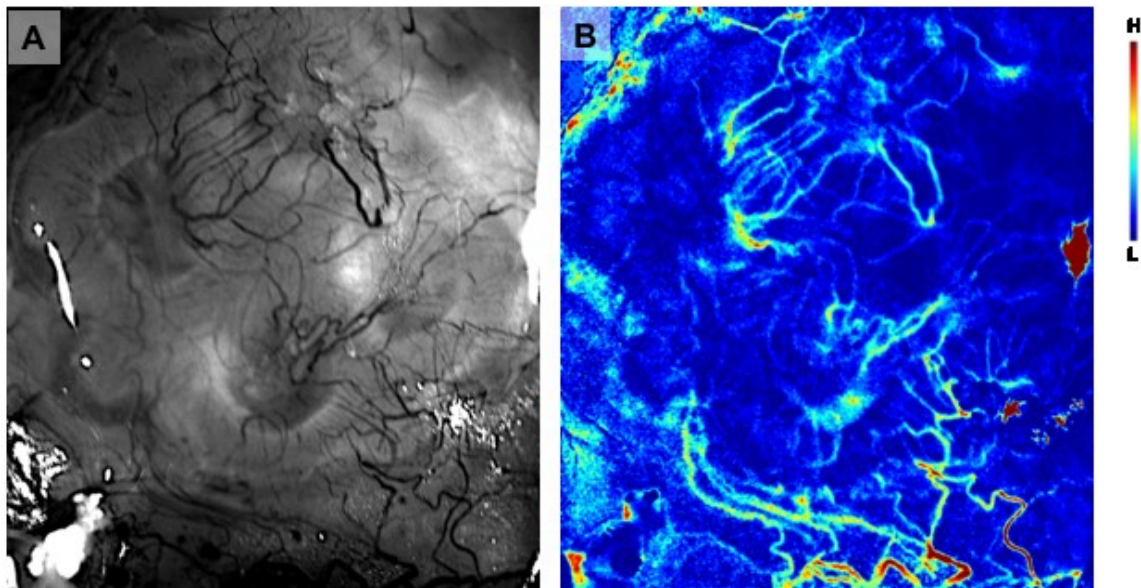
Figure 4-10 Live Imaging of Vascularization of Cranial Implants
(A) White light with a 496nm long pass filter is used to visualize the hemoglobin (absorption of 570nm light) in blood vessels present across a PCL scaffold at 12-weeks. (B) Laser speckle contrast was used to identify regions of relative blood flow in the scaffold area. Green and red indicate regions of high blood flow.
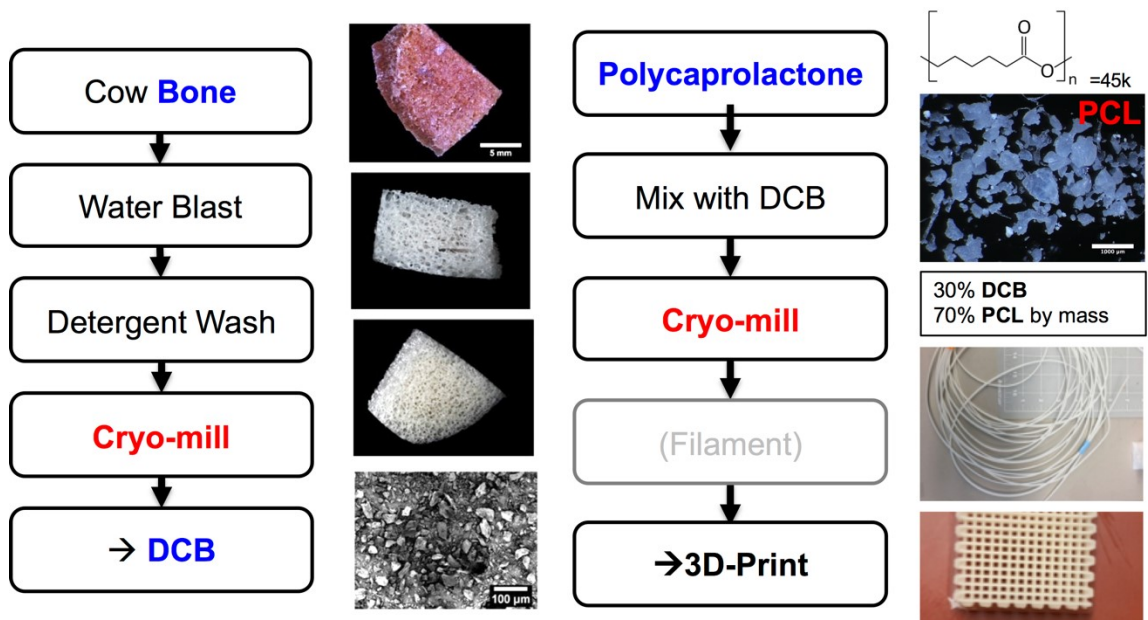
Figure 4-11 Flow Chart of PCL-DCB Preparation for 3D-Printing.

CHAPTER 5[‡‡]
COMPARISON OF 3D-PRINTED POLYCAPROLACTONE SCAFFOLDS FUNCTIONALIZED WITH DECELLULARIZED BONE, HYDROXYAPATITE

Summary

3D-printing facilitates rapid, custom manufacturing of bone scaffolds with a wide range of material choices. Recent studies have demonstrated the potential for 3D-printing bioactive (i.e. osteo-inductive) scaffolds for use in bone regeneration applications. In this study, we 3D-printed porous poly-ε-caprolactone (PCL) scaffolds using a fused deposition modeling (FDM) process and functionalized them with mineral additives that have been widely used commercially and clinically: tricalcium phosphate (TCP), hydroxyapatite (HA), Bio-Oss (BO), or decellularized bone matrix (DCB). We assessed the '*print quality*' of the composite scaffolds and found that the print quality of PCL-TCP, PCL-BO, an PCL-DCB measured ~0.7 and was statistically lower than PCL and PCL-HA scaffolds (~ 0.8). We found that the incorporation of mineral particles did not significantly decrease the mechanical properties of the graft, which were on the order of 260 MPa for solid blocks and ranged from 32-83 MPa for porous scaffolds. Raman spectroscopy revealed the surfaces of the scaffolds maintained the chemical profile of their dopants following the printing process. We evaluated the osteoinductive properties of each scaffold composite by culturing adipose-derived stromal/stem cells (ASCs) *in vitro* and assessing their differentiation into osteoblasts. The calcium content (normalized to DNA) increased significantly in

---

PCL-TCP (p<0.05), PCL-BO (p<0.001), and PCL-DCB (p<0.0001) groups relative to PCL only. The calcium content also increased in PCL-HA but was not statistically significant (p>0.05). Collagen 1 expression was 10-fold greater than PCL in PCL-BO and PCL-DCB (p<0.05) and osteocalcin expression was 10-fold greater in PCL-BO and PCL-DCB (p<0.05) as measured by qRT-PCR. This study suggests that PCL-BO and PCL-DCB hybrid material may be advantageous for bone healing applications over PCL-HA or PCL-TCP blends.

Introduction

The treatment of critical-sized or non-union bone defects resulting from congenital diseases, trauma, or cancer resection often requires bone grafts. The use of autologous grafts – the gold standard – is associated with additional pain, co-morbidities, and high costs [249–252]. Metallic (stainless steel and titanium) implants have been used to treat these defects but have limited lifespans (25 years) and excessive material strength, causing stress shielding[253]. Tissue engineering approaches combine biodegradable scaffolds with bioactive factors and cells to regenerate the regions of tissue loss[254]. The application of 3D-printing or, more broadly, additive manufacturing (AM) techniques to manufacturing of scaffold components has enabled precise patient-specific customization of macro-scale scaffold geometry (e.g. from CT images). Further, AM has also enabled greater control and optimization of the micro-scale porous structure which can be used to optimize bone healing and vascular infiltration.

A growing number of tissue engineering studies are utilizing 3D-printed scaffolds for bone regeneration[26,102,255–258]. Scaffolds have been manufactured using fused deposition manufacturing (FDM)[27], selective laser sintering[69], and

digital light projection[259] which utilize thermal fusion bonding[260], high temperature sintering[261], and photo-crosslinking[262], respectively. The specific 3D-printing technology selected impacts the choice of material used for the scaffolds. The relatively low cost of FDM machines over the past decade has enabled the widespread use of the technology for bone tissue engineering in convenient desktop formats[263]. FDM allows for sufficient resolution needed for structural and pore designs, and many materials suitable for FDM result in scaffolds which are bioactive and have similar stiffness as native bone[27].

Researchers have used a number of thermoplastic polymers to 3D-print tissue engineering scaffolds, including poly-ε-capro-lactone (PCL[26,102,264], poly(l-lactic acid) (PLLA), and poly-vinyl-alchohol (PVA)[265]. PCL is the most commonly used thermoplastic polymer for AM of bone scaffolds due to its prior FDA approval, excellent biocompatibility, and slow biodegradation via hydrolysis[235,238,266]. The low melting point of PCL (60°C) makes it an ideal thermoplastic ideal for benchtop FDM, and it maintains strong crystallization and moderate mechanical properties after manufacturing, particularly in compression[69,233]. However, synthetic PCL scaffolds are not inherently osteoinductive[267,268]. Several groups have functionalized PCL by incorporating various forms of calcium phosphate into the scaffolds[257]. The three most commonly used calcium phosphate mineral additives are tricalcium phosphates (TCP)[240,269,270], hydroxyapatite crystals (HA)[102,271–274], and decellularized bone matrix (DCB)[27]. These all vary in form and function: TCP contains readily available calcium and phosphates for bone production and degrade semi-rapidly (6 weeks) via hydrolysis into ions and via osteoclast resorption[275–278]. HA is the naturally occurring crystal form of bone mineral and is

similar to TCP except for a denser crystalline structure and increased mechanical properties. DCB is obtained from native (xenogenic and allogenic) bone sources and may include an organic protein phase such as collagen. However, a clinically available form of DCB, Bio-Oss, provides millimeter sized granules of bovine trabecular bone with the organic phase largely removed, However, doping PCL with any of these different mineral additives might impact the mechanical properties and present additional challenges with fabrication[271].

Previously, our group has demonstrated enhanced bone healing with DCB blended into a PCL scaffold, hypothesizing that the inclusion of collagen aided in cell attachment and migration[27]. We presently hypothesize that the collagen present in DCB in addition to the mineral phase may make DCB a better additive than TCP or HA. Despite the previous investigations into 3D-printed scaffolds incorporating HA[102,272] and TCP[240,269,270] hybrids, those various study outcomes cannot be compared with the effect PCL-DCB[27] since the methods of printing, the synthetic material, and the printing protocols may be different. In this study, we seek to directly compare the printability and bioactivity of PCL-DCB approach with PCL-TCP, PCL-HA, and PCL-BO, which do not have the organic phase of native bone. The objectives of this study are (**1**) to evaluate the relative manufacturability of bone scaffolds containing different bone-forming dopants in a biocompatible thermoplastic using fused-deposition manufacturing, (**2**) to compare the material properties of the resulting bone scaffolds, and (**3**) to determine the osteoinductivity of the scaffolds *in vitro*.

Materials and Methods

Supplies

All materials were obtained from Sigma unless otherwise stated. Calf knees were obtained from Green Village Packing Co in Green Village NJ.

Materials

Powdered polycaprolactone (PCL 43k-50k MW; Polysciences 25090) was combined with β-Tricalcium Phosphate (TCP; Sigma Aldrich 49963), Hydroxyapatite (HA, Aldrich 289396), Bio-Oss (BO) small granules (Geistlich 20111), or decellularized bovine bone extracellular matrix (DCB). TCP and HA were unaltered and used in their powder forms. BO granules were pulverized using a SPEX SamplePrep 6770 cryo-mill (SPEX SamplePrep, Metuchen, NJ) at a frequency of 10 cycles per second for 15 minutes to obtain particles. Bovine DCB was obtained by isolating trabecular bone from calf knees. The bone was decellularized using a protocol as described previously[27]. Briefly, bovine trabecular bone fragments were blasted with water to remove as much cellular debris as possible. The bone fragments were then placed in a series of four detergent washes of 0.1% EDTA for 1 h, 0.1% EDTA/10 mM Tris for 12 h, 0.5% SDS/10 mM Tris for 24 h, and 50 u/mL DNase, 1 u/mL RNase, and 0.1% EDTA/10 mM Tris for 5 h. Following the washes, the bone was rinsed with PBS and lyophilized. The decellularized bone fragments were cryomilled with a Spex 6870 Freezer Mill to form a powder.

3D-Printing of Scaffolds using Fused Deposition Modeling

Materials were mixed 30% w/w with PCL by sifting through a stainless steel 400 μm mesh three times. Scaffolds were manufactured using an in-house

pneumatic fused-deposition system mounted to a CNC machine with a nozzle diameter of 460 μm[26]. Briefly, a powdered mixture of material is loaded into the nozzle chamber, heated to a set temperature in order to bring the polymer to a liquid phase, and then a pneumatic pressure is applied to the top of the liquid to force it out the extrusion die at the bottom of the chamber. Scaffolds for cell studies were prepared using rectilinear patterns with 60% void volume and two layers in height (0.640mm) and punched to 4mm in diameter. Solid 1 cm^2 sheets that were also two layers in height were printed for surface analysis, and solid and 60% void 1 cm^3 cubes were printed for mechanical testing. Print temperatures, pressures, and extrusion head speeds were varied empirically for each composition in order to maximize print quality. Extrusion head speed was determined by measuring the length of material extruded for 5 minutes; temperature and pressure were raised within the range of the system until the material extruded at a steady rate. Prior to seeding cells, scaffolds were treated with 1M NaOH for 1h to increase hydrophilicity, washed with PBS, soaked in 100% EtOH for 1h to sterilize, and immersed in 100% FBS at 37 °C for 1h to facilitate protein adsorption to the surface of the scaffold prior to seeding. Scaffolds were imaged under computed tomography (CT) using a Gamma Medica X-SPECT small animal system (Gamma Medica, Salem, NH). Imaging was performed at 80 kV peak voltage and 600 μA current. Reconstruction was done with voxel size of 70 μm.

Differential Scanning Calorimetry

The melting point and degree of crystallinity was determined via differential scanning calorimetry (Perkin Elmer DSC 8000). Powder mixes of each group (5 ± 1 mg) and printed constructs (15 ± 5 mg) were measured at a scan rate of 3 °C/min

97

from 10 °C to 120 °C in flowing nitrogen gas (*n*=4). The melting point was determined at the maximum of the melting endotherm. The degree of crystallinity (X_c) in the PCL was calculated assuming proportionality to the reported heat of fusion (ΔH_c) of 139.5 J/g for 100% crystalline PCL[233]. Heat of fusion in the samples (ΔH_f) was determined using the peak area calculation feature of the Pyris software. Only the net weight of the PCL was considered in calculating the degree of crystallinity.

$$X_c = \frac{\Delta H_f}{\Delta H_c} \qquad\qquad eqn\ 6-1$$

Assessment of Print Dimensions and Quality

The strut and pore dimensions of two-layer porous scaffolds were analyzed post-hoc using the ImageJ plugin OrientationJ (NIH, Bethesda MD). Print quality was also computed comparing two-layer porous scaffolds pixel-by-pixel to a computer-generated ideal lattice. The percentage of pixels that matched between the two images was taken as a measure of print quality.

Mechanical Testing

Solid and porous cubes were subjected to unconfined compression using a MTS Criterion Model 43 (Eden Prairie, MN) with a 5 kN load cell. Solid specimens were assumed to have isometric mechanical properties, and compressive strain was applied along the print axis (*z-axis*) at 4 mm/min to determine the compressive modulus of the bulk material (n=3). Porous cubes were similarly measured to determine scaffold properties.

Raman Spectroscopy

To determine the molecular constituents of the hybrid material and confirm the presence of both the mineral and collagen phases of the DCB particles, Raman spectroscopy was utilized as previously described[279]. Briefly, Raman scattering spectra were measured in backscattering geometry using a Horiba Jobin-Yvon T64000 spectrometer equipped with an Olympus microscope. A 514.5 nm line of Ar+-Kr+ laser was used for excitation. The laser power was kept below 1 mW to avoid overheating of the sample. Spectra of printed sheets containing 30% dopant were recorded and spectra of each of the pure materials were recorded as controls. For recording spectra of BO and DCB samples, samples were photobleached for 30 min to reduce luminescence background.

Scanning Electron Microscopy

Scanning electron microscopy (SEM) was performed to assess the morphology of the particle additives and manufactured sheets. Particles and solid manufactured sheets were mounted on carbon tape and sputter coated with 30 nm of Au/Pd using a Denton Vacuum Desk III to make the samples conductive for imaging. Samples were imaged with a LEO/Zeiss Field-Emission SEM using the InLens detector and an accelerating voltage of 1 kV.

Cell Seeding

Adipose-derived stem cells (ASCs) were obtained under Institutional Review Board approved protocols with patient consent. Briefly, lipoaspirate was digested with 1 mg/mL collagenase I (Worthington Biochemical Corporation, Lakewood, NJ) for 1 hour at 37 °C. The released cells were centrifuged to obtain the stromal vascular fraction pellet and plated. Adherent cells were termed ASCs

and expanded for the current study. Expansion conditions consisted of Dulbecco's Modified Eagle Medium (DMEM; Life Technologies, Frederick, MD) with 4.5 g/L glucose, 10% v/v fetal bovine serum (FBS; Atlanta Biologicals, Flowery Branch, GA), 100 U/mL penicillin and 100 µg/mL streptomycin (P/S; Cellgro), and 1 ng/mL basic fibroblast growth factor (PeproTech, Rocky Hill, NJ). ASCs were cultured in standard conditions on tissue culture plastic at 37 °C with media changes every third day and seeded into the scaffolds at passage two in a suspension of fibrinogen-thrombin at 20,000 cells/µL. Fibrinogen concentration was 10 mg/mL and thrombin concentration was 10 U/mL. The volume ratio was 4:1 fibrinogen:thrombin for a final fibrinogen concentration of 8 mg/mL. Control media (DMEM with 4.5 g/L glucose, 10% v/v FBS, P/S) was used for *in vitro* control groups, while groups osteo-induced for osteoblastic differentiation used induction media (DMEM with 1 g/L glucose, 10% v/v FBS, P/S, 10 mM β-glycerol phosphate and 50 µM ascorbic acid-2-phosphate)

Biochemical Assays

Scaffolds were cultured for 3 weeks in control or induction conditions (n = 3 or 4 per assay). DNA quantities were assessed using the Quant-It PicoGreen dsDNA assay (Invitrogen, Carlsbad, CA) according to manufacturer instructions. Total calcium was measured by agitating scaffolds in 0.5N hydrochloric acid for 24 hours then measuring the calcium in solution using a Stanbio LiquiColor calcium assay (Stanbio, Boerne, TX) to determine calcium content. Calcium content was normalized to the amount of cellular DNA. Mineralized calcium was detected using Alizarin Red S (Sigma A5533) staining and detected using bright-field microscopy.

Gene Expression

After the culture periods, scaffolds were digested with TRIzol (Life Technologies) and isolated mRNA was used to produce cDNA. cDNA was subject to real-time polymerase chain reaction (RT-PCR) for osteogenic genes Col1a1, Runx2, osteopontin (OP), osteocalcin (OCN), and osteonectin (ON) as previously described[243]. The primers used are presented in **Table 6-1**. For analysis, the delta-delta Ct method was used in which β-actin served as the housekeeping gene, and gene expression was normalized to that of cells cultured in PCL scaffolds under control conditions at Day 21.

Table 6-1. PCR Primers

Gene Name	Direction	Sequence
Osteopontin	F	TTGCAGCCTTCTCAGCCAA
	R	GGAGGCAAAAGCAAATCACTG
Runx-2	F	GTCTCACTGCCTCTCACTTG
	R	CACACATCTCCTCCCTTCTG
Osteonectin	F	TCGGCATCAAGCAGAAGGATA
	R	CCAGGCAGAACAACAAACCAT
Osteocalcin	F	GTGACGAGTTGGCTGACC
	R	TGGAGAGGAGCAGAACTGG
Collagen 1	F	GAGAGGAAGGAAAGCGAGGAG
	R	GGGACCAGCAACACCATCT
β-Actin	F	AGTTGCGTTACACCCTTTCTTG
	R	TCACCTTCACCGTTCCAGTTT

Statistical Analysis

Statistical analysis was conducted using GraphPad Prism Software (GraphPad Software Inc.). One-way ANOVA nonparametric tests and Tukey's comparison posttest was sued to compare means for print quality, mechanical testing, and Ca/DNA. One-way ANOVA with a Dunnett's posttest to the control PCL group for each gene was used for qRT-PCR. $P < 0.05$ was considered significant. Data were calculated as the means ± SD.

Results

Particle Size Characterization & Printability

All scaffolds were manufactured using the 3D-printing process. Particles were all within a similar size range (20 – 50 µm), and had an irregular rough appearance except for HA, whose smooth spherical appearance is likely due to fabrication via crystallization in solution (**Figure 6-1**). Two-layer sheets (solid and porous) were manufactured reproducibly after empirically determining pressure and temperature parameters. However, porous and solid cubes required long manufacturing times (several hours), and the printing process with the mineral dopants was subject to clogging of the nozzle. Dopant particles were non-homogenously arrayed on the surface of HA, BO, and DCB constructs, while they were absent in TCP and highly present in BO (**Figure 6-1, 6-2**). The inclusion of the various dopants decreased the printability of the scaffolds, requiring an increase in print temperature and pressure in addition to a reduced print speed (~35% of speed of pure PCL prints; **Table 6-2**). The DCB and BO material mixes were more difficult to extrude than TCP or HA for the longer print times (> 1 hour).

Table 6-2. Manufacturing Settings for Pneumatic 3D-Printing

	Temperature (°C)	Pressure (psi)	Extrusion Head Speed (mm/min)
Pure PCL	80	85	70.09
30% TCP	100	85	32.50
30% HA	100	90	25.69
30% BO	115	90	3.00 - 26.00
30% ECM	110	90	5.50 - 28.00

	Particles	Printed Surface
TCP		
HA		
BO		
DCB		
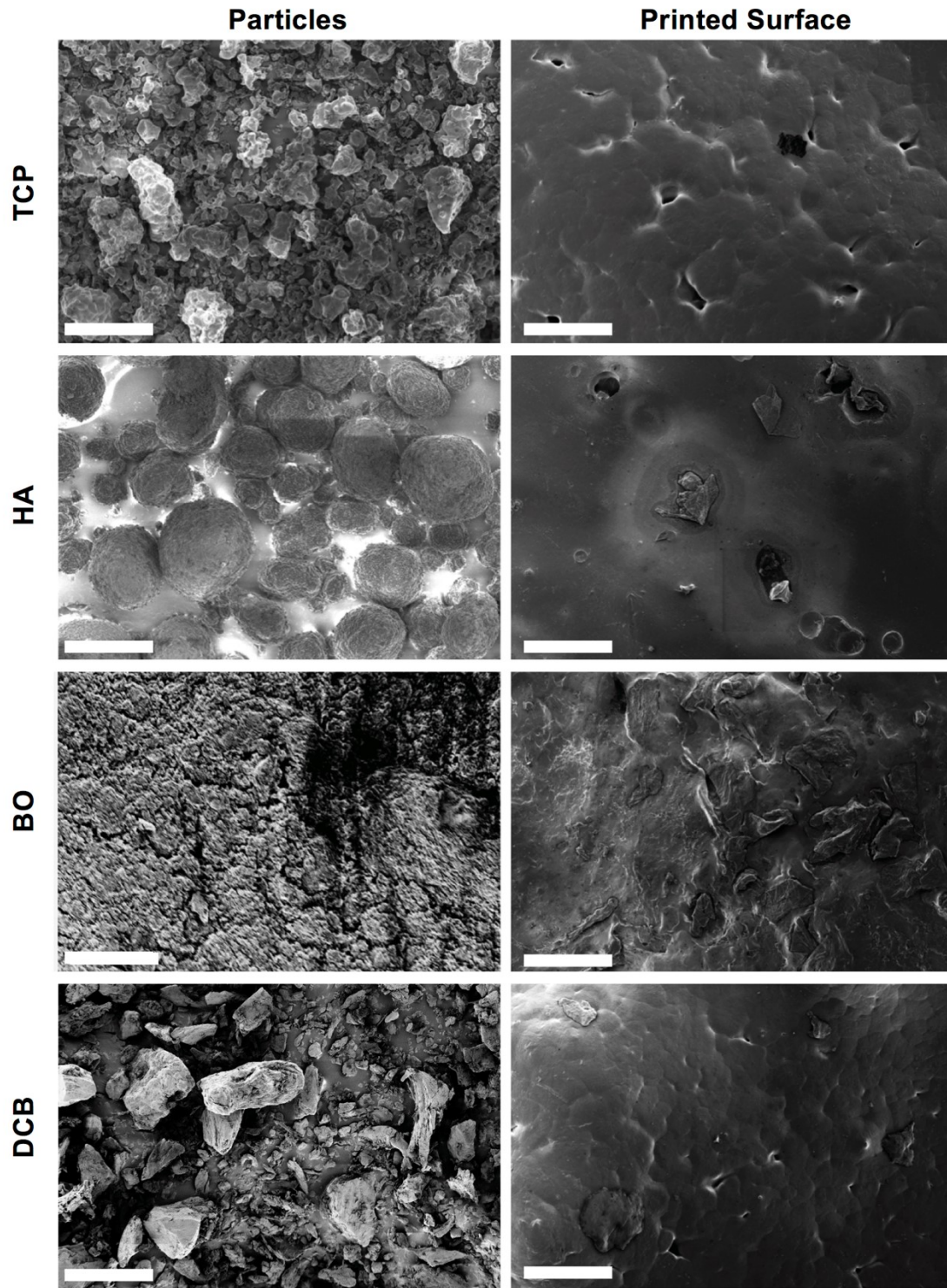
Figure 6-1. Morphological Assessment.

    SEM images show morphology and size range (~20 – 50 µm) of mineral particles (**left column**) and surface topography of the 3D-printed scaffolds (**right column**). Scale Bar = 50µm
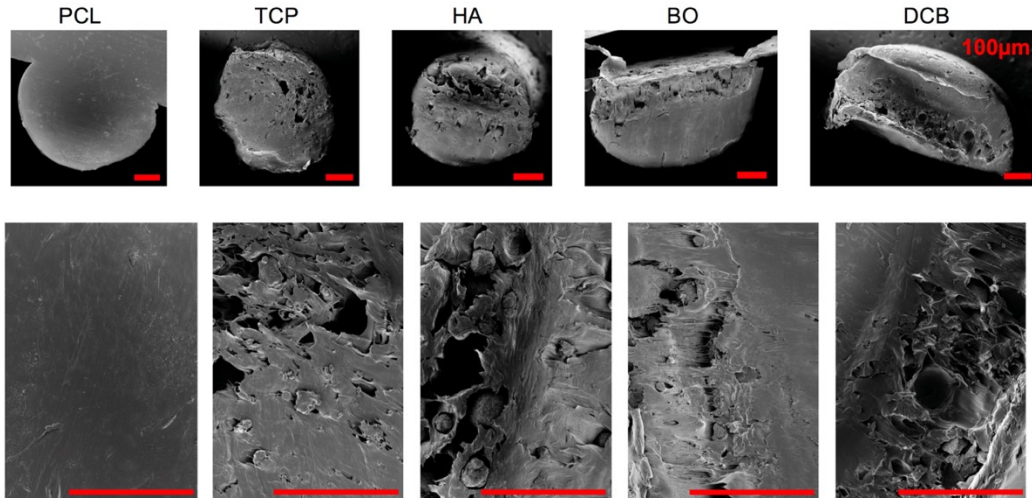
Figure 6-2. SEM of Scaffold Fiber Cross-Sections

Differential scanning calorimetry of the material mixes before (in powder form) and after printing revealed printing pure PCL scaffolds were highly crystalline (96% print vs 50% powder) and the various dopants decreased the crystallinity of the polymer phase to 40 – 46% (**Table 6-3, Figure 6-3**). The dopants did not drastically affect the melting (T_m) temperature from pure PCL: the T_m of pure printed PCL was 62.5 ± 0.5 °C while T_m of the printed materials of for all dopants prints was 60.6 ± 1.0 °C. The glass transition temperature, T_g, of all prints was 36 ± 1.0 °C. However, the printing process did decrease all T_m by 0.5-2 °C relative to the T_m of pure powdered PCL and similarly increase all T_g by 1.0-2.5 °C, highlighting a minor effect of thermal history upon the behavior of the material. This minor effect did not impact the printing process, as the temperature setting was 40-60°C greater than the measured melt temperatures.

Table 6-3. Percent Crystalline of Material

	Powder	**Print**
PCL	51 ± 2 %	96 ± 3 %
TCP	55 ± 2 %	46 ± 5 %
HA	60 ± 2 %	45 ± 2 %
BO	47 ± 2 %	40 ± 5 %
DCB	50 ± 1 %	45±2 %
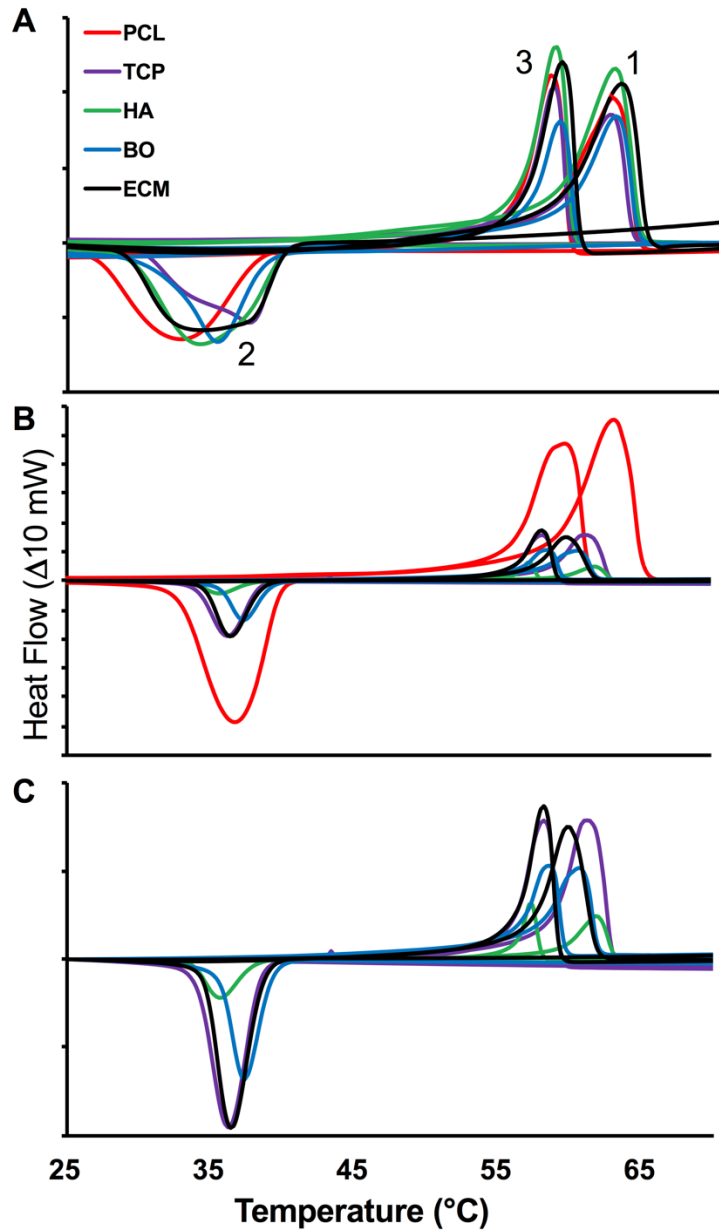
Figure 6-3. Melting Curves of Composite Mixtures.
The cycle moves from 10*C up to 100 through peak 1 (Melting Curve), then down through peak 2 (Crystallization) and up again through a second heating scan which has a lesser melting curve (3) because it has crystallized more perfectly in the machine than in the print bed. For interpretation please see ref [233]. **(A)** Thermally green samples of particle mixtures: PCL only, PCL + TCP, PCL + HA, PCL + BO, and PCL + DCB. **(B)** Samples of printed materials: PCL, PCL-TCP, PCL-HA, PCL-BO, and PCL-DCB. **(C)** Zoomed in image of curves for print samples of PCL-TCP, PCL-HA, PCL-BO, and PCL-DCB.

Print Quality

The mineral dopants caused the scaffolds to become radio-opaque (**Figure 6-4A**) in CT imaging. Alizarin red staining revealed a strong calcium presence in BO and DCB (**Figure 6-4B**). Expansion of the material after extrusion through the nozzle-die was evident in measurements of strut widths in all of the material combinations (**Figure 6-4C**) except for HA (460 μm, PCL = 501 μm, BO = 513, TCP = 546 μm, DCB = 614 μm). This expansion caused pore area to be reduced from its theoretical value in all cases, resulting in decreased void area fraction measured at 39% in HA, 37% in PCL, 35% in BO, 31% in TCP, and 25% in DCB (**Figure 6-4D**). All pores were greater than 500,000 $μm^2$, and struts were all greater than 400 μm, with overlapping struts accounting for 26% of the scaffold area. Print quality measurements compared the output layout of the scaffolds to the input design and demonstrated a decrease of 17% in PCL, 20% in HA, 28% in TCP and DCB, and 30% in BO (**Figure 6-4E**). Inspection of the radio-opacity of the materials along a centerline in a cross-section of a strut in CT images confirmed the increased strut diameter. Hounsfield intensities revealed a lower mineral density in DCB compared to HA and TCP, which were similarly intense but also slightly lower than a peak in BO (**Figure 6-4F**).
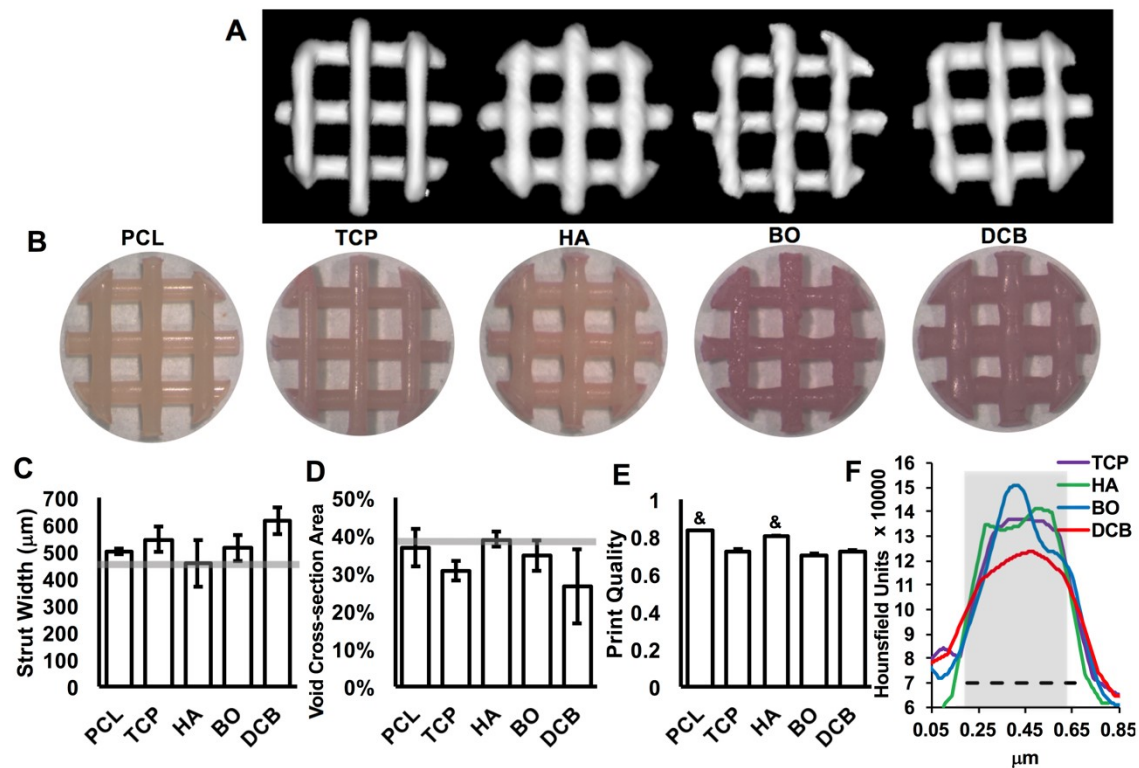
Figure 6-4. Determination of Print Quality.
(A) CT images of 3D-printed PCL scaffolds containing TCP, HA, BO, and DCB confirming the presence of mineral. (PCL only scaffolds were not visible via CT). **(B)** Stereomicroscope images of scaffolds stained with alizarin red. **(C)** Width of struts in each composite scaffold. Gray line represents theoretical width of 460 μm. **(D)** Cross-sectional area of void regions in scaffolds. Gray line represents theoretical design void area (40%). **(E)** Print quality: measure of how actual printed scaffolds compare with a theoretical ideal. PCL and PCL-HA are statistically higher than other groups (& $p < 0.05$; n=3). **(F)** Trace of radiographic intensity through the core of an individual strut (gray = design parameter of 460um).

Mechanical Properties

Porous and solid cuboidal scaffolds were subjected to unconfined compression along their print axis (**Figure 6-5A**) until reaching either 80% strain or 4.5 kN. Comparison of the scaffolds before (**Figure 6-5B**) and after (**Figure 6-5C**) illustrates the equidirectional and permanent (plastic) deformation of the scaffold along the xy-plane. Compressive moduli of the scaffolds were obtained by measuring the slope of the stress-strain curve in the linear region between 2 and 4% strain (**Figure 6-5D**) for porous scaffolds and solid blocks of manufactured material. Bulk PCL-TCP and PCL-DCB scaffolds had stiffness of 253 MPa and 241 MPa, compared to PCL (266 MPA). PCL-HA had a statistically higher modulus of 338 MPa (**Figure 6-5E**). Compressive moduli of porous scaffolds were all significantly reduced from the bulk values. The moduli of the various scaffolds were HA (83 MPa), PCL (51 MPa), TCP (37 MPa), and then DCB (32 MPa) (**Figure 6-5E**).

Raman Spectroscopy

Raman spectroscopy revealed the C-H bands characteristic for PCL (peaks 1 – 4) in all of the materials (**Figure 6-6**). Phosphate bands associated with the mineral (peaks 5 – 7) were observed in the prints containing PCL, HA, BO, and DCB indicating that mineral deposits were present on the surface of the materials. Amide bands that are indicative of the presence of collagen were observable in DCB and to a lesser extent in BO (**Figure 6-6**). Spectra of the pure dopant powders are provided in **Figure 6-7**.
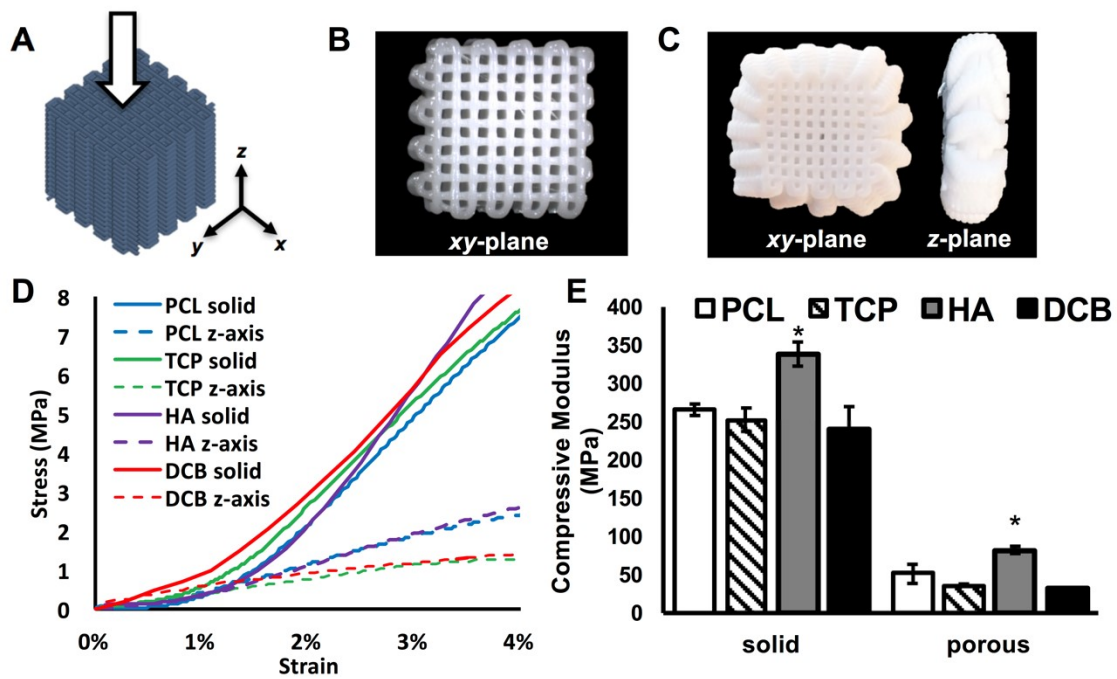
Figure 6-5. Mechanical Testing.
(A) Schematic of applied force along print axis (*z*-axis). **(B)** Top-down view of scaffold along print axis before applying strain. **(C)** Top-down and side vies of scaffold after 60% strain. **(D)** Representative stress-strain curves. **(E)** Compressive moduli of scaffolds. Modulus of PCL-HA is statistically higher than that of PCL only (* = p< 0.05; n=3).
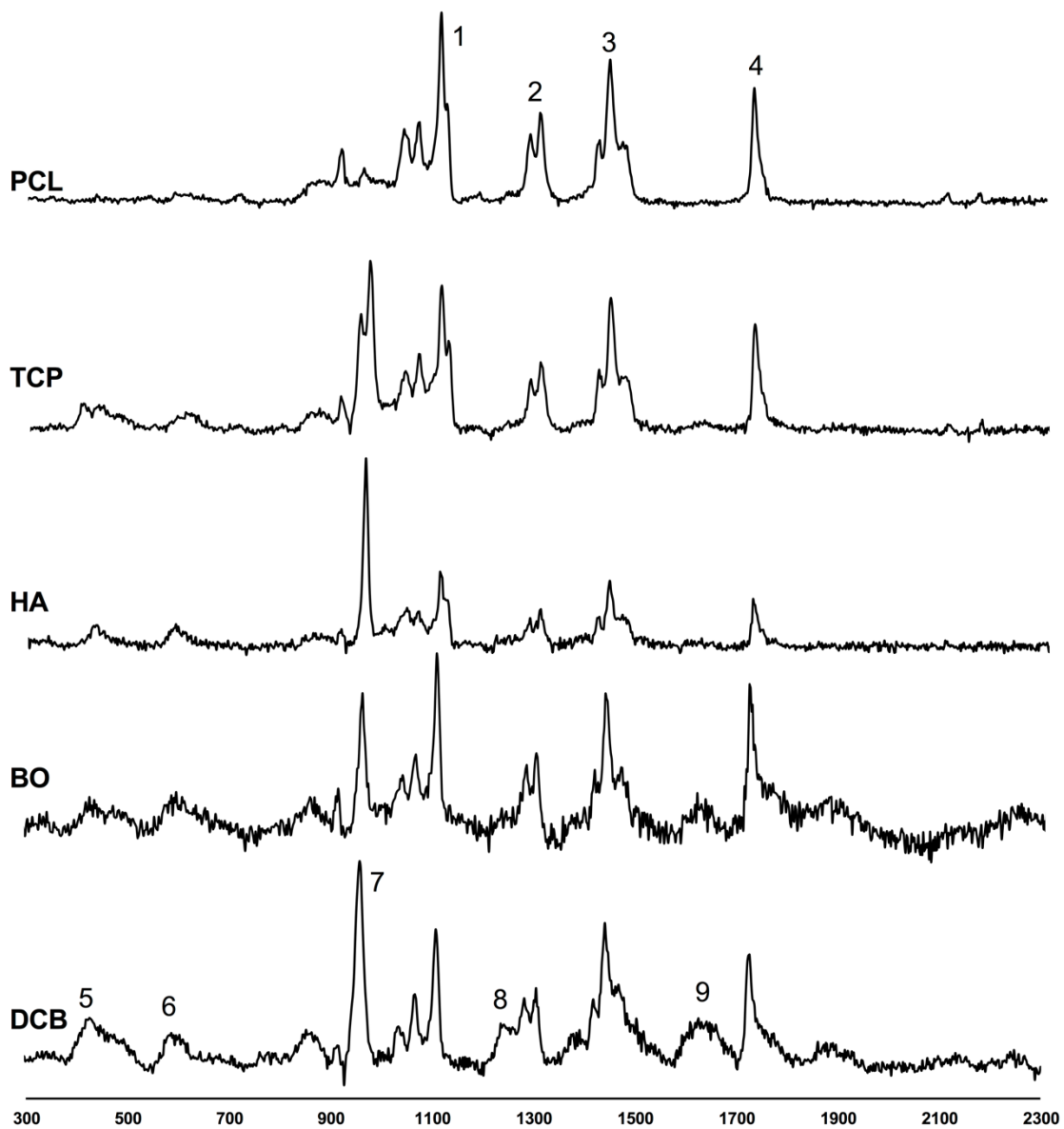
Figure 6-6. Raman Spectroscopy.

Raman spectra of printed materials showing characteristic peaks for PCL (1: 1110 cm^{-1} skeletal stretching; 2: 1300 cm^{-1} ωCH2; 3: 1450 cm^{-1} δCH2; 4: 1720 cm^{-1} C=O) and bone (5: 430 cm^{-1} 4v_2 PO$_4^{3-}$; 6: 590 cm^{-1} v_4PO$_4^{3-}$; 7: 960 cm^{-1} v_1PO$_4^{3-}$; 8: 1340 cm^{-1} Amide III; 9: 1660 cm^{-1} Amide I).
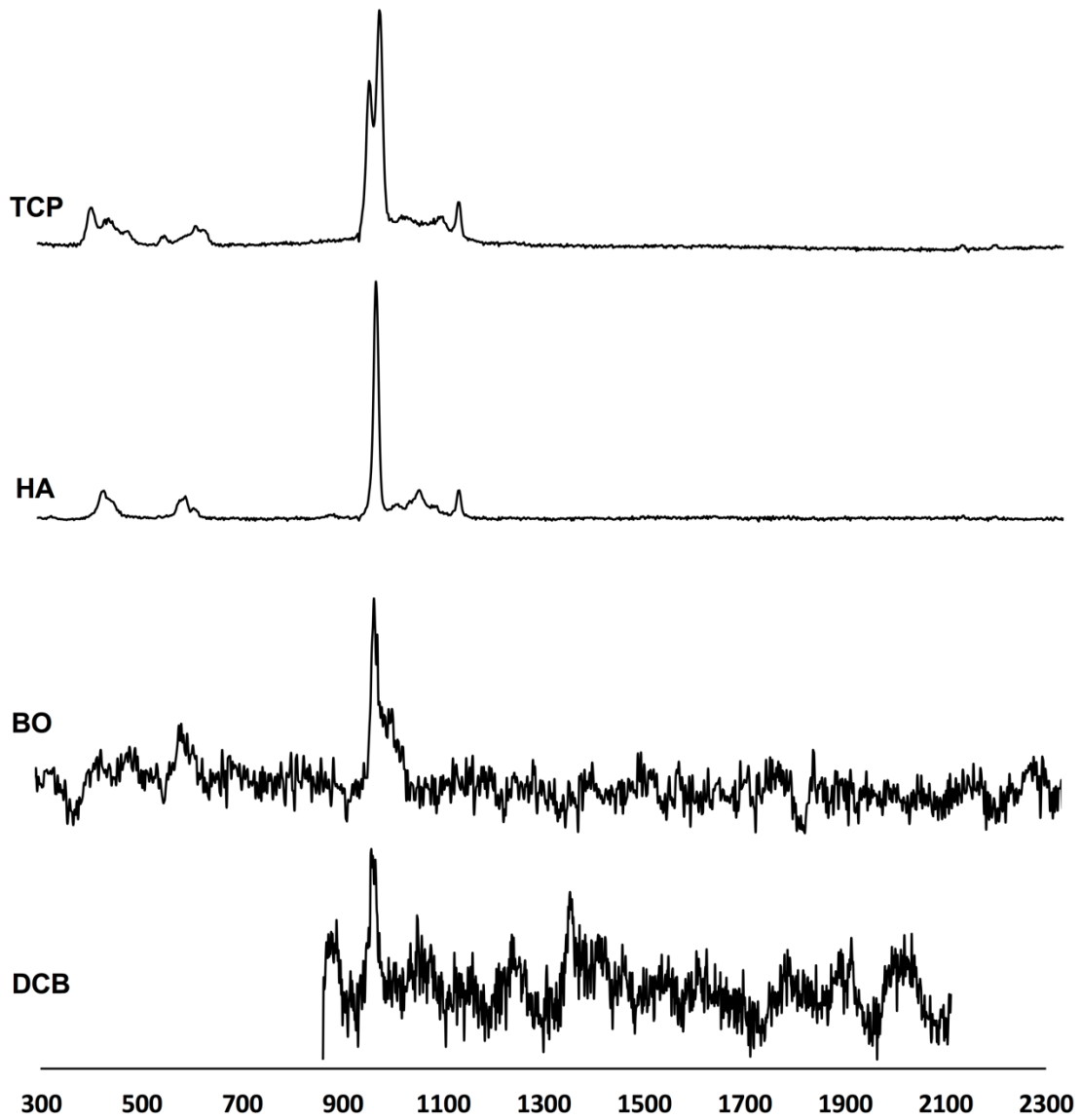
Figure 6-7 Raman Spectra of Pure Dopants.

Cell Seeding & Growth

The numbers of ASCs in the scaffolds after 3 weeks were generally higher in the control cultures relative to the osteo-induced cultures for the same materials. In the control cultures, cell numbers were significantly lower in PCL scaffolds relative to the other scaffold groups. The cell numbers in the PCL-TCP, PCL-HA, PCL-BO, and PCL-DCB were all statistically identical (**Figure 6-8A**). Cell numbers in the osteo-induced cultures were unchanged among the different biomaterial scaffolds (**Figure 6-8A**). For each scaffold composite, the amount of calcium/DNA deposited was greater in the osteo-induced groups compared to their controls. In the control groups, the amount of Ca/DNA was statistically higher in PCL-TCP (34.6±2.6 ng/ng), PCL-BO (60.0±21.7 ng/ng), and PCL-DCB (64.2±3.2 ng/ng) relative to PCL (5.6±5.2 ng/ng) and PCL-HA (17.5±2.4 ng/ng) (n=3). This trend was similar in the osteo-induced groups, with the greatest Ca/DNA in DCB and the least in HA and PCL (**Figure 6-8B**).
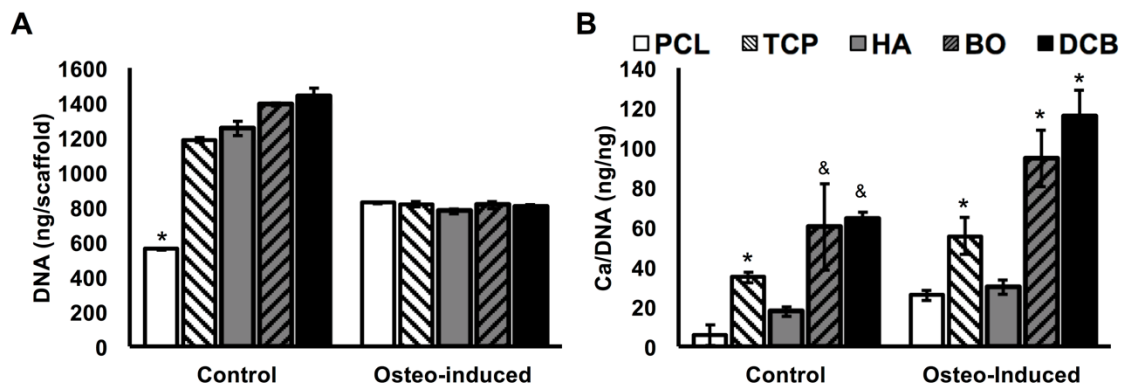
Figure 6-8. DNA and Calcium Content of ASC-seeded Scaffolds.
(A) Total DNA harvested from scaffold after 21 days of *in vitro* culture. (B) Calcium content normalized to the amount of DNA after 21 days of *in vitro* culture. * statistically different from all other groups (p < 0.05); & groups are similar to each other but statistically different from all other groups (p < 0.05 ; n=3).

Gene Expression

PCR analysis of the cell-laden constructs was performed on day 21. There were no clear trends in the expression of Runx2. Under control conditions, Runx2 expression was only roughly 17-fold higher in PCL-HA relative to PCL only. After 21 days of osteo-induction, Runx2 expression was elevated in PCL (13.1 ± 3.5 fold; $p = 0.0003$) and PCL-DCB (7.2 ± 3.5 fold; $p = 0.0489$) relative to control PCL (**Figure 6-9**). Similarly, there were no clear trends for osteocalcin expression: all of the scaffold groups were statistically similar to the control PCL under control or osteo-induced conditions (**Figure 6-9**). Osteopontin was upregulated roughly 4- to 5-fold in PCL-HA and PCL-TCP scaffolds in control conditions. Osteopontin expression increased 5- to 10-fold in all biochemically osteo-induced cultures though statistical significance was only observed with PCL-HA and PCL-DCB. In control cultures, the Osteonectin expression increased in PCL-TCP (3.6 ± 1.8 fold; $p = 0.5423$), PCL-BO (8.8 ± 2.2 fold; $p = 0.0040$), and PCL-DCB (10.1 ± 0.95 fold; $p = 0.0011$). The expression increased 10- to 5000-fold in all osteo-induced groups relative to the PCL control. Collagen 1 expression in control cultures showed a strong dependence on scaffold composition. Collagen I expression increased in PCL-TCP (4.6 ± 0.87 fold; $p = 0.9421$), PCL-BO (18.5 ± 8.2 fold; $p = 0.0197$), and PCL-DCB (19.8 ± 1.6 fold; $p = 0.0078$), but not in PCL-HA (0.48 ± 0.11 fold; $p = 0.9959$). With the addition of soluble osteo-inductive factors, expression levels increased in all groups relative to the PCL cultures in control conditions: PCL (11.7 ± 9.2 fold; $p = 0.9704$), PCL-TCP (74.7 ± 32.6 fold; $p = 0.0094$), PCL-HA (4.6 ± 1.7 fold; $p = 0.9970$), PCL-BO (14.8 ± 6.8 fold; $p = 0.04920$), and PCL-DCB (12.5 ± 6.5 fold; $p = 0.0480$) (**Figure 6-9**).
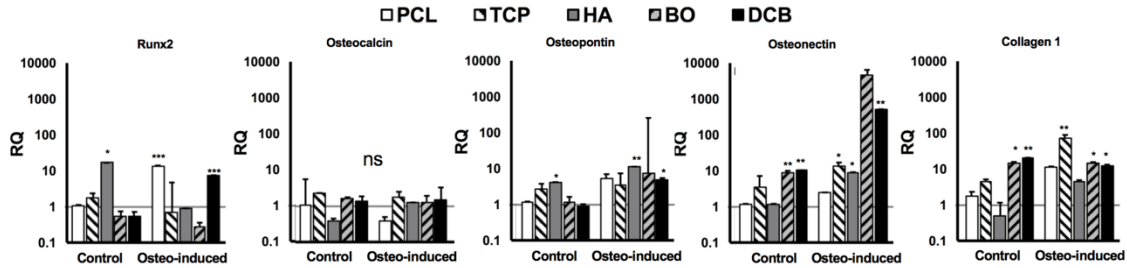
Figure 6-9. Expression of Osteogenic Genes in ASCs.
qRT-PCR assessment of Runx2, osteocalcin, osteopontin, osteonectin, and collagen I after 21 days of culture. Gene expression normalized to ASCs cultured in PCL with Control medium. *$p < 0.05$; **$p < 0.01$; ***$p < 0.001$.
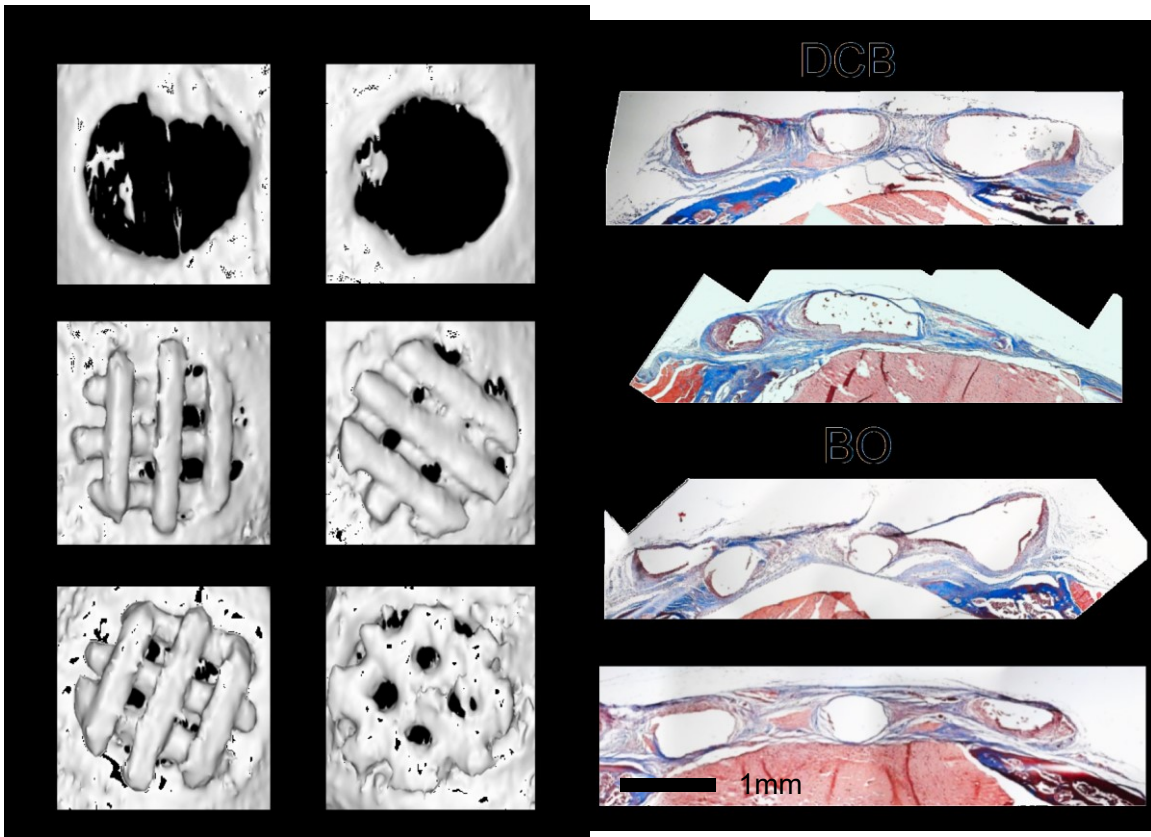
Figure 6-10. *In Vivo* Evaluation of Dopant Scaffolds at 12 Weeks.
Representative results. *Left:* CT of scaffolds after 12-weeks of healing. *Right:* Mason's trichrome staining of cross-sections of the defects. White void spaces are where the scaffold was located.

Discussion

Current commercially available bone substitutes include allografts and their derivatives (e.g. demineralized bone matrix), xenograft derivatives (e.g. Bio-Oss), collagen-derivatives, synthetic materials (e.g. TCP and HA), and combination products (e.g. collagen sponges with bone morphogenetic protein-2). Yet, none of these approaches is capable of producing adequate treatment of critical-sized defects that require the regeneration of delicate anatomic structures. 3D-printing has emerged as a promising strategy for producing scaffolds with an array of small features from a multitude of synthetic materials. In fact, several groups have demonstrated the potential for 3D-printing scaffolds from polymeric materials[236,280,281]. To enhance the bioactivity of 3D-printed, polymer-based scaffolds, they are often functionalized with mineral deposits including TCP[275], HA[272,277], and DCB[282]. In fact, a previous study from our group demonstrated that incorporating bovine DCB into 3D-printed PCL was sufficient to induce upregulation of bone-specific markers in ASCs[27]. We hypothesized that the presence of collagen in bovine DCB rendered it a more effective dopant than either HA or TCP, which are the two most commonly investigated materials in the field. To test this hypothesis, it was important to directly compare 3D-printed PCL-DCB with PCL-HA and PCL-TCP manufactured using similar protocols. Since the mineral phases of TCP and HA differ from that within native bone, we also included Bio-Oss in our analysis. Bio-Oss is a commercially available bovine bone substitute which is available as granules (Geistlich Pharma AG, Wolhusen, Switzerland). It is processed from bovine bone and is treated to remove the organic or protein phase from material, resulting in a structure enriched in inorganic

115

mineral. An identical 3D-printing procedure was used to create PCL-TCP, PCL-HA, PCL-BO, and PCL-DCB. The weight ratios were kept constant in all groups. While the osteo-inductivity of HA and TCP blends have been previously compared[271], this study provides the first comparison of PCL-TCP, PCL-HA, PCL-BO, and PCL-DCB with direct PCL for material and biological properties.

This study directly compared the printability of common mineral components. Particles for each material were readily available or easily manufactured into an appropriate particle size for mixing with PCL and extruding through a small diameter nozzle (20-50µm particle diameter / 460µm nozzle diameter). Despite this size ratio, the pulverized materials (BO, DCB) sometimes clogged the nozzle during printing suggesting that the particles may clump during the process. The viscosity of the PCL melts increased with the addition of the mineral dopants resulting in reduced linear print rates. Previous work studying a range of DCB concentrations in PCL demonstrated a reduced printability with increased dopant concentration[27], therefore 30% w/w was selected for this study to ensure that all groups would be manufacturable. While increasing the concentration of dopants also increased the osteoinductive effect and cell adhesion, it reduced the overall strength of the scaffold—we expect those trends would be replicated in the materials used in this study. Our print temperature and pressures are less than other reported values[102,264], despite being well above the measured melt temperatures of the polymer phase. Design parameters were chosen according to previous optimization of our 3D-printed scaffolds for bone formation: 60% porosity, 800µm pore size, and strut thickness 460 µm[26]. Porosity was chosen at 60% to enable space for tissue formation and to arrive at a design

with sufficiently large pores, as the porosity and strut size directly determine the pore size in our 3D-printing system. Large, 1000 μm sized pores have been previously shown to be enhance ASC-driven bone formation greater than smaller pores[283]. Strut thickness was chosen to impart sufficient strength to the material. Variation in the print features was present in all material blends and did not correlate with any obvious feature of the various dopants. Despite the variation in print features, the mechanical and porous design goals were preserved. Increased strut width and reduced pore area is likely due both to swelling of the polymer after extruding through the die, which a normal feature of thermopolymer extrusion. The variations of material speed might be due to the varying amount of material in the print nozzle during a print, or a change in the printing environment (such as humidity or temperature) during a print, as the print times were long (between 30-60 minutes for a two-layer sheet and 2-6 hours for a porous cube).

We employed differential scanning calorimetry and found that the percent crystallinity of the PCL constructs reduced significantly when doped with the mineral particles. The particles likely inhibited the crystal growth of the material during the cooling phase as physical barriers[284]. In spite of this, the mechanical properties of the composite scaffolds did not exhibit drastic changes. Compressive mechanics of the materials were well suited to bone scaffolds, with compressive moduli around 250-300 MPa for bulk and 32-83 MPa for porous. This exceeds some of the values typically reported for trabecular bone (compressive modulus 0.5-14.6 MPa)[285]. Our results are similar with other reports of compressive moduli in bulk and porous PCL[236,286–288]. The reduction in compressive moduli in the porous scaffold is related to the decrease in solid material in columnar contact

along the direction of force (26% in porous vs solid, while porous moduli were reduced to 20% of solid). Doping with HA particles increased the mechanical stability of the solid and porous scaffolds. This is consistent with other studies, which have found that the inclusion of HA particles within bulk PCL material phase hardened the material and increased the elastic modulus[274]. They ascribed this result to the greater hardness of HA relative to PCL[289,290]. However, the mechanism by which strengthening occurs is unclear, particularly as all other dopants resulted in slightly lower (though not statistically significant) compressive moduli than that of pure PCL scaffolds.

SEM images appeared to reveal sparse distribution of particles along the surfaced of the 3D-printed struts (**Figure 6-1**) with a greater amount within the center (**Figure 6-2**). However, the amounts of material on the surfaces were sufficient to be detected by Raman spectroscopy (**Figure 6-6**). See reference[291] for a complete list of bone wavelet assignments and reference[284] for PCL assignments. The presence of material on the surface is important for increasing cell adhesion and contact-based signaling (such as ECM-integrins). The presence of mineral in the inner regions of the struts may be advantageous for long-term accessibility of the particles as they become more exposed as the PCL degrades. This arrangement may be particularly useful for TCP, which degrades relatively quickly. This distribution of particles throughout the struts was corroborated by the CT data. The CT images revealed mineral distribution through the strut. There was a distinct increase in opacity at the center of the strut relative to the edges, however, this profile may be due to the 3D-cylindrical profile of the struts.

Even though ASCs were suspended in fibrin hydrogels in the pore spaces of the scaffolds, their proliferation and calcium deposition were influenced by the presence of mineral in the scaffold struts. For example, cell proliferation in control medium conditions was significantly higher in the mineral-containing scaffolds relative to PCL only scaffolds. While the mechanistic reason for this is unknown, it is possible that the release of ions from the various calcium phosphates could be influencing these increases in proliferation[292]. Alternatively, ASCs might be responding to changes in topography at the surfaces of the struts. In general, when biochemical osteo-induction was used, proliferation was lower possibly due to the low-glucose environment. Interestingly, mineralization detected using alizarin red stains within the scaffolds was apparent not only at the surface of the scaffold in the control groups, where cells would have direct contact and binding with the particles present on the surface—but also throughout the bulk of the fibrin gel. This suggests that the effects of the bioactive scaffolds are not limited only to direct physical interactions between the cells and the biomaterials. The expression of Runx2, osteocalcin, and osteopontin data did not exhibit clear trends. However, upregulation of collagen 1 and osteonectin was clearly observed in the PCL-BO and PCL-DCB groups relative to PCL only when ASCs were cultured in control and osteo-induced medium. These are both key secreted matrix proteins with roles in mineral formation. These data correlate with the increased Ca/DNA in the PCL-BO and PCL-DCB groups. This correlation suggests that the natural apatite structure present in DCB and BO may be more effective at osteo-induction than either of the synthetic TCP or HA minerals. It is also possible that the osteo-inductive signals are enhanced by the presence of the collagenous phase. While

Bio-Oss has been treated to remove the organic phase, the Raman spectroscopy data did reveal a small amide peak (# 9) that was also clearly evident in PCL-DCB but not in the PCL, PCL-TCP, or PCL-HA spectra. However, it may also be that fewer of the TCP and HA particles were present on the surface of the struts and, hence, less potent.

While the mineral dopant changes the bioactive and mechanical properties of PCL, we do not expect that the biocompatibility, degradation, or physiochemical properties will be reduced to invalidate PCL as the primary material choice for the scaffold. The biocompatibility and biodegradation of PCL[293], TCP[257], HA, and Bio-Oss[294] are well understood individually. PCL undergoes slow degradation via hydrolysis of the ester group[239], while calcium phosphates undergo slight ionic dissolution in combination with resorption by osteoclasts[295]. Yeo et al have shown that inclusion of TCP in PCL scaffolds produces a slightly acidic environment during degradation *in vitro*[269]. While we have not investigated the degradation and biocompatibility properties of these scaffolds directly, our previous in vivo work with 3D-printed PCL-DCB scaffolds did not give rise to any adverse inflammation events and the scaffolds were not visibly degraded after 12 weeks[27].

While this data confirmed clear advantages for using PCL-BO and PCL-DCB, further work is required to improve the printability, speed, and potential for scale-up of the mineral-polymer scaffolds. This might be addressed through the use of a filament-based system, as used in Albrecht *et al*[296]. Additionally, the use of a photo-crosslinker to polymerize the PCL[297] might be used in a digital light projection manufacturing system to improve the resolution and complexity of the scaffolds, in addition to enabling low-temperature production that might permit the

inclusion or retention of existing growth factors within an ECM or other GF-binding ingredient. The *in vitro* response of these materials combined with a more versatile manufacturing system will be further evaluated *in vivo* in a critical-sized or anatomically complex defect model.

Conclusion

We successfully 3D-printed several composite PCL-mineral scaffolds and compared their relative abilities to drive osteo-induction in ASCs. In this 3D-printing system, PCL-BO and PCL-DCB exhibited greater ability for osteoinduction than synthetic materials such as PCL-HA or PCL-TCP. PCL-DCB and PCL-BO blends induced significant increases in mineral deposition and upregulation of collagen and osteonectin relative to PCL only scaffolds. The PCL-TCP and PCL-HA scaffolds also showed some enhanced osteo-inductivity, though not to the same extent. This greater induction might be due to the presence of a collagen phase (as measured by Raman spectra), the structure of the apatite, or greater presence of the BO and DCB particles on the surface of the struts following the printing process. These results indicate that doping 3D-printed PCL scaffolds with DCB or BO might better support bone healing *in vivo* in comparison to TCP- or HA-doped grafts.

Acknowledgments

CHAPTER 6[§§]
PREASSEMBLY TIME MODULATES THE VASCULOGENIC POTENTIAL OF ADIPOSE-DERIVED STEM CELLS IN PSUEDO-IMPLANT AND IMPLANT CONDITIONS

Summary

Pre-vascularization of tissue engineered grafts is a promising strategy to facilitate improved viability of transplanted cells following *in vivo* implantation. In this process, endothelial cells form a primitive capillary-like vascular network that can anastomose with blood vessels from the host. Adipose-derived stem cells (ASCs) are a commonly used cell population for tissue engineering and contain a subpopulation of endothelial cells capable of assembling into robust vascular networks when cultured in 3D fibrin hydrogels. However, their initial vascular assembly is significantly impaired in hypoxic conditions (2% O_2). Previously our group found that a six-day period of normoxia (20% O_2) produced stable vascular networks. When these structures were transferred to hypoxic conditions, the vessels remained patent and continued to grow. In this study, we explored the minimum period of normoxic pre-treatment required to enable the formation of stable vascular networks and the *in vivo* response. To test this minimum time, we pre-assembled ASC-vessels in normoxia for 0, 2, 4, or 6 days and then transplanted the grafts into hypoxic environments for six days. We assessed total vascular length, pericyte coverage, cell proliferation, apoptosis rates, and ECM production. There was a steady progression in vascular assembly over the 6 days

---

[§§] Adapted from Nyberg, E., & Grayson, W. (2018). Assessing the Minimum Time-Period of Normoxic Preincubation for Stable Adipose Stromal Cell-Derived Vascular Networks. *Cellular and Molecular Bioengineering*, 1-11.

of culture. However, our data showed four days as the minimum period of time required for stable vascular assembly to occur. We compared the major differences in cell behavior and network structure at Day 2 and Day 4. There were no differences in proliferation or apoptosis, however, the Day 4 time-point was associated with a significant increase in pericyte coverage (46.1±2.6%) compared to Day 2 (24.3±5.3%). Pharmacologic inhibition of pericyte coverage during vessel assembly resulted in a similar reduction in vessel length. These data suggest oxygen tension may be a mediator of endothelial cell-pericyte interactions during vascular assembly.

Introduction

Tissue engineered implants have the potential to treat a number of large volumetric musculoskeletal disorders and defects[298] but are severely limited in scale by a lack of a perfused blood vessel networks[299]. The inclusion of functional vascular networks within tissue engineered constructs is a promising strategy when scaling from mouse- to human-sized applications in order to provide the oxygen, nutrients, and waste removal needed by tissues[300]. Neovascularization is a slow process with rates less than 1 mm/week[301] and cellular constructs with thicknesses greater than 400 µm become rapidly necrotic due to the diffusion limitation of oxygen[302]. Hence, the inability to provide sufficient vascularization has limited the clinical use of tissue engineered implants. Several approaches to create tissue engineered scaffolds with functional vascular networks have been reported. These include 3D-printing channels for vessel ingrowth[303], releasing angiogenic growth factors from the scaffold[212], and periods of *in vitro* culture to 'pre-vascularize' the construct before implantation[304,305].

Pre-vascularization is a highly promising strategy in which endothelial cells (ECs) are stimulated to form nascent capillary-like vascular network structures that can anastomose with the host vasculature. In order to form stable networks, ECs are typically co-cultured with fibroblasts[306], mesenchymal stem cells[307,308], or pericytes[309], which act as perivascular cells and stabilize the vascular networks. Recently, adipose-derived stem cells (ASCs) from human lipoaspirate tissues have been shown to be a suitable source of ECs and perivascular cells. The vascular potential of ASCs arises, due to a sub-population of endothelial cells (ECs) at early passages[310,311] as well as their limited ability to differentiate into ECs[312,313]. ASCs also include a pericyte or pericyte-like population[314] and pericytes have potential to modulate the effect of angiogenic therapies[315]. When cultured in fibrin hydrogels, the EC sub-population within ASCs exhibit the potential to form extensive, interconnected vascular network structures[131,316] that survive in vivo implantation[316].

The capacity of ECs and ASCs to assemble into vascular networks is highly oxygen-dependent. Specifically, hypoxic conditions (<5% O_2) inhibit the self-assembly of vascular networks. Hypoxia (5% O_2) prevented the self-assembly of vascular networks in a co-culture of human endothelial colony forming cells and multipotent stromal cells[317]. Griffith and George have shown that in addition to inhibiting self-assembly, challenging constructs with hypoxia after a period of preassembly leads to the degradation of capillary networks[318]. More recently, it has been shown that hypoxia inhibits *de novo* assembly of ASC-derived vascular networks[246]. These reports run counter to the predominant narrative of hypoxia as a pro-angiogenic stimulus. In fact, while hypoxia drives new blood vessel formation

via angiogenesis (and is a key mechanism underlying tumor vascularization), low oxygen tension is a known inhibitor of vascular assembly. Interestingly, while hypoxia inhibits the *de novo* vascular assembly of ASCs and their EC sub-populations, transferring pre-assembled ASC-vessels into hypoxic environments stimulated their growth[246]. Prevascularization strategies therefore require understanding the impact of oxygen on the kinetics of assembly and stabilization.

In this study, we aimed to determine the minimum amount of normoxic (20% O_2) preassembly time that is needed for ASC-vascular networks to stabilize so that they when transferred to hypoxic (2% O_2) conditions, the vessels would continue to elongate. To assess this, ASCs were cultured in fibrin hydrogels and allowed to pre-assemble into vascular network structures for 0, 2, 4, or 6 days. At the end of each of these pre-incubation periods, we split the cultures into two and transferred one group to continued normoxic cultures and the other group to hypoxic (2% O_2) culture conditions for a further 6 days (**Figure 7-1**). We assessed geometric and cellular properties of the networks to establish the underlying mechanism mediating the switch in behavior of endothelial cells to hypoxic environments. These studies suggest that the interactions between endothelial cells and pericyte-like populations are strongly oxygen-and time-dependent. Further understanding of these interactions may be critical for exploiting the vascular capacity of ASCs in pre-vascularization strategies.
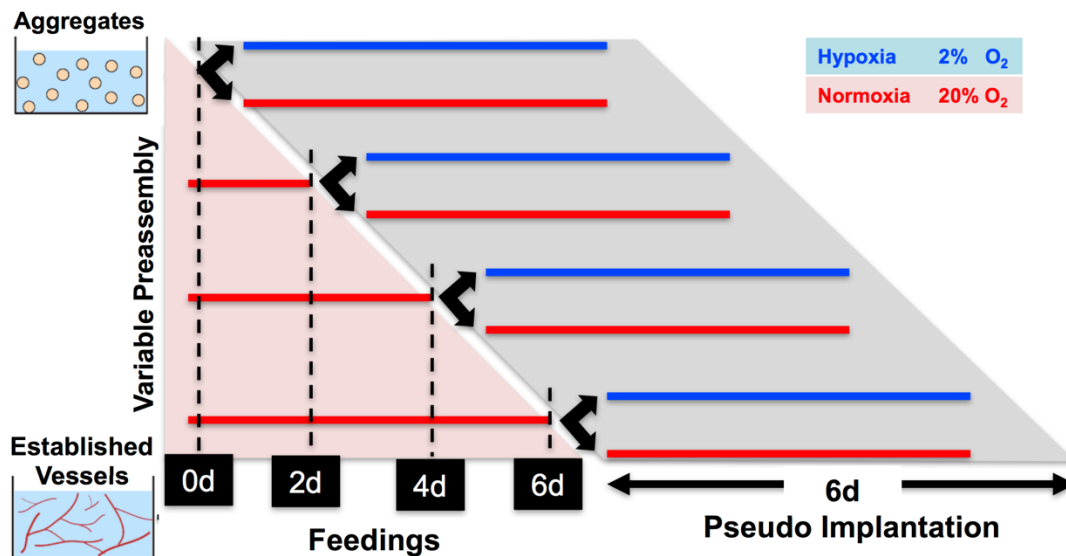
Figure 7-1: Schematic of the Psuedo-Implantation Study.
Gels of ASC aggregates were allowed to preassemble for 0, 2, 4, or 6 days in normoxia with regular feedings before moving into a psuedo-implant condition for 6 days.

Materials and Methods

ASC Isolation and Culture

Human subcutaneous adipose tissue was obtained in the form of lipoaspirate from 3 female Caucasian donors undergoing elective surgery and with written informed consent under the approval of the Johns Hopkins Medicine Institutional Review Board. ASCs were isolated as previously described[246,319]. Briefly, tissue was digested with collagenase (1 mg/mL; Worthington Biochemical Corp.) to isolate the stromal vascular fraction of cells. These cells were plated onto tissue culture plastic and were termed "passage 0 ASC" when they reached 80-90% confluence. ASCs were used at passage 2 for all experiments. Growth medium consisted of: high glucose DMEM (Gibco) with 10% fetal bovine serum

126

(FBS; Atlanta Biologicals), 1% penicillin/streptomycin (Gibco), and 1 ng/mL basic fibroblast growth factor (FGF-2; PeproTech).

Cell Aggregation *via* Suspension Culture

Cells were trypsinized and resuspended at a concentration of 250,000 cells/mL in growth medium containing 0.24% (w/v) methylcellulose (Sigma). The cell suspension was pipetted into 10-cm Petri dishes coated with 2% (w/v) agarose to minimize cellular adherence to the dish. After overnight suspension culture, cellular aggregates were collected with a pipette, and then centrifuged before encapsulation procedures.

Aggregate Encapsulation and Culture

Pre-assembly culture: Cell aggregates were suspended in fibrinogen (8 mg/mL final; Sigma) and thrombin (2 U/mL final; Sigma) at a final cell concentration of 2×10^4 cells/µL. Fibrin gels were formed by pipetting 12 µL of gel solution into 4-mm diameter wells and incubating at 37ºC for 30 min to allow complete gelation before adding medium. Each gel sample was fed with 1 mL of culture medium containing: Endothelial Basal Medium-2 (EBM-2, Lonza), 10% FBS, and 1% penicillin/streptomycin. The media was not supplemented with growth factors beyond those naturally present in serum. To assess the effect of preassembly on future hypoxic cultures, freshly encapsulated cells were cultured in normoxia (20% O_2) for 0, 2, 4, or 6 days with the medial changed every other day to create different degrees of vascular networks.

Pseudo-implantation culture: On the last day of preassembly, the samples were fed once more and then cultured in either normoxia or hypoxia (2% O_2) for an additional 6 days with no media changes (**Figure 7-1**). Normoxic samples were

127

maintained in a 37ºC incubator with 5% CO_2, 95% ambient air. Hypoxic samples were placed in a modular incubator chamber (Billups-Rothenberg) that was flushed every day with pre-mixed gas (2% O_2 / 5% CO_2 / N_2 balance) and placed in a 37ºC incubator.

Proliferation Labelling

Cells were incubated with bromodeoxyuridine (BrdU, Sigma) to detect proliferating cells. Briefly, 10 µM BrdU was pipetted into existing culture medium (i.e. medium was not changed), and samples were quickly returned to their appropriate oxygen environment (less than 5 minutes of normoxic exposure) for a 20-hour incubation. Samples were then washed with PBS and fixed with 3.7% formaldehyde.

Whole-mount Immunostaining

Whole-mount immunostaining of fibrin gels was performed as previously described[131]. Briefly, samples were fixed with 3.7% formaldehyde for 3 hours at 4ºC, washed with PBS, and blocked with 5% normal goat serum / 0.2% Triton X-100 / PBS for 3 hours at 4ºC. Antibodies were incubated overnight at 4ºC, followed by three 1-hour washes in PBS with 0.1% Tween. Primary antibodies included: mouse anti-human CD31 (4 µg/mL, Sigma), mouse anti-human collagen IV (20 µg/mL, Santa Cruz Biotech), and Cy3-conjugated mouse anti-alpha smooth muscle actin (αSMA; 7 µg/mL, Sigma). Secondary antibodies used included: DyLight 488-conjugated goat anti-mouse (3.75µg/mL, Jackson ImmunoResearch), cy3-conjugated donkey anti-mouse (7 µg/mL, Jackson ImmunoResearch), biotin-conjugated goat-anti mouse (5.5 µg/mL, Jackson ImmunoResearch) and fluorescein-conjugated streptavidin (4.5 µg/mL, Jackson ImmunoResearch). Prior

to secondary labelling for incorporated BrdU, samples were stained for all other antigens and post-fixed with 3.7% formaldehyde for 30 min to preserve the stain. Samples were then denatured with 2N HCl / 0.5% Triton X-100 for 45 minutes at room temperature, washed, re-blocked, and then incubated with AlexaFluor 647-conjugated mouse anti-BrdU (4 µg/mL, Invitrogen) overnight at 4ºC. Cell nuclei were counterstained with 4'-6-diamidino-2-phenylindole (DAPI; Sigma).

Apoptosis Staining

The APO-BrdU TUNEL assay kit (Invitrogen) was used following manufacturer protocol before staining for other antigens. Briefly, samples were fixed in 70% ethanol at -20ºC for one week, rinsed in wash buffer for 20m twice, incubated with DNA-labelling solution for 4h in a shaking water bath, washed with rinse buffer twice for 20m at 4ºC, and stained with Alexa Flour 488-conjugated mouse anti-BrdU overnight at 4ºC. Samples were co-stained with DAPI.

Imaging and Analysis

Immunostained gels were mounted on glass slides and imaged using a Zeiss LSM 510 confocal microscope (5x and 20x objectives). Confocal z-stacks were z-projected and thresholded for quantification. AngioQuant[320] software was used to quantify total vessel length (sum of the lengths of all vessel branches within a gel). Matlab (Mathworks) was used for all other image analysis. Pericyte coverage was defined as αSMA+ area within at least 5 µm of the abluminal face of vessel networks. Briefly, vessel networks were selected in the CD31 channel of thresholded image composites. Selections were enlarged by 5 µm at all edges and applied to the αSMA channel. αSMA+ area fraction within the selected area was measured and displayed as "Percent SMA Coverage". BrdU+ nuclei were counted

and counts from the whole gel indicate overall proliferation within the culture (displayed as "# BRDU/CD31 (#/mm^2)". To assess proliferation within the vessels only, CD31+ vessel area was selected and applied to the BrdU channel prior to counting within the selected area. This count was normalized to the CD31+ vessel area to account for differences in vessel density and is displayed as "#BRDU in CD31".

Animal Studies

All studies were approved by the Johns Hopkins University IACUC. Male nude immunocompromised mice (*fox1n1*, Charles River) were used at 8 weeks of age. To locate cells after implantation, cells were prepared and seeded as above into porous 3D-printed polycaprolactone (4mmx8mmx2mm, 70% porous) scaffolds. Four subcutaneous pockets were created on the dorsum of each mouse via blunt dissection. After one week, constructs were recovered *en bloc* with the surrounding skin and imaged on a Zeiss Discovery V8 stereoscope.

Statistical Analysis

Quantitative data are expressed as mean ± standard error. Statistical analyses were performed using GraphPad Prism 5 software. Statistical significance was determined by one-way ANOVA with Tukey's post-test and is denoted as $*p < 0.05$, $**p < 0.005$, $***p < 0.0005$.
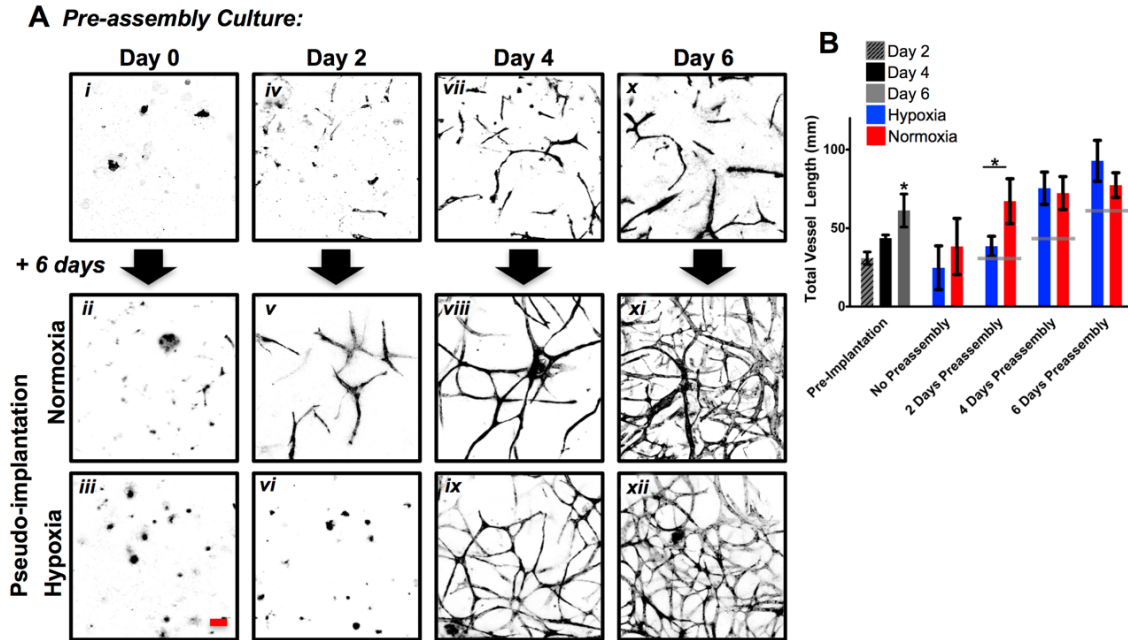
Figure 7-2. Assessing Vascular Length.

A. ASCs grown in fibrin hydrogels for 6 days sprouted into vascular network structures that stained positively for CD31. At 0, 2, 4, and 6 days ASCs were transferred to either normoxic or hypoxic pseudo-implantation conditions for a subsequent 6 days. **B**. Measurements of total vessel length. Gray lines indicate preimplantation length. * = $p < 0.05$, *n* = 4. Scale bar = 100µm.

Results

Preassembly-Mediated Vascular Assembly

ASC aggregates underwent vascular morphogenesis and developed a highly-branched vascular morphology when cultured in the fibrin hydrogel for 6 days in normoxic conditions (**Figure 7-2A**). The ASCs used in this study are isolated via plastic adherence and contain a minute population of CD31-positive cells[246,310], which we understand to be the building block of the vascular network, rather than ASCs differentiating into ECs. The vascular lengths at 2, 4, and 6 days were 30.9±7.7mm, 43.6±10.9mm, and 61.2±15.3mm, respectively (**Figure 7-2B**). With 0 days pre-assembly, subsequent culture in either normoxia or hypoxia for 6

131

days without media changes (pseudo-implantation model) resulted in no visible vascular assembly, demonstrating the nutrient-starving nature of the pseudo-implant condition alone is sufficient to impair vascular assembly. However, with two days of preassembly, ASCs in the normoxic pseudo-implant condition assembled into preliminary branching structures with significantly greater vessel length (67.2±16.8mm) than the hypoxic pseudo-implant (38.4±9.6mm). After four days of preassembly, transplantation of the vascular structures into either normoxic or hypoxic pseudo-implantation conditions for 6 days resulted in continued vascular development and the formation of interconnected networks (72.3±17.8mm vs. 75.4±18.5mm, respectively). Similarly, with a full six days of preassembly ASC vascular networks continued to branch and develop into highly interconnected and dense vascular networks after pseudo-implantation in normoxia (77.4±19.3mm) and hypoxia (92.8±23.2mm). Hence, with 0 or 2 of preassembly in a favorable, normoxic environment, transfer to hypoxic microenvironments had detrimental effects on vascular morphogenesis. However, following 4 or 6 days of pre-assembly, transfer to hypoxic microenvironments appeared to be supportive of subsequent vascular assembly. Thus, we observed a time-dependent change in the effect of hypoxia on ASC-derived vascular networks between Days 2 and 4 of pre-assembly.
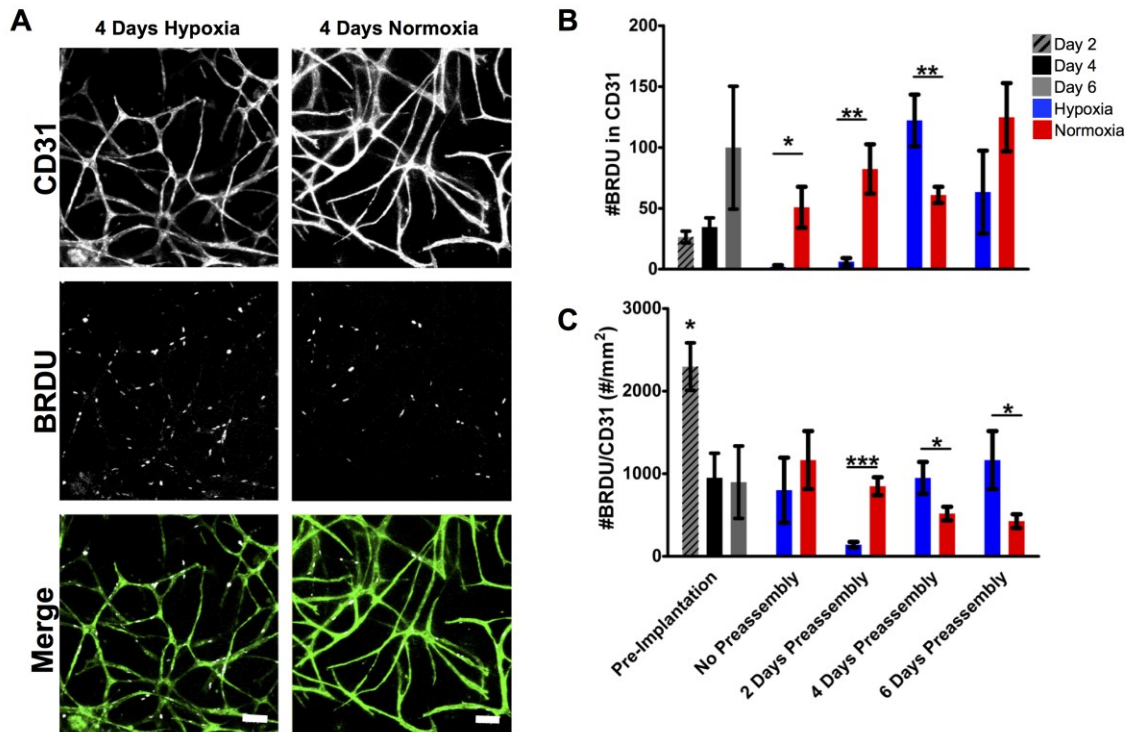
Figure 7-3. Proliferation Analysis.
A. BRDU staining overlaid with CD31. **B**. Total number of BrdU+ nuclei within CD31 in each gel. **C**. Number of BrdU+ nuclei normalized to the area of CD31 in each gel. * = p < 0.05, ** = p < 0.005, *** = p < 0.0005, n = 5, Scale bar = 100μm.

Endothelial Cell Proliferation

Endothelial cell proliferation was assessed by monitoring the incorporation of the thymidine analog BrdU into CD31+ cells during mitosis over the final 20h of culture (**Figure 7-3**). Proliferation predominantly occurred within CD31+ areas. We hypothesized that endothelial cells might be in a more proliferative state with increasing amounts of preassembly. While this hypothesis is supported by the large increase in number of BrdU+ nuclei within CD31+ regions at six days of preassembly, only a slight increase was observed between two and four days of preassembly (**Figure 7-3B**, day 2 and 4: 22.8±9.2 and 32.7±4.6, day 6: 99.3±49). However, this trend is not present when the number of BrdU+ nuclei was normalized to the CD31+ area (**Figure 7-3C**). The spike in #BrdU/CD31 at two

days of preassembly (2295.9±276.2 #/mm^2) is due in part to the very small area fraction of the gel that is CD31+ at that time, resulting in division by a very small number. After pseudo-implantation, proliferation is greater in normoxic than hypoxic groups with zero (hypoxic 870.0±381.1, normoxic 1201.7±340.1 #/mm^2) and two days of preassembly (hypoxic 270.0.0±38.8, normoxic 995.1±143.1 #/mm^2), and then switches to be increased in hypoxic groups with four (hypoxic 1038.6±226.6, normoxic 594.4±132.7 #/mm^2) and six days of preassembly (hypoxic 1304.7±341.6, normoxic 437.9±68.0 #/mm^2). These results are similar to our total vessel length analysis, indicating that cultures with four or more days of pre-assembly entering a more proliferative state after exposure to hypoxia.

Apoptosis Analysis

To determine if cells were undergoing apoptosis at an increased rate in hypoxia—as opposed to proliferating at an increased rate—a TUNEL assay was used to label the nicked ends of nuclear DNA as it was reduced into 200bp fragments by the apoptotic cascade (**Figure 7-4**). There was an increase in the number of apoptotic cells during the preassembly period (days 2, 4, 6: 52.5±4.2 to 129.0±20.3 to 228.2±10.1), and in the normoxic groups after the pseudo-implantation period relative to parallel hypoxic conditions (228.0±68.7 to 1120.0±333.6 with 4-day preassembly; 688.5±55.9 to 1164.0±293.9 with 6 days preassembly). Therefore, it is more likely that cells are simply not proliferating in hypoxic conditions instead of undergoing apoptosis.
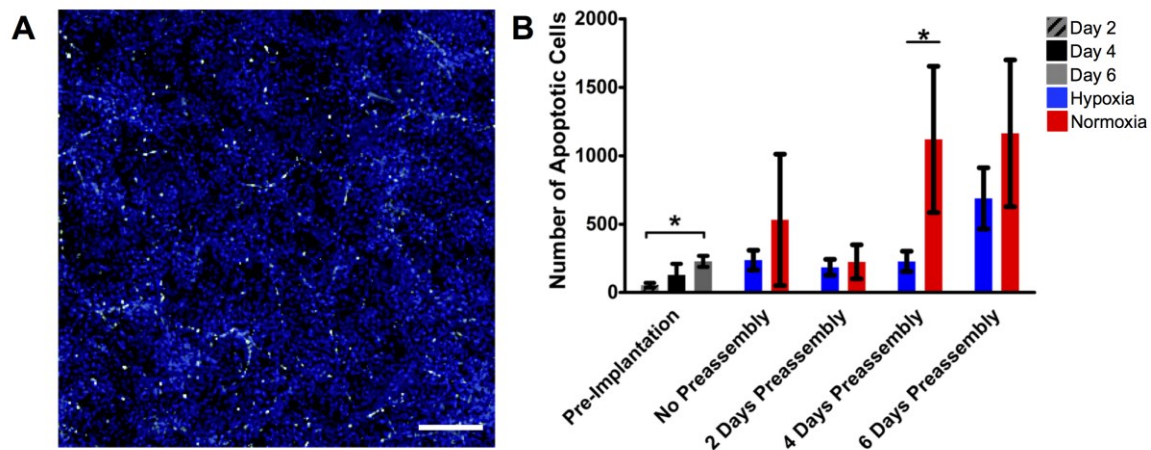
Figure 7-4. Quantification of Apoptotic Cells.
    A. TUNEL staining of apoptotic cells in the fibrin hydrogel. TUNEL = green, DAPI = blue. **B.** Quantification of apoptotic cells during preassembly and post-pseudo implantation * = p < 0.05, *n* = 4, Scale bar = 400μm.

Pericyte and Collagen IV Coverage Analysis

Pericyte coverage of vessels was analyzed by staining for αSMA fibers co-localized within 5μm of CD31+ areas (**Figure 7-5 and 7-6**). Pericyte coverage was significantly increased from two to four days of preassembly (24.3±5.3% to 46.1±2.6%; p < 0.005). αSMA coverage in normoxic groups post-pseudo implantation with 4 and 6 days of preassembly was greater than parallel hypoxic groups. In fact, despite the hypoxic groups increasing total vascular length with time, they demonstrate decreasing αSMA coverage post-psuedo-implantation from two to four to six days of preassembly (51.9±7.2% to 25.2±4.8% to 9.8±1.9%). This decrease in αSMA coverage might be due to pericytes migrating away from their classical position on the abluminal wall of a tubule to facilitate greater growth in hypoxia[321].

Therefore, we hypothesized that a more mature vascular structure with greater pericyte coverage was surviving and thriving in the hypoxic environment

and tested by using a pharmaceutical inhibitor of pericyte coverage. Additionally, one of the functions of the pericytes is to deposit collagen IV into a basement membrane which can provide supportive signaling to endothelial cells during hypoxia[322]. Pericytes were inhibited with AG1295 and the vascular assembly was contrasted with co-localization of collagen IV. AG1295 significantly inhibited vascular assembly at days four and six of preassembly relative to untreated controls (**Figure 7-7A,** day 4: 6.22±0.55 to 2.57±0.26; day 6: 7.73±0.55 to 3.57±0.52 mm/mm2) and almost totally eliminated collagen IV deposition throughout the construct (**Figure 7-7B**, day 6: 20.7±2.80% to 2.2±0.13%, p < 0.05). Within CD31+ regions, AG1295 significantly reduced collagen IV deposition at all timepoints (**Figure 7-7C**, p < 0.005).
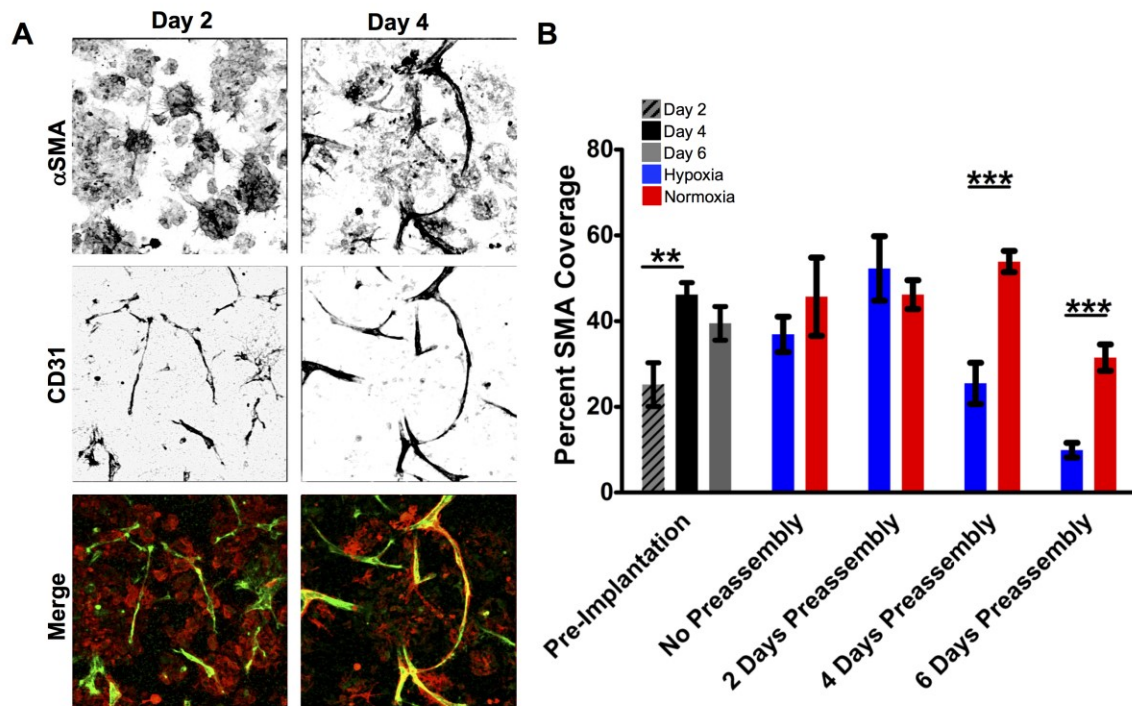
Figure 7-5. Analysis of Pericyte Coverage.
   A. Constructs at days 2 and 4 of preassembly stained for pericytes (aSMA, red) and endothelial cells (CD31, green). **B.** Quantification of αSMA+ coverage of CD31+ vessels during vascular assembly of ASCs during preassembly and following transfer to pseudo-implant conditions. ** = p < 0.005, *n* = 5, Scale bar = 100μm.
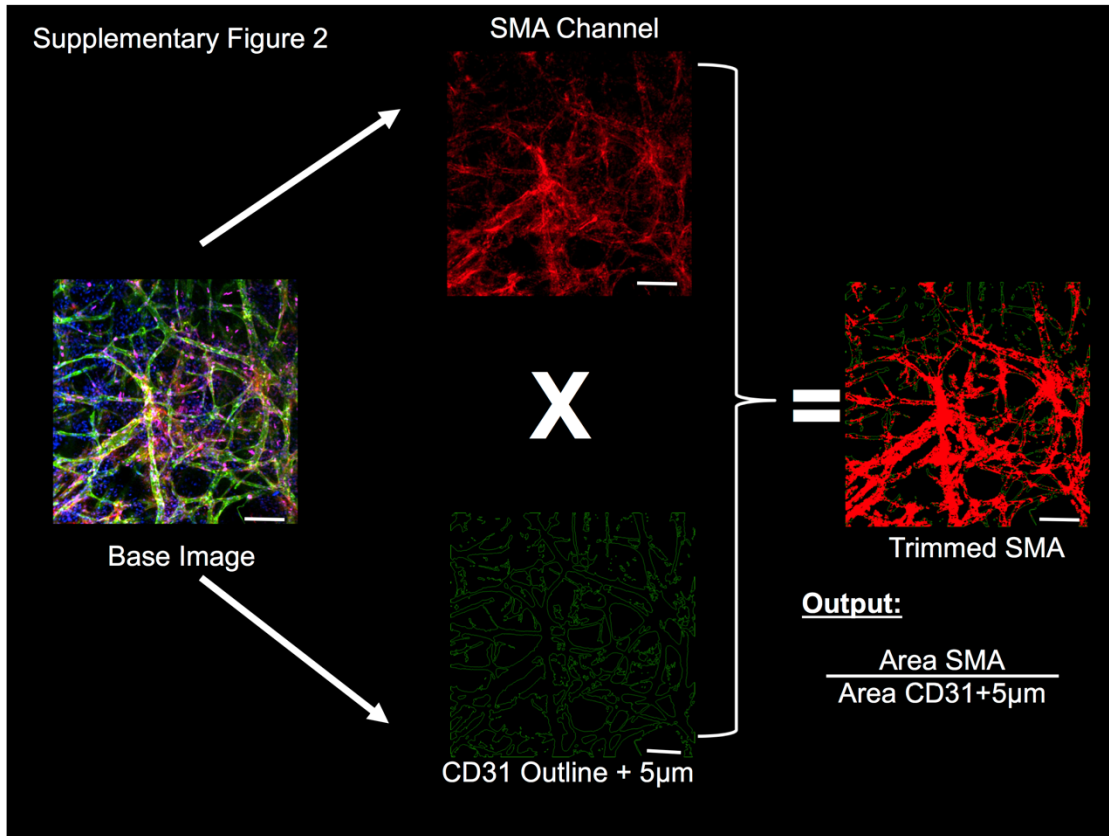
Figure 7-6 Schematic of Pericyte Coverage Calculation.
First the CD31 channel was isolated and the resulting vessels dilated 5µm. The SMA channel was then isolated and trimmed to the area of dilated vessels, and the trimmed area of SMA relative to the dilated vessel area is reported. Scale bar = 100µm.
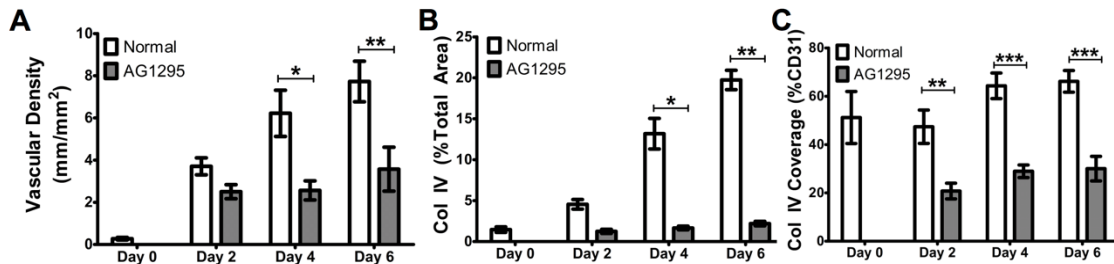
Figure 7-7. Assessment of Vascular Structure Following AG1295 Inhibition.
A. Vascular density of CD31+ networks. **B.** Total area fraction of Col IV in the gel. **C.** Area fraction of CD31 positive for Col IV. * = $p < 0.05$, ** = $p < 0.005$, *** = $p < 0.0005$, $n = 3$.

Subcutaneous Implantation

After one week of implantation in the subcutaneous environment, cell-laden constructs were recovered and imaged. Constructs without preassembly show poor vascularity, while constructs with four and six days of preassembly have visible vasculature (**Figure 7-8**).
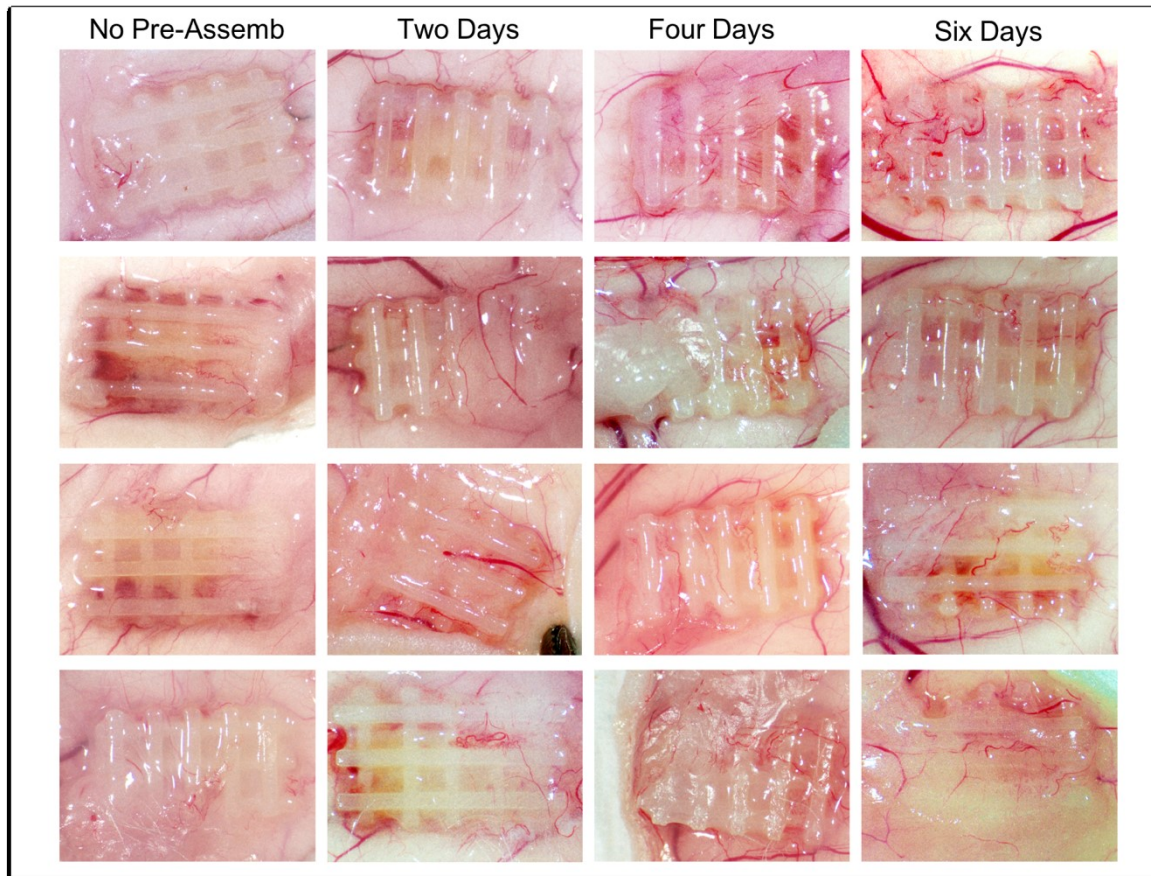
Figure 7-8. Gross Pictures of Subcutaneous Implants.
Cells with varying amounts of preassembly were implanted into mice for one week subcutaneously. Porous 3D-printed scaffolds were used as a carrier and location marker. n = 4 implants.

Discussion

The hypoxic microenvironments within volumetric tissue defects provide serious challenges to cell-based regenerative strategies. Hypoxia impairs cell survival and hypoxia vascular assembly of transplanted ECs used to rapidly vascularize engineered grafts[246,317,318]. The data in the current study confirm that hypoxia is inhibitory to the earliest stages of vascular assembly. To overcome this limitation in the therapeutic application of ASCs, one solution is to preassemble the vascular networks before implantation. A preassembly period allows for a number of organizational and construction steps in vascular assembly to take place in a metabolically favorable environment. However, preassembly approaches have regulatory and manufacturing drawbacks. In this study, we modeled preassembly using a culture period with abundant nutrients and oxygen. Additionally, we investigated several parameters of vascular assembly during the preassembly period to characterize the tissue features that would support further growth in hypoxia. The data herein suggest that at minimum, four days of normoxic and nutrient-rich conditions are required before implantation into a hypoxic or ischemic environment. Such a period allows for a sufficient amount of pericyte and collagen IV coverage to develop and supports the growth and proliferation of endothelial cells in a future hypoxic and nutrient-starved environment.

We found that pericyte-like cells in ASC cultures are essential stabilizers of vascular structures. Inhibition of pericyte-like cell recruitment via blocked PDGF-BB signaling closely mimics inhibition of vascular assembly in hypoxia. This suggests that hypoxia delays the contributions of pericyte-like cells during vascular assembly. Previous work identified pericyte-like ASCs as an important component

of ASC-vascular assembly (via heterotypic cell assembly)[310]. Pericytes have well defined functions in microvascular systems controlling EC proliferation, sprouting, and stabilization[323] via factor signaling, regulation of the basement membrane ECM, and cell-cell contact signaling via Notch pathways[324,325]. Indeed, pericyte-EC interactions are required for proper basement membrane ECM formation with fibronectin, laminin, vitronectin and collagen IV proteins, which together tune vascular tube formation via EC integrin interactions[322,326]. Further, EC integrin sensing of vitronectin drives expression of the antiapoptotic protein Bcl-w and autocrine expression of VEGF-A[327,328].

Hypoxia inhibits vascular assembly of individual ECs but promotes angiogenesis of ASC-vessels that have at least four days of preassembly. In general, hypoxia at physiologic (20 mmHg in bone vs 160 mmHg in atmospheric air) or slightly lower levels causes an increased amount of EC proliferation and angiogenesis[329]. However, EC-vasculature also regresses via apoptosis in response to severe hypoxia (1% or less)[330,331] in contrast to the positive angiogenic effects of less severe hypoxia. The idea of a sufficient amount of preassembly is required for hypoxic function supplants the idea that exposure to hypoxia supports vascular growth, via increased expression of VEGF and increased tubule formation[332]. These hypoxic vascular-boosting effects have traditionally been observed with vascular explants or other structures that have already been assembled, and not with individual ECs.

These findings suggest that direct implantation of a vascular population may not be sufficient to provide assembled vasculature to the construct before the development of anoxia and associated necrosis. However, this four day period of

assembly might be achievable *in vivo* using approaches that can deliver oxygen and other nutrients during the first four days of implantation[333]. One such approach utilizes oxygen-releasing materials in 3D-printed bone scaffolds, and can sustain delivery periods up to 48 hours long[334].

While the time-scale of vasculogenesis in fibrin hydrogels depends on the cell types and growth media, the assembly of a robust vascular network can commonly be observed in as little as six days in a number of systems[322,335,336]. Chen et al. compared vascular fibrin constructs with and without one week of preassembly *in vivo* and found that preassembly accelerated anastomosis with host vasculature, increased proliferation of implanted cells, and increased production of ECM, confirming that a period of preassembly is critical to *in vivo* use of vascular hydrogels [336]. However, it is important to limit the amount of preassembly as vessels may regress without perfusion and other physiological maturation cues[337]. Additionally, there are potential benefits to limiting culture time as studies have shown that culture on tissue culture plastic could induce cell fate plasticity[338,339]. Perfusion of vascular networks drives their maturation and remodeling[340,341] and was not included in the current study. The increased apoptotic rate observed in normoxia might be due to natural pruning/regression as they have matured without a hypoxic or fluid shear stress signal. Remodeling is further driven by the transport demands of the surrounding tissue exceeding the ability of diffusion[329].

The distance between individual ECs impacts the paracrine gradient and might have an impact on the rate of vascular assembly. Previous experience[310] revealed higher seeding densities lead to a more rapid assembly of vascular

networks, perhaps due to the close positioning of ECs to each other at high seeding densities. MacGabhann *et al* demonstrated local gradients of VEGF have an effect on vascular assembly in skeletal muscle over distances as short as 10μm[128]. Other groups[342,343] have modeled tip cell interaction by pairing computational and experimental models, but highlight that there are additional complicating factors beyond tip distance and VEGF gradients (such as Notch and EC-PC signaling) which add complexity to the system. This gradient-sensing and -directed vascular growth is increasingly important as systems become more complicated with anatomic geometries and physical barriers to vascular networks, avascular border regions between implant scaffold and host vasculature, and approaches where the cell density is limited.

ECs are highly sensitive to changes in oxygen levels through the hypoxia induced factor (HIF) family of transcription factors, metabolism, hypoxia-regulated microRNAs, causing upregulation of vascular endothelial growth factor (VEGF) and its receptors[329]. VEGF is a potent mitogenic for ECs, which supports network assembly via angiogenesis or vasculogenesis[344]. While we did not measure variable production of growth factors as a function of preassembly here, previous studies found VEGFA production by ASC-vessels was only upregulated in severe (0.2% O_2) hypoxia after normoxic preassembly for 6 days[246]. Such induction of VEGFA expression might be useful in large scale applications, where despite vascular preassembly, anastomosis and blood flow to interior regions might be delayed, result in network regression, and the associated VEGFA aiding those regions in undergoing revascularization.

Conclusion

This study sought to elucidate the processes active during ASC-vascular assembly that might support the beneficial response of ASC-vasculature morphogenesis in hypoxia. It builds upon previous work that *de novo* assembly of ASC-vasculature is inhibited in hypoxia. In ASC-fibrin constructs with less than 4 days of preassembly, hypoxia drove disassembly of vascular structures. However, with a minimum of 4 days preassembly before exposure to hypoxia resulted in robust vasculature network formation, whereupon hypoxia drove increased network formation. The main difference observed between 2 and 4 days of preassembly was a significant amount of pericyte coverage, and inhibition of that coverage similarly inhibited vascular formation. This suggests the interactions between ECs and PCs in *de novo* vascular assembly is oxygen-mediated.

CHAPTER 7[***]
COMPARISON OF STROMAL VASCULAR FRACTION AND PASSAGED ADIPOSE-DERIVED STROMAL/STEM CELLS AS POINT-OF-CARE AGENTS FOR BONE REGENERATION

Summary

Large craniofacial bone defects remain a clinical challenge due to their complex shapes and large volumes. Stem cell-based technologies that deliver osteogenic stem cells have shown remarkable regenerative potential but are hampered by the need for extensive *in vitro* manipulation prior to implantation. To address this, we explored the bone forming potential of the clinically-relevant stromal vascular fraction (SVF) cells obtained from human lipoaspirate. SVF cells can be isolated for acute use in the operating room and contain a sub-population of adipose-derived stem cells (ASCs) that can develop mineralized tissue. ASCs can be purified from the more heterogeneous population of SVF cells via secondary and tertiary culture on tissue culture plastic. In this study, the relative potential for using SVF cells or passaged ASCs to induce robust bone regeneration was compared. Isogenic SVF and ASCs were suspended in fibrin hydrogels and seeded in 3D-printed osteoinductive scaffolds of decellularized bone matrix and polycaprolactone. *In vitro,* both cell populations successfully mineralized the scaffold, demonstrating the robust bone formation properties of SVF. In murine critical-sized cranial defects, ASC-loaded scaffolds had greater (but not statistically significant) bone volume and bone coverage area than SVF-loaded scaffolds. However, both cell-laden interventions resulted in significantly greater bone

healing than contralateral acellular controls. In conclusion, we observed substantial *in vitro* mineralization and robust *in vivo* bone regeneration in tissue engineered bone grafts using both SVF and passaged ASCs.

Introduction

Annually, there are over 200,000 bone replacements for reconstruction of craniomaxillofacial (CMF) bones in the United States[1]. Reconstructive surgeries are performed following trauma, congenital malformation, or cancerous re-sectioning. While bone is a self-healing organ, critical-sized (non-healing[345]) CMF bone defects are challenging to treat due to their geometric complexity and the volume of viable bone needed. Compared with other bony defects, massive loss of CMF bone structure is more likely to cause disfigurement and psychosocial pathologies[250,346]. The current standard of care is the free fibular bone graft, which poorly replicates the mechanics and anatomy of defects, is resorbed at high rates[16], exhibits a slow rate of conduction from the surrounding bone (~1cm/month)[347], and may be negatively impacted by other comorbidities that impair bone healing, such as radiation osteonecrosis[348]. Alternatively, stem cell-mediated bone regeneration[349] using tissue engineering strategies has significant potential for regenerating massive CMF defects.

Adipose-derived stem cells (ASCs) have been considered as a potent cellular agent for tissue engineering and regeneration: they are readily available in patients, their isolation causes limited morbidity, they possess multipotency for bone and cartilage, and they are potent agents of neovascularization[26,245]. Compared to the bone marrow mesenchymal stem cells (MSCs) however, ASCs reportedly have lower relative osteogenic potency[350,351]. Consequently, additional

processing steps are required to promote osteogenic differentiation and thus for them to function as skeletal progenitor stem cells[352]. Accordingly, most reported strategies are limited by the need for extensive *in vitro* manipulation of the ASCs to generate an osteogenic phenotype prior to implantation. ASCs are derived from the adherent sub-population of the stromal vascular fraction (SVF) of cells from lipoaspirate. They are a less heterogenous population of cells than SVF[311,353]. In particular, the sub-population of endothelial cells is reduced in ASC cultures. Prior studies have demonstrated that bone forming cells and endothelial cells together elicit greater bone formation responses than alone[354,355]. Therefore, the inherent heterogeneity of SVF might be advantageous to bone regeneration.

SVF is a potential alternative cell source for bone regeneration to ASCs that may be used intraoperatively[356–358]. Prior uses of SVF in small-animal models and in human clinical trials[24] have yielded mixed results. Güven *et al.* compared SVF seeded for five days in a perfusion bioreactor before ectopic implantation in rats with isogenic ASCs and bone marrow stem cells (MSCs) that had been similarly prepared. They found SVF-seeded constructs had faster tissue in-growth, increased vasculature, and bone formation compared to ASCs and MSCs[359]. Rhee *et al.* used syngeneic rat SVF in a cranial model which increased regeneration from 13% in acellular controls to 58% in SVF groups[360]. Finally, Prins *et al.* used autologous SVF in maxillary elevation surgery in humans and found very slight improvements in bone volume and area when SVF was included compared to acellular contralateral treatments[361].

There are several case reports of SVF/ASCs used to treat volumetric CMF defects in human. First, Lendeckel *et al.* reported on SVF in combination with

milled iliac bone, resorbable microporous sheets, and fibrin glue with excellent results 3 months post-operatively[362]. Mesimäki *et al.* used ASCs, bone morphogenic protein-2, and beta-tricalcium phosphate to develop an ectopic bone flap to successfully create a neomaxilla with good results 1 year postoperatively[363]. Sándor et al. used autologous cultured ASCs as an adjuvant to implants/bone granules in a variety of craniofacial defects. They found acceptable hard-tissue graft function in mandibular and midface locations. However, cranial defects showed unexpected resorption rates[364] and the six-year follow-up was unsatisfactory[365]. SVF treatments have not demonstrated a robust amount of bone formation in humans, nor have they improved bone healing compared to standard-of-care or acellular treatments.

In this study, we explored the potential of human SVF to enable robust bone regeneration *in vitro* as well as within orthotopic *in vivo* murine calvarial defect implantation models. The SVF was obtained from human donors and immediately combined with 3D-printed osteoinductive scaffolds[232,366] in the absence of growth factors to mimic an intraoperative procedure. Further, we sought to determine whether the bone regeneration potential of the SVF was comparable to that of isogenic ASC populations similarly seeded in 3D-printed scaffolds. We performed similar study in scaffolds of larger volumes and implanted intramuscularly to evaluate the angiogenic characteristics of SVF and ASCs. To our knowledge, this is the first study to directly compare the osteogenic and angiogenic potential of intraoperative SVF with isogenic ASCs.

Materials and Methods

Study Design

SVF was isolated from human lipoaspirate and cultured to obtain isogenic ASCs. Flow cytometry characterization was performed on all cell populations. The bone forming potential of the cells was then assessed in 3D-printed scaffolds *in vitro* and orthotopically *in vivo.* The vascular potential of the cells was also examined *in vivo* using an intramuscular model. *In vitro* results were the average of all six donors, while only one donor was used for *in vivo* studies. The study design is summarized in **Figure 7-1**.
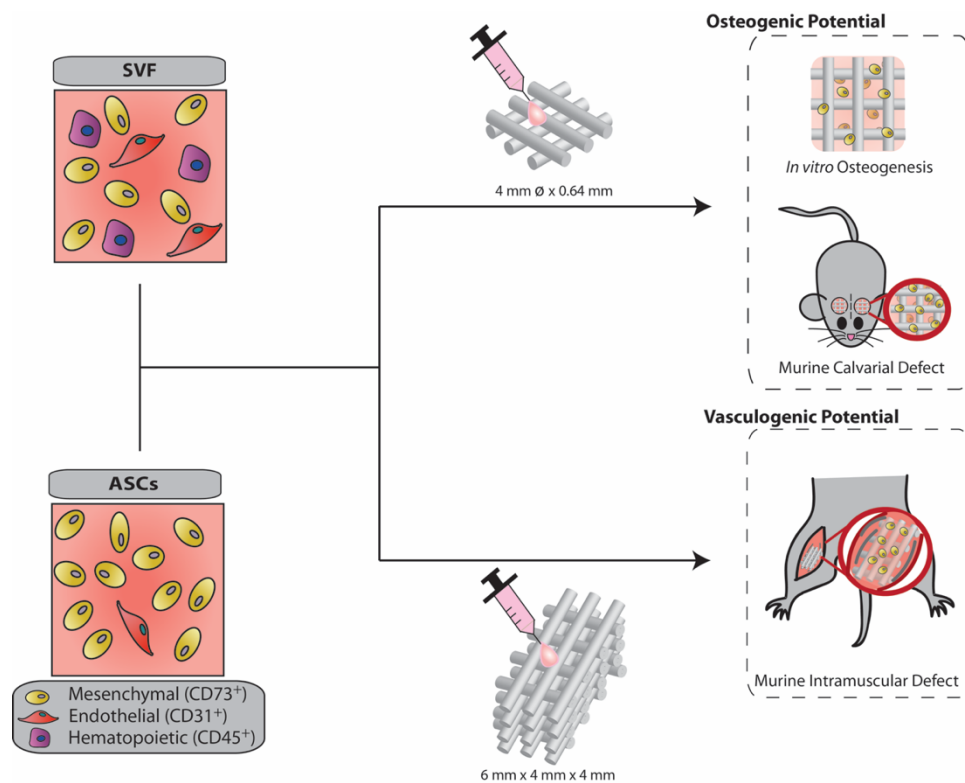
Figure 7-1. Schematic of study design
Cells were sourced from human donors undergoing elective cosmetic liposuction. Freshly isolated cells (SVF) and isogenic cultured cells (ASCs) were used in all the experiments. Cells were evaluated with flow cytometry and used for *in vitro* differentiation and *in vivo* tissue formation assays.

Cell Isolation and Culture

Human subcutaneous adipose tissue was obtained in the form of lipoaspirate from six female Caucasian donors undergoing elective surgery, with written informed consent, and with Institutional Review Board approval (#846242-1). ASCs were isolated as previously described[246,319]. Briefly, tissue was digested with collagenase type 1 (1 mg/mL; Worthington Biochemical Corp.) to isolate the stromal vascular fraction of cells. Cells were filtered through a 100µm filter and termed "SVF." SVF was directly seeded into scaffolds or used for flow cytometry. Cells not used as SVF were plated onto tissue culture plastic and were termed "passage 0 ASC." Cells were passaged with trypsin when they reached 80-90% confluence, termed "passage 1 ASCs". Upon reaching 80-90% confluence, these cells were lifted with trypsin and used as "passage 2 ASCs" for all experiments with ASCs groups. Growth medium consisted of: high glucose DMEM (Gibco) with 10% fetal bovine serum (FBS; Atlanta Biologicals), 1% penicillin/streptomycin (Gibco), and 1 ng/mL basic fibroblast growth factor (FGF-2; PeproTech).

Flow Cytometry

Cell surface markers were analyzed using flow cytometry to determine cell phenotype: mesenchymal (CD73), endothelial (CD31), stem/progenitor (CD34), and hematopoietic (CD45). Briefly, SVF cells were resuspended and passaged ASCs were detached and resuspended in phosphate buffered saline (PBS) containing 2% fetal bovine serum. Cells were then incubated with monoclonal antibodies conjugated to fluorescein isothiocyanate, phycoerythrin, or PerCP-Cy5.5 for 30 minutes at 4°C and cell surface markers were analyzed on a Sony SH800 cell sorter. All markers were acquired from BD Biosciences (**Table 7-1**).

Table 7-1. Flow Cytometry Antibodies

	Isotype	Clone	Stain	Manufacturer	Catalog #
CD34	Mouse IgG1 κ	8G12	PerCP-Cy5.5	BD Biosciences	347203
CD45	Mouse IgG1 κ	HI30	PerCP-Cy5.5	BD Biosciences	564106
CD31	Mouse IgG1 κ	WM59	FITC	BD Biosciences	555445
CD73	Mouse IgG1 κ	AD2	PE	BD Biosciences	561014

Preparation of DCB

All materials were obtained from Sigma unless otherwise stated. Calf knees were obtained from Green Village Packing Co (Green Village, NJ). Decellularized bovine bone extracellular matrix (DCB) was obtained by isolating trabecular bone from calf knees. The bone was decellularized using a protocol as described previously[27]. Briefly, trabecular bone fragments were blasted with water to remove as much cellular debris as possible. The bone fragments were then placed in a series of four detergent washes of 0.1% EDTA for 1 h, 0.1% EDTA/10 mM Tris for 12 h, 0.5% SDS/10 mM Tris for 24 h, and 50 u/mL DNase, 1 u/mL RNase, and 0.1% EDTA/10 mM Tris for 5 h. Following the washes, the bone was rinsed with PBS and lyophilized. The decellularized bone fragments were pulverized using a SPEX SamplePrep 6770 cryo-mill (SPEX SamplePrep, Metuchen, NJ) at a frequency of 10 cycles per second for 45 minutes to obtain powdered bone.

3D-Printing of Scaffolds

Cryo-milled decellularized bone powder was mixed 30% w/w with powdered polycaprolactone (PCL; 43k-50k MW; Polysciences 25090) by sifting through a stainless steel 400 μm mesh three times. PCL-DCB scaffolds were manufactured using an in-house pneumatic fused-deposition system mounted to a CNC machine with a nozzle diameter of 460 μm[26]. Briefly, a powdered mixture of PCL-DCB was loaded into the nozzle chamber and heated to 100°C in order to bring the polymer

to a liquid phase. Pneumatic pressure was then applied to expel the liquefied mixture out a 460µm brass extrusion die at the bottom of the chamber. Scaffolds for cell studies[27,232,366] were prepared using rectilinear patterns with 60% void volume and two layers in height (0.640mm) and punched to 4mm in diameter. Intramuscular PCL-DCB scaffolds were printed in the same pattern and cut to 6mm × 4mm × 4mm (length × width × height). Intramuscular scaffolds are larger to provide 3-dimensional depth to assess vascular formation. Prior to seeding cells, scaffolds were treated with 1M NaOH for 1h to increase hydrophilicity, washed with PBS, soaked in 100% EtOH for 1h to sterilize, and immersed in 100% FBS at 37 °C for 1h to facilitate protein adsorption to the surface of the scaffold.

Scaffold Seeding

Cells were suspended in fibrinogen (8 mg/mL final; Sigma) and then mixed with thrombin (2 U/mL final; Sigma) for a final cell concentration of 2×10^4 cells/µL gel. Constructs were seeded by pipetting 12 µL of gel and cell solution into 4-mm diameter scaffolds and incubating at 37 ºC for 30 min to allow complete gelation before the addition of medium. Twice the gel volume (24 µL) was used for intramuscular scaffolds to account for the larger porous volume of the scaffold. For *in vitro* culture, Control Medium (CM) scaffolds were fed with 0.5 mL of low glucose DMEM (Gibco) supplemented with 10% FBS and 1% penicillin/streptomycin. Osteogenic Medium (OM) scaffolds were fed with 0.5 mL of control media supplemented with 10 mM β-glycerol phosphate and 50 µM ascorbic acid-2-phosphate. Media was exchanged every other day. For in vivo studies, scaffolds were incubated for 10 hours in 0.5 mL of low glucose DMEM (Gibco) supplemented with 10% FBS and 1% penicillin/streptomycin before implantation.

Gene Expression

After the culture periods, scaffolds were digested with TRIzol (Life Technologies) and isolated mRNA was used to produce cDNA. cDNA was subject to real-time polymerase chain reaction (RT-PCR) for osteogenic genes *COL1A1*, *RUNX2*, osteopontin (*OP*), osteocalcin (*OCN*), and osteonectin (*ON*) as previously described[243]. The primers used are presented in **Table 7-2**. For analysis, the delta-delta Ct method was used in which β-actin served as the housekeeping gene, and gene expression was normalized to that of SVF cells at the time of isolation.

Table 7-2. PCR Primers

Gene	Direction	Sequence
Osteopontin	F	TTGCAGCCTTCTCAGCCAA
	R	GGAGGCAAAAGCAAATCACTG
Runx-2	F	GTCTCACTGCCTCTCACTTG
	R	CACACATCTCCTCCCTTCTG
Osteonectin	F	TCGGCATCAAGCAGAAGGATA
	R	CCAGGCAGAACAACAAACCAT
Osteocalcin	F	GTGACGAGTTGGCTGACC
	R	TGGAGAGGAGCAGAACTGG
Collagen 1	F	GAGAGGAAGGAAAGCGAGGAG
	R	GGGACCAGCAACACCATCT
β-Actin	F	AGTTGCGTTACACCCTTTCTTG
	R	TCACCTTCACCGTTCCAGTTT

Biochemical Assays

Scaffolds were cultured for 3 weeks in control or osteogenic conditions (n = 4 per assay). Calcium and DNA were measured as previously described[366]. Briefly, cellular DNA quantities were assessed using the Quant-It PicoGreen dsDNA assay (Invitrogen, Carlsbad, CA) according to manufacturer instructions. Total DNA at 21

days and the fold change from day 0 total DNA are reported. Total calcium was measured by agitating scaffolds in 0.5N hydrochloric acid for 24 hours and then measuring the calcium in solution using a Stanbio LiquiColor calcium assay (Stanbio, Boerne, TX) to determine calcium content. Samples were mixed with the color reagent 1:100 and the absorbance was read on a plate reader at 550nm according to assay instructions. Samples were reduced by the absorbance from wells without sample and interpreted as a fraction of the absorbance of the standard (10 mg/dL). PCL-DCB scaffolds were also reduced by the amount of calcium retrieved from acellular scaffolds, resulting in 'deposited calcium'. Calcium content was normalized to the amount of cellular DNA. Mineralized calcium was detected using Alizarin Red S (Sigma A5533) staining and detected using bright-field microscopy.

Animal Studies

In conducting research using animals, the investigator(s) adhered to the laws of the United States and regulations of the Department of Agriculture. All studies were approved by the Johns Hopkins University Institutional Animal Care and Use Committee (Protocol Number M016M468). Male nude immunocompromised mice (*fox1n1*, Charles River) were used at 8 weeks of age.

Assessing Bone Regeneration in Cranial Defects

To determine the effect of cells and scaffolds *in vivo*, the critically-sized murine calvarial defect model was used as previously described[243,367,368]. Briefly, a 4-mm circular knife (Medicon, Tuttiligen, Germany) was used to excise a 4-mm disk of calvaria between the coronal and lambdoid sutures and 1 mm lateral to the sagittal suture. Constructs consisting of SVF or ASCs seeded in fibrin inside DCB-

PCL scaffolds were press-fit into the resulting defect. A total of 14 mice were operated, 7 for SVF and 7 for ASCs, with n = 3 at 6 weeks and n = 4 at 12 weeks. The contralateral sides of each animal were also operated and treated with acellular control scaffolds. Post-mortem imaging of defects with computed tomography (CT) used a nanoScan PET/CT (Mediso, Budapest). Imaging was performed at 35 kV peak voltage and 800 μA current (0.48mAs). Reconstruction was done with a voxel size of 40 μm. Scans were conducted at 6- and 12-weeks post-implantation. Samples were fixed in 3.7% formalin overnight for histological analysis.

Assessing Vascular Potential in Intramuscular Implantation

Blunt dissection was used to create pockets in the hamstring portion of each leg[369]. Scaffolds were placed into the pockets and the tissue was sutured closed. Each animal received an SVF or ASC-loaded scaffold and a contralateral acellular control. After 10 days (n = 3) or 6 weeks (n = 4), mice were sacrificed and MicroFil-MV® (Flow Tech Inc, Carver MA)[370], a radiopaque polymer, was perfused through the vasculature. MicroFil-MV was mixed at 20:8:1 (dilutent:compound:curing agent) and perfused intracardially at 250 μL/min following perfusion of heparinized saline (5 U / mL). Samples were dissected out and fixed in 3.7% formalin overnight. Finally, μCT (Bruker SkyScan 1275, 10μm resolution, 65keV with 1mm aluminum filter, 0.3° rotation between images) was used to determine the extent of scaffold vascularization in implanted scaffolds. Analysis was done in Mimics (Materialise, Belgium). First, the vasculature and the scaffold were identified by thresholding. Second, the vasculature was manually segmented from the scaffold based on the different morphologies of scaffold and vasculature. Finally, the segmented

vasculature was cropped to the boundaries of the scaffold, and the volume of cropped vasculature within the scaffold was reported.

Histology

Samples were decalcified in 14% EDTA for 14 days and then trimmed to the cranial region. Samples were then embedded in 2% w/v agarose gel, dehydrated, and placed in chloroform overnight to remove the PCL phase. They were then washed three times with hot paraffin to remove residual chloroform and cast into paraffin wax blocks. Blocks were sectioned at 7μm using a microtome (Leica). Masson's trichrome staining was performed according to manufacturer specifications (Sigma HT15). Stained sections were imaged at 5x and 20x magnification on an upright microscope (Zeiss) and stitched[371] in ImageJ (Bethesda MD).

Statistical Analysis

Quantitative data are expressed as the mean ± standard error. Statistical analyses were performed using GraphPad Prism 5 software. Statistical significance was determined by one-way ANOVA with Tukey's post-test and is denoted as $*p < 0.05$, $**p < 0.005$, $***p < 0.0005$.

Results

Cell Characterization

Cells were collected from six donors; the donor demographics and cellular yields are summarized in **Table 7-3.** Cell populations were analyzed using flow cytometry and markers for endothelial cells, hematopoietic cells, and stem cells (**Figure 7-2A**). There was little donor-to-donor variability in the number of cells positive for each cell surface marker. The percentages are presented as the average ± standard deviation of the six donors. There was a greater presence of endothelial cells (CD31+) in the SVF population (12.9 ± 0.82%) compared to the ASC population (1.3 ± 0.13%). Likewise, we observed a decline in hematopoietic cells (CD45+) in the SVF (15.6 ± 1.6%) compared to ASCs (0.60 ± 0.065%). We observed a decrease in CD34 (SVF = 68.2 ± 2.54%; ASCs = 8.116 ± 0.63%) and increase in CD73 from SVF to ASCs (SVF = 17.6 ± 1.25%; ASCs = 95.7 ± 1.43%) (**Figure 7-2B**).

Table 7-3. Donor Profiles and Cellular Yield

Donor	Age	Race	Sex	BMI	Location(s)	Yield (cells / mL of clean fat)
1	54	Caucasian	F	25	Flank / Scapular	63,750
2	37	Caucasian	F	23.9	Flank / Inner Thigh	120,000
3	54	Caucasian	F	28.6	Flank / Scapular	700,000
4	43	Caucasian	F	20.8	Flank / Abdomen	145,000
5	32	African Am	F	25.8	Flank	676,000
6	22	African Am	F	25.7	Flank / Abdomen	278,000
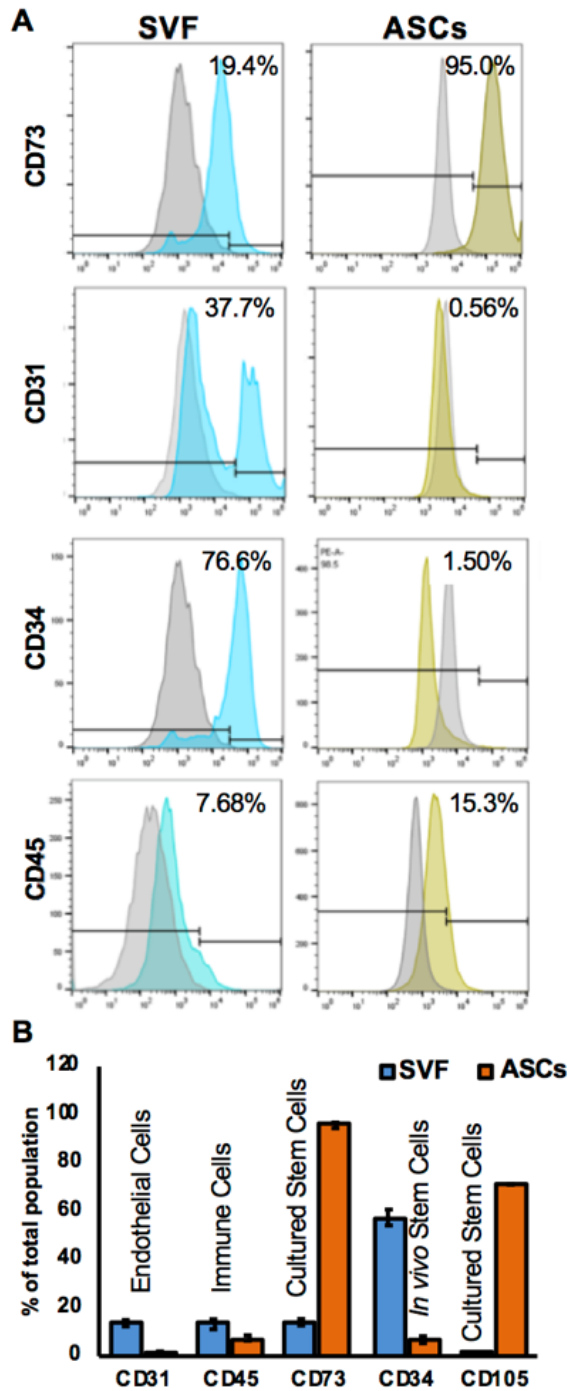
Figure 7-2. Flow Cytometric Analysis of Cell Populations.
(A) Representative flow cytometry histograms for endothelial (CD31), hematopoietic (CD45), and stem cell (CD34, CD73) markers before and after culture. **(B)** Surface marker profiles averaged for all 6 donors. Data shown as average ± standard deviation.

In Vitro Mineral Deposition

DNA and calcium contents as well as gene expression in the PCL-DCB scaffolds were measured after 21 days (**Figure 7-3**). There were greater cell numbers in osteogenic (OM) vs. control (CM) media and SVF scaffolds had less total DNA than those seeded with ASCs (**Figure 7-3A.** OM: SVF = 704.2 ± 72.6ng; ASCs = 944.7 ± 9.0ng; p < 0.005. CM: SVF = 433.8 ± 18.6ng; ASCs = 757.3 ± 15.2ng; p < 0.005.). SVF scaffolds had greater proliferation than ASCs in OM (**Figure 7-3B.** SVF = 1.5 ± 0.15-fold, ASCs = 1.3 ± 0.012-fold). *In vitro* cell cultures were used to test whether SVF had the potential to mineralize PCL-DCB scaffolds to a similar extent as passaged ASCs. *In vitro* culture over three weeks revealed that both SVF and ASCs mineralized scaffolds. While, SVF and ASCs grown on PCL-DCB scaffolds had similar total mineralization (**Figure 7-3C.** OM: SVF = 59.0 ± 3.3 µg Ca^{+2}; ASCs = 56.2 ± 3.2 µg Ca^{+2} n.s.), SVF had a greater mineralization per cell (**Figure 7-3D.** DCB-OM: SVF = 75.6 ± 4.3 ng Ca^{+2}/ng DNA; ASCs = 61.0 ± 3.8 ng Ca^{+2}/ng DNA; p<0.005). To confirm that the DCB in the scaffolds was osteoinductive, we measured DNA and calcium in PCL only scaffolds (**Figure 7-4.** PCL-OM: SVF = 51.2 ± 3.2 ng Ca^{+2}/ng DNA; ASCs = 45.3 ± 3.6 ng Ca^{+2}/ng DNA; SVF vs ASCs p<0.005, PCL vs PCL-DCB p>0.05). Both SVF and ASCs responded to osteoinductive cues in the PCL-DCB scaffolds. The cells also responded to the PCL-DCB scaffolds by upregulating key bone forming genes independent of media condition. While *RUNX2*, *OCN*, and *OPN* were significantly more upregulated in ASCs in OM, *COL1A1* was more significantly upregulated in SVF groups regardless of media condition (**Figure 7-3E;F.** OM: SVF = 11.3 ± 0.41; ASCs = 1.4 ± 0.41; p < 0.005. CM: SVF = 9.8 ± 0.53; ASCs = 2.6 ± 0.25; p < 0.005).
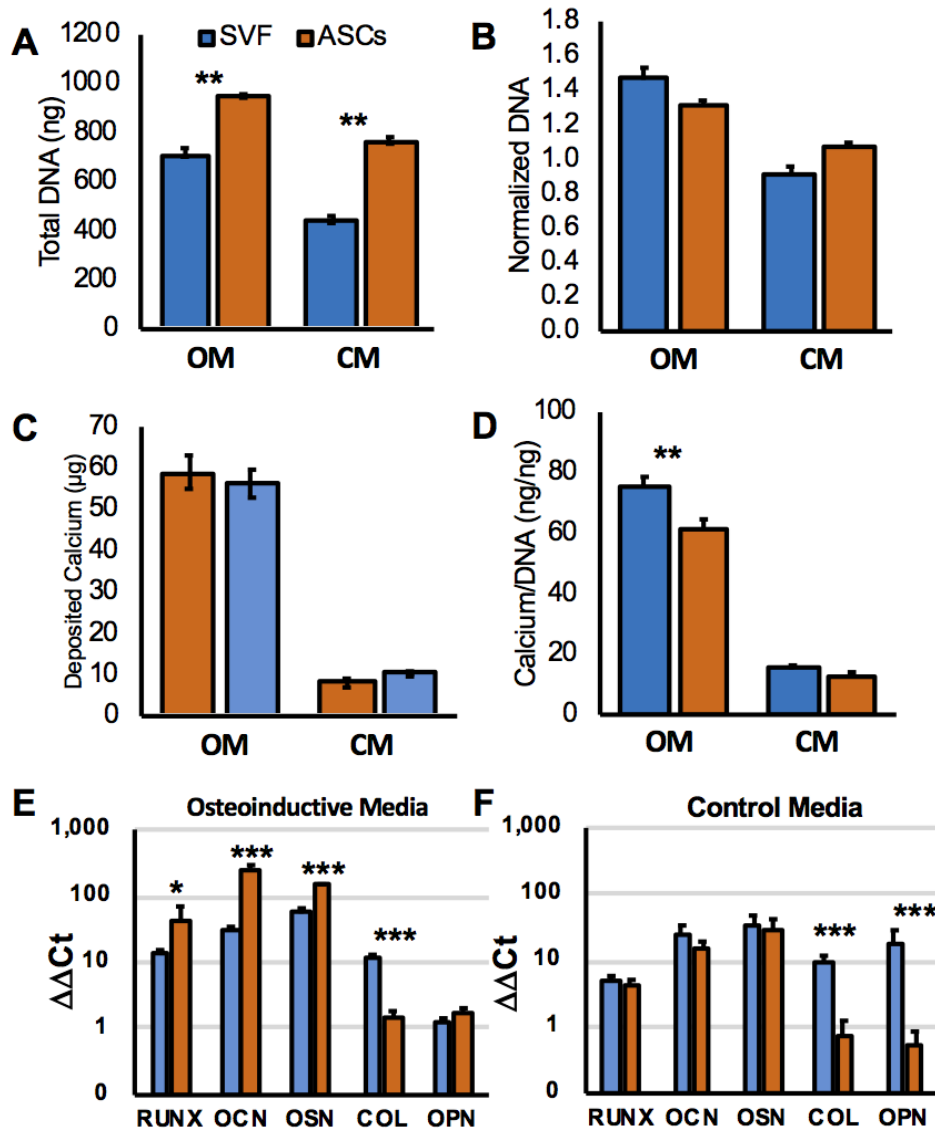
Figure 7-3. *In vitro* mineralization of SVF and ASCs in PCL-DCB scaffolds
SVF and ASCs from 6 donors were cultured in osteoinductive (OM) and control (CM) media in PCL-DCB scaffolds over 21 days.
(A) Total DNA content. (**B**) DNA normalized to day 0 amounts. **(C)** Deposited calcium in the scaffolds. (**D**) Deposited calcium normalized to total DNA. **(E, F)** Bone gene expression of one donor at 21 days, on PCL-DCB scaffolds.
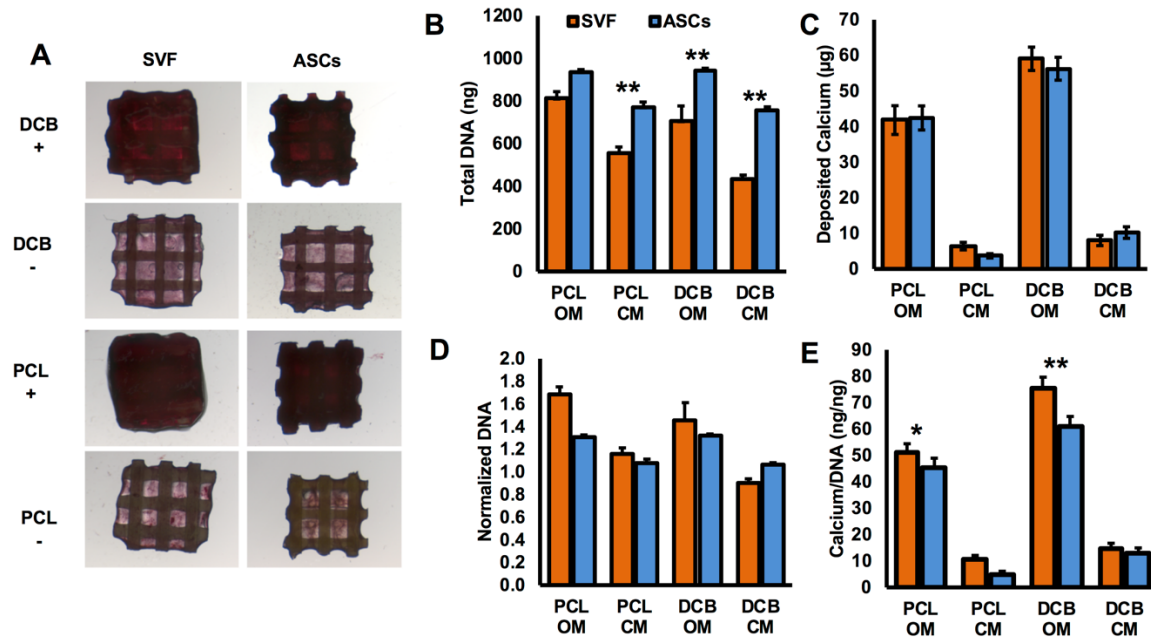
Figure 7-4 *In Vitro* Osteoinduction of DCB Scaffolds.
(A) Scaffolds were stained with alizarin red after three weeks of culture. + = osteoinductive media (OM), − = control media (CM). Dark red staining is distributed throughout the induced groups, and the DCB- group is slightly darker than the PCL- group. (B) Total DNA in PCL or PCL-DCB scaffolds after 21 days. (C) Total calcium recovered from PCL or PCL-DCB scaffolds after 21 days. (D) Total DNA normalized to day 0 amounts. (E) Total calcium normalized total DNA at day 21.

Bony Healing

To test the ability of these cells to regenerate bone in an orthotopic environment, SVF and ASCs were loaded onto PCL-DCB scaffolds and implanted into critical-sized cranial defects in mice (**Figure 7-5A, 7-6**). The inclusion of cells led to an increased amount of bone volume when compared to contralateral acellular defects. At twelve weeks after surgery, SVF (**Figure 7-5B,** paired SVF = 4.72 ± 0.10 mm^3 and Acellular = 4.10 ± 0.12 mm^3; $p < 0.005$) and ASCs (**Figure 7-5C,** paired ASCs = 5.07 ± 0.24 mm^3 and Acellular = 4.11 ± 0.14 mm^3; $p < 0.05$) both had significantly more bone volume.

At six and twelve weeks, acellular scaffolds had open pore spaces with slight amounts of bone formation along the border of the defect (**Figures 7-5, 7-6, 7-7)**. Acellular groups had less than 40% of the porous space filled (**Figure 7-5C,** 6-weeks = 46 ± 5%; 12-weeks = 34 ± 10%). SVF groups had increased amounts of bone filling the pore spaces (**Figure 7-5C,** 6-weeks = 73 ± 6%; 12-weeks = 78 ± 7%), and bone volume increased between weeks six and twelve (**Figure 7-5D,** BV-PV at 6-weeks = 0.32 ± 0.052 mm^3; 12-weeks = 0.62 ± 0.04 mm^3, p < 0.05). ASCs filled the most pore volume with bone (**Figure 7-5C,** 6-weeks = 83 ± 11%; 12-weeks = 100 ± 18%).
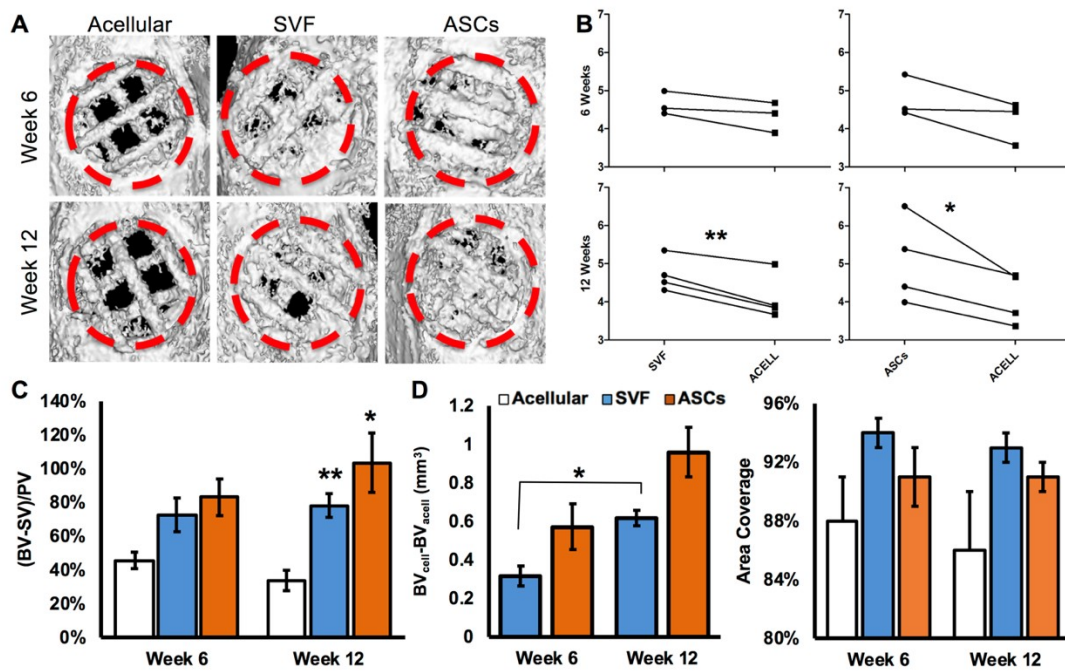
Figure 7-5. *In Vivo* Bone Forming Potential.
(A) microCT reconstructions of 4mm diameter cranial defects (red outline) **(B)** Pair-wise comparison of bone volume per animal. Each connected pair indicates a single animal containing two defects (cellular and acellular). **(C)** Percentage of porous space filled with bone. Bone volume reduced by the initial scaffold volume and normalized to the porous volume: (Bone Volume-Scaffold Volume) / Pore Volume. **(D)** Bone volume within defect reduced by contralateral acellular defect bone volume. **(E)** Area coverage of defect area. Measured in ImageJ as (number of non-black pixels) / (total number of pixels) in the 4mm-diameter circle.
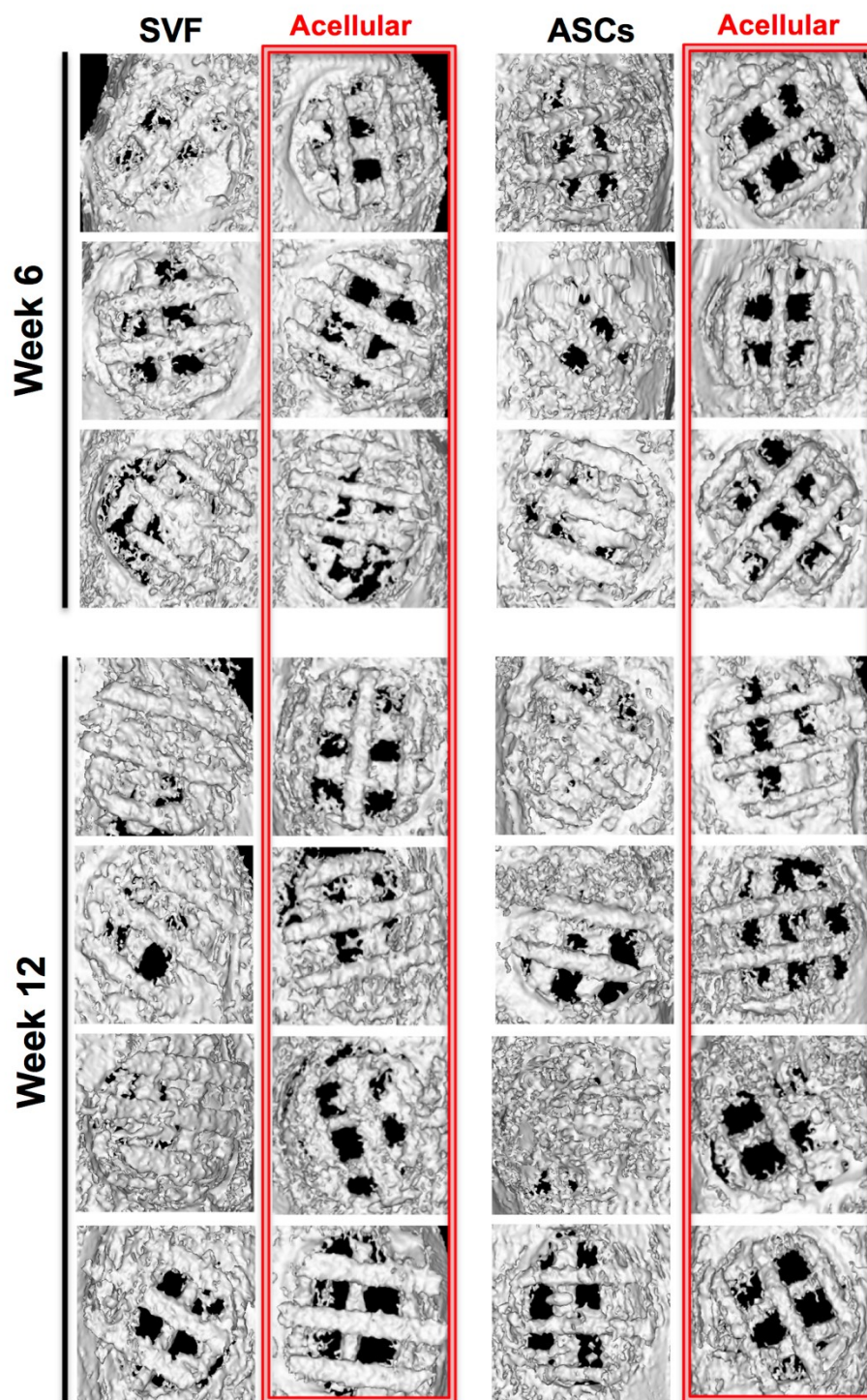
Figure 7-6. Complete Set of Orthotopic Defects.
CT reconstructions of defects. Each mouse has contralateral acellular
(red outline) and cellular sides. n = 3 at 6 weeks and n= 4 at 12 weeks
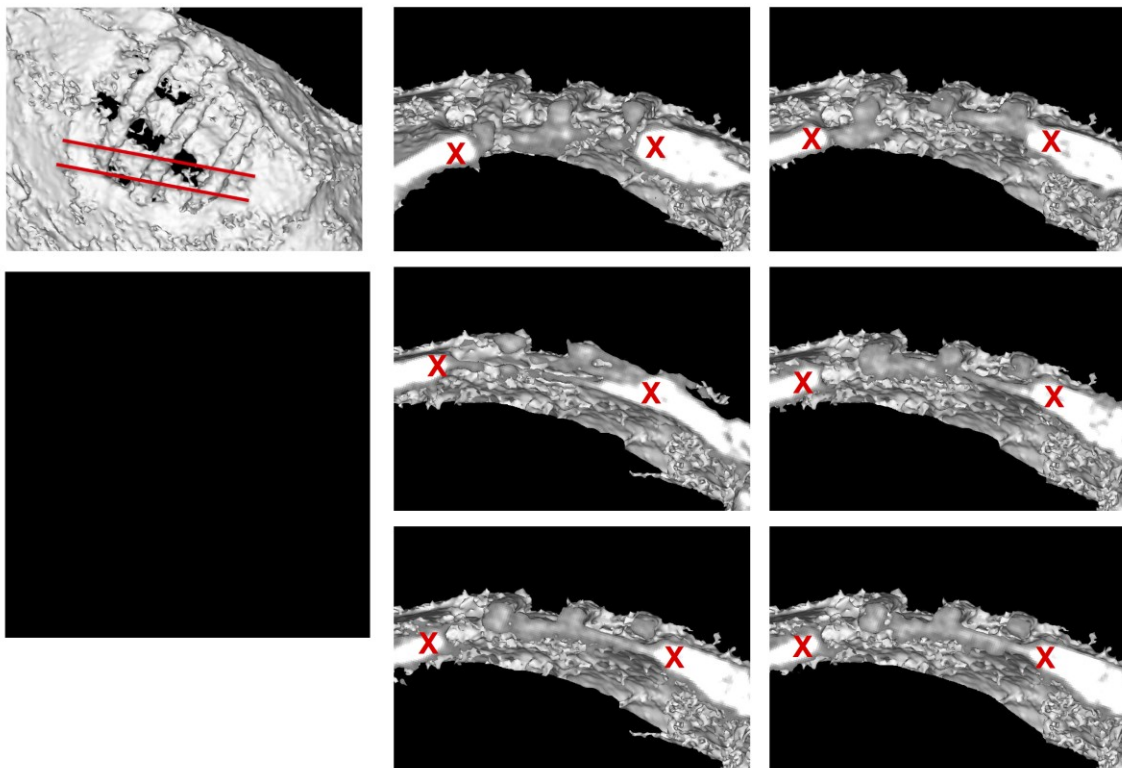
Figure 7-8. Cross-sectional CT Views of a Cranial Defect.
The CT is thresholded and a 3D-pobject is created with the resulting bone signal (*upper* left). Cross sections from that object along the red lines are shown on the right. The red X indicated the border of the host bone, and the scaffold is visible between the Xs as thin and darker grey.
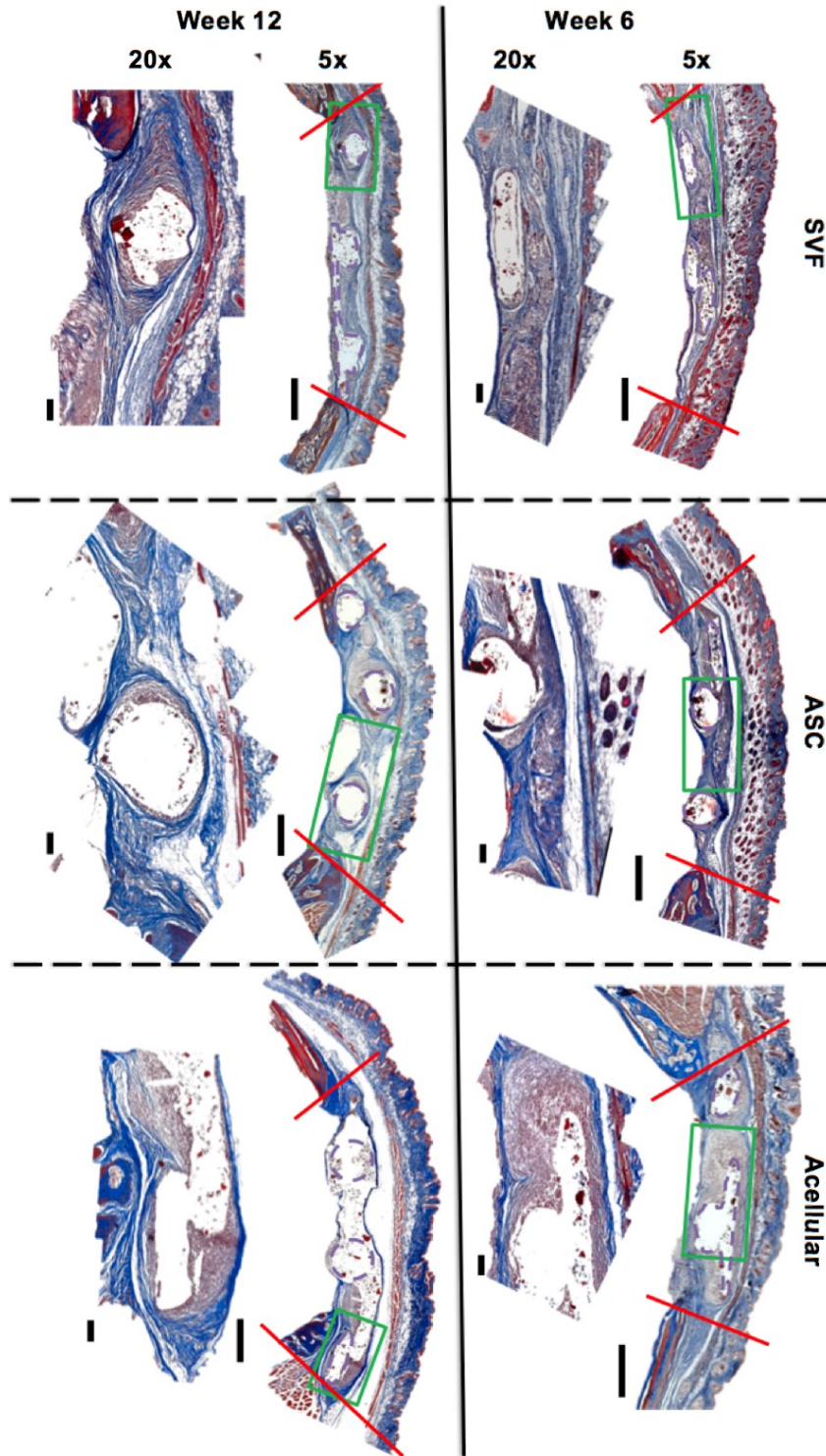
Figure 7-9. Histology Staining of Murine Cranial Defects.
Mason's Trichrome Staining on cross sections of samples at 6 (top row) and 12 weeks (bottom row). Scaffold struts indicated by empty white space, dense collagen as blue. Red lines indicate boundaries of the defect, and green boxes are the zoomed in section. Scale bars 5x = 500µm, 20x = 100µm.

Histology

The osteogenic performance of implanted scaffolds at 6 and 12-week post-surgery was evaluated using Mason's Trichrome stain. Cell-laden scaffolds (both SVF and ASC) showed greater amounts of dense collagen formation, as indicated by the dark blue coloring around scaffold struts, when compared to the acellular scaffolds, which showed more open red-colored fibrotic tissue around the struts (**Figure 7-9**). Scaffolds with ASCs showed denser collagen formation, particularly between scaffold struts, at 6 and 12 weeks; although, by 12 weeks, SVF scaffolds also had dense collagen indicative of bone matrix deposition between struts. In ASCs, the new boney matrix also appeared integrated into host bone on both sides of the defect. By 12 weeks, the defect was filled with new tissue in both SVF and ASC scaffolds, with a high concentration of collagen around scaffolds struts and bridges of collagen in between them. By contrast, acellular scaffolds showed very little dense collagen present anywhere in the defect.

Vascular Infiltration

To observe the ability of cells to promote an angiogenic response, larger constructs were implanted in the hindlimbs of mice (**Figure 7-10A**). MicroFil perfusion was used to examine the extent of vascularization at 10-days and 6-weeks (**Figure 7-10B)**. At 10 days, there was minimal vascular infiltration in the acellular and ASC groups (**Figure 7-10C,** 0.30 ± 0.058 mm^3 and 0.19 ± 0.044 mm^3 respectively), and some infiltration into the SVF group (**Figure 7-10C,** 0.65 ± 0.068 mm^3, $p < 0.05$ vs acellular and ASCs). At 6 weeks, cellular groups were both significantly greater than the acellular groups (**Figure 7-10C,** ~3-fold, SVF = $1.71\pm$

0.10 mm^3, ASCs = 1.47 ± 0.22 mm^3, acellular = 0.45 ± 0.045 mm^3, p < 0.05) and

the SVF group was similar to the ASCs group.
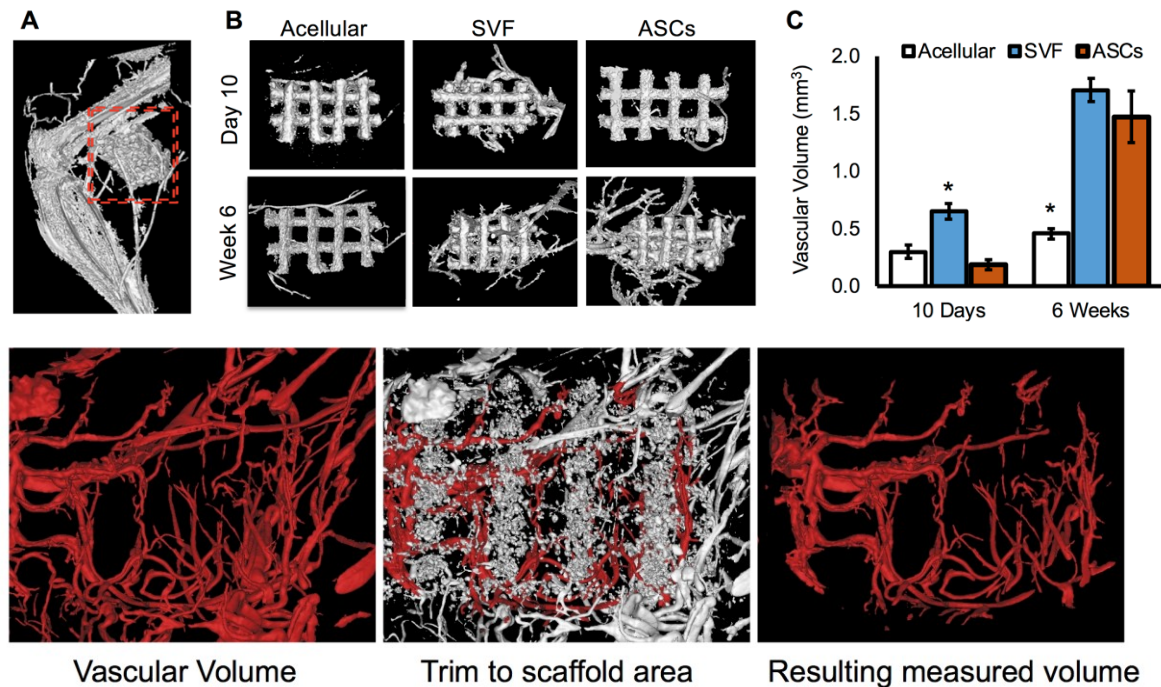
Figure 7-10. Intramuscular Implantation and Microfil Perfusion
Top: (A) Example CT showing scaffold implant (red box) in relation to leg. (B) microCT reconstructions of scaffolds implanted intramuscularly, with the vasculature filled with radiopaque microFil. (C) Total vascular volume within scaffold. *Bottom:* Example of the methodology of trimming the vascular volume (red, left) to the scaffold boundaries (middle, particles in white), and the resulting vascular volume of interest (right).

Discussion

The inability to effectively regenerate bone within critical-sized craniofacial defects is a present clinical challenge and overcoming this limitation using tissue engineering strategies would significantly advance current treatment modalities. One approach would be to harvest SVF, combine it with 3D-printed osteoinductive scaffolds, and within the same surgical procedure, implant it into the bone defect to stimulate regeneration. This approach offers a number of advantages compared to traditional tissue engineering methods where cells (e.g. ASCs) are culture

expanded and maintained in the scaffold *ex vivo* for a period of time prior to implanting into the defect site. Specifically, it would reduce the required number of operations for the patient, eliminate the cost and practical limitations associated with manipulating the cells *ex vivo*, and leverage the regulatory feasibility of an intraoperative vs multi-operative procedure. This study addresses two potential limitations of this strategy, which is (i) whether minimally-processed SVF delivered to a critical-sized bone defect within an osteoinductive scaffold in a manner that mimics a clinical intraoperative procedure could promote robust bone regeneration, and (ii) determining whether the bone-formation by SVF is as effective as that obtained from culture expanded ASCs.

To assess the feasibility of the SVF-based bone regeneration, we first characterized the isolated cells. While there was donor-to-donor variability in cell yield, the trends of osteoinduction and proliferation remained the same across donors, and we were able to isolate large quantities of cells that would be suitable for acute clinical use. Potential intervention for a defect of 4 - 10cc would require on the order of 10^7 -10^8 cells if seeded at concentrations ranging from 1 to 25 × 10^6 cells/mL. This corresponds to 250 mL of lipoaspirate. For this study, we obtained over 500 mL from each donor of average BMI of 25. Cell marker distributions were also consistent across donors. The values in our study also correlated with those reported previously by other groups, which describe decreases in endothelial (CD31), hematopoietic (CD45), and CD34 sub-populations and a concomitant increase in mesenchymal (CD73) sub-populations[311,353,372].

As reported in a recent review, several groups are working to implement SVF or ASCs in clinical trials for bone regeneration[24]. Yet, the ability of SVF or ASCs to directly differentiate into osteoblasts and produce bone *in vivo* remains contested. A recent study reported that despite the ability of ASCs to deposit mineral and turn on bone-forming genes *in vitro,* they were unable to spontaneously form ectopic bone[351] even though promoted a robust angiogenic response and exhibit trophic function[373]. Hence, demonstrating bone regeneration capacity in a critical-sized defect remains a crucial hurdle in the clinical translation. While others have used autologous rodent SVF[360] in bone healing, we believe this is the first reported case of non-pre-differentiated human SVF significantly contributing to new bone volume in small animals. As such, this work corroborates other studies which have shown SVF used in humans is safe and effective in promoting bone regeneration[361].

This current study applied the SVF to the calvarial defect with minimal manipulation to simulate a clinically applicable intervention for bony regeneration that did not rely upon *ex vivo* culture or 'priming' of the cells prior to implantation. While the ASCs were cultured for two passages, they were also implanted in the defect site without prior *in vitro* osteogenic differentiation, yet both cell types promoted mineral deposition that was significantly greater than the acellular controls. The amount of bone formation formed by the SVF was lower than that formed by ASCs though the difference was not statistically significant. The reason for this is not clear: While, this result could potentially correlate with the relatively lower number of mesenchymal (CD73$^+$; believed to be osteogenic progenitors) sub-populations present in SVF than ASCs, if this were true, the same trend should

have been observed *in vitro*. Yet, both SVF and ASCs exhibited similar osteogenic potential *in vitro*. In our prior studies, we have shown that human cells are present at the site of new bone formation[243] though we have not validated in either study that the cells responsible for new bone formation are human. Alternatively, it is possible that the cells act on endogenous cells to affect bone formation. Recent work has shown that transplanted mesenchymal stem cells act on surrounding host cells with trophic, paracrine, and immunomodulatory functions[115,374,375]. In future studies, we will use cells transduced with bone-forming gene reporter labels to probe the direct contribution of transplanted cells. This study is limited by the xenogenic nature of evaluating human cells in immunocompromised mice and also by the nature of the size and scale difference between murine and human bones.

These experiments highlight the strength of a 3D-printed bioactive material-based approach to mediate bone regeneration. 3D-printing technologies are powerful tools to facilitate patient-specific approaches[376]. Regenerative approaches that utilize 3D-printed scaffolds may avoid the stress-shielding, loosening, and implant extrusion that cause permanent plastic, metal, and ceramic implants to fail[377,378]. We have previously reported that 3D-printed PCL-DCB scaffolds enhanced the expression of bone-related genes (*RUNX1, COL1A1, OCN*) in ASCs[366] and regenerated bone in murine calvarial defects[27] in a dose-dependent manner, i.e. the higher the concentration of DCB in the 3D-printed scaffolds, the greater the amount of mineral deposition *in vitro* and *in vivo* bone formation[366]. We have also shown that embedded DCB in 3D-printed PCL scaffolds was a more potent osteoinductive stimulus than other clinically-used bone replacement materials such as tricalcium phosphate and hydroxyapatite[232].

In this study, SVF and culture-expanded ASCs were encapsulated in 3D-printed PCL-DCB scaffolds and implanted orthotopically *in vivo* without prior osteogenic differentiation and still gave rise to significant amounts of new bone formation. Several groups have demonstrated that pre-differentiation of ASCs to osteoblasts results in substantial bone formation[350,359,379,380]. Moving that differentiation process to the implanted-scaffold environment eliminates *in vitro* preparation time and enables the osteoinductive signals to act, additionally, on endogenous cells. It should also be noted that the addition of exogenous growth factors induces robust bone regeneration[203,381,382] but the limitation is that they are provided at supra-physiological levels, which is not the case with the PCL-DCB 3D-printed scaffold system. Even the acellular scaffolds induced some bone healing, showing the robustness of the PCL-DCB-based scaffold approach.

The study also evaluated the relative angiogenic potential of SVF and ASCs. The formation of healthy regenerated bone in large, critical-sized defects in humans would rely on well-established vascular networks. To assess the vascular response induced by the cells, we used an ectopic model that enabled us to test scaffolds of larger volumes. Scaffolds were filled with fibrin hydrogel which promoted vascular ingrowth even in acellular scaffolds and we assessed specifically the perfused vascular networks by using MicroFil-MV. Both SVF and ASCs exhibited roughly three-times greater vascular responses than acellular scaffolds at six weeks. This later time point was chosen to investigate sustained vascular networks. At the early time-point (10 days), only SVF-seeded scaffolds showed increased vasculature compared to the acellular controls. This early vascular presence correlated with the greater presence of endothelial cells in the

SVF, suggesting those endothelial cells might assemble into vasculature and patently anastomose with the host. In this study, we did not investigate the contributions of blood vessels of human or mouse origin. It may also be due to a higher secretion of pro-angiogenic factors by SVF compared to ASCs[383]. This early vascular response in our system might enable more of the implanted cells to survive implantation conditions and contribute to subsequent mineralization. Thus, the robust vascular formation and bone formation observed in this study using SVF and ASCs may be correlated.

Conclusion

The data from this study demonstrated that SVF isolated from lipoaspirate and used *in vivo* with minimal processing could promote substantial bone healing. The SVF-seeded scaffolds filled 80% of the void volume of scaffolds in critical-sized murine calvarial defects. In an ectopic intramuscular model, the SVF also induced a robust angiogenic response that was sustained at 6 weeks post-implantation. We compared both the bone healing and angiogenic responses with that obtained from isogenic, passage 2 ASCs. We found that the SVF and ASCs behaved comparably. The ASCs stimulated new bone formation that filled up to 100% of the pore volume of the scaffolds and exhibited similar levels of vascularization at 6 weeks. Altogether, the study supports the potential intraoperative use of SVF combined with bone scaffolds for the treatment of critical-sized bone defects.
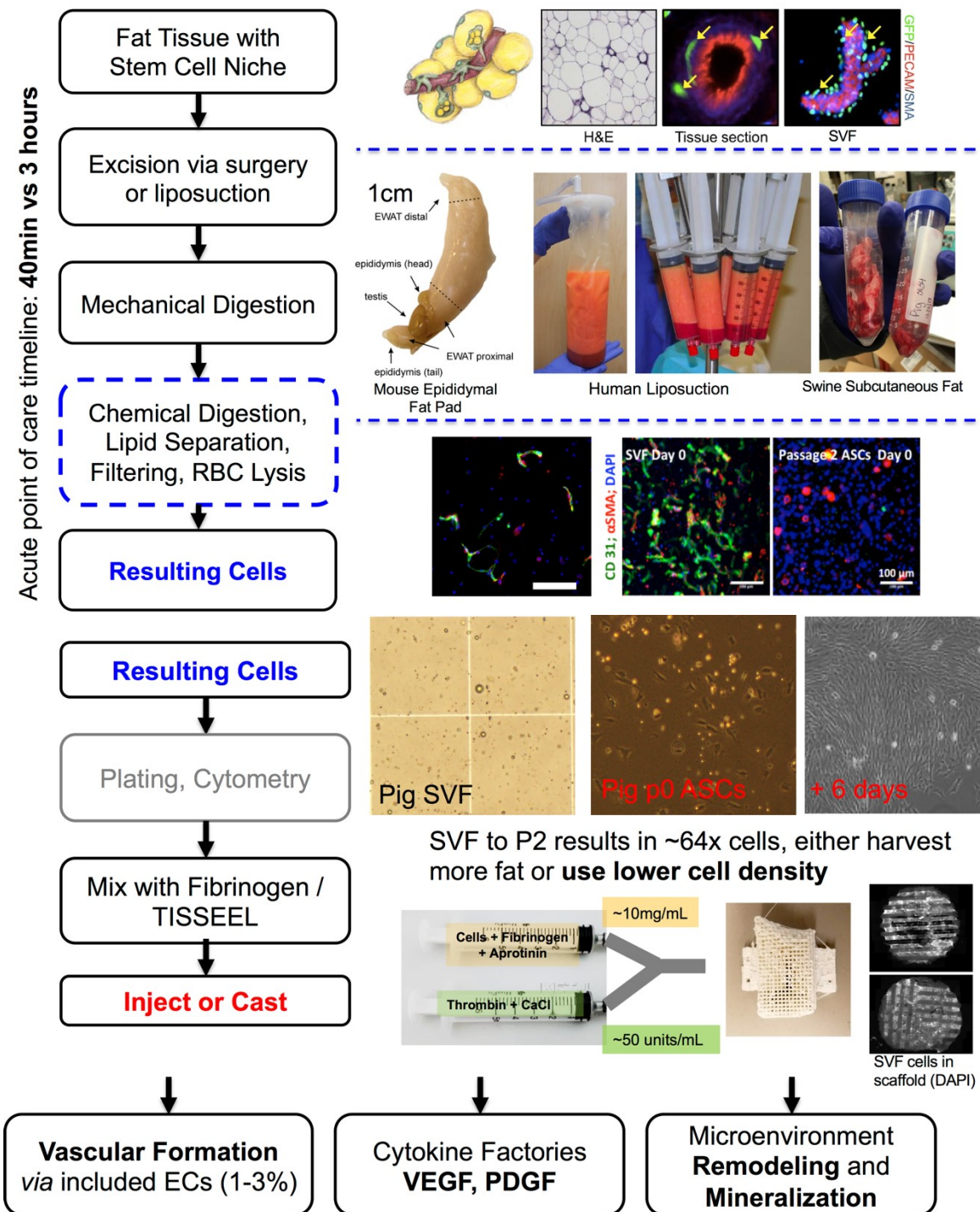
Figure 7-11 Isolation and Use of Stromal Vascular Cells.

Flow chart shows how fat tissue contains a stem cell niche in the perivascular space. Isolated fat tissue can be in a number of forms. The resulting SVF contains a high percentage of ECs, which is mostly lost during culture. Cells are mixed with hydrogel (fibrin/thrombin) and injected into a scaffold. The cells work to form blood vessels (ASCs retain 1-3% ECs), produce cytokines, and deposit ECM.

CHAPTER 8
3D-PRINTING SCAFFOLDS WITH CONTROLLED HETEROGENEOUS POROUS AND MECHANICAL PROPERTIES

Summary

3D-printing is a powerful manufacturing tool which can create precise microscale architectures across macroscale geometries from various materials. Within biomedical research, 3D-printing has been used to fabricate rigid scaffolds for cell and tissue engineering constructs, where the precise microarchitecture has direct effects on behavior and function of the construct. While 3D-printing hardware has become low-cost due to modelling and rapid prototyping applications, there is no common paradigm or platform for the controlled design and manufacture of 3D-printed constructs for tissue engineering. Specifically, controlling the tissue engineering features of pore size, porosity, and pore arrangement is difficult in currently available software. We have developed a MATLAB approach (scafSLICR) to design and manufacture tissue engineered scaffolds with precise microarchitecture and with simple options to enable spatially patterning pore properties. Using scafSLICR, we designed, manufactured, and characterized tissue engineering scaffolds in ABS with a variety of pore sizes, porosities, and gradients thereof with a high degree of accuracy. We found that transitions between different porous regions maintained an open, connected porous network without compromising mechanical integrity. Further, we demonstrate the usefulness of scafSLICR in patterning different porous designs throughout large anatomic shapes and in preparing craniofacial tissue engineering bone scaffolds. Finally, scafSLICR is distributed as open source MATLAB scripts and as in a stand-alone graphical interface.

Introduction

3D-printing has grown into a widely available technology since the patents surrounding the core technology expired in 2009[384]. As a result of this technological expansion, a large number of low-cost hardware systems and printable materials have become commercially available[385,386]. A growing number of tissue engineering studies have utilized such 3D-printing techniques to fabricate scaffolds for tissue regeneration[26,102,255–258]. The specific 3D-printing technology selected impacts the choice of material and available microarchitectures that can be used for the scaffold[387]. One prominent technique, fused deposition manufacturing (FDM)[27], utilizes thermal fusion bonding[260] to additively join fibers of thermoplastic polymer into porous and solid 3D-shapes. The relatively low cost of FDM machines over the past decade has enabled the widespread use of the technology for tissue engineering in convenient desktop formats[263]. Additionally, FDM allows for sufficient resolution needed for structural and pore designs, out of many relevant materials[27].

Thus far, much of the work using FDM to produce constructs for tissue engineering has focused on developing suitable biomaterials for 3D-printing[386]. Such work has led to a wide array of biomaterials which may be used in FDM with a variety of mechanical and biological properties[388]. The resulting constructs function as cell scaffolds and have the potential be directly manufactured in precise anatomic shapes. However, the scaffold material is not the sole contributor to the success of the scaffold.

Scaffolds for tissue engineering necessarily contain highly-defined porous networks, which are essential for cell seeding and nutrient diffusion throughout the

174

scaffold. These networks also allow room for cells to effect tissue formation. The interplay between scaffold mechanics, porous volumes for cell and tissue growth, and the diffusion of nutrients throughout presents a challenging paradox in determining the optimal microarchitectural design for a scaffold. Principally, it is necessary to provide sufficient material to promote strong mechanical properties while also creating sufficient connected porous space to allow for cell seeding, growth, and nutrient transport.

The fiber deposition process of FDM can be used to control the scaffold mechanics and porous network properties. FDM works by passing a thermoplastic filament through a small-diameter hot element which moves in *x*, *y*, and *z* directions. Extruded molten material (termed a *fiber*) rapidly cools and sets in the position it was deposited, fusing with any adjoining fiber portions. By operating in a *layer-by-layer* manner, the print can be constructed via many *xy*-print layers assembled in the *z*-print direction. Spacing between fibers in the *xy*-plane creates a porous space, which can be designed to connect between different print layers and result in a connected porous network.

The interconnectivity, size, and extent of the porous network directly and indirectly influence cell behavior[26,283,389,390]. Patterns of these porous properties across 3D-printed objects could result in complex tissues with spatial specificity that have thus far only been achieved via directly printing cells in different spatial patterns[102].

An ongoing tissue engineering design goal is the ability to create patterns of porous properties throughout 3D-space in anatomic shapes. Spatially controlling pore properties would also enable the spatial control of mechanical properties, as

porosity and mechanical strength are closely linked. The most common method of creating patterns of porous properties is modifying the fiber-fiber spacing between *z*-levels, which results in different pore sizes at different heights in the print. For example, Sobral *et al.* designed a gradient of pore sizes by systemically increasing or decreasing fiber-fiber spacing in each print layer[391]. Additionally, Woodfield *et al.* 3D-printed cartilage constructs with a gradient of pore sizes in the *z*-direction[392].

These fiber-spacing approaches are constant across an xy-plane and limit designs to changes in spacing in the *z*-direction. While such an approach is applicable in small-scale prints, it does not easily transfer to human-scale complex anatomic shapes. One group, Di Luca *et al.,* has demonstrated fiber-fiber spacing across the *xy*-plane, resulting in a step gradient across the plane[393–395]. Therefore, fiber-fiber spacing could be controlled in *xy*, and *z* directions simultaneously, enabling designs with different pore sizes across 3D-space. Thus far, this approach has only been shown in a small scale, cuboid scaffold with a three-pattern linear gradient. Implementation of such gradients in the x-y plane across a variety of large, more complex geometries remains an unmet challenge for bone tissue engineering.

Additionally, specific control over pore architecture is desirable. Fiber height is often mismatched from desired pore sizes, and cross-hatching fiber patterns on alternating print layers result in pore diameters that are determined by the versatile fiber-fiber spacing in the *z*-direction but limited by fiber height in the *xy*-direction. Varying the fiber height can change the height of the pores in the *xy*-plane, but this approach must be implemented across the entire print plane which prevents in-plane patterning. Further, fiber height is limited by the range of nozzle hardware.

However, repeating the same print pattern without changing the fiber location could result in stacked, taller fibers and therefore pores, as shown by Moroni[396] and Xu[397]. Struts designed from congruent, stacked fibers could be used to make pore microarchitectures isotropic and vary pore size in all three spatial dimensions.

The process of transforming a 3D-design into the *xy*-layers of hot element paths is termed *slicing.* The slicing process determines the fiber laydown pattern, and the resulting porous and mechanical properties and microarchitectures of the print. Slicing is often achieved using a slicing software, which operates on a 3D-shape and "slices" it into individual *z*-level layers. Traditional slicing software systems create a solid wall or shell around the exterior surface of the shape with a single, infilling, truss pattern applied to the interior bulk of the shape.

By intention, these software systems facilitate the manufacture of models and prototypes with solid shells and compartmentalizing, internal trusses. These resulting designs are not useful for tissue engineering constructs as they do not contain interconnected pore networks. Research groups have been limited by the set of functionalities in broadly-used hobbyist software (such as Slic3r[398] or Cura[399]) or in the proprietary software delivered with the bioprinter – which has restricted the availability of useful tissue engineering designs.

To overcome the limitations of the available slicing software, research groups have prepared custom porous designs through 'brute force' design. They manually design each pore and strut in CAD programs and then pass the CAD file to a traditional slicing program, which best approximates fiber placement across the design[256,400]. This design process is labor and computationally intensive and

disconnects the design process from the design space of the 3D-printer, which can cause infidelities in the final product.

Alternatively, custom slicing software can enable the creation of gradients or custom porous structures. For example, the Atala group at Wake Forest University developed an integrated tissue-organ printer and custom software integrated into the system for design and manufacture of constructs. While they published the source code, it is unique to their hardware and does not appear to allow for the design of gradients[102]. Trachtenberg *et al.* developed a Python and Pronterface system to generate GCODE that can vary the fiber-fiber spacing on different print levels on a custom-built 3D-printer[401]. However, these programs are specialized to each design and manufacturing system and are not easily replicable or adaptable.

Therefore, currently available slicing programs do not allow precise control over porous patterns and microarchitectural features needed for tissue engineering scaffolds. Here, we present an approach to designing 3D-printed scaffolds with patterns of porous and mechanical properties. The goals of this approach are to (i) achieve isotropic pore architectures appropriate for tissue engineering, (ii) create manufacturable designs with patterns of pore properties throughout 3D-space, and (iii) provide this approach as a tool that researchers can use when 3D-printing tissue engineering scaffolds. Additionally, we demonstrate that the resulting approach allows the independent patterning of pore size and porosity.

The goals of this approach are to (i) develop a software which can design and implement patterns of pore properties throughout 3D space which contain

isotropic, fully connected pores relevant to tissue engineering, (ii) validate the printability and mechanical integrity of such designs, and (iii) provide this software as a tool that researchers can use when 3D-printing tissue engineering scaffolds. Additionally, we demonstrate that the resulting approach allows the independent patterning of pore size and porosity across a variety of anatomic shapes relevant to craniofacial bone regeneration.

Methods

3D-Printing on Lulzbot

The methods in this paper were developed on a Lulzbot Taz 5 3D-Printer (Aleph Objects, Loveland, CO), which is representative of the many low-cost desktop 3D-printers that are broadly in use by researchers. The printer uses gears to drive a solid polymer filament through a melt chamber and narrow extruder nozzle. The nozzle is moved in the *x* and *y* directions as it deposits material in a single *z* level before proceeding in a layer-by-layer fashion until the build is complete. The cooling and solidification rate of the extruded polymer is critical for determining print quality, and it is controlled by adjusting air fans and the heat of the print surface.

Most importantly, the Lulzbot uses the Marlin operating system to process the standard RepRap flavor of GCODE instructions to control the robotic behavior of the system. The machine responds to commands to deposit a fiber of material (*extruder diameter*) at a given temperature (*extruder temperature*), at a given rate (*extrusion rate*), and move in x-y space (*tool paths, extruder movement speed*). Additionally, the print surface can be heated to prevent warping (*bed temperature*)

and the print can be cooled by turning the fan on at various print heights (*fan speed*,

fan start height) (**Table 8-1**).

Table 8-1: Terminology for 3D-Printed Tissue Engineered Scaffolds

Term	Definition
Bed Temperature	The temperature of the print surface
Extruder	The assembly containing gears which drive filament into the melt chamber, the melt chamber, and the die element.
Extruder Diameter	The diameter of the die element where molten material is extruded.
Extruder Movement Speed	The constant velocity of the extruder as it moves along toolpaths
Extruder Temperature	The temperature of the die element and melt chamber where the material undergoes solid to molten transition.
Extrusion Rate	The rate at which the gears driving filament into the melt chamber turn (mm / min).
Fan Speed	The relative speed of the fan (0 – 100%) blowing from the extruder onto the deposited fibers
Fan Start Height	The print height at which the fan powers on
Fiber	a single extruded strand of polymer from the extruder
Fiber width	determined by extruder nozzle diameter
Layer-by-layer	Additive manufacturing approach whereby the object is manufactured by sequentially depositing layers of planar thin sections
Pore size	Width and height of square pore
Porosity	void volume fraction of scaffold (referring to macro-porosity not porosity within the actual fiber)
Slicing	Transforming a 3D-object into sequential, thin, planar sections, and creating tool-paths for each planar section.
Strut	solid trusses made up of adjacent, touching fibers
Strut width	determined by number of fibers in a single strut
Toolpaths	lines that the extruder follows in x-y plane

Scaffolds in this paper were printed using ABS plastic filament (IC3D, Columbus, OH) with the following printer settings. A 0.5mm diameter extruder was used with the extruder temperature set to 240°C and bed temperature set to 110°C. The layer height was set to 0.2mm and fans were turned on to 50% speed after the first layer was deposited. The federate was set to 1200 mm/min and a 1% over-extrusion factor was applied throughout the entire scaffold.
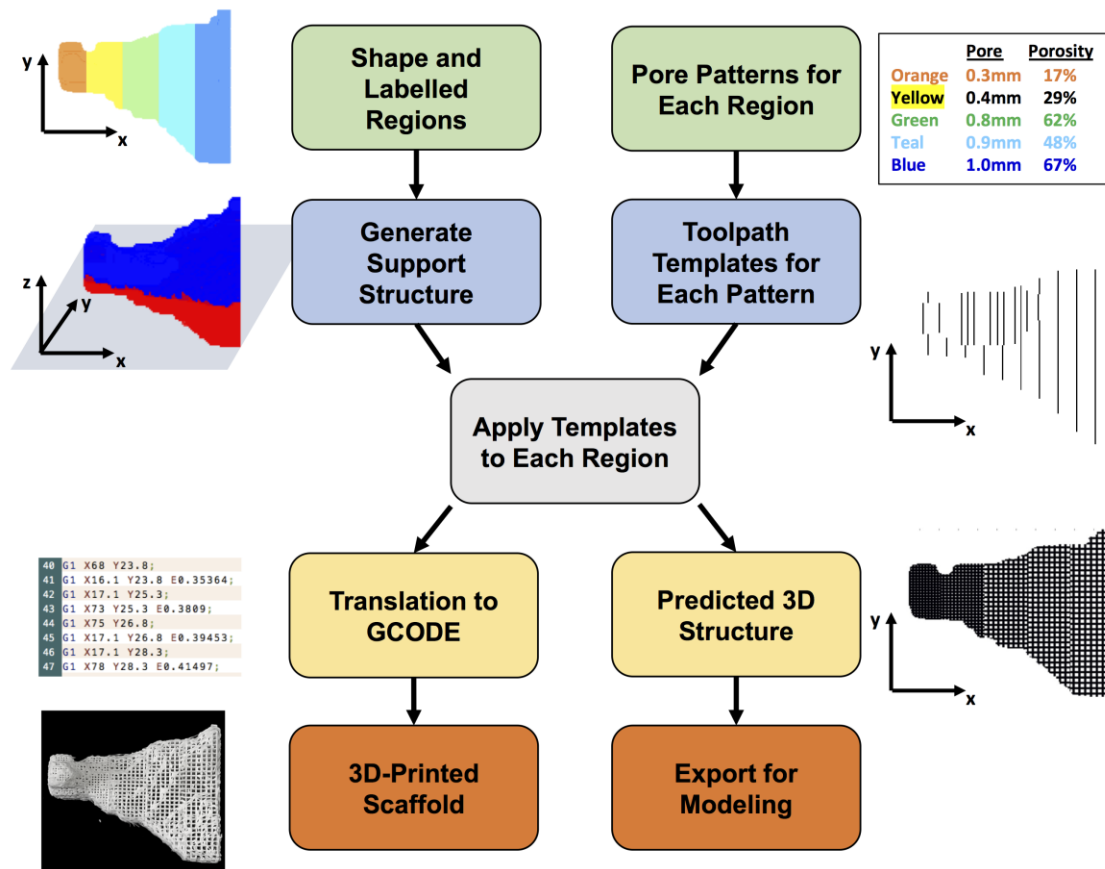
Figure 8-1: Overview of scafSLICR Approach.
User inputs a labelled 3D shaped and the pore properties for each label (green boxes). The program then generates support structure between the shape and the print bed (blue/red shape) and tool path templates for each pore pattern (blue boxes). The slicing process convolves these tool path templates with each x-y level of the shape according to the label (gray box). The result of this convolution is then translated into a set GCODE instructions or into a predicted porous model of the shape (yellow boxes). These outputs can be manufactured on a 3D-printer or used for *in silico* modeling (orange boxes).

Scaffold Design with MATLAB Script

The code was written to enable the feature-driven design of tissue engineering scaffolds. The key features of porosity and pore size are used to create a 3D-template, which is then applied to the desired areas of the scaffold shape (**Figure 8-1**). Pores are designed as isotropic square pores. Porosity is tuned by both the pore width and the strut width (**Equation 8-1**). The strut width can be increased by placing multiple fibers directly adjacent to each other (fiber-fiber spacing = 0mm) and pore width is controlled by the strut-strut distance. By repeating the same strut pattern on consecutive layers, the strut height can be increased to equal the pore width and result in square pores. Squares are computationally easy to implement on cubic voxels at low resolutions. Further, linear fibers and struts have a higher manufacturing fidelity than curved equivalents because of the drawing action of the extruder head as it moves.

$$porosity = \frac{pore\ width}{pore\ width + strut\ width} \qquad eqn\ 8-1$$

The inputs to the code are 3D-shape, pore sizes, and porosities. The possible combinations of pore sizes and associated porosities are dependent on the thickness of the struts and are available as design options. The shape can be easily adapted from CT scans, STL files, or other 3D-data. The pore size and porosity can be inferred from the initial biologic data (e.g. CT density), mathematically defined in a variety of gradients, or any desired pattern that can be applied to a 3D-matrix.

The scafSLICR function generates templates of toolpaths in both *x* and *y* directions based on these parameters and convolves them with the shape matrix.

Additionally, it generates support material between the input shape and the print bed surface. The function includes the options to improve print quality by pausing, back-tracking, or retracting material at the end of each fiber to prevent dragging strands across pore spaces.

The program outputs include common GCODE instructions that are conserved across many common FDM (tested on the RepRap Marlin system[402]) printers and 3D rendering of expected design (as STL and volumetric data). For ease-of-use the function was incorporated into a graphical user interface (**Appendix A**). It uses 3D-plotting[403] and STL import[404] scripts from the Mathworks repository.

scafSLICR is freely distributed in supplements and appendices to this chapter.

Scaffold Manufacturing

Scaffolds were manufactured to assess print quality of different porous patterns (homogenous scaffolds), the transition between different patterns (hybrid scaffolds), and gradients of patterns in three dimensions (gradient scaffolds). Homogenous and hybrid scaffolds were 20x20x10 mm and gradient scaffolds were 30x30x30 mm. The exact porous features of all scaffold groups are listed in **Table 8-2**.

Table 8-2: Pore features of homogenous, biphasic, and gradient scaffolds.

Homogenous		Hybrid		Gradient	
Pore Size (mm)	Porosity (%)	Pore Size (mm)	Porosity (%)	Pore Size (mm)	Porosity (%)
0.2	28%	0.2 → 0.5	28% → 25%	0.2	28%
0.5	25%	0.5 → 0.8	25% → 28%	0.35	26%
	28%	0.2 → 0.8	28% → 28%	0.5	50%
0.8	45%	0.8 → 0.8	28% → 45%	0.65	56%
	62%	0.8 → 0.8	45% → 62%	0.8	62%
		0.8 → 0.8	28% → 62%		

Print Quality Assessment

Design features were measured in manufactured scaffolds and evaluated for accuracy to the input values. scafSLICR was used to design and print scaffolds (20x20x10mm) with a variety of combinations of pore size and porosity, along with a solid ABS cube. The porosity of printed porous scaffolds was determined by mass measurements compared to solid prints of the same dimensions (**Equation 8-2**).

$$Porosity_{mass} = 1 - \frac{mass_{porous}}{mass_{solid}} \qquad eqn\ 8-2$$

Scaffolds were imaged on a stereoscope (Zeiss Z8). Images were taken of top and side views at 2x magnification. Pore size and strut width were measured separately for top and side views. Pore size was analyzed using the DiameterJ plug-in for FIJI[405,406] by measuring the area of each pore of the binarized image. The size of pore was then reported as the square root of the pore area. All of the pores were measured in each scaffold and each scaffold design was printed in triplicate. Strut widths were measured by hand in FIJI using the original stereoscope image.

Between 59 and 69 struts were measured over three scaffolds per group. For pore size and strut width the ratio of measured value to predicted value was report +/- standard deviation.

Mechanical Testing

Scaffolds were tested to assess base mechanical properties of homogenous and hybrid scaffolds. Scaffolds measuring 20x20x10mm were loaded into an MTS Criterion Model 43 (Eden Prairie, MN) with a 5 kN load cell and subjected to unconfined uniaxial compression. The scaffolds were compressed perpendicular to the print axis at a rate of 1.27mm/min. The compressive modulus was determined from the linear region of the stress-strain curve (n=3).

Analysis of Porous Boundaries

In order to assess the connectivity of pores between regions of different porous microarchitectures, the total connected area was analyzed in MATLAB. The area of each connecting pore was measured and transformed into width by assuming the pores were square. The porous area fraction of the boundary surface was found by summing the individual pore areas and dividing by the surface area of the boundary between regions.

Anatomic Shapes

Large portions of the craniofacial skeleton were selected to serve as anatomic test shapes. STLs or DICOMs of the shapes were exported from MIMICs (Materialise, Plymouth, MI) and imported into scafSCLICR. The shapes were divided into regions arranged linearly along the length of the shape (zygoma), or according to shape thickness (orbital bones), or according to depth (hemimandible). Different porous patterns appropriate for tissue engineering were selected from the design space and applied to the different regions of the anatomic shapes.

Results

scafSLICR was used on a standard desktop to generate the designs in this study (**Appendix A, Examples 1-9**). The largest shape (orbital bone) took six minutes to slice and generate the GCODE file, which is similar to the computing time when using Slic3r. Designed scaffolds were manufactured using the output GCODE without complications. Isotropic, regular, cubic pores were visible from top-down and side-on views of the scaffold (**Figure 8-2A**). Support material was automatically generated for anatomic shapes and removed from prints with minor artifacts.
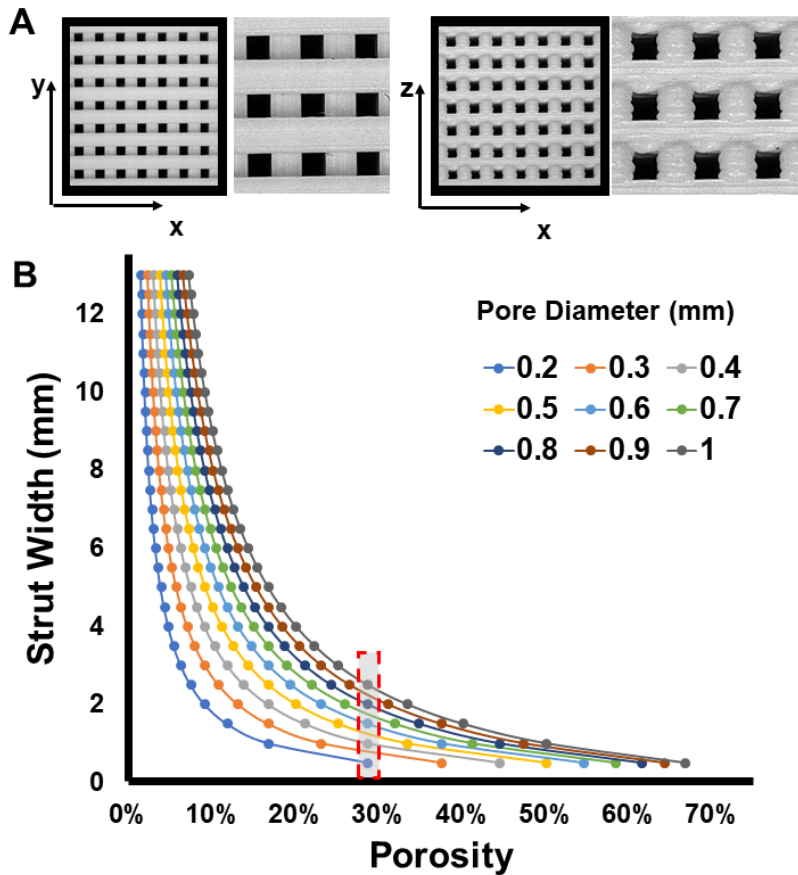
Figure 8-2: Available Design Space.
(A) Stereoscope pictures (1x, 5x) of scaffolds produced with scafSLICR demonstrating isometric pores. (B) Modulating the width of struts can produce a range of discrete porosities that are manufacturable at a given pore diameter for 0.5mm nozzle.

Available Design Space

Based on the diameter of the printer nozzle in use, the strut width can be modulated by depositing adjacent fibers (**Figure 8-2A**), thus a variety of strut widths may be achieved that are integer multiples of the printer nozzle diameter. This allows the decoupling of pore diameter and overall porosity. By modulating the strut width, a multitude of porosities may be achieved for a given pore diameter (and *vice versa*) as shown in **Figure 8-2B**. Pore diameters ranging from 0.2mm to 1.0mm were successfully printed using the 0.5mm nozzle on the Lulzbot Taz5 printer. Within this range of pore diameter, many different porosities may be

achieved by varying the strut width. For example, for a pore diameter of 500μm, eight different porosities may be achieved between 11% and 50% by increasing the strut width from 0.5mm to 4mm.

The maximum porosity is determined by the pore size and printer nozzle diameter. The maximum porosity for pore diameters ranging from 0.2mm to 1.0mm are summarized in **Table 8-3**. For a 0.5mm nozzle diameter, porosities may be achieved between 29% and 67%, and the porosity may be further increased to 74% by using a printer nozzle with a diameter of 0.35mm.

Table 8-3. Maximum Porosity Across a Range of Pore Diameters

Pore Size	Upper Porosity Limit (0.5mm nozzle)	Upper Porosity Limit (0.35mm nozzle)
0.2mm	29%	36%
0.3mm	38%	46%
0.4mm	44%	53%
0.5mm	50%	59%
0.6mm	55%	63%
0.7mm	58%	67%
0.8mm	62%	70%
0.9mm	64%	72%
1.0mm	67%	74%

Similarly, a specific porosity may be achieved using multiple different pore diameters. A porosity of 28.57% can be achieved at 0.2, 0.4, 0.6, 0.8, and 1.0mm pores by modulating the strut width between 0.5mm and 2.5mm (**Figure 8-2B**).

Print Quality/Validation of Predicted Designs

This study used five combinations of pore size and porosity that represented useful porous patterns for tissue engineering (summarized in **Table 8-2**). These designs were printed and used to validate that the predicted designs from scafSLICR could be successfully manufactured with a high degree of fidelity. Printed scaffolds are shown with their respective design previews in **Figure 8-3A**. Manufactured scaffolds matched predicted designs to a high degree in both the top and side views. There was slight over-deposition of material, with pore sizes consistently below the predicted value irrespective of the actual pore diameter (**Figure 8-3B**). Pore diameter ranged from 76% to 93% of the expected value while the strut width varied from 3.5% under deposition to 13% over deposition.

The measured gravimetric porosity (**Figure 8-3D**) is strongly correlated to the specified porosity of input design. The deviation of measured porosity from input porosity is due to the dimensions of the printed scaffold not being exact multiples of the characteristic distances of the individual microarchitectures (pore width in z, pore width + strut with in x and y).
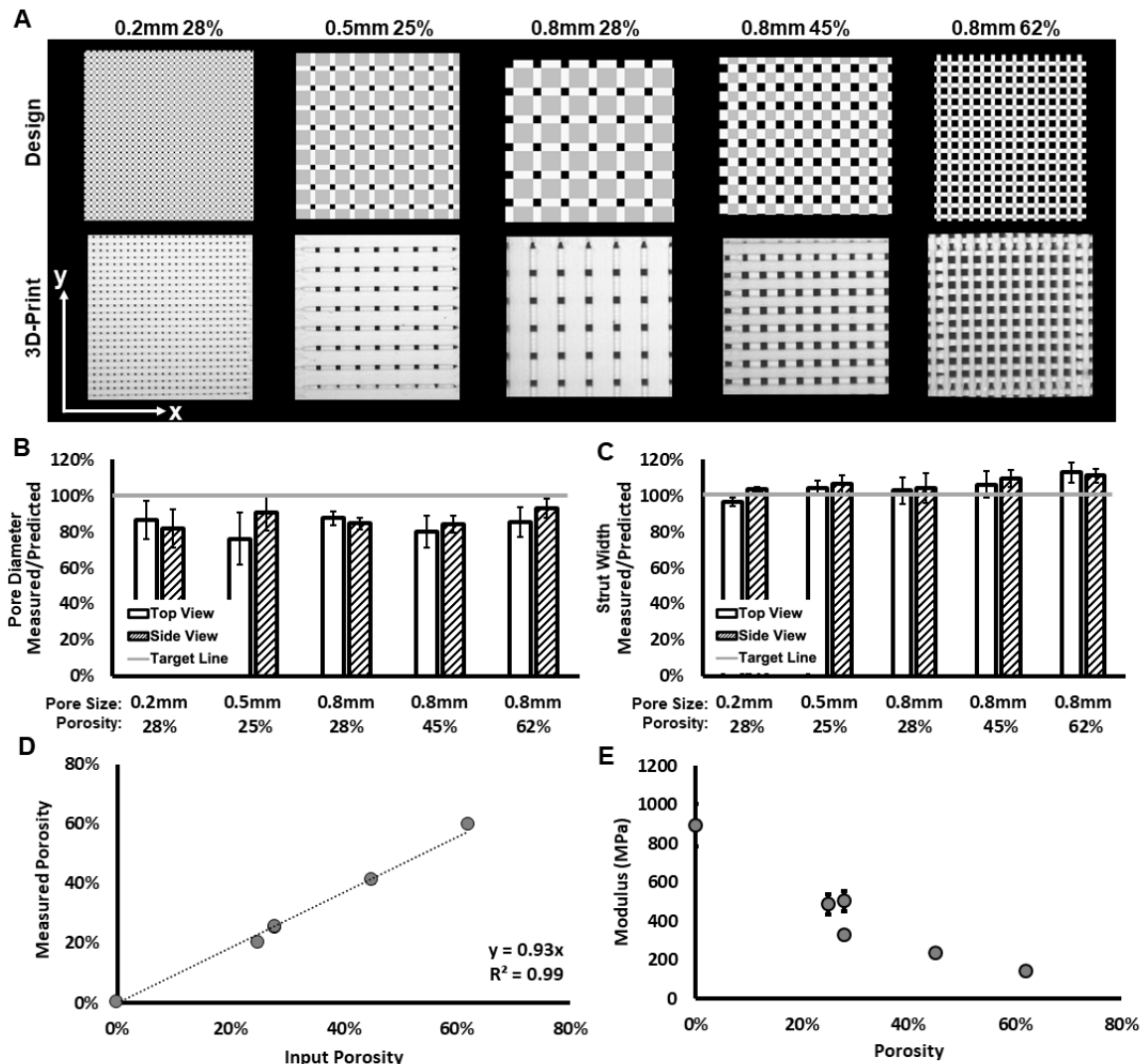
Figure 8-3: Homogenous Scaffolds.
(A) Side-by-side comparison of scaffold preview (top row) and printed ABS scaffold (bottom row) for different patterns of pore size and porosity. (B, C) Assessments of print fidelity of pore diameter and strut width to design from top and side views. (D) Observed gravimetric porosity and expected design values. (E) Compressive modulus varies with porosity.

Compressive Modulus

Homogenous scaffolds were compressed to find the effective compressive modulus (**Figure 8-3E**). Primarily, the effective compressive modulus decreased with increased porosity. Increasing the porosity from a solid cube to 28% porosity with 200μm pores resulted in a 44% decrease in compressive modulus. Further

increasing the porosity to 62% with 800μm pores resulted in an 84% decrease in compressive modulus relative to the solid cube. Despite the clear inverse relationship between porosity and compressive modulus, the three designs with near 25% porosity had different compressive moduli, demonstrating that the mechanics also vary with the specific microarchitecture (pore size and strut size). Increasing pore size also resulted in decreased modulus with scaffolds containing 200, 500, and 800μm pores with near 28% porosity having a compressive modulus of 503, 486, 327.5 MPa, respectively.

Hybrid scaffolds were also tested for mechanics in compression normal to the plane of transition between microarchitectures (**Figure 8-4B&D**). The modulus of the hybrid scaffold was compared to the modulus of the more porous (softer) design and less porous (stiffer) design. In all cases, the hybrid scaffolds had moduli between those of the two constitutive homogenous designs. This result indicates that the transition between microarchitectures did not weaken the mechanics of the scaffold.

Pore Interconnectivity Between Regions

The porous interconnectivity between different microarchitectures was analyzed in predicted designs (**Figure 8-4C**). Because the nature of the interface depends on the position, extent, and curvature of the interface surface, pattern-to-pattern interconnectivity could not easily be physically measured and was instead measured in *in silico* designs of the presented examples. All interface designs included connected pores. A portion of the connected pores were often reduced in individual area, but together represent a large area fraction of connected porous space (10-30% of boundary area) per interface.
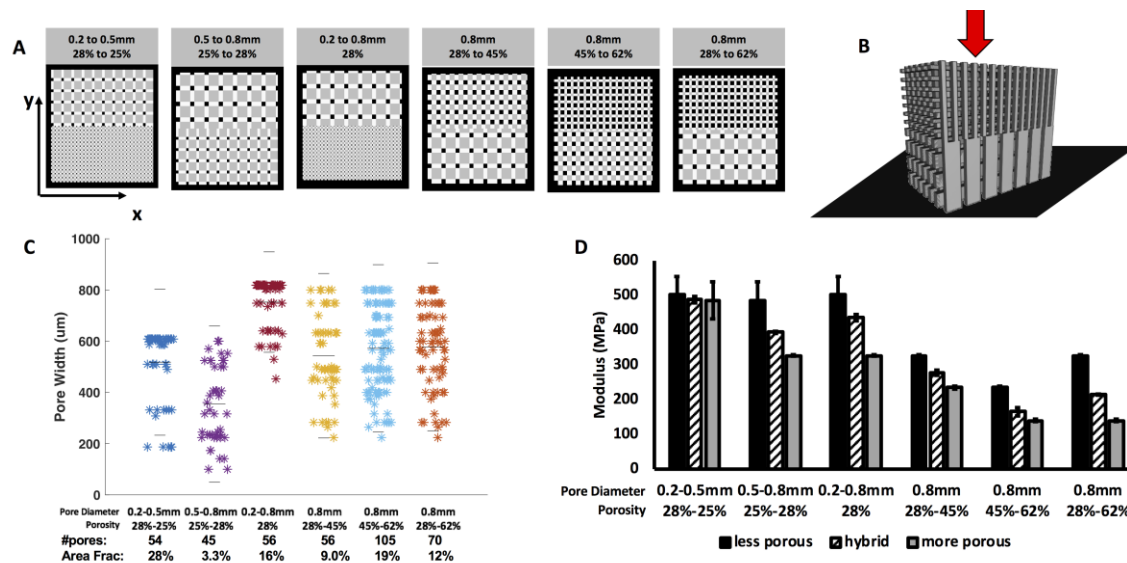
Figure 8-4: Hybrid Scaffolds.
(A) 3D previews of scaffold designs featuring a more porous half and less porous half which meet at a center boundary. (**B**) Schematic showing application of force and alignment of scaffold **(C)** Pore connectivity of transition plane: measured pore areas, number of pores, and area fraction of boundary plane that is connected pore space. **(D)** Compressive modulus of each transition scaffold compared to homogenous scaffolds composed of one of the pore diameter-porosity combinations found in the transition scaffold.

Examples of Gradients of Pores and Porosity

Gradient patterns of different porous microarchitectures were applied to cubes (**Figure 8-5**). First, we demonstrate the ability of scafSLICR to prepare gradients. It readily applied gradients in the print (*z*) direction (**Figure 8-5A**) or across the print layer (*xy* plane) (**Figure 8-5B**). Further, a 3D gradient was applied which graded the porous microarchitectures from the exterior to interior of the cube (**Figure 8-5C**). The cubes were larger than homogenous or hybrid scaffolds in order to accommodate the characteristic sizes (twice the sum of the pore and strut width) of the five patterns. The designs were 3D-printed without complication.
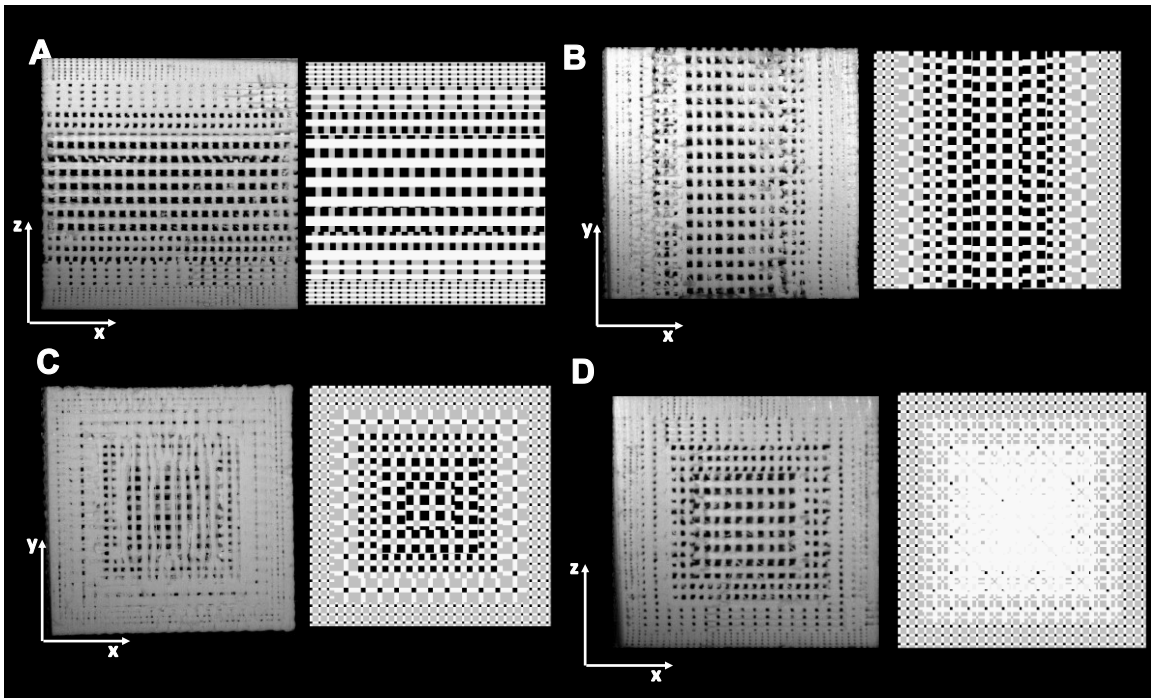
Figure 8-5: Gradients in Cubic Scaffolds.
Pictures of cross-sections of 2x2x2 cm³ ABS scaffolds (left) and design (right). **(A)** Graded in z. **(B)** Graded in x. **(C)** Graded in xy. **(D)** Graded in xyz.

Examples of Anatomic Shapes

Portions of the craniofacial skeleton were used to test shape complexity, pattern complexity, and scale. The zygomatic bone (**Figure 8-6A**) was printed with regular regions from left to right, arranged so the less porous design was at the narrow portion of the bone and the more porous was at the wider portion of the bone. The gradient of increasing pore sizes is visible to the naked eye.

The hemi-mandible (**Figure 8-6B**) was graded into shells based on depth from the surface of the shape. A more porous pattern was applied to the outer shell, versus a more solid pattern along the inner core. This shell design could allow for cell ingrowth into the scaffold along the surface with some added stability from the inner core. There is good porous connection between the outer two shells,

however the inner core was nearly solid and did not have many pores for connectivity.

3D-printing thin structures is difficult, more so when the structure is manufactured with a porous pattern. The orbital bone shape (**Figure 8-6C**) has characteristically thin bones across the orbital floor. To print these faithfully, the shape was divided into regions based on the average thickness, which allowed the thin regions to be assigned a less porous, more stable pattern. Thicker, more stable regions were assigned more porous patterns. The arrangement of the patterns resulted in curved and interwoven boundaries throughout the shape. These boundaries maintained 10% and 20% area pore-connectivity for the three most porous patterns while the less porous designs had much lower connectivity (1.4% and 4.1% area fraction) concurrent with their decreased porosity and pore size.

These large, curved shapes show step/staircase artifacts (particularly in the zygoma example) because there are multiple print levels for a single level of input voxels (input voxel edge = 0.600mm, slicing voxel edge = 0.100mm, printing layer height = 0.200mm). This staircase artifact could be resolved by smoothing the surface of the slicing design 3D-matrix.
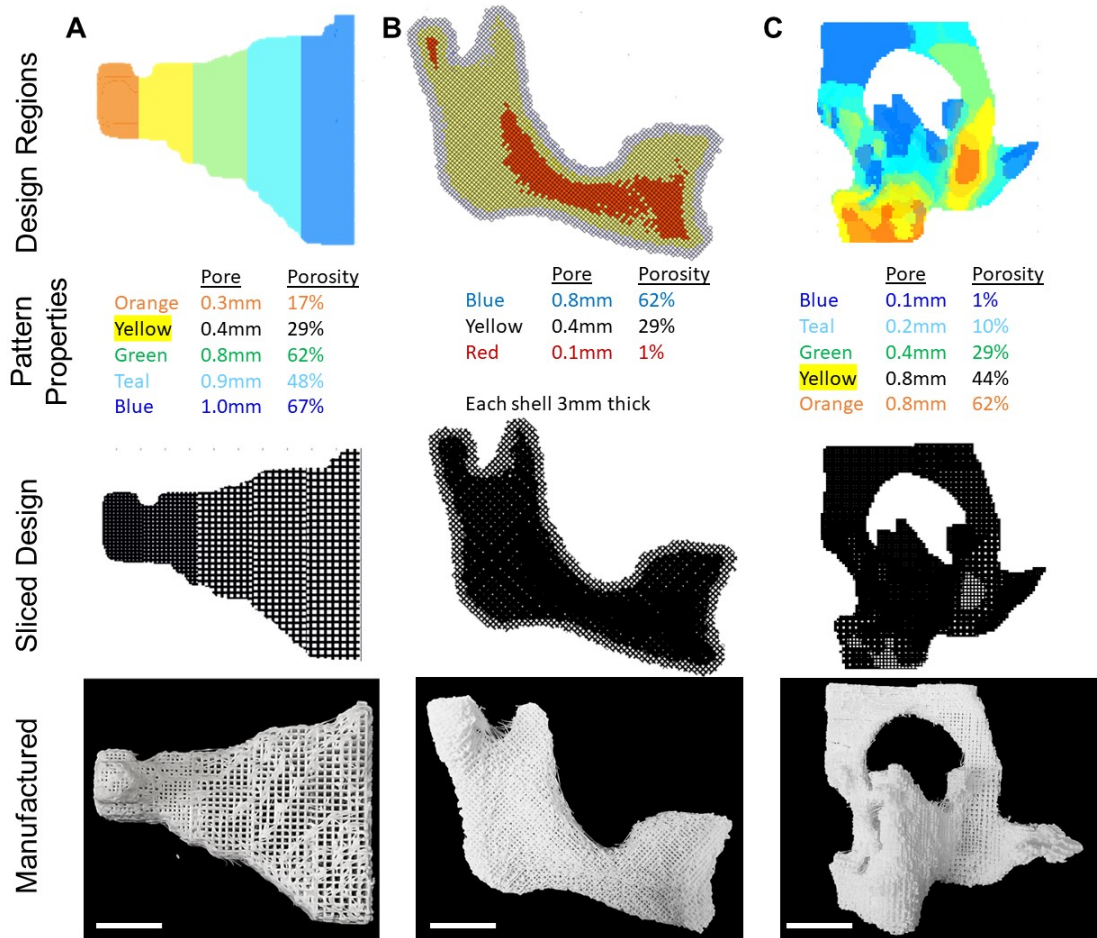
Figure 8-6: Anatomic Scaffolds.

Anatomic shapes from the craniofacial skeleton were labelled with different design regions, sliced with scafSLICR, and 3D-printed in ABS. **(A)** Zygomatic arch patterned linearly left-to-right. **(B)** Hemi-mandible patterned with shells from exterior to interior. **(C)** Orbital midface complex patterned according to average shape thickness.

Discussion

This work develops and implements an approach for the design and manufacture of 3D-printed scaffolds for tissue engineering applications. scafSLICR provides the ability to easily leverage the available design and manufacturing space available in additive manufacturing. In particular, the broad subset of porous microarchitectures can be dependably mixed together in patterns with mechanical integrity and porous interconnectivity.

The cubic cross-hatch pore pattern used in scafSLICR has been used broadly throughout tissue engineering applications of 3D-printing. This structure is further varied here by changing both fiber-fiber spacing and the width and height of struts *via* adjacent and stacked fibers. scafSLICR operates across the design space of the hardware (nozzle diameter) to create porous micropatterns according to desired features (pore size, porosity). This design approach permits multiple porosities with the same pore size and multiple pore sizes with the same porosity. The availability of this breadth in the design space is important because porosity is most directly attuned with print mechanics and pore size with biologic function. Thus, by decoupling the pore size and overall porosity, one could change one of the properties throughout the scaffold without sacrificing the other.

Different strut patterns beyond the classic cross-hatched rectangular patterns are possible. By off-setting the print direction to different angles or curves, the base pattern can be drastically alternated by *z*-layer and *xy*-location to create more complex patterns. Changing the base design from regular cubic cross-hatched struts to another with different offset angles or arching fibers would increase the design space further, and perhaps influence mechanics and porosity

196

in beneficial ways. For example, Moroni *et al.* manufactured scaffolds with 0-45-90 degree patterns of strut offset in order to closely match scaffold mechanics to the cartilage microenvironment[396]. Additionally, Szojka *et al.* 3D-printed scaffolds with alternating layers of parallel fibers with layers of radial ring fiber pattern[407]. Such changes could be implemented into scafSLICR by changing the template creation sub-routine.

The design limits of the microarchitectures of this study are well suited to bone tissue engineering. There are well established constraints for bone tissue engineering scaffolds with regards to porosity, pore size, and mechanics. Porosity should be greater than 30% to provide space for tissue growth and regeneration[408–410]. Pores should range between 100μm and 1mm[408,411,412]. Mechanical moduli needed to mimic bone vary from 14MPa of trabecular bone to 2GPa of cortical bone[27,408,413,414].

Scaling the manufacture of unique porous architectures to large shapes has been a challenge in the field, limiting the 3D-printing of anatomically shaped scaffolds. Many studies establish their techniques at scales less than 2cm in regular cubes and cylinders, which poorly reflects the challenges tissue engineering seeks to address. The complex geometric nature (curves, gaps, peaks, and small walls and divots) of anatomic shapes challenges the 3D-printing processes developed for cubes and cylinders. Moreover, when developing a slicing system for tissue engineering scaffolds, it is essential that the system can readily adapt to a variety of complex anatomic shapes. scafSLICR easily scaled to large prints, with regional heterogeneity that did not compromise porous or mechanical interconnectivity.

One of the major weaknesses of this study is the choice of material. While it is bioinert, ABS was used because of the manufacturing simplicity, speed, and cost. The mechanical assessments were used to validate that porosity influenced mechanics and were not to intended to demonstrate appropriateness for bone scaffold implantation. Towards that end, our research group has used scafSLICR to design and manufacture scaffolds in polycaprolactone and bioactive variations thereof (data not shown).

Direct assessment of interior pores and transitions between different patterns is difficult. We assessed the boundary and the connected pores at the boundary in the sliced design and expect it to be similar to the manufactured case because the exterior print features are of high fidelity. Cracking or cutting the scaffolds were too imprecise to directly examine the boundary plane. Computer tomography scans are one potential method to directly assess the porosity at boundary surfaces. Scans could be registered with the sliced design matrix which would enable further validation of manufacturing quality.

One strength of the programmatic nature of the MATLAB script is the rapid generation of GCODEs that vary tunable properties such as extrusion speed and temperature. **Example 9** (**Appendix A**) demonstrates a higher throughput test of the parameter space by generating designs that vary in pore size and print speed.

While the examples demonstrate the applicability of 3D-printing for bone tissue engineering, many other tissue engineering applications require porous scaffolds with known pore structures and mechanics.

The outputs of scafSLICR enable design validation *in silico* before proceeding to manufacturing or implantation. The manufactured scaffolds in this study precisely

matched the porous designs. These digital porous models of the scaffolds could be used to assess properties such as mechanics, diffusion, or degradation. Such properties are difficult to directly measure, particularly in complex anatomic shapes. The ability to validate such critical attributes are within desired ranges before manufacturing or implantation provides a low-cost means to assure implant functionality.

Despite the validation of print quality and print accuracy, scafSLICR is not validated at the level needed for medical software. It would need additional dimensional and resolution tests to demonstrate reliability with many complex shapes, design transitions, and materials. Importantly, the software validation can be compromised by the resolution and calibration of the specific 3D-printer and its ability to properly execute the GCODE.

At a base-level, scafSLICR operates on a volumetric 3D-matrix. This matrix approach can be memory intensive (design matrix variables sometimes reach 5GB) but allows for the inclusion of more spatial specific information across the 3D-shape. Additionally, the 3D-matrix has direct correlation to the DICOM format used to obtain patient-specific anatomic shapes and allows for minimal manipulation of that data along the design and manufacturing process. In contrast, many slicing software systems operate on the common STL format, which only includes information on the surface topography and therefore slice based on 2D contours of the design.

Conclusion

This work developed an approach to designing and manufacturing 3D-printing scaffolds for tissue engineering, with direct control over scaffold features. It was successfully implemented in MATLAB (or the open-source OCTAVE) and is available at Mathworks Repository as modifiable source code and as a user-friendly graphical user interface. Scaffolds manufactured with the approach were validated with sliced designs. Complex designs of graded pore patterns were demonstrated in regular cubes and complex anatomic shapes at scale. scafSLICR provides both an approach to designing tissue engineering scaffolds with controlled, heterogeneous complexity and scale as well as a readily available tool for tissue engineers to use in designing and manufacturing scaffolds across a variety of 3D-printing systems.
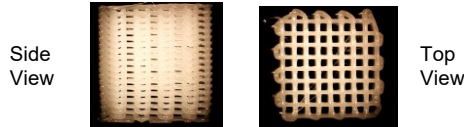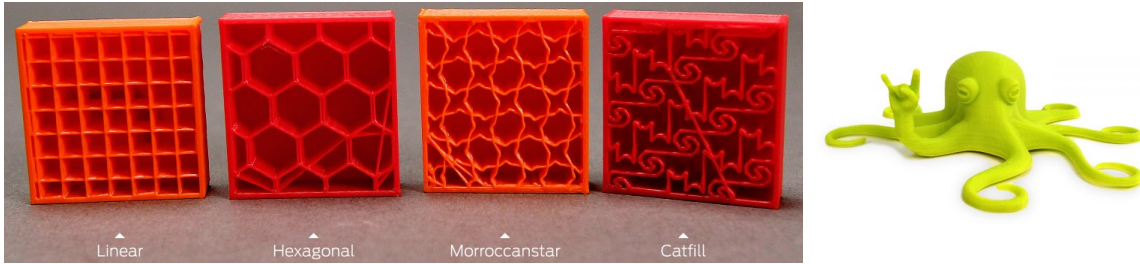
Figure 8-7 Limitations of Hobbyist 3D-printing Software.

    Hobby modelling software creates structures with a thin exterior shell and supporting interior struts, which sub-divides the construct into isolated regions. Adapting this software to create scaffolds results in poorly controlled pore designs that are nearly totally occluded from the side view.
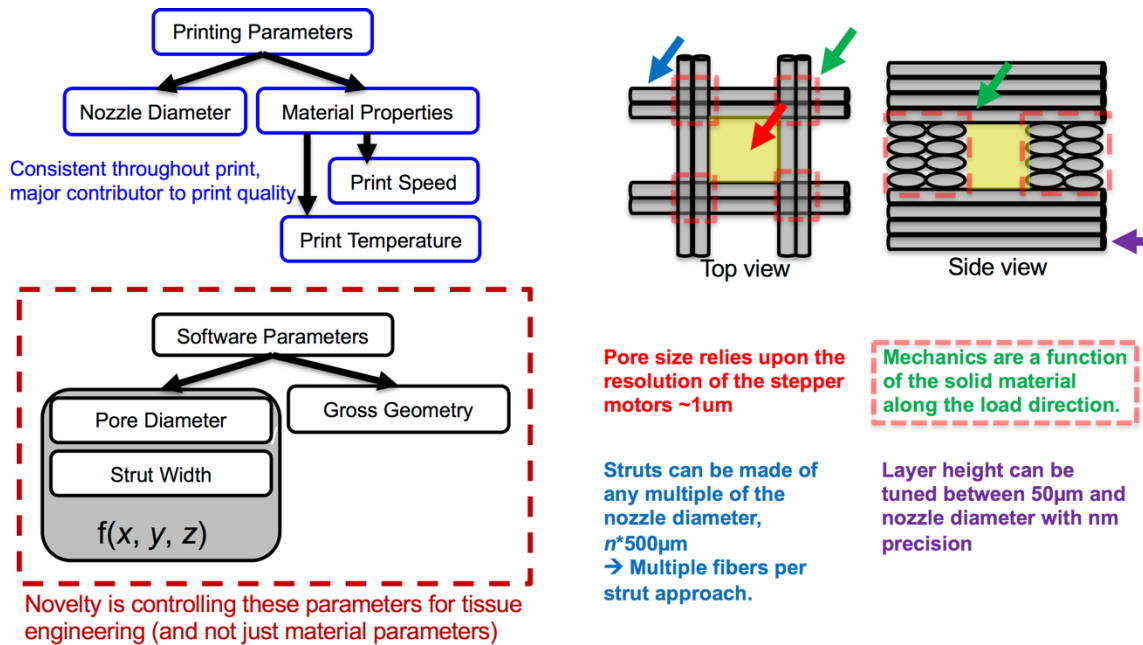
Figure 8-9 Design Paradigm for 3D-Printing Tissue Engineering Scaffolds.

    The common approach to studying 3D-printed scaffolds has manipulated the hardware properties (blue boxes) because the available software did not enable the precise control of fiber deposition. By controlling fiber deposition, we could control pore and strut parameters exactly (red box), resulting in an improvement to the characteristic cross-hatch scaffold structure (right panel).

CHAPTER 9
OPTIMIZED DESIGN TO PATTERN POROUS AND MECHANICAL
PROPERTIES IN HUMAN CRANIOFACIAL BONE DEFECTS

Summary

Regenerative CMF implants function as a temporary structure to position and pattern cells for tissue formation as well as a replacement for the mechanical function of the absent bone volume. Therefore, the designs of 3D-printed CMF implants must meet mechanical and regenerative design requirements. These design requirements are in conflict—for bone regeneration, implants must be both porous and mechanically strong. This work uses optimization algorithms in an approach to design 3D-printed craniofacial bone implants with both pores and mechanical strength. The algorithm is constrained to be, on the average, 50% porous and works to minimize deformation caused by physiologic load by patterning different regions of 30%, 50% and 70% porous microarchitectures throughout the design domain on the implant shape. Optimized implant designs were created and manufactured (3D-Printed) for a variety of craniofacial bones. Finite element modeling showed reductions in design deformation across zygomatic, cranial, and mandible implants. Reductions were greater in large implants (> 4mL, 20-30% vs unoptimized design) than small implants (< 2mL, 8 to 12% vs unoptimized design). The approach was also successfully used to design implants for a retrospective patient case.

Introduction

Annually, there are over 200,000 bone replacement procedures for the reconstruction of craniofacial bones[1], which repair bone losses caused by trauma, congenital malformation, or cancerous re-sectioning. Compared with other skeletal defects, defects of the craniofacial bones are likely to cause disfigurement and psychosocial pathologies[250,346]. While bone has some self-healing capacity, bone replacement is required because these boney defects can be large in size and slow or impossible to heal. Additionally, craniofacial bone defects are challenging to treat due to their geometric complexity, large volume, and incident mechanical forces.

These craniofacial defects have unsatisfying treatment options. The current gold standard of care is autologous bone grafting, which poorly replicates the mechanic and anatomic features of the predecessor bone and is resorbed at high rates[16]. Additionally, autologous bone grafts cause donor site morbidity and are limited in supply. Due to the low availability of bone grafts, permanent plastic, metal, and ceramic implants have become common. However, these artificial implants suffer from stress-shielding, loosening, implant extrusion, and infection rates—all conditions which lead to implant failure[377,378].

Over the past decade, there have been design improvements to reduce these failure rates. To reduce stress-shielding, the material preference changed from medical steel to PEEK which more closely matches that of the bone[415]. Infection rates were associated with the poor vascularity of implants, thus pores were added through the implants to permit blood vessel growth across the

implant[416]. Despite these improvements, cranial implants still fail relatively often and there remains a need for improved craniofacial bone replacement technology.

3D-printed implants have emerged as a promising alternative treatment. Importantly, 3D-printing has the ability to manufacture implants in patient-specific shapes, enabling improved restoration of the original anatomy and aesthetic. In addition to the macro-scale anatomic shape, specific micro-scale architectures can be controlled and manufactured in the 3D-printing process. Different microarchitectures influence the mechanics and permeability[417] of the implant as well as the biologic functions of cells[283]. The small-batch nature of 3D-printing also leverages the burgeoning field of biomaterials, where the material can be functionalized with bone forming signals[232], biodegradation[418], immune modulation[419], or metabolites such as oxygen[333]. Together, these microarchitectures and biomaterials can impart a regenerative capacity to 3D-printing implants, especially when combined with a drug[420] or stem cell therapy[421]. Particularly our research group has developed 3D-printed bone scaffolds using fused deposition manufacturing[26,232]. When combined with stem cells these scaffolds lead to promising bone regeneration outcomes in mouse studies[421].

The design requirements of 3D-printed implants are in conflict as the technologies are translated to human scale. Implants intended to replace craniofacial bone have essential design criteria pertaining to mechanical support, anatomic shape, cell infiltration/seeding and growth, and fluid permeability/metabolite transport.

- **Anatomic shape:** Bones of the craniofacial skeleton are highly curved, often thin/narrow projections, contain sinuses, or interact with teeth. Because

normative shape and defect shape vary from patient to patient, each implant design has different values for the design criteria, and each implant design is necessarily individualized.

- **Mechanics:** The craniofacial bones provide vital support for mastication, respiration, and central nervous system protection (**Figure 9-1**). The forces from the loading regimens are conducted throughout the whole craniofacial skeleton as each bone buttresses others[28,422]. The base mechanical strength of 3D-printed biomaterials—especially when they are in porous patterns—is often less than that of native bone (3D-printed polycaprolactone[232] porous 50 MPa, solid 250 MPa *vs* trabecular bone[423] 0.1 to 2 GPa *vs* cortical bone[423] 15-25 GPa).

- **Pores:** The broad and sometimes wall-like function of the facial bones can separate the outside layer of soft tissue from steady vascular input. This lack of vascular influx can lead to tissue thinning, detachment, and resilient infection. Additionally, if the intention of the implant is to be regenerative, the pores function as a space for tissue formation and growth to occur. Implant porosity is the only way to for cells to dwell and function within the implant, and generally, regenerative implants should be between 50 and 70 percent porous with large pore from 100um to 1mm in width[424]. Pore microarchitecture also impacts overall implant mechanics: increase of porosity directly decreases the mechanical strength of the implant. The inclusion of pores also reduces the manufacturability of small or thin features, especially when the pore size is on the same order of magnitude of the feature.
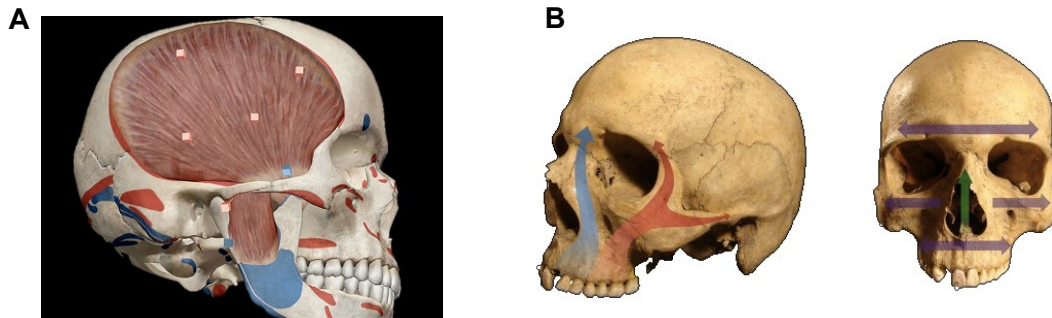
Figure 9-1 Forces on Craniofacial Skeleton.
A. Muscle attachments across the craniofacial skeleton create forces and loads on the bones. Adapted from Smith, *Visible Body* 2014. B. Buttress lines show how the forces are transferred from bone to bone across the craniofacial skeleton. Adapted from Janovic, *Annals of Anatomy* 2013.

In combination, these desired mechanical, porous, and shape features of 3D-printed implant conflict with each other.

Porous heterogeneity could be used to solve the conflict between porous spaces and mechanical stability: portions could be less porous (mechanically stronger) to withstand forces, while other parts could be more porous (mechanically weaker) to provide space for vascular infiltration and tissue regeneration. Generic gradients and stock patterns could be used to automatically design implants with heterogenous porosity. While these patterns could improve the implant design, they are not optimal and poorly individualized. Optimization algorithms can be directly integrated within the design process.

Topology optimization algorithms have been used to design solid implants for the midface skeleton in response to geometric and loading constraints[425,426]. More similar to the work herein, Hollister *et al*. have used topology optimization algorithms to design porous bone implants for spine[427] and mandible[428]. This work

uses an optimization algorithm to determine the optimum heterogenous pattern of porous microarchitectures that resist deformation from physiologic loads on individual, anatomic-shaped implants.

Approach

Designing a Patient-Specific Shape

In most cases, the normative anatomy to replace the missing bone can be obtained from pre-injury scans or simple reflection of the contralateral side (**Figure 9-2**). This shape can provide geometric constraints with regards to the outside surface of the bone and the joining with the remaining surrounding bone. However, craniofacial bones have thin walls surrounding a sinus cavity, and 3D-printed (especially porous patterned) implants do not work well with these thin walls or narrow standalone features. Further, the thin walls would not provide ample design space/domain for the optimization to occur. Thus, to enable 3D-printing and to increase the overall strength of the implant, the design shape is a solid version of the intended bone, with sinus and cavities filled in.

Fixation hardware can be added in the form of plates and screws at the time of surgery or included as a part design shape. Herein, designs include solid fixation plates that can be screwed into the surrounding bone and hold the implant in place. The possible fixation points can be identified from the edge of the defect with surgeon input. Generally, the buttress lines of the craniofacial skeleton which intersect with the implant are preferred locations for implant fixation.

CT scans were imported into MIMICs (Materialise, Belgium) where the contralateral bone was selected, the wrap function was used to remove sinus cavities, and the resulting 3D-object was exported as an STL file. The STL file was

opened in SolidWorks (Dassault Systèmes, France), reflected across the midsagittal plane, and saved as a new STL file. The reflected STL file was imported into MIMICs and positioned into the defect space. The overlap of reflected and remaining host bone was removed, resulting in a smooth and precise joining between host bone and implant. STL of plate fixation was imported into MIMICs and placed along the buttress lines where the implant met the skeleton. Finally, the whole implant and fixation design was exported as color-coded DICOM sets and imported into MATLAB at a voxel resolution of 500μm.
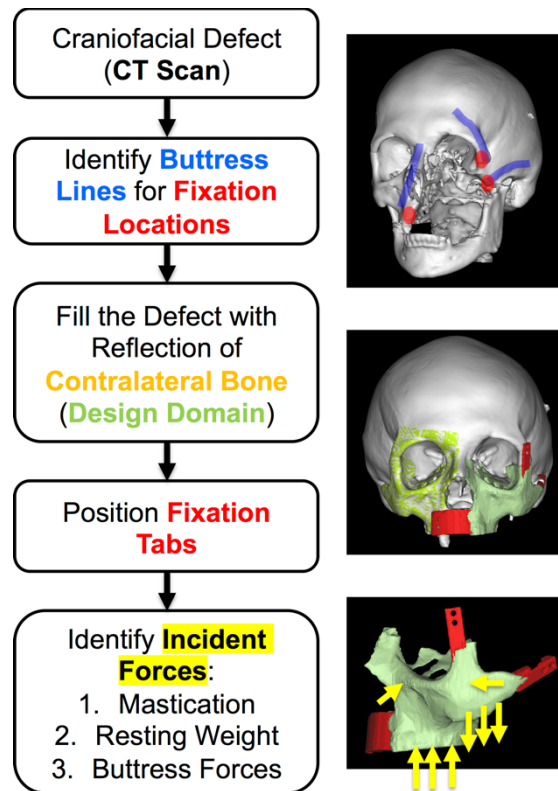
Figure 9-2 Flow Chart of Anatomic Shape and Physiologic Forces.
A CT scan reveals the defect shape and a contralateral uninjured anatomic shape. The uninjured shape is reflected and attached with fixation tabs along buttress lines. Finally, physiologic forces are applied to the shape.

Approximating Physiological Loads

Implants need to endure the forces acting on the craniofacial skeleton. Herein, the loads on the craniofacial skeleton are generalized into three conditions: mastication, resting weight, and impact. Mastication forces are distributed across the craniofacial skeleton with the different muscles involved, and the buttressing action which conducts those forces. On teeth, mastication is approximately 20N, and varies by food type and chewing pattern[429]. The resting weight of the head on a persons' hand, pillow, or other position is substantial (a human head weighs approximately 5kg or a resting force of 50N). Examples of impact forces to the face include falling and hitting the head, a punch or other blunt trauma to the head.

In the MATLAB implementation, static forces can be input as point loads or dispersed loads and the resulting deformation is calculated. Because it is difficult obtain exact measures of expected force, simplifications are used as inputs, with the goal of reducing compliance for such general loads. Therefore, the location, angle and relative scale of the forces is sufficient for the optimization to produce useful designs. The resulting optimized designs can be failure-rated to find the yield or deformation force for each type of load to provide user assurance of function.

3D-Printing Material and Microarchitectures

Solid material and three different porous patterns were considered as microarchitecture options to be assigned throughout the shape (**Figure 9-3**). An 800-micron width was chosen as a uniform pore width in each of the porous designs in order to keep the designs similar in pattern and biologic influence. Polycaprolactone was selected as the material because of printability,

biocompatibility, biodegradation, and common use throughout the literature[241]. The effective compressive moduli of the different pattern choices were measured. This measurement does not fully recapitulate a mechanical modulus and Poisson's ratio.

There are regions of craniofacial skeleton that are below the print resolution of the printer. Further, each of the porous pattern options has a different minimum characteristic pattern width (determined by the strut and pore dimension), which influences the minimum permittable region in the optimization algorithm. Therefore, thin or narrow structures are automatically identified. Those that are below the solid domain resolution are dilated to meet that resolution (e.g. 350µm to 1mm) and those regions less than the porous options minimum pattern width were moved from the design domain to the solid material domain. These adjustments ensure the manufacturability of the shape as well as the inclusion of fine features (**Figure 9-3**).

Porosity: 0%   28%   45%   62%
Pore Size: 0   0.8mm   0.8mm   0.8mm
Modulus: 900 MPa 305 MPa   230 MPa   110 MPa (ABS)
Min. Reg: 1mm   2.3mm   1.8mm   1.3mm

Yellow = thin regions, Green = Design / Optimization Domain, Red = Solid Domain
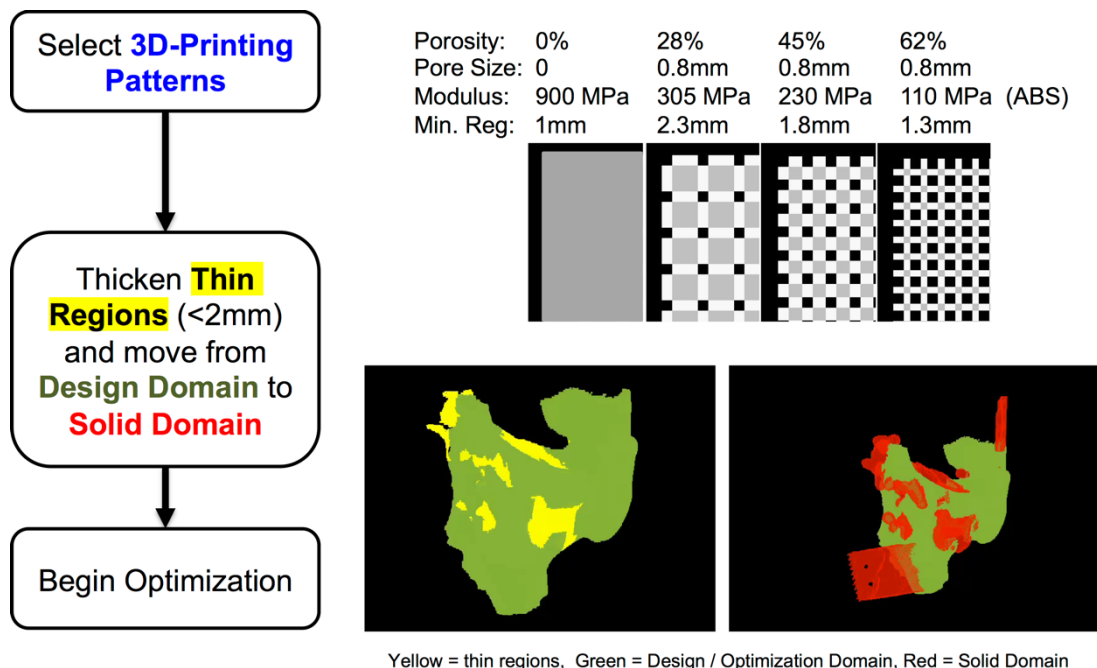
Figure 9-3 Flow Chart of 3D-Printing Constraints.
The 3D-printing patterns used in this work. To ensure manufacturability, portions of the design thinner than the manufacturable size are dilated to the minimum manufacturable size. The adjusted design and solid domains are passed into the optimizer.

Optimization Algorithm

Using topology optimization algorithms adapted for the constraints (shape, pore microarchitectures, porosity) of craniofacial bone implants, designs were optimized to minimize the compliance of the scaffold at static physiologic loads. The algorithm models compliance according to Hooke's law. This finite element model uses the moduli and incident force to approximate each element's displacement, and the corresponding global compliance. The moduli are modeled using the simplified isotropic material with penalization[430] (SIMP) approach to create penalized intermediate moduli values of the moduli (**Figure 9-4**). This penalization creates derivatives towards the design options. The sensitivities are

also calculated for each element's compliance with respect to changes in porous pattern choice. The combined sensitivities are used to shift elements to new design (porous microarchitectures) values according to optimality criteria, within a certain step size. Finally, a filtering step prevents the appearance of checker box patterns and allows implementation of a minimum region size[431]. The total of the changes in each iteration is constrained to keep a minimum porosity across the design domain.
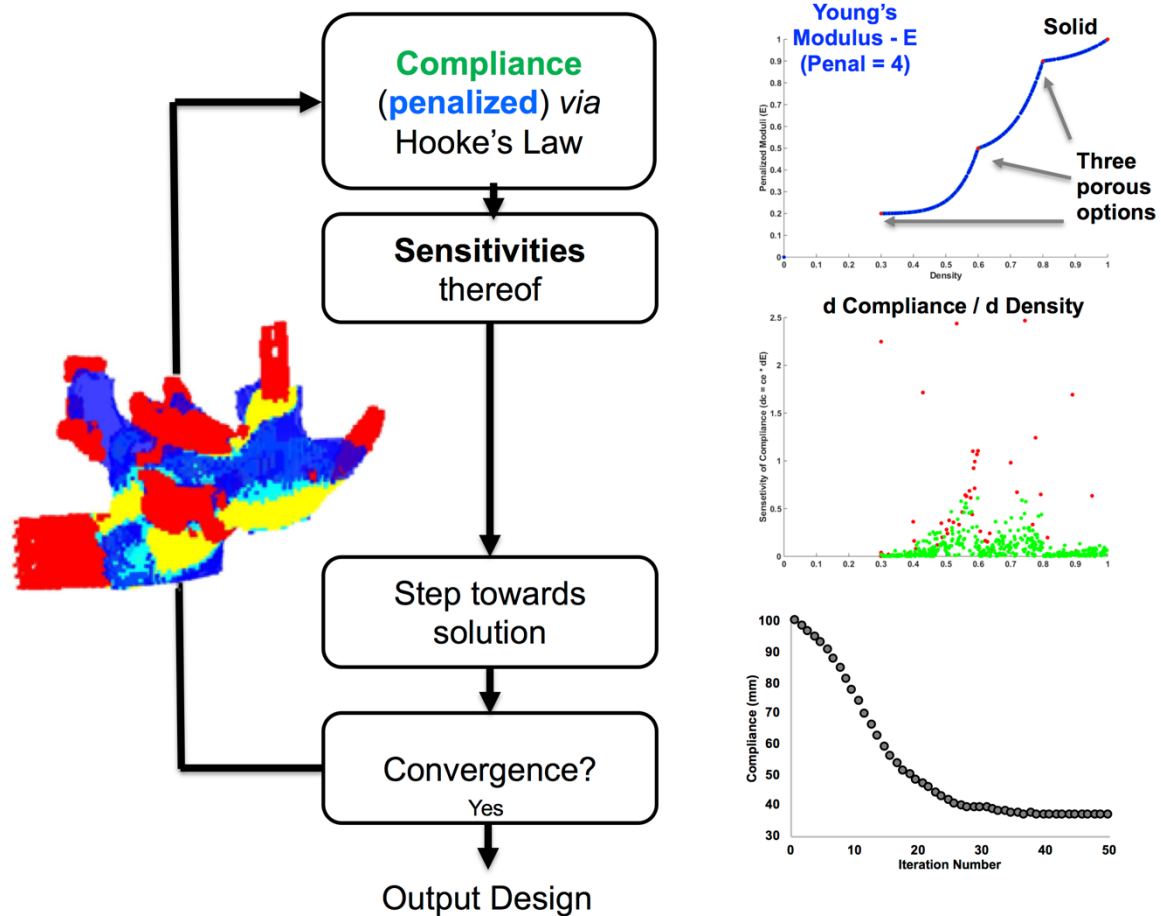
Figure 9-4: Flow Chart of Optimization Algorithm.
    The compliance is calculated using penalized moduli and the sensitivities of it are filtered and then used select new designs with greater or weaker moduli. The new design is then used to calculate the compliance for the next iteration. If the improvements in compliance converge, the final design is output.

Algorithm Implementation in MATLAB

The algorithm was implemented in MATLAB (MathWorks, Natick, Massachusetts) by combining the code from a 3-dimensional optimization approach Liu and Tovar[432] and a multi-material 2D optimization approach from Zuo and Saitou[433]. It maintains the ordered simplified isotropic material with penalization interpolation from the multi-material approach. The finite element model uses nodes, as implemented Tovar *et al*, across the combination of the design domain and the solid domain.

The optimization software was run on a desktop computer with a quadcore 3.4 GHz processer and 32 GB of memory. The shapes ranged from 3,000 to 100,000 elements, which required twenty to forty minutes to prepare the mesh and between one and fifteen minutes for each iteration of the optimization algorithm. Because the shapes are non-regular, we developed a graphical user interface to easily assign loading and fixation locations. Code and an example are provided in **Appendix B**.

3D-Printing Methods

The resulting optimized design was passed to a custom MATLAB slicing algorithm (**Chapter 8**) which prepared a GCODE file with different microporous architectures patterned throughout the shape according to the design. The GCODE file was 3D-printed on a Lulzbot Taz 5 3D-Printer (Aleph Objects, Ohio) using ABS or PCL (IC3D, Columbus, Ohio).

Results

In addition to a patient defect, different facial bones were isolated and designed as implants. The optimization ran on a desktop computer. Generally, the optimized designs had connections of low porosity-high strength pattern between fixation and loading points. Compliance of the designs decreased from the homogenous starting condition in every case.

The available designs fed to the optimization all contained 800μm pores, with porosities of 28%, 45%, and 62%. The normalized moduli of those designs (compared to solid material) were 0.39, 0.26, and 0.12. The total porosity of the design region was constrained to 50%. Screw holes were fixed in 3D-space.

Case 1: Zygomatic Arch

The portion of the zygomatic arch was isolated; it was 2.7cm in length and had a volume of 1.5mL. As fixation, a single screw plate was designed on the posterior, narrow edge and a double screw plate was added on the anterior, maxillary edge. The design was constrained by buttress planes at the edge surfaces which connected to the zygoma and maxillary bones. The load was input to mimic the masseter attachment along the transverse frontal edge of the implant (**Figure 9-5**).

As a result of the optimization, there was a beam-like continuity of denser patterns along the region of muscle attachment and connected to the fixation points. The displacement of the implant was reduced by 11% from an unoptimized, homogenous porous design to the optimized design.

The 3D-printed model closely matched the expected design. The individual zones of different patterns were grossly evident and contained 2 – 10 pores per

zone. The dimensions were accurate to the design. However, there were artifacts from the support structure used along the frontal surface of the print, resulting in a slightly more solid appearance than expected.
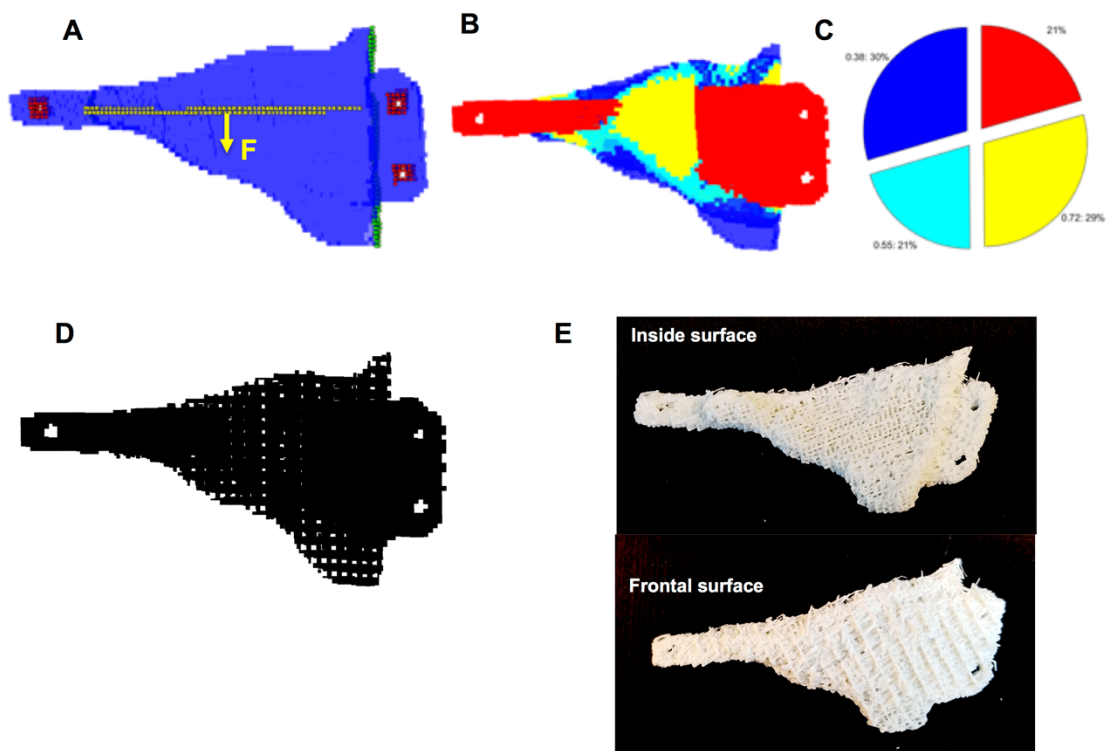
Figure 9-5 Optimization of a Zygomatic Shape.
 (A) The input to the optimization algorithm: shape (blue), fixation points (red), force (yellow), and buttress planes (green). (B & C) The resulting optimized design with different microarchitectures: solid (red), 72% solid / 28% porous (yellow), 55% solid / 45% porous (teal), and 38% solid / 62% porous (blue). (D) The design with the corresponding pores microarchitectures patterned throughout. (E) Views of the 3D-printed optimized design from the frontal and inside surfaces.
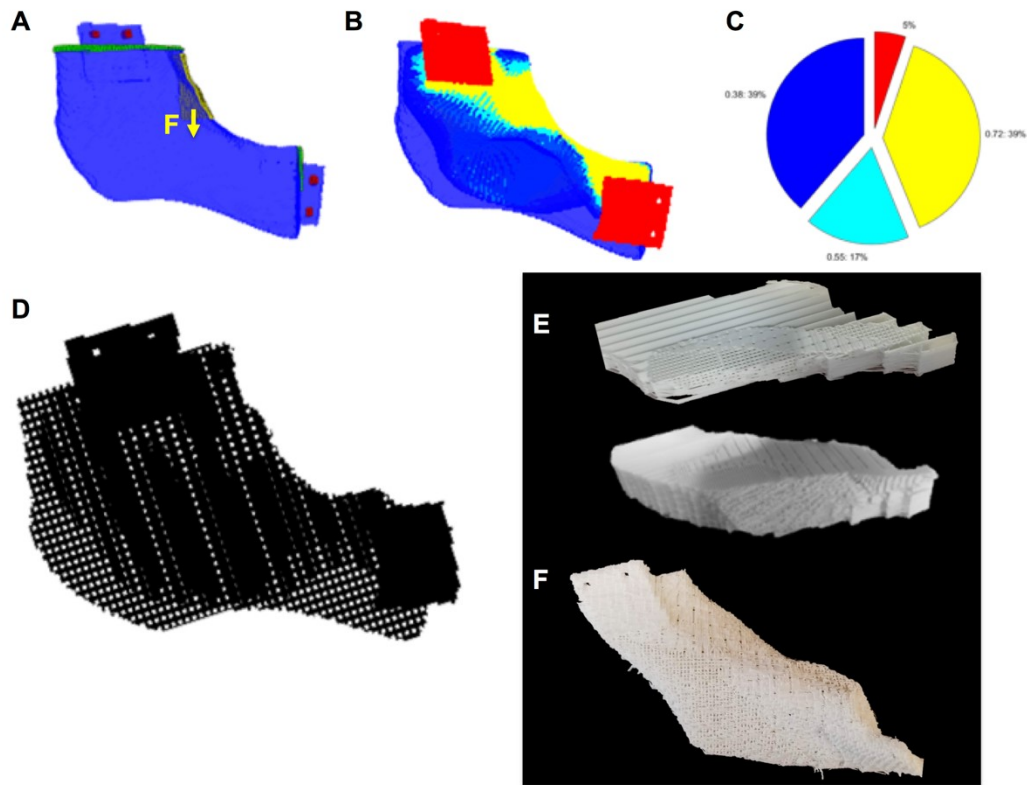
Figure 9-6 Optimization of Portion of Mandible

  (A) The input to the optimization algorithm: shape (blue), fixation points (red), force (yellow), and buttress planes (green). (B & C) The resulting optimized design with different microarchitectures: solid (red), 72% solid / 28% porous (yellow), 55% solid / 45% porous (teal), and 38% solid / 62% porous (blue). (D) The design with the corresponding pores microarchitectures patterned throughout. (E) Views of the print during the printing process with 20% and 60% of the print complete. These views highlight the different regions of porous patterns within the design. (F) Views of the 3D-printed optimized after support structures were removed.

Case 2: Mandibular Ramus

A hemimandible (approximately from the mental foramen to 1cm from the temporomandibular joint) was selected (**Figure 9-6**). It was approximately 5.2cm in length, 2.7cm in thickness, and had a volume of 13.6mL. Double screw plates were added to the design to attach the implant to the body of the mandible anteriorly and the ramus of the mandible at the joint, posteriorly. The load was applied along inner angle.

The optimization patterned denser patterns along the interior of the implant shape and along the mastication surface, connecting to the fixation points. The displacement of the implant was reduced by 22% from the unoptimized control case.

The 3D-printed model matched the design as expected. However, rotations applied to the optimized design matrix and contraction (from cooling) during the printing process skewed the final output shape and increased the angle of the implant between the two fixation points. The different porous regions were clearly visible and correlated with the optimized design. The fixation tabs were very strongly integrated into the body of the print.

Case 3: Cranium

A section of the frontal cranial bone was selected (**Figure 9-7**). It was 16.2 mL in volume and approximately 6.5 cm x 2.1 cm x 7.5 mm in size. Double screw plates were added on every adjoining edge and the load was applied in an orthogonal direction to the center of the implant. The optimization pattern had denser patterns in the middle of the implant connecting to the fixation tabs, with the less dense patterns along the outer portions of the implant that were in contact

with the hose bone. The displacement of the implant was reduced by 25% from the unoptimized control case. The 3D-printed model very closely matched the design, and the different porous patterns were grossly observed and matched the optimized design.

Case 4: Patient Case

Designs were created for a patient case (**Figure 9-8**). The anterior cranial scaffold was 47.0 mL in volume and had a size of 7.89cm x 9.6cm x 9.6mm. The optimization resulted in a design with a 45% reduction in displacement compared to the homogenous control design. The posterior cranial scaffold was 62.0 mL in volume and had a size of 11.0cm x 8.0cm x 1.2cm. After optimization, the design had a 44% reduction in displacement.

The 3D-prints of the patient case implants were less curved than the design, which is likely due to warping of the plastic as the print cooled. The anterior case used tabs for fixation, while the posterior case used a lip design to hold the implant in the defect.
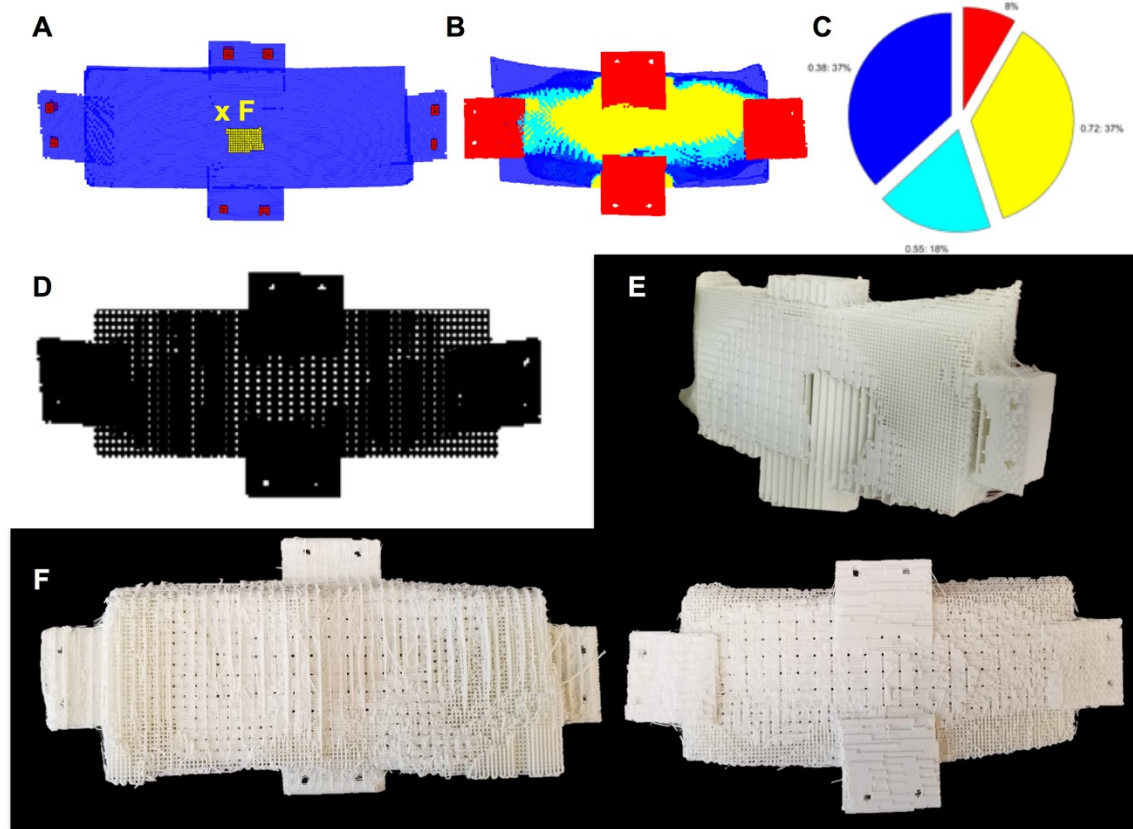
Figure 9-7: Optimization of a Portion of the Frontal Bone.
(A) The input to the optimization algorithm: shape (blue), fixation points (red), force (yellow), and buttress planes (green). (B & C) The resulting optimized design with different microarchitectures: solid (red), 72% solid / 28% porous (yellow), 55% solid / 45% porous (teal), and 38% solid / 62% porous (blue). (D) The design with the corresponding pores microarchitectures patterned throughout. (E) Mid-print view of the implant shows the different porous regions in the interior of the scaffold. (F) Views of the 3D-printed optimized design from the inside (left) and outside (right) surfaces.
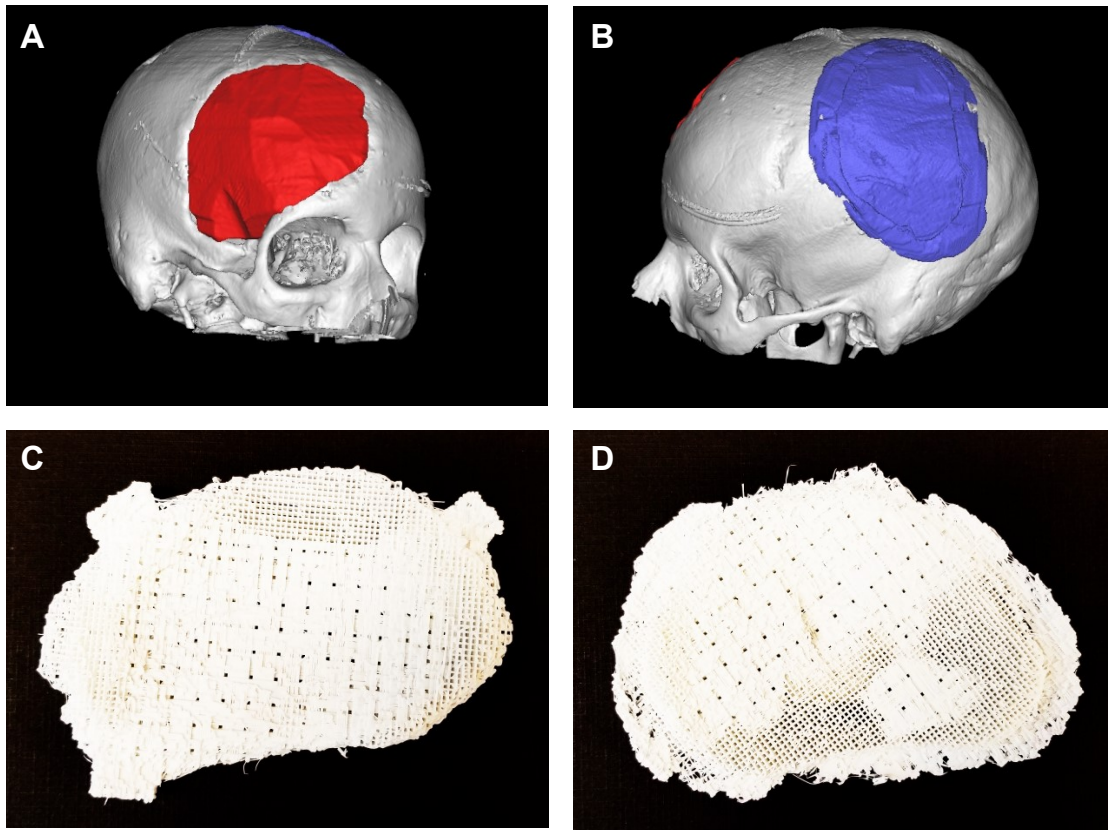
Figure 9-8: Optimization of a Patient Case.
    (A & B) Shape design of scaffolds to replace bone in a patient with two cranial bone defects. The red shape uses tabs to fixate the implant to the remaining skeleton, and the blue shape uses a lip structure to hold the implant in place. (C & D) The optimized designs for each case were 3D-printed and demonstrate the different pore patterns across the shape of the implant.

Discussion

The design of regenerative CMF implants is difficult due to their conflicting design goals. The goal of this study was to design implants with improved mechanical function and with porosities appropriate for regeneration. We tested the hypothesis that heterogeneous mixtures of microarchitectures could be designed according to the fixation and physiologic forces on the implant, and that such designs deform less than homogenous patterns. While the optimized designs were stronger than the homogenous designs, the degree of improvement was dependent on sufficient volume for the optimization algorithm to create useful designs— the improvements of the large scaffolds (cranial, mandible) were twice that of the smaller zygomatic design.

The design process for patient specific implants herein is dependent on a normative contralateral side. Cases where there is no normative anatomy to reflect could rely on modeling of the normative shape from the remaining portions of the skull[434].

By making thin features solid and non-porous there is a risk of the implant degrading without any bone formation occurring there, which could lead to implant failure. This risk could be alleviated by leveraging true multi-material 3D-printing and placing a permanent implant material in that region.

The optimization has a requisite porosity limit (50%), and regions of stiffer material are spatially patterned throughout the shape to reduce deformation caused by input loads. The entire shape must have some material placed there, and to meet the requisite porosity, there is a limited amount of higher stiffness regions that can be patterned. None of the optimized designed eliminated

deformation with that available design space. The optimization goal and major constraint could be switched: the mechanics could be constrained to non-deformative designs and the objective goal could be maximization of porosity.

Because the model operated on cubic elements, the resolution of the model impacts the resulting design. Generally, the designs from the CT scan are down-sampled to enable the MATLAB scripts to operate on the desktop computer. These down-sampled resolutions (1-2mm), minimum region size of the 3D-printed patterns (1-3mm), and the resolution of the xy-positioning of the print features (~10μm) all combined nicely in designing and 3D-printing these implants. Design accuracy could be improved by up-sampling the optimized design and applying it to the high-resolution CT shape. This extra step would also remove staircase effects from the design process from the surface of the implant.

There were a number of assumptions in the modelling portion of this work. First was the assumption of using a measured effective modulus of large, regular scaffolds of homogenous pore microarchitecture as an input to model the mechanics of irregular patterns that did not always finish on a complete repeating unit. This assumption significantly simplified the model and enabled desktop implementation. Further, the model does not account for the anisotropy of the porous patterns or of layer-by-layer 3D-printed implants. We have shown[27] that print direction can influence the strength of the implant: mechanical strength along to the print axis was 150% that of the mechanical strength in directions orthogonal to the print axis. A more accurate model would measure the modulus and directly model the porous strut designs.

Second, the magnitude and complexity of the incident loads were assumed and simplified from literature. In addition to the static load cases modelled in the examples, the CMF skeleton undergoes more complex cyclic loading from mastication and sharp impacts from collisions. Additionally, the model combines all the input loads into a single case and minimizes the resulting deformation, rather than considering each load case separately.

Third, Hooke's law is not well suited to modeling the mechanics of plastic fibers—it works on the premise that there is no plastic deformation, which is untrue in polycaprolactone and other thermoplastics used in 3D-printing. The results herein use Hooke's law and only accurately describe the small elastic deformation that occurs at low strains.

Perspectives

Other optimization goals for craniofacial implants are possible. For example, there could be a need to ensure diffusion throughout the porous space of the scaffold. Indeed, unit cells with specific permeability properties have been designed[417,435]. The objective function could be weighted to include these features. This design approach could also be applied to different additive manufacturing approaches. Different microarchitectures with a range of regenerative properties (mechanics, porosity, pore size, permeability, etc) could be prepared for the manufacturing approach. Then the algorithm could pattern them throughout the space according to the objective function.

Conclusion

This chapter developed an approach to designing craniofacial implants while addressing conflicting design goals. The approach herein balanced those design goals and results in designs that demonstrate improved mechanical properties and were able to be 3D-printed. This process is readily applicable to defects of various portions of the craniofacial skeleton—however the improvement that results from patterns of different microarchitectures is most pronounced in large defects. While the mechanical modeling used is simplistic, the resulting designs intuitively correspond to the applied load schemes and provide a mechanically improved design compared to homogenous scaffolds. Altogether, this study provides a design perspective to improve the mechanics of 3D-printed tissue engineering scaffolds which suffer from a weak biomaterial.

CHAPTER 10
PORCINE MODEL OF CRANIOFACIAL BONE REGENERATION USING 3D-PRINTED SCAFFOLDS AND STROMAL VASCULAR FRACTION CELLS

Summary

Human-scale, living, mammalian models are necessary for developing regenerative craniofacial bone treatments. Our regenerative 3D-printed scaffold and stem cell treatment demonstrated full regeneration of critical-sized defects in mice, but that study could not address the concerns of scale, mechanical integration, and immune interactions. Herein, we test that technology in a large preclinical animal model: the swine zygomatic arch. Scaffolds were designed, 3D-printed, and within a design and manufacturing validation framework. The resulting scaffolds were implanted into 'patient-specific' matched osteotomies in the zygomatic arch of skeletally mature Yucatan mini-pigs. Concurrent with implantation, stromal vascular fraction cells were isolated from the pigs and seeded into the implants to model a point-of-care application. At 6-weeks and 3-months, the scaffolds pore spaces were filled 40% and 60% with bone, respectively. This work demonstrates the regenerative ability of these patient-specific 3D-printed scaffold in the context of full thickness craniofacial bone defects.

Introduction

Among craniofacial bone injuries, mid-face and periorbital injuries represent a unique surgical challenge due to the orbit and the buttressing structure of the zygomaticomaxillary complex. There is a high incidence of orbital fractures and severe globe injuries in mid-face injuries, conjoint with a high complication rate

(30%) with current treatment modalities that include malalignment, implant exposure, and infection.

Stem cell and scaffold combination treatments represent a promising alternative to bone grafting or solid implants treatments. In particular, the stromal vascular fraction of the adipose tissue (SVF) contains stem cells that are readily accessible and applicable for bone regeneration. The passaged form of these cells, ASCs, have been the focus of a large amount of literature and are well characterized. In human studies thus far, the outcomes of SVF in boney healing has focused on safety outcomes, and do not present convincing data for or against the role of SVF in bone metrics. In mice, we have demonstrated that ASCs and SVF (in combination with the 3D-printed bone scaffold) lead to high levels of bone regeneration[421].

While tested in these small animal studies, only a few groups have tested SVF or ASCs for bone regeneration in large, preclinical animal models. Of note, Bhumirta *et al.* tested ASCs in a mandibular defect by seeding autologous ASCs into a decellularized bone graft and culturing in a bioreactor before implantation and found increased bone volume and vascularity, and reduced resorption of the implants[379]. Therefore, there is an urgent need to test the potential of the approach in a large-animal preclinical models, because small animal and human studies have only demonstrated the effectiveness of SVF in small scales, and that it can be safely used in humans, respectively.

A living, mammalian model approximating human size is necessary for evaluation of scaffold and cell combination approaches. Mathematical models or computer simulations cannot duplicate the complex immune responses or bone

healing and remodeling required to evaluate reconstructive surgery. Further, large animal testing is an important step in translating technology from the lab to the clinic because it demonstrates the safety, effectiveness, and implementation of the technology to the United States of America Food and Drug Administration and the surgeons that might adopt the approach. Only a large animal model can inform the mechanical integration of the implant, bone growth dynamics, and unforeseen complications.

Swine is an advantageous species for the study interventions of the craniofacial bones before human implementation. The similarities of the oral maxillofacial region in swine and humans regarding anatomy, development, physiology, and disease occurrence allows the study of craniofacial skeletal structures in a clinically relevant manner[436,437]. Particularly, the constitution of the orbit and its position with respect to the periorbital bones are closer in anatomy and scale to humans than other preclinical models such as dog or monkey[438,439].

In order to test our 3D-printed scaffold and stem cell approach for bone regeneration, we developed a novel, zygomatic, full thickness, bone defect model in swine. The zygomatic arch has some anatomic complications: the maxillary sinus extends into the zygoma and connects this mucosal airway with the implant; the sinus also reduces the purchasing power of screws used along the maxillary edge of the defect. Compared to other craniofacial bone defects, a transcutaneous approach avoids complications with interfacing with the brain cavity or oral environment.

To test the approach in immune competent swine, we developed a standard procedure to isolate autologous SVF from pigs, with comparable results to isolating

human SVF. Additionally, that isolation was optimized to happen within an intraoperative time period of forty minutes. Excised fat tissue from pig is very different from liposuction aspirate obtained from humans: it is exceedingly fibrous, solid at room temperatures, and often contaminated with muscle or dense fascia. The primary alterations to standard digestion were extensive mincing at the outset of the isolation, the increased concentration of collagenase, the shortening of the collagenase digestion period, and the overlap of the size filtering and red blood cell lysis steps.

This study is designed to closely mimic the logistics of the envisioned clinical application: treatment in a single surgical session. First, a preoperative CT scan obtains the geometric information of the defect and the implant. Then the implant is designed, manufactured, and sterilized. Second, at the time of surgery, fat tissue is recovered from the patient and stem cells are isolated. While the cells are isolation from the tissue (a period of 30-40min), the surgeons implant the 3D-printed bone. Finally, at the end of the surgery, the isolated cells are injected directly into the implanted bone. Third, the stability and regeneration of the implant is monitored over time with CT scans (**Figure 10-1**).

Thus, this study has the following goals: (1) Design a non-healing defect to test bone regeneration in peri-orbital bone. An empty control group will show non-healing nature of the defect. (2) Prepare scaffold implants for the model in 'patient specific' manner with design and manufacturing validation. (3) Use the defect model to assess the bone regeneration caused by 3D-printed bone scaffolds and SVF cells.

Methods

Study Design

To test our 3D-printed craniofacial scaffolds with SVF for periorbital bone regeneration, we compared the bone healing outcomes in three groups: (1) empty defects, (2) acellular 3D-printed implants, and (3) 3D-printed implants and SVF. We hypothesize: (1) that the 3D-printed, bioactive scaffold and stems cells enable the rapid formation of vascularized bone in the same shape as the implant and (2) that the untreated empty defect will not heal over the course of the study. The study occurred in two parts: first a small 6-week pilot study to test the approach and implant fixation, as well as test the non-healing nature of the defect; and second a larger cohort to examine the implant regeneration over a long period of time.

Figure 10-1 Swing Zygomatic Implant Study Outline
> (A) Labelled (red box) region of interest on the zygomatic arch of swine in a pre-operative CT. (B) Using the pre-operative CT scan, an implant is designed. (C) To validate the design, a model is 3D-printed and the dimensions and rigidity is assessed. (D) Using a validated design, the implant is 3D-printed in PCL-DCB material. (E) The implant is scanned to confirm the presence of DCB particles throughout, and the open and structured porous network. Then in a single surgical procedure, SVF cells are isolated, placed in the implant, an osteotomy is created, and treated with the implant. (F) Post-operative CTs monitor the fate of the implant and regeneration over time.
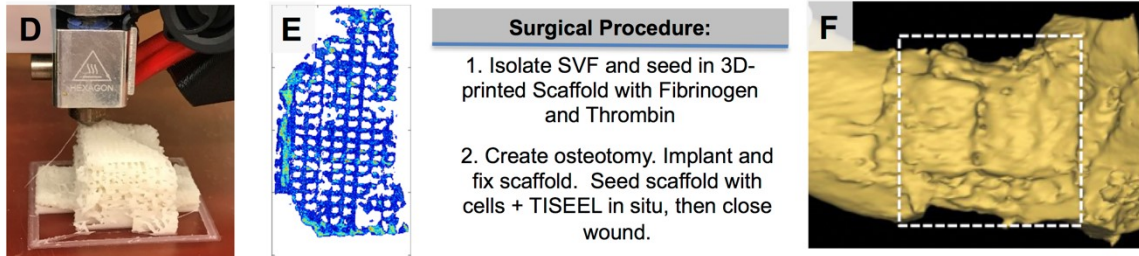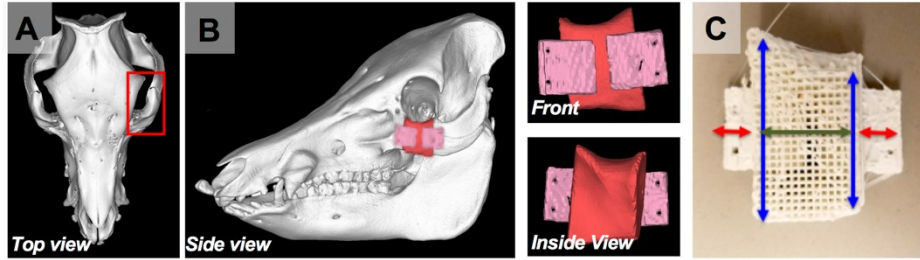
Figure 10-1
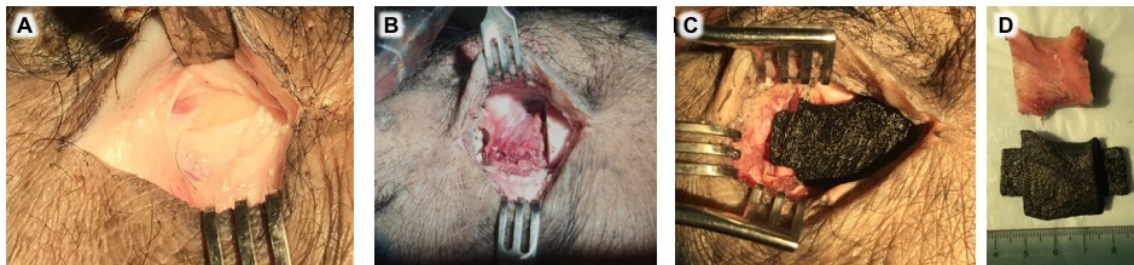
Figure 10-2 Designing the Zygomatic Defect in Cadaver Samples.
(A) A transcutaneous approach is used to access the zygomatic arch. (B) A 2cm full thickness osteotomy is created in the body of the zygoma. osteotomy. (C) A (prototype) scaffold is placed in the osteotomy. (D) There is good agreement between the excised bone and the matched implant.

Design of Animal Model

A cadaver head of Yucatan swine was obtained from Exemplar Genetics (Sioux Center, IA), and a CT scan was conducted. The scan and the head were used to prototype the defect design and surgical approach. Given the anatomy of the zygomatic arch, a defect was designed between the anterior prominence and the posterior suture line. This defect position avoids the complicating curvature of

the prominence and reduces the potential of fracturing the suture line during the creation of the osteotomy.

The defect was developed in collaboration with an expert maxillofacial surgeon to closely mimic current clinical procedure, and a characteristic width of 2cm was chosen to model a non-healing critical size. Because this is a novel defect, we will establish that a full thickness defect of this size and location is non-healing in swine. A transcutaneous surgical approach was selected because of anecdotal evidence of swine developing infection and serious complications with intra-oral approaches. This approach is a deviation from human care, where the general preference is intra-oral to prevent scarring on the cheek. Cadaveric exploration revealed the dense periosteum, attachments of the masseter muscle on the bottom rim and inside rim (**Figure 10-2**). There was an absence of complicating anatomy such as nerves or large blood vessels.

A CT scan of each study animal was used to plan the osteotomies in an animal-matched manner. The scans were loaded into MIMICs software suite. A characteristic 2.0cm osteotomy was designed in each zygomatic arch (bilateral defects in each animal). The defects were, on average, 6mL in volume, and 2.0cm along the frontal contour and 1.5 cm along the interior contour. This 0.5cm decrease from exterior to interior width accommodates the curvature of the zygomatic arch, it allows both saw cuts to be perpendicular to the bone surface at their locations.

Further the defects were approximately 2.5cm height and 1.5cm depth, a full thickness gap in the zygomatic arch. A control group of empty, non-treated

defects confirms that these defects do not spontaneously heal over the course of one year.

Cutting guides were designed so the osteotomy precisely matches the design (**Figure 10-3**). The guides covered the entirety of the anterior surface of the defect, were 2mm in thickness, and contoured flush with the surface of the bone. This thin profile aided in placing the cutting guide in the incision site and left room for fingers and surgical tools to manipulate the site. The cutting guides were manufactured by 3D-printing the guide in ABS and sterilized with ethylene oxide.
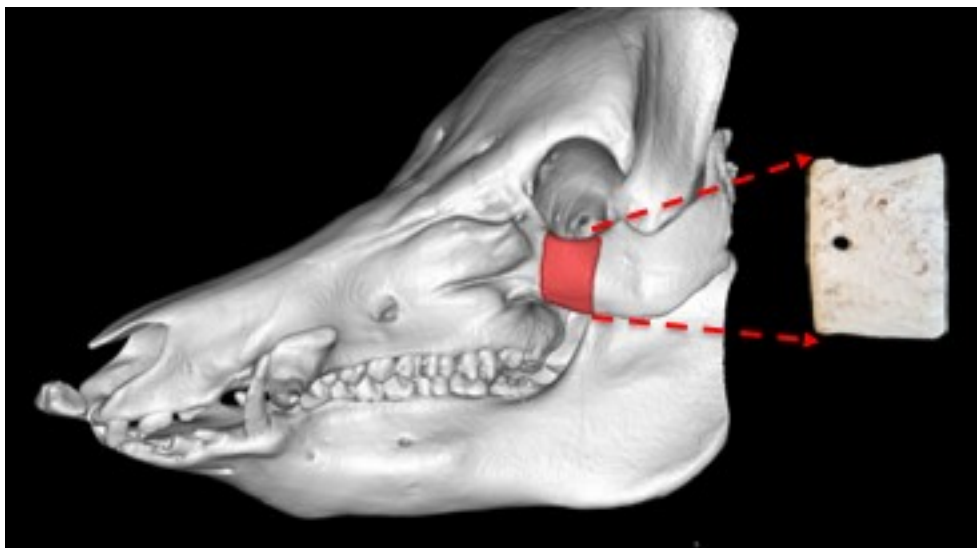
Figure 10-3: Cutting Guide Design
The cutting guide design (red) is a 3mm thick shell over the anterior surface of the osteotomy. It is 3D-printed in ABS, with a hole on the nasal side of the guide to ensure correct orientation.

Design of the Implant

Implants were designed to exactly match the shape of the resected bone. The digital design of the osteotomy was used to create an implant that matches surface of the resected bone. The sinus cavity was removed from the design to create a uniform implant. Finally, fixation plates (1cm x 2cm x 2mm) were attached on the frontal surface of the implant to hold in place. The final design was exported to MATLAB slicing software (scafSLICR, chapter 8) to generate a final design that was 60% porous with 800µm pores throughout the body of the implant and 100% solid along the fixation arms (**Figure 10-4**).

Design Validation

To validate scaffold design, scaffolds were 3D-printed in ABS. The critical dimensions were measured and checked against the design value in mimics. The congruence of the print shape to the design shape was also confirmed. Errors in the dimensions and congruence were corrected by editing the MATLAB code which imported the designs from Mimics to the scafSLICR program.

Mechanics of the tab attachment is depended on the number and location of 3d-printed fibers connecting the fixation tab to the porous region of the scaffold. This attachment was testing by hand: scaffold tabs were twisted with egg-cracking force. Additionally, the ABS scaffolds were placed in a bending rig and loaded with a 200g weight. Scaffolds that bent under handheld twisting or the rig were redesigned to improve the fixation tab connection (**Figure 10-5**).
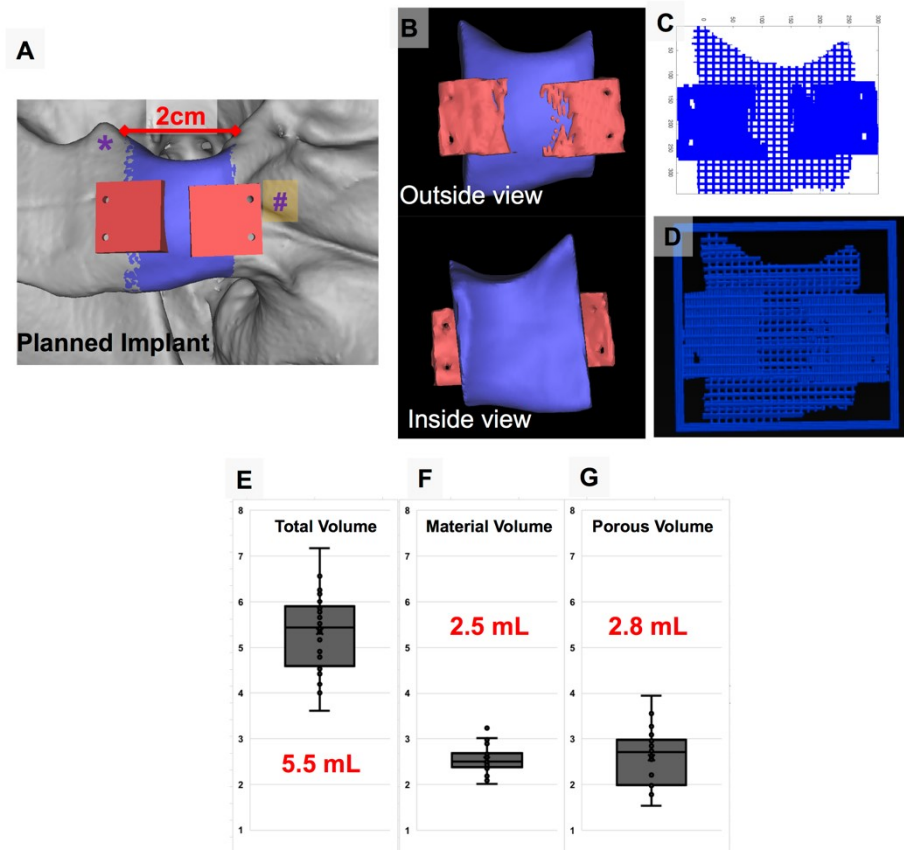
Figure 10-4: Zygomatic Implant Design Process.

(A) The pre-operative CT was used as a base. A 2cm region (blue) between the notch (purple asterisk) and the curve of the maxilla (purple #) was used as the body of the implant, and fixation tabs were placed to hold the implant in the predicted osteotomy. (B) The resulting design had curving prominences on the front and back of the implant. It is exported to MATLAB. The blue region will become porous and the fixation tabs (red) will be solid. (C) The porous and solid regions are exactly designed in scafSLICR. (D) The design is transformed into matching GCODE instructions for the 3D-printer. Over 18 animals, the scaffold volumes (E), material volumes (F), and porous volumes (G) varied from animal to animal and from defect to defect.
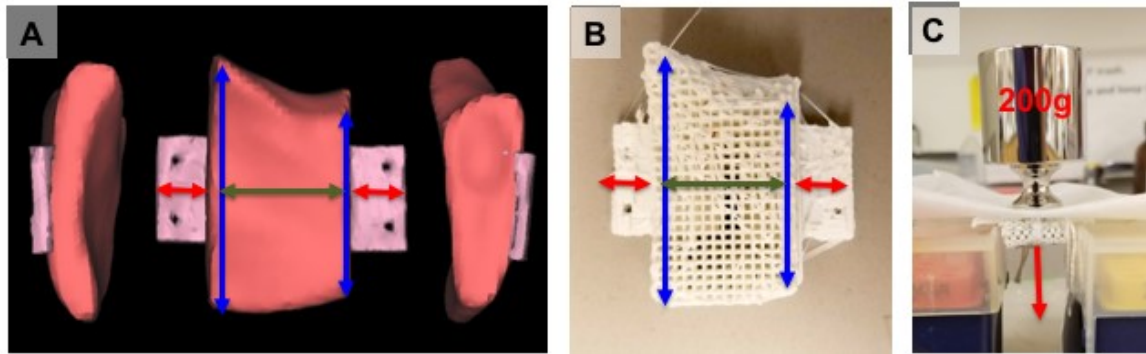
Figure 10-5 Zygomatic Scaffold Design Validation
(A) The design of the implant with important characteristic dimensions labelled. (B) The prototype of the design 3D-printed in ABS to confirm the dimensions and orientation of manufacturing the design. (C) Rig to test the rigidity of the design, especially of the connection between the fixation tabs and the porous region.

Manufacture of Bioactive Implant

Scaffolds were manufactured of clinical-grade materials. Purac PC12 (Corbion, Netherlands) was used for polycaprolactone. Bio-Oss granules (Geistleich, Australia) were used for decellularized bone. Materials were handled in a sterile manner whenever possible, however portions of the manufacturing process were completed on an open-air benchtop. Therefore, the scaffolds were extensively washed and sterilized before implantation.

The Bio-Oss was cryo-milled as described in chapter 4. Then the Bio-Oss particles and Purac were cryo-milled at a 30:70 weight-weight ratio. This second cryo-milling process generated a well-mixed particulate of both ingredients. This particulate mixture was fed into a laboratory mixing extruder (Dynisco, Germany) to melt the mixture and prepare it as 2.8mm diameter filament to use in 3D-printing (**Figure 10-6**).

The filament was loaded into a Lulzbot Taz5 3D-printer (Aleph Objects, Ohio), at 40mm/min, with a 500µm diameter brass nozzle, heated to 110°C, onto a glass bed heated to 40°C and covered with double-sided tape. Porous designs and corresponding GCODE files were prepared in scafSLICR (chapter 8). Final scaffolds had an average mass of 3g.

To enable cell attachment, scaffolds were washed in 3M NaOH, and then washed with PBS 3x 20min. Scaffolds were then extensively washed in an ethanol ladder and then sterilized with ethylene oxide gas treatment.

Manufacturing Validation

Manufactured scaffolds were imaged with a stereoscope to validate critical dimensions and print quality. Width, height, and depth measurements with calipers

and the stereoscope confirmed that the scaffolds were manufactured to specification and within a tolerance of 200µm (**Figure 10-7**).

Scaffolds were also scanned using cone beam computed tomography (Carestream C-arm, 65 kiloVolt peaks, 0.1mm resolution). Mimics was used to measure the connectivity of the porous network, the average pore size, the pore volume, the material volume, the surface-to-volume ratio, and the range and average density of the scaffold. The scans were also imported into MATLAB, where they were divided into 4mmx4mmx8mm sub-volumes. The density, porosity, and print quality were assessed across the sub-volumes (**Figure 10-8, 10-9, 10-10)**.
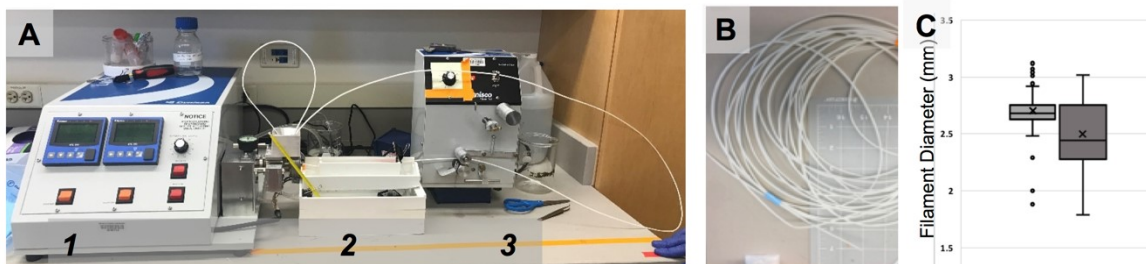
Figure 10-6: Filament Manufacturing Process
(A) A filament extruder mixes and extrudes the PCL-DCB powder as a 3mm filament (1), which is then passed through a chilled water bath (2), and collected using a filament winder (3). (B) This process results in long filaments 1-3m in length. (C) Measurements of the diameter of two filaments at multiple points along the filament.
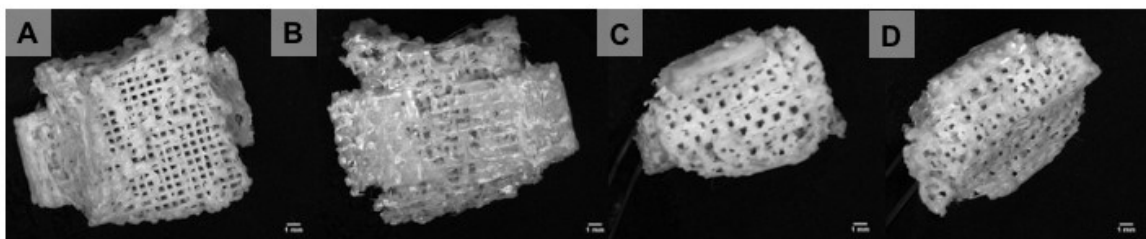
Figure 10-7: Stereoscope Images of 3D-Printed PCL-DCB Implants.
(A) Interior side of implant, final print layer. (B) Exterior side of implant, where the support material was removed. (C) Maxillary and (D) zygomatic facing faces of the scaffold.
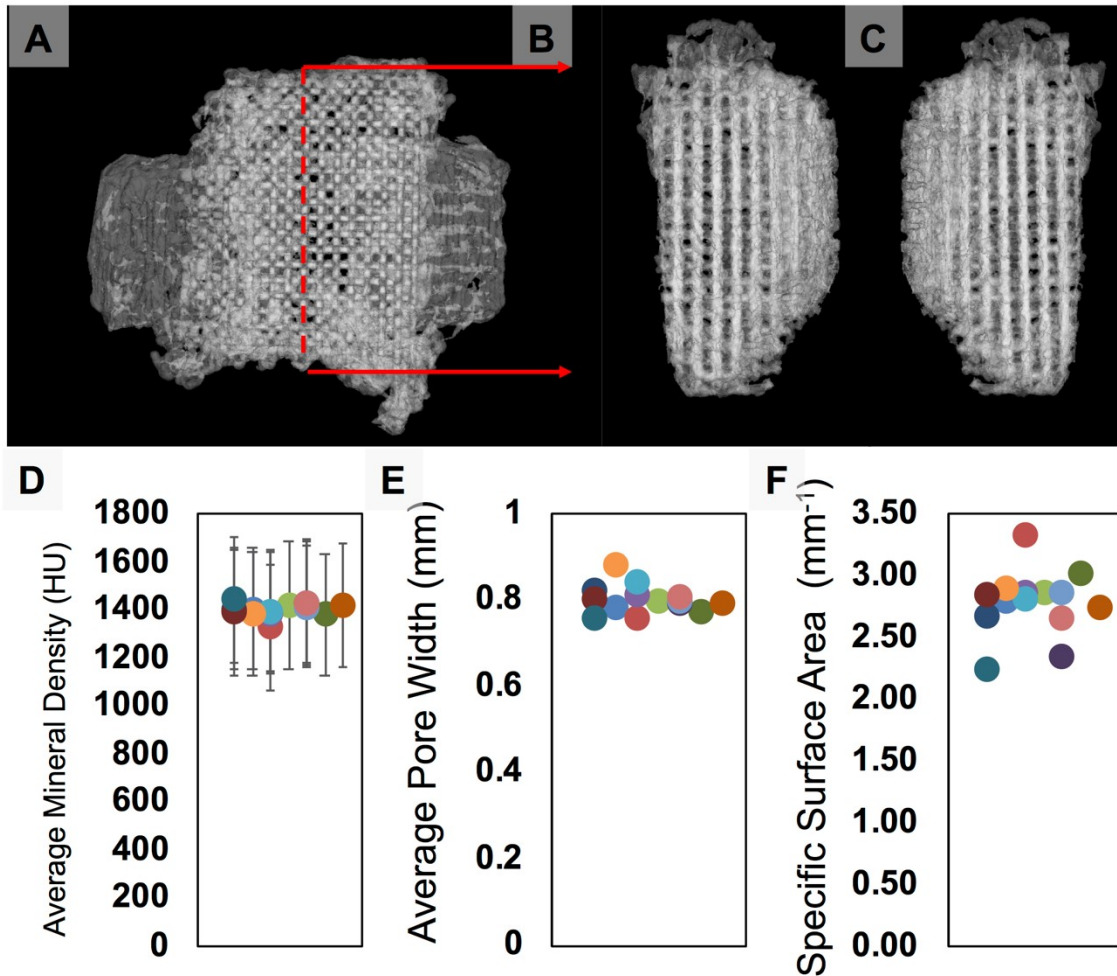
Figure 10-8: Cone Beam CT Scans of the 3D-printed implants.
(A) Semi-transparent rendering of the scan shows the porous, regular interior of the scaffold. (B & C) Interior view cutaways of the scaffold. (D) Average mineral density of the scaffolds (with standard deviation). (E) Average pore diameters of the scaffold. (F) Specific surface area of the scaffolds (SSA = surface area / volume)
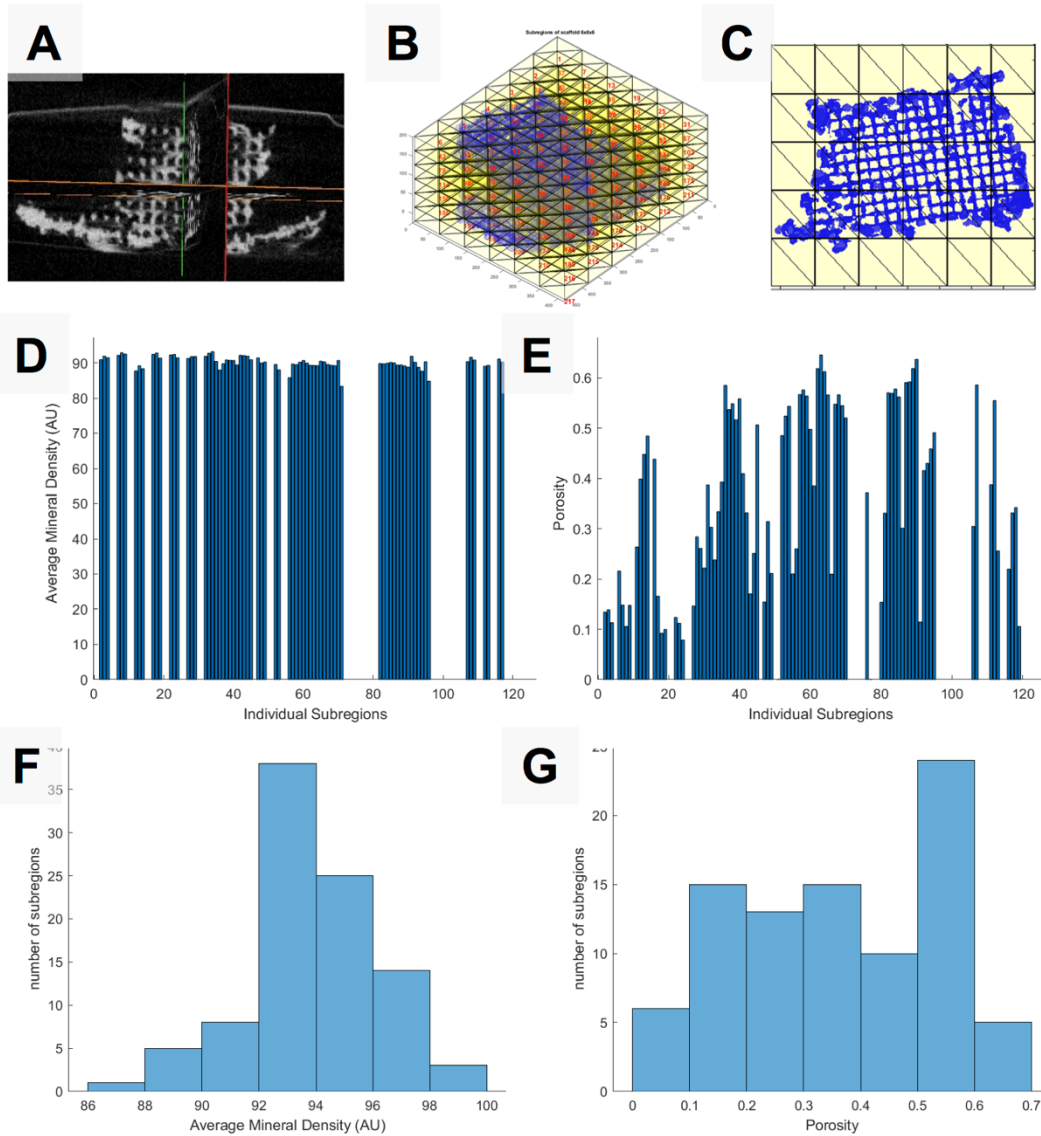
Figure 10-9 MATLAB validation of manufacturing
(A) CT scan of an implant. (B&C) the imported scan is divided into sub-volumes (4mmx4mmx6mm, 120/scaffold). (D) Average mineral density of each individual sub-volume. (E) Effective porosity of each subregion. Some sub-volumes contain no portion of the scaffold. (F) Histogram of the average density of the sub-volumes. (G) Histogram of the effective porosity of the sub-volumes.
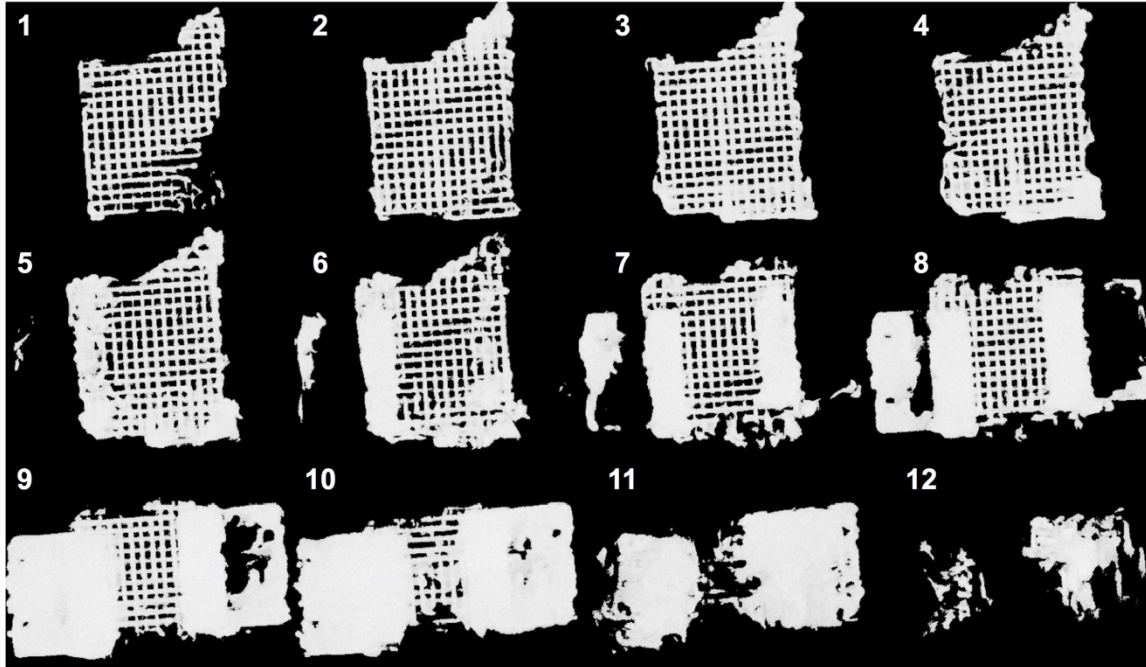
Figure 10-10 Pore layer validation of print quality.
The scan of the scaffold divided into 800µm thick planar sections parallel with the print bed plane. This shows porous regions that have the expected regular cross-hatch pattern and the solid regions that are slightly curved to fit flush against the curving surface of the maxilla and zygoma.

Animal Study

In conducting research using animals, the investigator(s) adhered to the laws of the United States and regulations of the Department of Agriculture. The animal implantation study was conducted at the Louisiana State University under an approved Institutional Animal Care and Use Committee protocol (#18-037). A total of 10 skeletally-mature Yucatán minipigs (Sinclair Bio-Resources, Auxvasse, Missouri) were divided into three groups: (1) control (n=2) (2) treatment (n=6) and (3) bone graft (n = 2). Each pig was operated bilaterally to maximize the use of each animal. Pigs were 1-year old castrated males.

The cell harvest and scaffold implantation procedure occurred after 12-hours of food withdrawal. Intramuscular administration of ketamine (10mg/kg;

Vedco Inc.) midazolam (0.2 mg/kg; Hospira Inc.) and dexmedetomindine (2 µg/kg; Pfizer Animal Health) were used to sedate the animal. Anesthesia was induced 15 min later with 5% isoflurane in 100% oxygen flow (1.5L/min) via facial mask. The animals were intubated with a cuffed Murphy's endotracheal tube and anesthesia was maintained at 1.5% in a circular breathing system. Pigs were prepped and draped in standard sterile fashion (**Figure 10-11**).

Following euthanasia, the animals were immediately decapitated, and the samples were shipped from Louisiana State University to Johns Hopkins University on ice. The skin covering the implant was reflected, and the zygomatic arch was cut at the anterior and posterior ends. Samples were fixed in agitated 10% formalin for one week at 4°C, where the solution was replaced daily. Thereafter, the samples were stored at 4°C and a PBS solution containing 1% sodium azide.

Autologous Porcine SVF Isolation

Subcutaneous fat (about 20g) was harvested from the dorsal lumbar region of each animal at the same time as the zygomatic defect procedure. Briefly, a 6cm skin incision was made approximately 3cm lateral from to dorsal midline at the level of L3-L6. The subcutaneous fat was sharply dissected and excised. A two-layer closure followed: subcutaneous tissue (2-0 or 3-0 absorbable suture in a running or simple interrupted pattern) followed by skin (3-0 absorbable suture, intradermal pattern).

The fat tissue was sterilely transferred to a cell culture biosafety cabinet, washed 3x in PBS. Any attached muscle tissue was carefully removed. The tissue was then minced with sharp scissors into 2-3mm chunks.

Minced tissue was mixed 1:1 by volume with a solution of collagenase type 1 at 4mg/mL and then incubated for 30min at 37°C and 200rpm. Then the solution was centrifuged twice at 300g for 5min at 25-37°C (warmed to prevent oil solidification). The supernatant was removed, and the pellet was resuspended in RBC lysis solution.

To remove any remaining tissue chunks, the resuspended solution was filtered through a 500-micron stainless steel mesh (Utah Biodiesel Supply), and then a 100μm nylon cell filter. The filtered solution was spun down at 300g for 5min and the resulting cell pellet was termed 'SVF'.

Isolated stromal vascular fraction cells were suspended in clinical grade fibrinogen-thrombin hydrogel (TISSEEL fibrin sealant, 2mL Duplojet frozen syringe, Bayer) at 5e6 cells / mL. The components of the TISEEL kit were each thawed and then diluted 1:5 with sterile saline before use. The thrombin and cells + fibrinogen components were prepared in a dual syringe with the Duplojet mixer needle at total volumes of 5mL per defect.

Osteotomy Creation, Scaffold Implantation, and Cell Injection

Concurrently with the cell isolation, bilateral osteotomies were created in both zygomatic arches. A transcutaneous approach was used *via* a 6cm incision along the prominent ridge of the zygomatic arch. The incision was made in the malar region through the dermis, sub-cutaneous tissue and periosteum to expose the zygomatic bone. Hemostasis was achieved with monopolar electrocautery. The attachments of the masseter muscle along the inferior edge were detached using a combination of blunt and sharp dissection, and electrocautery hemostasis. A sub-periosteal dissection was performed, exposing the body of the zygoma.

Thereafter, a laterally based zygomatic osteotomy was performed. The custom cutting guide was placed onto the exposed bone, and the surgeon adjusted it until it exactly matched the contour of the underlying bone. A cautery tool was then used to mark the edges of the cutting guide along the bone. The resulting 2.0cm osteotomy was performed with a reciprocating saw (27mm blade, Synthes) lateral to the infraorbital nerve and encompass the inferior lateral portion of the zygoma to minimize disruption of the origin of the masseter muscle. After the two sides were cut, the osteotomy bone was free moving. The surgeon elevated the bone and dissected the periosteum from the interior surface, and then fully excised the bone. The defect was washed with saline and filled with absorbent gauze until time of implantation.

3D-printed bone scaffold implants were placed in the defects. Minimal trimming of two of the twenty-four implants was required—the implants were excellent fits with the osteotomies. Placed implants were fixed into place using self-tapping screws through the fixation arms and adjacent bone. Four, 8mmx2mm screws (Synthes) were used to fixate the implants. Implants were rigidly fixed in place and firm under palpation.

The TISEEL dual syringe was used to inject the cells into implant directly after it was fixed into the osteotomy. The surgeon inserted the needle into the porous surface of the implant and filled the implant and surrounding space with the cell-laden gel. Implants were 3mL porous, so there was excess gel and cells surrounding the osteotomy. Gelation was complete in 30 seconds, and the incisions were closed.

Incision Line   Cutting Guide   Excised Bone   Suture and Bandage
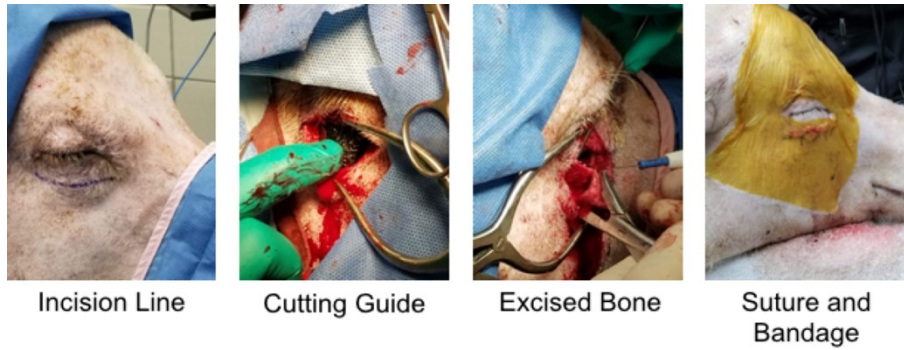
Figure 10-11: Pictures of the surgical process.
The incision was along the prominent ridge of the zygomatic arch. After incision and periosteal dissection, the cutting guide was placed on the bone and the edges were marked with a cautery tool. A reciprocating saw was used to cut the borders of the osteotomy, and the bone piece was excised. After the implant was securing in place, the incision was sutured and bandaged.

The defect was closed in a layer-wise fashion: the periosteal layer was closed with #0 PDS*II sutures, and the dermal layer was closed with BioSyn #2-0 sutures. Finally, surgical glue was applied to the surface of the incision. Animals completed a course of antibiotics post-surgery.

CT Assessment of Bone Formation

CT scans were conducted four weeks before surgery, immediately post-operatively, at six weeks, six months, and twelve months (GE lightSPeed16; 120 kiloVolt peaks, 625µm resolution). Scans were analyzed in MIMICs (Materialise, Belgium). The volume of interest was labelled in the post-operative scans as the implant region between the cuts and was maintained across timepoints. The range of mineral density and the average mineral density were recorded.

CBC and Blood Serum Panel

Blood was drawn at the CT timepoints and sent for a complete blood count and serum panel.

Results

Design, Manufacture, and Validation of 3D-Printed Implants

Each of the implants were unique to the animal and the side of the face they were designed to treat. The bone volume they were replacing ranged from 3.5mL – 5.3mL. They varied from 1.8cm – 3.2cm in height. The width and fixation hardware was kept consistent across all 36 implants. As a result of the anatomic variation, the volume of PCL-DCB material used in implants ranged from 2.11 to 2.94 mL, and the porous volume from 1.4 to 2.6 mL.

To validate the design and manufacturing process, prototype scaffolds for each defect were 3D-printed in ABS. These prototypes were used to identify problematic features the initial designs. Some of the interior contours of the designs were thin peak-like structures printed as globes. Based on the curvature of the zygomatic arch, the host-bone to implant edge sometimes had a sharp prominence which did not print well or easily broke off. Finally, in some implants the fixation tabs were placed too closely together and completely closed off the pores on the frontal surface of the implant. These defects were most clearly evident in the printed prototypes, and the corresponding designs were iterated to correct them (45% of designs were iterated).

The ABS prototypes were also used to validate the mechanical integrity of the fixation tab. The implant tabs were twisted away from each other with egg cracking force, and they were assessed for deformation in a bridge test with a 200g load. If deformation was observed in the body of the tab, the design was iterated so the tab was thicker. More common, the interface between the fixation tab and the porous region failed. This delamination was resolved by changing the design

to include extensions of the fixation tab several millimeters deeper into the porous region of the implant, which resulted in more struts connecting the porous portion to the solid fixation tab.

After the designs were validated, the scaffolds were printed in clinical grade materials and scanned with cone beam CT to assess the 3D-structure and mineral distribution throughout the material. The PCL-DCB scaffolds all had consistent average mineral densities: each scaffold had an average Hounsfield unit of ~1250, and standard deviation of 250. Across all the scaffolds the mean mineral density was 1404 HU, and there was, on average, a standard deviation of 258 HU within each scaffold. The scans were also used to confirm there were no areas of unusually high density that might indicate metal particles from the cryo-milling or manufacturing process, however that is limited to the resolution of the scanner (100μm).

The porous features of the scaffolds were validated in the CBCT scans. All scaffolds had a pore width of 0.800mm, which met design value (scaffold-to-scaffold standard deviation of 0.032). The porous networks were all fully interconnected—there were no porous areas that were isolated from the outside of the scaffold. Although not a design parameter, the specific surface area (mm^{-1}) of the scaffolds was measured: it ranged from 2.25 to 3.33, had a mean of 2.79, with scaffold-to-scaffold standard deviation 0.254.

In MATLAB, the scan of the implant was divided into sub-volumes of 4mmx4mmx6mm to validate mineral density across the different regions of the scaffold. The mineral density was extremely consistent across all of the sub-volumes, across all of the scaffolds. The effective porosity of each sub-volume was

also measured. The majority of the sub-volumes were at the intended porosity (60%), however a significant fraction of the sub-volumes was at lower porosities. These might be lower due to over deposition at the edge of the scaffold.

Finally, the scan was viewed as 800mm planar sections parallel to the print plant. This view enabled the inspection of each pore-layer. These views confirmed that the areas of low print quality were localized to the surface of the scaffold, and that the interior region was highly accurate.

Surgical Outcomes and Point-of-Care Cell Isolation

All animals recovered within two hours and were eating food normally within the same surgical day. Post-operation CT scans showed the implants were placed correctly in the defect and had contour lines which matched the zygomatic arch. Bone-scaffold volume within the osteotomy on the post op scan matched design values. Blood work six days post-operatively was normal. Additionally, blood work at 6-weeks and 3-months was also normative.

Cells were successfully isolated within the intraoperative timeframe (**Figure 10-12**). Osteotomy creation and implant placement averaged 35min, while cell isolation and transport time averaged 40min (**Figure 10-13**). The surgeries were ordered by animal weight from least to greatest, and the amount of fat obtained from the first pig was used for all future pigs in order to keep the number of cells placed into the defects consistent. The extra volume of gel and cell mixture was seeded into the scaffold to ensure filling of the complete pore space, and the surplus volume dispersed in the surrounding tissue pocket, to connect the implant with surrounding periosteum and soft tissue.
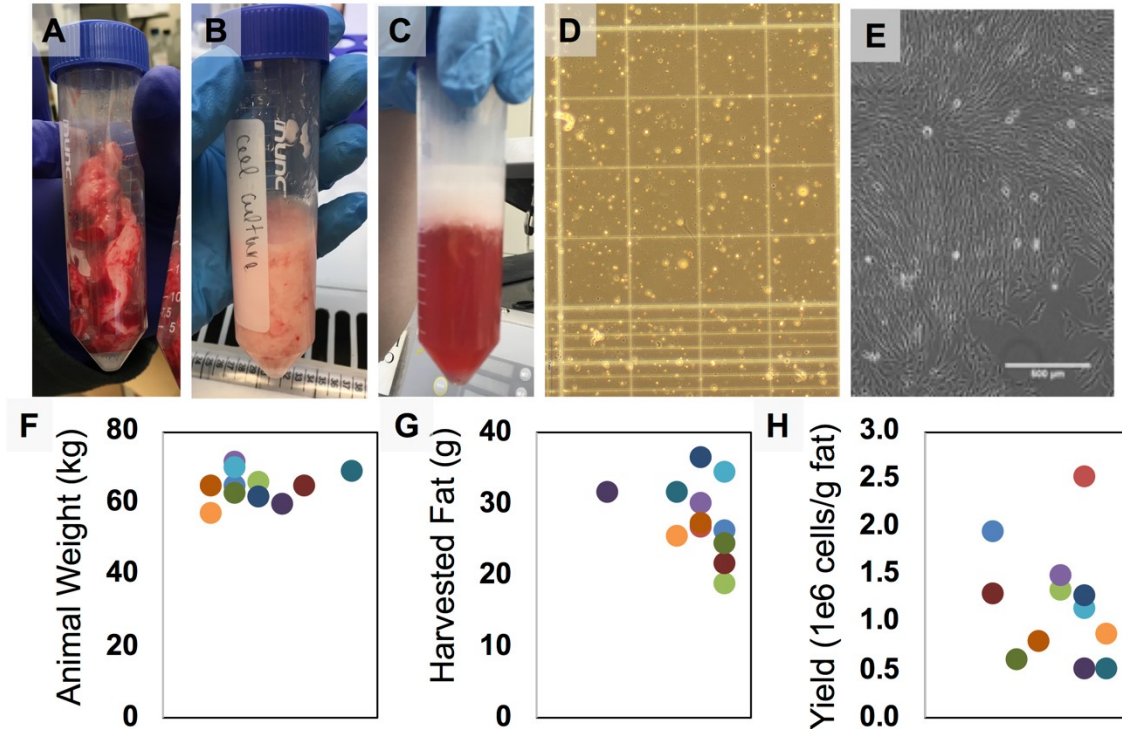
Figure 10-12: Isolation of SVF Cells from Swine.
A. Fat harvested from the lumbar region. B. Fat tissue was washed extensively. C. Tissue was minced, digested with collagenase, and stromal vascular fraction cells were separated from the fat tissue via centrifugation (supernatant = fat, infranatant = collagenase, pellet = cells). D. Cells appeared on the hemocytometer and were counted. E. A fraction of the cells were plated and were confluent at 8 days. F. The weight of the animals. G. The amount of fat harvested from each animal. H. The yield of each isolation process.
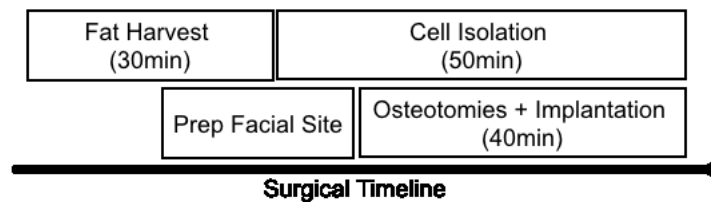
Figure 10-13 Surgical Timing for Acute Cell Isolation.

In three of the twenty-four implants, the screws along the anterior edge of the implant displaced from the underlying bone. This partial fixation failure is likely due to lack of screw purchase in the thin wall of the maxillary sinus at that fixation point. However, these implants remained rigid to palpation and did not displace

from the osteotomy. One implant fractured and became mobile just after three months. Because the implant was intact at a CT-time-point one week prior, we assume the implant was fractured during transport for the imaging or during recovery from anesthesia.

CT Analysis of Bone Regeneration

Empty defects were non-healing over the time period. There was rounding of the defect edges, and the opening of the maxillary sinus into the defect closed over (**Figure 10-14**). The width of the defect along the anterior surface shrunk 2mm over 6 weeks, from 21.9mm, to 19.9mm (**Table 10-1**).

Table 10-1. Defect width in Untreated Osteotomies

Defect #	Post Op	6-week	Change (mm)
1	23.67	22.24	-1.43
2	20.34	17.12	-3.22
3	21.54	21.35	-0.19
4	21.92	18.93	-2.99
Average	21.87	19.91	-1.96
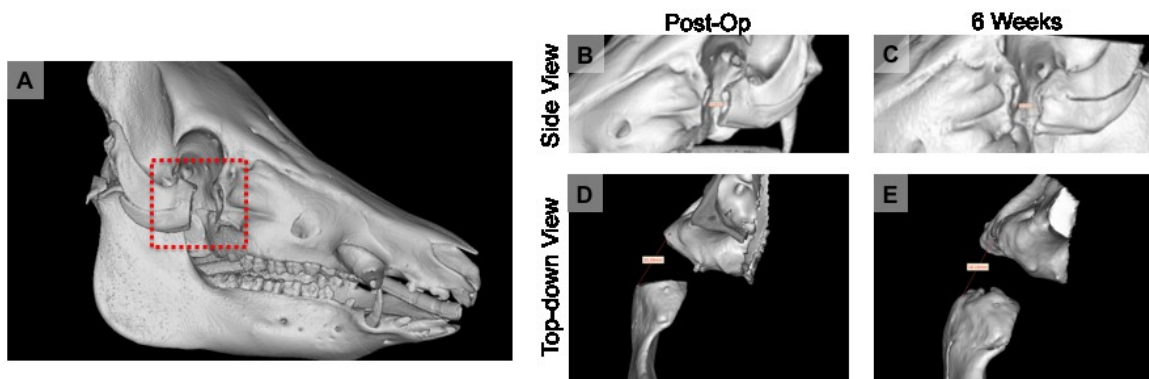
Figure 10-14: Post-operative CT scans.
A. Frontal view shows the successful placement and size of the osteotomy (red box). Frontal views (B & C) and superior views (D & E) show the 2cm gap along the frontal surface of the osteotomy.

In treated scaffold and cell groups, there was marked increase in bone volume and volume fraction over six weeks of healing (**Figure 10-15**). In post-operative scans, the implant was visible. The contours and shape of the implant matched up with the surrounding bone as designed. To quantify bone volume, a threshold of 240 HU was used to separate bone from soft tissue, and the volume of interest was identified using the screw locations. The bone volume in the volume of interest at post-op was entirely due to the radiopacity of the scaffold. At 6 weeks, the scaffold structure was visibly less porous than at post-op. The bone volume increased between 1 and 1.4mL over those 6 weeks. Because the porous space available in the implant is on average 2.2mL, this is a striking amount of bone formation.

In 3-month timepoints, the bone formation was greater. The average bone volume was 4.0 mL with a standard deviation of 1.3mL. The treatment resulted in had a majority of the defect volume being filled with bone: 75.0% ± 8.9%. This is an encouraging result that the implants continued to heal.
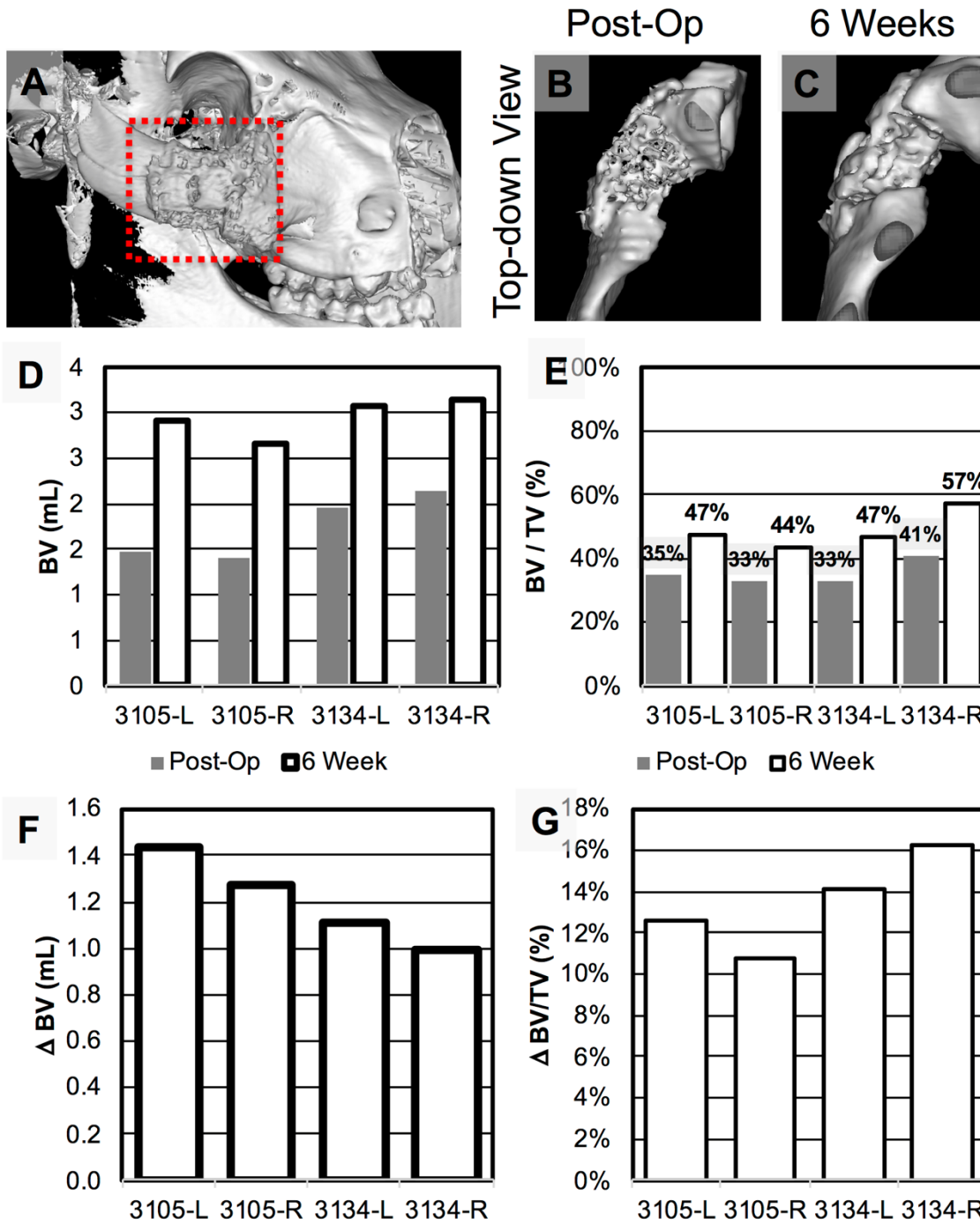
Figure 10-15 Bone Regeneration in Swine over Six Weeks.
A. Front view of the implant (red box). B. top-down view of implant at post op, C. and at 6-weeks. D. Bone volume within the volume of interest – Thresholded at 180 HU. E. Volume fraction of the volume of interest filled with bone. F. and G. are the changes in D. and E, respectively, from post-op to 6 weeks.

Discussion

We successfully manufactured our scaffolds in a design and manufacture validation framework. Further, we implemented the resulting scaffolds with point-of-care autologous cells, and demonstrate that the scaffold and cell treatment supports bone regeneration in a large animal pre-clinical model. Importantly, we can conclude that the scaffold and SVF system does not prevent or inhibit the formation of bone. Nor does the system cause adverse events. While this study is limited by the short, 6-week nature of the timepoints, ongoing timepoints and additional animals continue to investigate the nature and effect size of this bone formation.

The patient-specific design process introduces animal-to-animal variation in implant size and required the development of a process to rapidly validate the design. For financial and speed purposes, designs were prototyped in ABS (~$2 vs $2000, and 20 min vs 3 hour per print). This validation proved to be an important step, as half of the designs were iterated once to correct deficiencies. This process improved the objective quality of the implants.

Manufacturing validation was also implemented to confirm the critical quality attributes of the final product. In addition to the dimensional and mechanical validation during the design portion, the pore size, pore interconnectivity, and mineral distribution were assessed. These are critical features of the implant because they effect biologic outcomes: cells need pores of a certain size for seeding, nutrient transport, and tissue formation; the mineral must be present throughout the scaffold to act as a bone forming cue to the cells.

To the best of our knowledge, this study is the first test of the zygomatic full thickness defect in pig. The non-treated osteotomies in this study showed remodeling at the edges of the defect but did not heal, nor was there new bone formation on the scale seen in the treated group. While this study only looks at the early timepoint of 6-weeks, we feel that the defect will continue to be non-healing over the year-long course of this study.

In treated animals, the scaffolds recreated the shape of the excised bone and, post-surgery, healed without changing the contour of the cheekbone. This excellent result is due in part to the exact design on the implant to match the excised bone, as well as the surgical technique using the periosteal envelope to supplant the fixation screws in holding the implant in place.

To isolate SVF cells from pigs in an acute-use manner, we made alterations to the collagenase digestion by increasing the enzyme concentration and decreasing the reaction time. These alterations might be the cause of the variability in yield. Further, cells isolated with this process might be more traumatized and less viable that they otherwise might be. Flow cytometry to assess the viability, morphology, and markers of these cells is ongoing. Actual use of the SVF in humans would rely on an optimized, consistent protocol, likely using an automated device.

One important shortcoming of this work is that a defect of this size in human would clinically be treated by an iliac crest graft rather than an implant. The current clinical need in the field is larger defects for which a solid implant or a bone graft is untenable. Future work would consider a larger defect of the zygomatic arch in swine, on the order of 5cm or the entirety of the zygomatic arch.

Conclusion

This study made progress in translating the 3D-printed bone grafts to clinical use. It made advancements in the design and manufacture of implants of clinical scale and materials. The scaffolds manufactured with these advancements were implemented in a point-of-care approach in a large animal preclinical model using autologous SVF cells. As a result of the treatment, there was stark bone formation in the defects at 6 weeks and 3 months. These early results are promising, however long-term CT timepoints at 6 and 12 months will determine if the approach can fully regenerate the missing bone. Endpoint histology and high-resolution CT will inform the quality of the regenerated bone and the degree of its integration with the surrounding host bone. Overall, this study has made contributions to the design and manufacture validation of patient-specific 3D-printed implants, the acute-use of SVF for bone regeneration, and these two facets bring both this present technology and others closer to clinical use in humans.
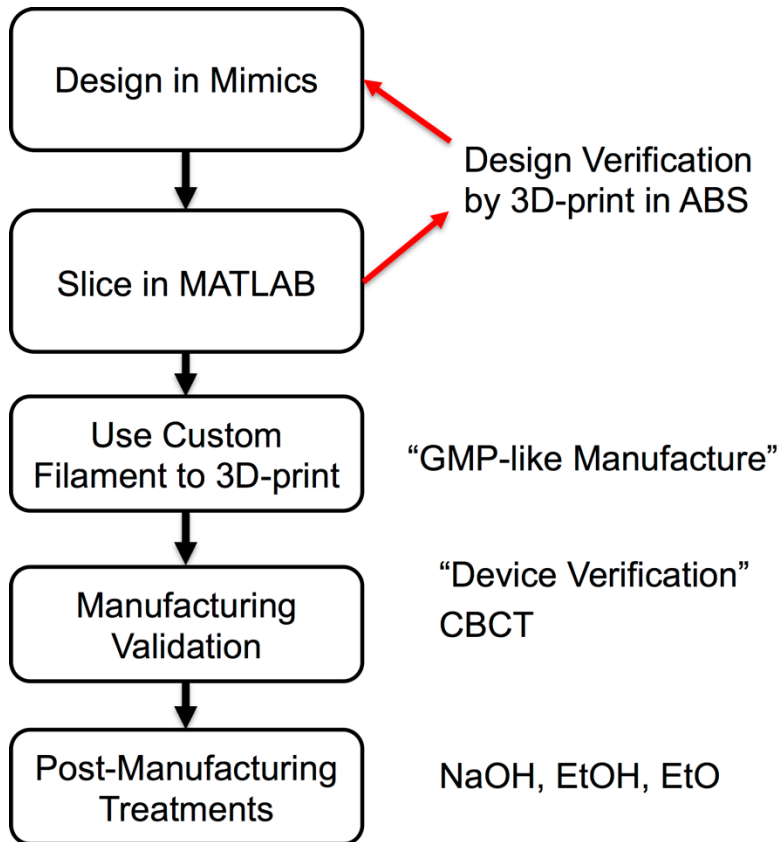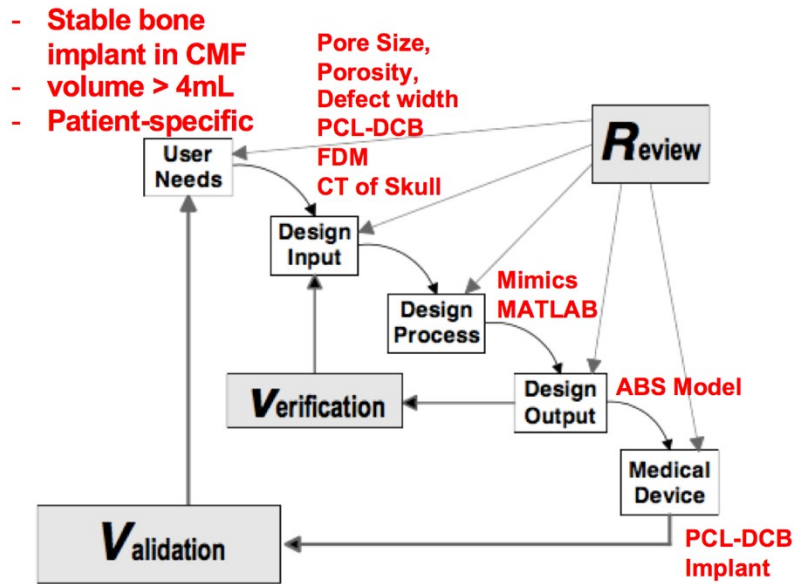
Figure 10-16 Validation and Verification Process for Zygomatic Implants.
Top: A design control waterfall chart with the relevant correlate steps from this study in red text.
Bottom: Step-by-step flow chart for the design and device verification process.
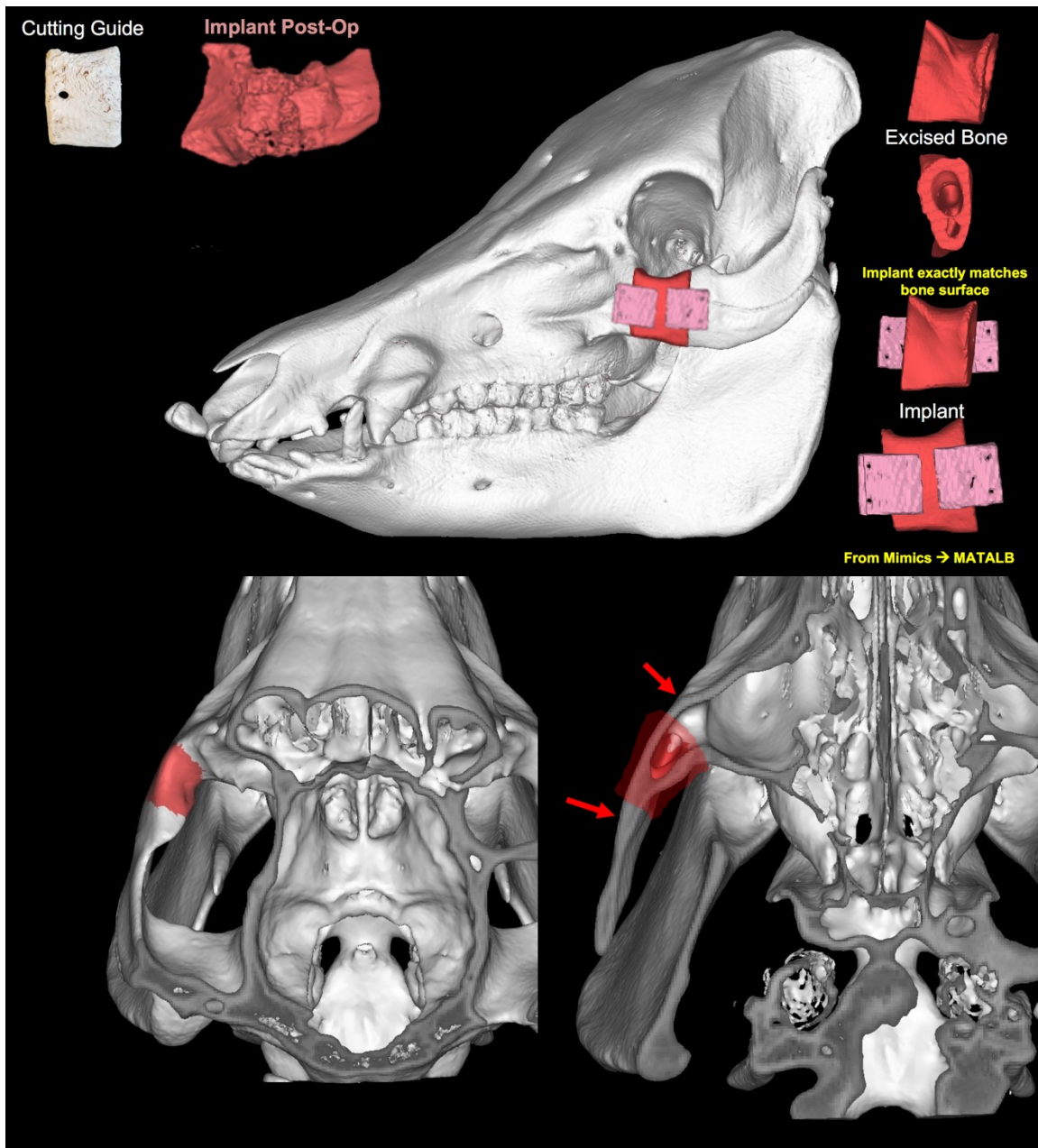
Figure 10-17 Swine Implant Design.
Top: the implant is designed to exactly match the excised bone from the zygomatic arch.
Bottom: complications of the osteotomy site come from the curvature at the maxillary portion of the arch. Additionally, the screw locations (red arrows) on the maxillary portion dwell directly into the maxillary sinus cavity, which could result in a weaker fixation unless long screws that reach the rear wall of the sinus are used.
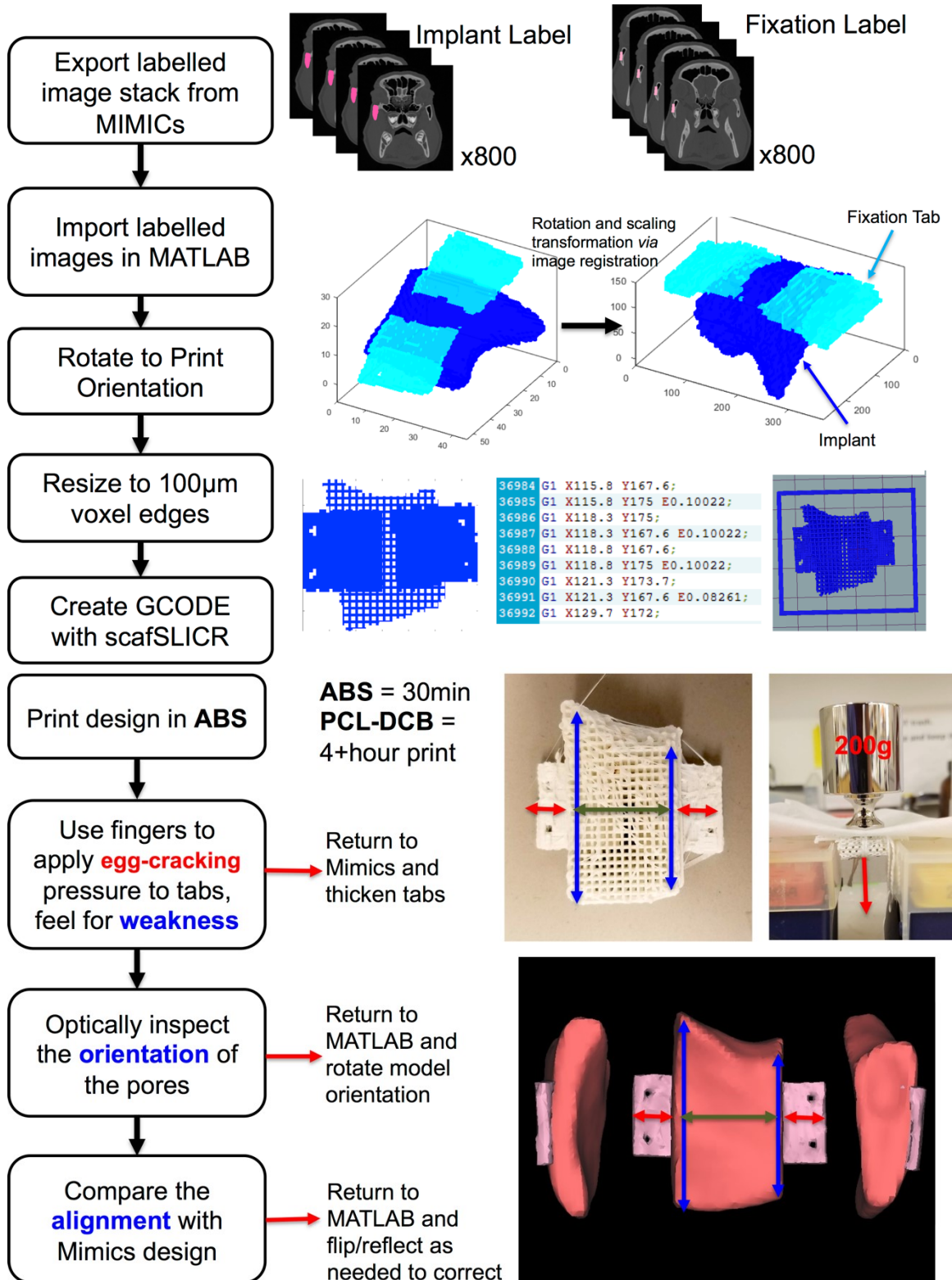
Figure 10-18 Flow Chart for 3D-Printing Design Validation Scaffolds.

Print design in PCL-DCB

Remove support material

Stereoscope images of every side

Open pores on all sides
Pores are 800μm
Contours are defined
Struts are good quality

PCL-DCB Scaffold

Optically inspect against white paper for **discoloration** → Re-print burned scaffold

2 / 25

Feel for **protruding** strands → Trim with sharp blade

Look for **over / under** extrusion

Mass the Scaffold → Double check input filament diameter, check k value, re-print

Support Material

Top   Bottom - Print Bed

Left Side   Right Side

Filament diameter QC

QbD by controlling the filament diameter more precisely we can control the over / under deposition problem.

Predicted Mass = Predicted Volume * Density of Material
Mass Error = (Measured Mass - Predicted Mass) / Predicted Mass

5% Mass Tolerance

Figure 10-19 Flow Chart for Device Verification of Implants.
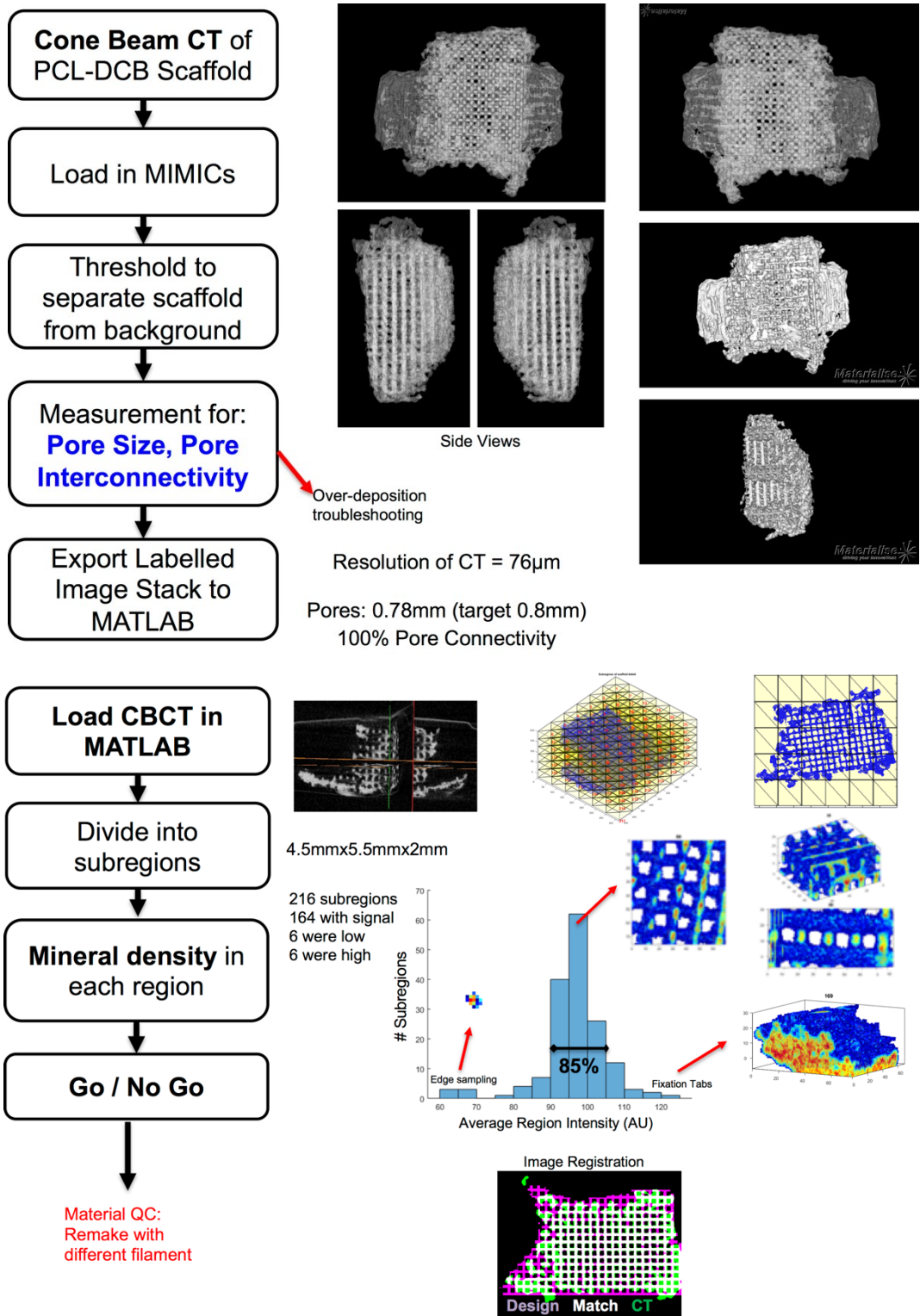
Figure 10-20 Flow Chart for Manufacturing Verification of Implants via CBCT. Mimics tools are used to assess the scaffold for pore size and porosity. Then the scan is imported into MATLAB, sub-divided into 216 smaller volumes, which were assessed for print consistency and critical quality attributes.

Conclusions and Contributions

The work in the thesis was centered on two main goals: (1) scale the 3D-printing system to human sizes and applications and (2) translate the scaffold with cells approach of boney regeneration to clinical grade components. In scaling the biomaterial manufacturing system, we were able to print shapes accurate features and dimensions of human face bones. Further, these prints were designed with porous networks that varied in 3D-space according to mechanical design goals.

The biomaterial system was transitioned to clinical grade components and testing models. All the of included materials (PCL, DCB, and TISEEL) are of human clinical grade. While we demonstrated the ability to isolate SVF from multiple donors with sufficient volumes and mineralizing ability, the cells were not isolated or prepared using clinical grade reagents and handling. There currently exists no FDA approved device or kit for isolation SVF that could be applied, however both GID and tissueGenesis are working towards FDA approval. Finally, the testing of the approach was scaled from small to large preclinical animal models demonstrated effective bone regeneration at both scales.

The cells were extensively assessed for their vascular potential, as the rapid vascularization of the implant is key to preventing cell death (thereby enabling regeneration) and the enduring vascularization of the implant is critical to providing an enduring resistance to infection. While we found that ASCs can assemble into robust vascular networks, the assembly was inhibited by the hypoxic nature of an

implant environment. In murine animal trials, the small scaffolds were more robustly vascularized by SVF cells (likely due to the greater presence of ECs in SVF). Nevertheless, there is ongoing research to provide oxygen to the scaffold environment to enable vascular assembly from the cells.

Barriers to Clinical Translation

While the tools and data herein bring the approach closer to treating humans, there remain barriers to the translation and adoption of the technology. First, there are regulatory barriers—the approach uses combination of regulated medical products. The scaffold is an implanted orthopedic device (with significant safety concerns when it comes in contact with the brain cavity). The DCB particles, fibrin hydrogel, and cells are drugs or biologics. Such a combination product is complex and regulated in multiple dimensions. Second, an approved product would need to find systemic approval from Medicare/Medicaid and other insurance agencies in order for it to be widely used and reimbursed.

Third, the product would need to compete with other well-established products. DePuy Synthes, Stryker, and Medtronic have patient specific implants on the market. Successful marketing would depend on demonstrating cost and efficacy improvements relative to other treatment options. Fourth, there might be barriers to licensing necessary technologies and products to prepare this product—while the patents on 3D-printed machines have expired, freedom to operate may be limited by the materials, processing, or methods.

Fifth and finally, there are challenges to implementing the desired manufacturing and clinical delivery in a financially profitable manner. Point-of-care manufacturing seems infeasible, the workflow would require a CT, design with a

surgeon and design engineer, manufacturing a test and actual product, design and manufacturing validation, and shipping to the point-of-care.

Broad Contributions to Regenerative Medicine and 3D-Printing

Regardless of the barriers to the specific product envisioned throughout the dissertation, this work has made several contributions to the field that are broadly applicable and independently enable tissue engineering of craniofacial bones. Towards effecting boney regeneration, we identified SVF as an enabling agent of bone formation in mice, where implants with SVF cells in them demonstrated near 100% regeneration of the defect bone volume. The promising regenerative outcomes of early time-points in swine is one of the few cases of SVF forming frank and observable amounts of bone.

The comparison of different—clinically used—mineral dopants in 3D-printed scaffolds is one of the few head-to-head comparisons of these dopants and provides broadly relevant information about the relative bioactivity caused by these dopants.

The different tools used to design and manufacture these scaffolds—scafSLICR, the design optimization algorithm, and the process for design and manufacturing validation—are readily applicable to other material systems and manufacturing systems.

Future Perspectives

Throughout this work, we repeatedly asked the guiding question: "Is the current state of the technology enough to start treating humans? If not, what else does it need?" Much of the work in chapters 8, 9, and 10 were singularly focused on pushing the technology towards a first in human study. While there are specific

tasks to complete before bringing this specific technology to human cases, there are also a number of other interesting directions the research could encompass in the future.

Model Dynamic Physical and Biologic Properties

The output porous designs from scafSLICR were provoking because they provided an exactly defined digital model of 3D-printed implants. This model could be used to model different regenerative properties, such as diffusion of nutrients and waste products, cell seeding and growth, blood vessel assembly and ingrowth, and tissue formation. These properties could be modelled before manufacturing or implantation, enabling the iteration of the design process at lower costs and time burden. A good example of these types of modelling can be found in the doctoral dissertation of Carlier—albeit at mouse scales. Combing those models with the scales considered in this dissertation could increase understanding of why implant failure rates have remained high.

Similar to modelling those biologic regenerative properties, the mechanical and material properties of the 3D-printed implants could be better modelled. An accurate model of the mechanics of the thin thermoplastic fibers combined with the porous design of the scaffold could be used to better predict the function of the scaffold in tension and shear, and thereby lead to improvements in the design of the fixation used in these implants. Additionally, these mechanics could be forecast as by modelling the degradation of the model. Pairing models of degradation, mechanics, and regeneration could provide a design basis for pediatric implants.

Finally, these accurate models could provide improvements and justifications to the design process. The pore and porosity designs used throughout

this work are based on the literature surrounding porous implants, but that literature has not reached the scale or number of microarchitectures enabled in this work. Such studies in animals are prohibitive but well-suited to modelling.

Increase Scaffold Functionality

Changes to the scaffold functionality could also improve the regenerative outcomes and reduce the need for cell implantation. PCL is a well-defined biomaterial that has potential to enable more complicated drug delivery than the simple presentation of DCB particles. PCL could also be loaded with a long-lasting antibiotic to prevent infections over the life of the implant. There are stem cell activating pharmaceutical agents which could be included in the scaffold to increase stem cell circulation, homing, and function. Finally, scaffold could serve as tool to effect immune modulation, perhaps by releasing a cytokine profile to modulate T-cell and macrophage functions towards regeneration.

The DCB integration can also be re-considered to increase efficacy. DCB particles could be localized to the surface of the structs using condensation or mineralizing processes. On the surface of the scaffold, but in a fixed position, the particles would interact more with the cells than they would when they are mostly encased in PCL, as they are here. Alternatively, the scaffold surface could be purposefully degraded in advance of implantation to increase the presentation of the embedded particles—this type of process would need to be paired with careful strut design to prevent the premature mechanical weakening of the scaffold.

APPENDIX A: SCAFSLICR EXAMPLES AND CODE

Files available by request: ethan.nyberg@gmail.com or wgrayson@jhmi.edu

Overview of scafSLICR

This program takes 3D-shapes as an input and applies patterns of pores and struts to different regions. It then generates the GCODE necessary to manufacture that structure.

Directory Set Up

The *scafSLICR.mlapp* file should be in the current MATLAB directory. The subdirectories *sub functions*, *Shapes*, *Properties*, *Output*, and *gcode* should also be in the current directory.
- ***sub functions*** contains the sub-functions and scripts needed.
- ***Shapes*** contains some example shapes and the shapes used in these examples
- ***Output*** is used to pass data from the slicing function back to the GUI, and where the final output gcode file is deposited.
- ***gcode*** contains the gcode header and footer files applied to the gcode.

Initialize the program with the **scafSLICR** command in command window, not by opening the mlapp files.
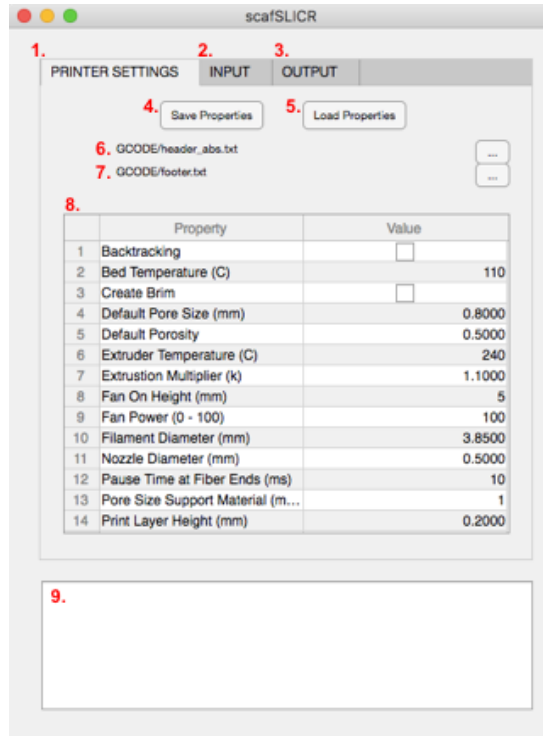
Program Tabs

1. **Printer Settings** This tab contains all the settings needed to alter the printer (hardware) and material-specific settings of the slicing algorithm.
2. **Input**. This tab contains the controls to input a shape and manipulate the porous properties throughout the shape.
3. **Output.** This tab contains toolpath previews of the sliced design.

Properties Buttons

4. **Save Properties.** This button saves the printer and material settings to a file to re-use.
5. **Load Properties.** This button loads previously saved printer settings.

GCODE Header / Footer. The GCODE header and footer files are identified. These can be edited directly in the text files using standard programs (TextEdit or Notepad). The **...** buttons can be used to select different text files to use as the header and footer.

6. **Header.** The GCODE header contains machine instructions to prepare the printer to manufacture the print. This text file is appended to the front of the shape-specific GCODE instructions.
7. **Footer.** Similar to the header, these instructions are appended after the shape-specific print is completed and might move the extruder head out of the way, kick the bed out, and set the temperatures to cool off.

Printer Settings Table (8)

The Printer Property table contains the machine and material specific settings. See the table in the slicerFN section for explanation of each property.

266

Output Console (9)

The output console is in the lower panel of the program. Status updates and errors are displayed here. The text can be edited to include user notes. This console is for output only, and it does not take any inputs.
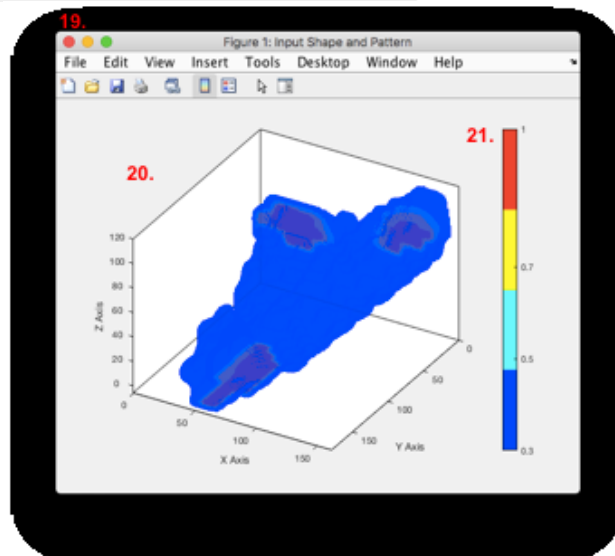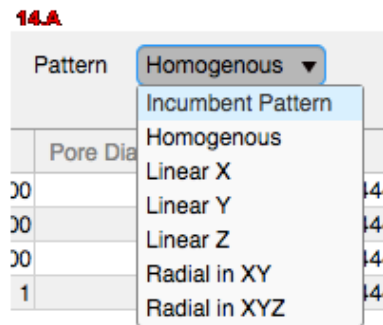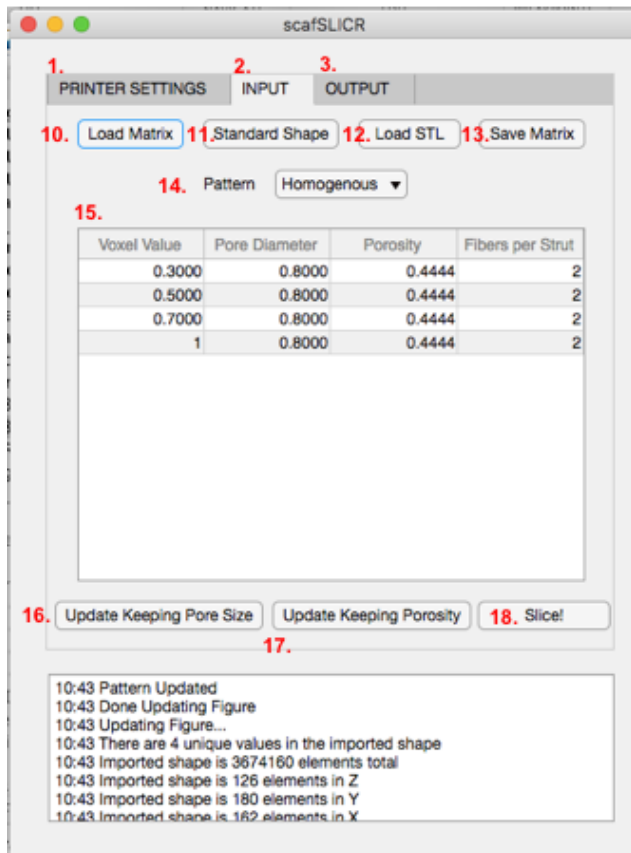
Load A Shape

10. **Load Matrix:** Import a matrix (*x* x *y* x *z*). The values of each element / voxel can be used to pattern a design value in the shape. The scale of a voxel in the imported model is set on the printer settings table.
11. **Standard Shape:** Click through the resulting dialog boxes to generate a cylinder or rectangular standard shape.
12. **Load STL**: Import an STL. This process may take a minute or two depending on the size of the STL. It is assumed that the STL is scaled in millimeters.

After the shape is loaded and patterned, it can be saved it as a matrix to re-use or manipulate further. Because loading matrices is faster than creating a standard shape or loading an STL, this format can speed up recurring designs. Matrices can be exported as to use in other modeling programs.

19. Input Shape Window. This window shows the loaded shape (20) where the different colors (Legend 21) correspond to the voxel values in the table (15).

Pattern Options (14A). Clicking a new pattern option from the dropdown menu will change the input shape and pore properties table to match that pattern. Some patterns require additional input via dialog boxes.

- **Incumbent Pattern**
- **Homogenous**
- **Linear X**
- **Linear Y**
- **Linear Z**
- **Radial in XY**
- **Radial in XYZ**

15. Porous Properties. This table displays the different regions of the shape (voxel values) and can be edited to assign different pore size and porosity to each region. This screenshot shows the same porous pattern applied to the different regions to result in a homogenous scaffold.

16. & 17. Update Buttons. Because there are only certain manufacturable combinations of struts and pores, the update buttons below the table will fit the input pore size / porosity to the nearest manufacturable set.

18. Slice. This button starts the slicing algorithm. Check all the inputs (printer settings, shape, and pore table) before clicking it.
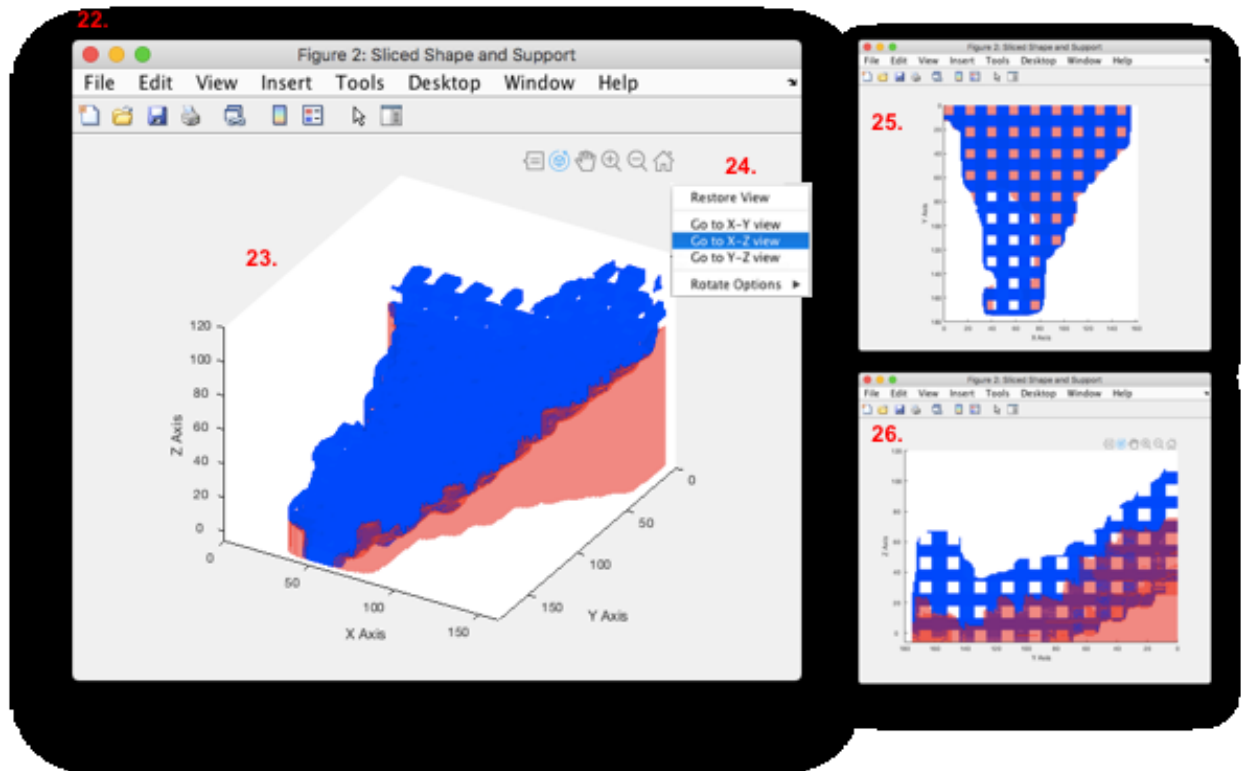
Sliced Shape and Support Window (22). This window displays the sliced shape and its support (23). Blue is the print structure and red is support structure. Right-click (24) gives the view options. X-Y view (25) and Y-Z view (26) both show the pores throughout the structure.

27. 2D Toolpath Previews. The tool paths are shown in the third tab. Each tool-path is a separate color. The different layers can be viewed by moving the scroll bar (28) through the different z-levels.

The generated GCODE is saved in the *output* folder as 'SlicedCode.gcode' (29), and it can be opened in a program such as Slicr or Repetier to ensure that the toolpaths are as desired in 3D.

Using SlicrFn as MATLAB Function Directly

The slicing function can be implemented programmatically in MATLAB instead of through the GUI.

<u>Syntax</u>

```
SlicrFn(V, VoxelSize, PoreDiameter, Porosity, Position)
SlicrFn(___, Name, Value)
[gcode, toolPaths, preview] = SlicrFn(___)
```

<u>Description</u>

V
A 3D-volume matrix describing the shape to be sliced. Each unique value in V corresponds to a pore/porosity design choice.

VoxelSize
The length of a voxel edge in mm. e.g. 0.100

PoreDiameter
A matrix corresponding to the ordered unique values of V, where each element is the pore size for that design choice. Provided in mm. e.g. [0.800 0.400 1.200]

Porosity
A matrix corresponding to the ordered unique values of V, where each element is the   porosity for that design choice. Provided in fractions. e.g. [0.90 0.45 0.23]

Position
[x_pos y_pos] The initial x and y position of the printed scaffold on the print bed. The program places the origin of the scaffold at this location.

Name, Value pairs provide additional inputs to the slicing program.

Table A-1 Additional SlicrFN Inputs

Name	Value	Description
Backtracking	Boolean	Option to backtrack along the last portion of the toolpath so that oozing and drawn strands do not close off the side pores. Default = true.
BedTemp	Celsius	The temperature of the bed during printing. Degrees Celsius. Default = 100
CreateBrim	Boolean	Option to create a brim around the perimeter of the object on the print bed. Default = true.
ExtruderTemp		the heat setting of the nozzle during printing. In degrees Celsius. default = 285. If multiple extruders, provide as [temp1 temp2].
ExtrusionMultiplier	0.8 – 1.5	increases the material flow rate to account for over / under deposition of material. A value of 1 would result in a perfect flow rate. Slight over deposition 1.05 is generally good. Default = 1.05
FanHeight	mm	z-height at which the fan turns on. Default = 1mm.
FanPower	0 – 100	Intensity of the fan, when it is turned on. Default = 100.
FilamentDiameter	mm	The diameter of the filament used. Default – 2.85mm. If using multiple extruders, provide as [diam1 diam2].
LayerHeight	mm	the z-change for each print layer. default = 0.200mm
NozzleDiameter	mm	the diameter of the primary printer nozzle, and determines the width of a strand. Struts can be integer multiples of the strand width (1, 2, 3 times the nozzle width.) default = 0.500mm. If multiple extruders provide as [diam1 diam2]
PauseTime	ms	Option to pause at the end of each toolpath to let it cool before starting the next move. Default = 50. If 0, no pause time.
PrintSpeed	mm/min	the speed of the nozzle. mm/min. default = 90.
SupportPoreDiam	mm	The spacing between the support struts. Default = 1mm.

Outputs:

By default, SlicerFn creates the outputs in the Output directory, and it saves three files:
- preview.mat: contains the 3D-matrix Tt and the 1D-matrix Zz. Tt(:,:,Zz(i)) is the toolpaths selected for the ith print layer. Preview with imshow(Tt(:,:,Zz(i))).
- Graphic_Matrix.mat: contains the 3D-matrices of the scaffold and support. Inspect with plot_3d
- glines.mat: contains a string array of the different lines of gcode, which is ready to be packaged into a text file with start up and shut down machine specific gcode.

If outputs are specified:

gcode   An array of the gcode commands. It does not include header / footer gcode, and should be compiled with those to create useful gcode files.

toolPaths   A structured output with two parts:
             .z_heights is an array where each element is one of the slices and indicates the z-height of that slice
             .ToolPaths is a 3D-matrix of the tool paths for each print layer. The nth member of
             .z_heights is height of ToolPaths.ToolPaths(:,:,n)

preview   A structured output with two parts:
                 .scaffold is the graphic preview of the sliced scaffold
                 .support is the graphical preview of the support structure

Example 1: Zygomatic Scaffold

```matlab
load('Shapes/zygoma.mat')
V = A;
VoxelSize = 0.100;
PoreDiameter = [ 0.3 0.5 0.7 1.0 ];
Porosity = [ 0.375  0.5 0.4118 0.500 ];
% Porosity and PoreDiameter must be the same length as the number of
% non-zero unique values in V, and are ordered respectively to the
% non-zero output of unique(V).
position = [15 15];

[glines, toolPaths, preview] = SlicrFn  (   V, ...
                                        VoxelSize, ...
                                        PoreDiameter, ...
                                        Porosity, ...
                                        position,...
                                        'Backtracking', false,...
                                        'BedTemp', 110,...
                                        'CreateBrim', true,...
                                        'ExtruderTemp', 285,...
                                    'ExtrusionMultiplier', 1.1,...
                                        'FanHeight', 1,...
                                        'FanPower', 95,...
                                     'FilamentDiameter', 2.85,...
                                        'LayerHeight', 0.200,...
                                        'NozzleDiameter', 0.500,...
                                        'PauseTime', 200,...
                                        'PrintSpeed', 600,...
                                        'SupportPoreDiam', 0.95...
                                        );

%% Graph the output preview
figure, p = plot_3d(preview.scaffold,0.1, 1);

%% Complete the GCODE as file
% Get GCODE Header and footer files
    fileID = fopen(fullfile('gcode','header_abs.txt'),'r');
    gstart = textscan(fileID,'%s','delimiter','\n');
    gstart = string(gstart{1});
    fclose(fileID);

    fileID = fopen(fullfile('gcode','footer.txt'),'r');
    gend = textscan(fileID,'%s','delimiter','\n');
    gend = string(gend{1});
    fclose(fileID);

% Read GCODE lines into output file
    fileID = fopen(fullfile('gcode','SlicedCode.gcode'),'w');
    formatSpec = '%s\n';
    fprintf(fileID,formatSpec,gstart);
    glines(glines == '')=[]; %remove empty dimensions
    fprintf(fileID,formatSpec,glines');
    fprintf(fileID,formatSpec,gend);
    fclose(fileID);
```

Example 2: Figure 3 Homogenous Scaffolds

```matlab
clearvars
addpath('sub functions')
load('Shapes/rectangular.mat')

%Get GCODE Header and footer files
    fileID = fopen(fullfile('gcode','header_abs.txt'),'r');
    gstart = textscan(fileID,'%s','delimiter','\n');
    gstart = string(gstart{1});    fclose(fileID);

    fileID = fopen(fullfile('gcode','footer.txt'),'r');
    gend = textscan(fileID,'%s','delimiter','\n');
    gend = string(gend{1});          fclose(fileID);

% Read GCODE lines into output file
    fileID = fopen(fullfile('Output','Figure3_Cubes.gcode'),'w');
    formatSpec = '%s\n';
    fprintf(fileID,formatSpec,gstart);

VoxelSize = 0.100;
PoreDiameter = [0.200 0.500 0.800 0.800 0.800] ;
Porosity = [0.280 0.250 0.280 0.450 0.620] ;
XPOS = 30; YPOS = 30;      position = [XPOS YPOS];

for i = 1:length(PoreDiameter)
[glines, toolPaths, preview] = SlicrFn  (    V, ...
                                        VoxelSize, ...
                                        PoreDiameter(i), ...
                                        Porosity(i), ...
                                        [XPOS YPOS],...
                                        'Backtracking', false,...
                                        'BedTemp', 110,...
                                        'CreateBrim', true,...
                                        'ExtruderTemp', 285,...
                                        'ExtrusionMultiplier',
1.1,...
                                        'FanHeight', 1,...
                                        'FanPower', 95,...
                                        'FilamentDiameter',
2.85,...
                                        'LayerHeight', 0.200,...
                                        'NozzleDiameter', 0.500,...
                                        'PauseTime', 200,...
                                        'PrintSpeed', 80,...
                                        'SupportPoreDiam', 0.95...
                                        );
 glines(glines == '')=[]; %remove empty dimensions
 fprintf(fileID,formatSpec,glines');  % Write to file
if XPOS > 230, XPOS = 30; YPOS = YPOS+40; else, XPOS = XPOS+40; end %if
end %for loop

%% Complete the GCODE as file
    fprintf(fileID,formatSpec,gend);
    fclose(fileID);
```

Example 3: Figure 4 Hybrid Scaffolds

```matlab
clearvars
addpath('sub functions')
    VV = ones(200,200);
    VV(1:100, :) = 2;                   VV = repmat(VV,1,1,100);
    V = zeros(202, 202, 102);           V(2:201, 2:201, 1:101) = VV;

%% Prepare the GCODE as file
    fileID = fopen(fullfile('gcode','header_abs.txt'),'r');
    gstart = textscan(fileID,'%s','delimiter','\n');
    gstart = string(gstart{1});    fclose(fileID);

    fileID = fopen(fullfile('gcode','footer.txt'),'r');
    gend = textscan(fileID,'%s','delimiter','\n');
    gend = string(gend{1});     fclose(fileID);

% Read GCODE lines into output file
    fileID = fopen(fullfile('Output','Figure4_Hybrid.gcode'),'w');
    formatSpec = '%s\n';
    fprintf(fileID,formatSpec,gstart);

VoxelSize = 0.100;
PoreDiameter = [0.200 0.500; 0.500 0.800; 0.200 0.800; 0.800 0.800;
0.800 0.800; 0.800 0.800] ;
Porosity = [0.280 0.250; 0.250 0.280; 0.280 0.280; 0.280 0.450; 0.450
0.620; 0.280 0.620];
XPOS = 30; YPOS = 30;       position = [XPOS YPOS];

for i = 1:length(PoreDiameter)
[glines, toolPaths, preview] = SlicrFn  (   V, ...
                                        VoxelSize, ...
                                        PoreDiameter(i, :)', ...
                                        Porosity(i, :), ...
                                        [XPOS YPOS],...
                                        'Backtracking', false,...
                                        'BedTemp', 110,...
                                        'CreateBrim', true,...
                                        'ExtruderTemp', 285,...
                                       'ExtrusionMultiplier',1.1,...
                                        'FanHeight', 1,...
                                        'FanPower', 95,...
                                       'FilamentDiameter', 2.85,...
                                        'LayerHeight', 0.200,...
                                        'NozzleDiameter', 0.500,...
                                        'PauseTime', 200,...
                                        'PrintSpeed', 80,...
                                        'SupportPoreDiam', 0.95...
                                        );
 glines(glines == '')=[]; %remove empty dimensions
 fprintf(fileID,formatSpec,glines');  % Write to file
if XPOS > 230, XPOS = 30; YPOS = YPOS+40; else, XPOS = XPOS+40; end %if
end %for loop

%% Complete the GCODE as file
    fprintf(fileID,formatSpec,gend);
    fclose(fileID);
```

Example 4: Figure 5 Gradients in Cubes

Choose the case to create the 3D pattern.

Graded along Z

```
VV = ones(200,200,200);
num = 10; width = 200/num; x1=0; x2=width;
        for i=1:num
            VV(:,:, x1+1:x2) = i;
            x1=x2; x2=x2+width;
        end
V=zeros(202,202,202);
V(2:201, 2:201,1:201) = VV;
```

Graded along X

```
VV = ones(200,200,200);
num = 10; width = 200/num; x1=0; x2=width;
    for i=1:num
        VV(:,x1+1:x2,:) = i;
        x1=x2; x2=x2+width;
    end
V=zeros(202,202,202);
V(2:201, 2:201,1:201) = VV;
```

Graded along XY

```
VV = ones(200,200);
num = 10; width = 200/num; x1=0; x2=200;
for i = 1:(num/2)
    VV(x1+1:x2,x1+1:x2) = i;
     x1=x1+width; x2=x2-width;
end
 VV = repmat(VV, [1, 1, 200]);
V=zeros(202,202,202);
V(2:201, 2:201,1:201) = VV;
```

Graded along XYZ

```
VV = ones(200,200, 200);
num = 10; width = 200/num; x1=0; x2=200;
for i = 1:(num/2)
    VV(x1+1:x2,x1+1:x2, x1+1:x2) = i;
     x1=x1+width; x2=x2-width;
end
V=zeros(202,202,202);
V(2:201, 2:201,1:201) = VV;
```

```matlab
addpath('sub functions')
VoxelSize = 0.200;
PoreDiameter = ([ 0.2 0.3 0.5 0.6 0.8 0.8 0.6 0.5 0.3 0.2]');
Porosity = ([0.28 0.26 0.5 0.56 0.62 0.62 0.56 0.5 0.26 0.28]);
position = [30 30];
[glines, toolPaths, preview] = SlicrFn  (   V, ...
                                            VoxelSize, ...
                                            PoreDiameter, ...
                                            Porosity, ...
                                            position,...
                                            'Backtracking', false,...
                                            'BedTemp', 110,...
                                            'CreateBrim', true,...
                                            'ExtruderTemp', 285,...
                                          'ExtrusionMultiplier', 1.1,...
                                            'FanHeight', 1,...
                                            'FanPower', 95,...
                                           'FilamentDiameter', 2.85,...
                                            'LayerHeight', 0.200,...
                                            'NozzleDiameter', 0.500,...
                                            'PauseTime', 200,...
                                            'PrintSpeed', 80,...
                                            'SupportPoreDiam', 0.95);
% Get GCODE Header and footer files
    fileID = fopen(fullfile('gcode','header_abs.txt'),'r');
    gstart = textscan(fileID,'%s','delimiter','\n');
    gstart = string(gstart{1});
    fclose(fileID);

    fileID = fopen(fullfile('gcode','footer.txt'),'r');
    gend = textscan(fileID,'%s','delimiter','\n');
    gend = string(gend{1});
    fclose(fileID);


% Read GCODE lines into output file
    fileID = fopen(fullfile('output','Figure5-subpart.gcode'),'w');
    formatSpec = '%s\n';
    fprintf(fileID,formatSpec,gstart);

    glines(glines == '')=[]; %remove empty dimensions
    fprintf(fileID,formatSpec,glines');

    fprintf(fileID,formatSpec,gend);
    fclose(fileID);
```

Example 5: Graded Zygoma

```matlab
clearvars
addpath('sub functions')

load('Shapes/zygoma-5regions.mat')
VoxelSize = 0.600;
PoreDiameter = ([ 0.2 0.3 0.5 0.7 0.9]');
Porosity = ([0.3 0.3 0.5 0.5 0.8]);
position = [30 30];

[glines, toolPaths, preview] = SlicrFn  (    V, ...
                                        VoxelSize, ...
                                        PoreDiameter, ...
                                        Porosity, ...
                                        position,...
                                        'Backtracking', false,...
                                        'BedTemp', 110,...
                                        'CreateBrim', true,...
                                        'ExtruderTemp', 285,...
                                      'ExtrusionMultiplier', 1.1,...
                                        'FanHeight', 1,...
                                        'FanPower', 95,...
                                       'FilamentDiameter', 2.85,...
                                        'LayerHeight', 0.200,...
                                        'NozzleDiameter', 0.500,...
                                        'PauseTime', 200,...
                                        'PrintSpeed', 80,...
                                        'SupportPoreDiam', 0.95...
                                        );

%% Complete the GCODE as file
% Get GCODE Header and footer files
    fileID = fopen(fullfile('gcode','header_abs.txt'),'r');
    gstart = textscan(fileID,'%s','delimiter','\n');
    gstart = string(gstart{1});
    fclose(fileID);

    fileID = fopen(fullfile('gcode','footer.txt'),'r');
    gend = textscan(fileID,'%s','delimiter','\n');
    gend = string(gend{1});
    fclose(fileID);

% Read GCODE lines into output file
    fileID = fopen(fullfile('output','SlicedCode-
PorcineZygoma.gcode'),'w');
    formatSpec = '%s\n';
    fprintf(fileID,formatSpec,gstart);
    glines(glines == '')=[];
    fprintf(fileID,formatSpec,glines');
    fprintf(fileID,formatSpec,gend);
    fclose(fileID);
```

Example 6: Orbital Bone

```matlab
clearvars
addpath('sub functions')
% Import STL
file = 'Shapes\MassiveOrbitalScaffold.stl';

% Get the dimensions of the STL in millimeters.
[stlcoords] = READ_stl(file);
xmax = max(max( squeeze( stlcoords(:,1,:) ) ));
ymax = max(max( squeeze( stlcoords(:,2,:) ) ));
zmax = max(max( squeeze( stlcoords(:,3,:) ) ));
xmin = min(min( squeeze( stlcoords(:,1,:) ) ));
ymin = min(min( squeeze( stlcoords(:,2,:) ) ));
zmin = min(min( squeeze( stlcoords(:,3,:) ) ));

% Convert to voxel matrix where one voxel is 1mm
V = double(VOXELISE(round((xmax-xmin)*1),...
    round((ymax-ymin)*1),...
    round((zmax-zmin)*1),...
    fullfile(path,file),...
    'xyz'));

%% Weighted Average
% V is the VOI, one voxel is 1mm
[a,b,c] = size(V);
d = size(V(:),1);
output = V*0;
for i=1:d
    if V(i)==0, continue, end
    [x,y,z] = ind2sub([a,b,c],i);
    top = x + 4; if top>a, top = a; end
    bottom = x - 4; if bottom<1, bottom = 1; end
    left = y - 4; if left<1, left = 1; end
    right = y + 4; if right>b, right = b; end
    in = z - 4; if in<1,  in =1; end
    out = z + 4; if out>c, out = c; end
V_small = V(bottom:top, left:right, in:out);
    output(i) = sum(sum(sum(V_small)));
end

figure, histogram(output(output>0));
figure, plot_3d(output, 10, .5)

%% Smooth the weighted average twice
avg_out = output*0;

for i=1:d
    if V(i)==0, continue, end
    [x,y,z] = ind2sub([a,b,c],i);
    top = x + 8; if top>a, top = a; end
    bottom = x - 8; if bottom<1, bottom = 1; end
    left = y - 8; if left<1, left = 1; end
    right = y + 8; if right>b, right = b; end
    in = z - 8; if in<1,  in =1; end
    out = z + 8; if out>c, out = c; end
V_small = output(bottom:top, left:right, in:out);
```

```matlab
V_small = V_small(:);
V_small(V_small==0)=[];
    avg_out(i) = round(mean(V_small(:)));
end

figure, histogram(avg_out(avg_out>0));
figure, plot_3d(avg_out, 10, .5)
avg_out1 = output*0;

for i=1:d
    if V(i)==0, continue, end
    [x,y,z] = ind2sub([a,b,c],i);
    top = x + 8; if top>a, top = a; end
    bottom = x - 8; if bottom<1, bottom = 1; end
    left = y - 8; if left<1, left = 1; end
    right = y + 8; if right>b, right = b; end
    in = z - 8; if in<1,  in =1; end
    out = z + 8; if out>c, out = c; end
V_small = avg_out(bottom:top, left:right, in:out);
V_small = V_small(:);
V_small(V_small==0)=[];
    avg_out1(i) = round(mean(V_small(:)));
end

figure, plot_3d(avg_out1, 10, .5)

%% Bin smoothed range into 4 levels
avg_sort = sort(avg_out(avg_out>0));
fifths = round(size(avg_sort, 1) / 5);

figure, histogram(avg_out1(avg_out1>0)); hold on
line([avg_sort(fifths), avg_sort(fifths)], ylim, 'LineWidth', 2, ...
'Color', 'r');
line([avg_sort(fifths*2), avg_sort(fifths*2)], ylim, 'LineWidth', 2, ...
'Color', 'r');
line([avg_sort(fifths*3), avg_sort(fifths*3)], ylim, 'LineWidth', 2, ...
'Color', 'r');
line([avg_sort(fifths*4), avg_sort(fifths*4)], ylim, 'LineWidth', 2, ...
'Color', 'r');

bin_out = avg_out;
bin_out(0 < avg_out & avg_out  < avg_sort(fifths)) = 1;
bin_out(avg_sort(fifths) <= avg_out & avg_out  < avg_sort(fifths*2)) = ...
2;
bin_out(avg_sort(fifths*2) <= avg_out & avg_out < avg_sort(fifths*3)) = ...
3;
bin_out(avg_sort(fifths*3) <= avg_out & avg_out  < avg_sort(fifths*4)) ...
= 4;
bin_out(avg_sort(fifths*4) <= avg_out & avg_out <= avg_sort(end)) = 5;

figure, histogram(bin_out(bin_out>0));
figure, plot_3d(bin_out, .5, .5)
```

Example 7: Hemi-Mandible

```matlab
clearvars
addpath('sub functions')

% Import STL
file = 'Shapes/HemiMandible_001.stl';

% Get the dimensions of the STL in millimeters.
[stlcoords] = READ_stl(file);
xmax = max(max( squeeze( stlcoords(:,1,:) ) ));
ymax = max(max( squeeze( stlcoords(:,2,:) ) ));
zmax = max(max( squeeze( stlcoords(:,3,:) ) ));
xmin = min(min( squeeze( stlcoords(:,1,:) ) ));
ymin = min(min( squeeze( stlcoords(:,2,:) ) ));
zmin = min(min( squeeze( stlcoords(:,3,:) ) ));

% Convert to voxel matrix where one voxel is 1mm
V = double(VOXELISE(round((xmax-xmin)*1),...
    round((ymax-ymin)*1),...
    round((zmax-zmin)*1),...
    fullfile(file),...
    'xyz'));

V = flipud(permute(V,[3 1 2]));

%% Rotate
h(1) = figure;
p1= plot_3d(V, 0.5, 0.5);
title('Input Shape')
xlabel('X')
ylabel('Y')
zlabel('Z')

%% Rotation about each axes
tx = 0;
ty = 0;
tz = 0;
tx = pi*1.1 + pi/5;
ty = pi/6 +pi/2; %about Z

Rx = [1 0 0 0; ...
    0 cos(tx) -sin(tx) 0; ...
    0 sin(tx) cos(tx) 0;...
    0 0 0 1];
Ry = [cos(ty) 0 sin(ty) 0; ...
    0 1 0 0;...
    -sin(ty) 0 cos(ty) 0;...
    0 0 0 1];
Rz = [cos(tz) -sin(tz) 0 0; ...
    sin(tz) cos(tz) 0 0;...
    0 0 1 0;...
    0 0 0 1];

% Complete Rotation Transformation
t = Rx * Ry *Rz ;
tform = affine3d(t);
```

```matlab
% Transform Image
V_rot = imwarp(V,tform, 'nearest');

% Crop V_rot
Ibw = V_rot~=0;
I_xy = sum(Ibw,3);
I_x = squeeze(sum(I_xy,1));
I_y = squeeze(sum(I_xy,2));
I_xz = squeeze(sum(Ibw, 2));
I_z = squeeze(sum(I_xz, 1));

x1 = find(I_x, 1, 'first');
x2 = find(I_x, 1, 'last');
y1 = find(I_y, 1, 'first');
y2 = find(I_y, 1, 'last');
z1 = find(I_z, 1, 'first');
z2 = find(I_z, 1, 'last');
V_rot = V_rot(y1:y2, x1:x2,z1:z2);

h(2) = figure;
p(2) = plot_3d(V_rot, 0.1, 0.5);
title('Out Shape')
xlabel('X')
ylabel('Y')
zlabel('Z')

% Depth-based Regions
% V_rot is the VOI, one voxel is 1mm
% Want to make shells from the outside --> inside
% that are 3mm in thickness
V = V_rot;
output = V*0;
V_shell = V>0;
finished = false;
i = 1; j = 1;
while ~finished
    shell = bwmorph3(V_shell, 'remove');
    if ~any(shell(:))
        finished=true;
    continue
    end
    output = output + double(shell*i);
    V_shell = V_shell-shell;
    j = j+1;
    if j>3
        i = i+1;
        j=1;
    end %if
end %while not finished
```

```matlab
%% Slice Scaffold
output(output>3)=3;
V = rot90(output);
VoxelSize = 1;
PoreDiameter = [ 0.8 0.4 0.1 ]';
Porosity = [ 0.6154 0.2857 0.0099 ];
% Porosity and PoreDiameter must be the same length as the number of
% non-zero unique values in V, and are ordered respectively to the
% non-zero output of unique(V).

position = [15 15];

[glines, toolPaths, preview] = SlicrFn  (   V, ...
                                            VoxelSize, ...
                                            PoreDiameter, ...
                                            Porosity, ...
                                            position,...
                                            'Backtracking', false,...
                                            'BedTemp', 110,...
                                            'CreateBrim', true,...
                                            'ExtruderTemp', 285,...
                                        'ExtrusionMultiplier', 1.1,...
                                            'FanHeight', 1,...
                                            'FanPower', 95,...
                                          'FilamentDiameter', 2.85,...
                                            'LayerHeight', 0.200,...
                                            'NozzleDiameter', 0.500,...
                                            'PauseTime', 200,...
                                            'PrintSpeed', 600,...
                                            'SupportPoreDiam', 0.95...
                                            );

% Complete the GCODE as file
% Get GCODE Header and footer files
    fileID = fopen(fullfile('gcode','header_abs.txt'),'r');
    gstart = textscan(fileID,'%s','delimiter','\n');
    gstart = string(gstart{1});
    fclose(fileID);

    fileID = fopen(fullfile('gcode','footer.txt'),'r');
    gend = textscan(fileID,'%s','delimiter','\n');
    gend = string(gend{1});
    fclose(fileID);

% Read GCODE lines into output file
    fileID = fopen(fullfile('gcode','SlicedCode.gcode'),'w');
    formatSpec = '%s\n';
    fprintf(fileID,formatSpec,gstart);
    glines(glines == '')=[]; %remove empty dimensions
    fprintf(fileID,formatSpec,glines');
    fprintf(fileID,formatSpec,gend);
    fclose(fileID);
```

Example 8: Throughput Testing Example

Cylinders, with pore sizes 0.200mm to 0.800 in 0.2mm steps and print speed from 100mm/min to 500mm/min
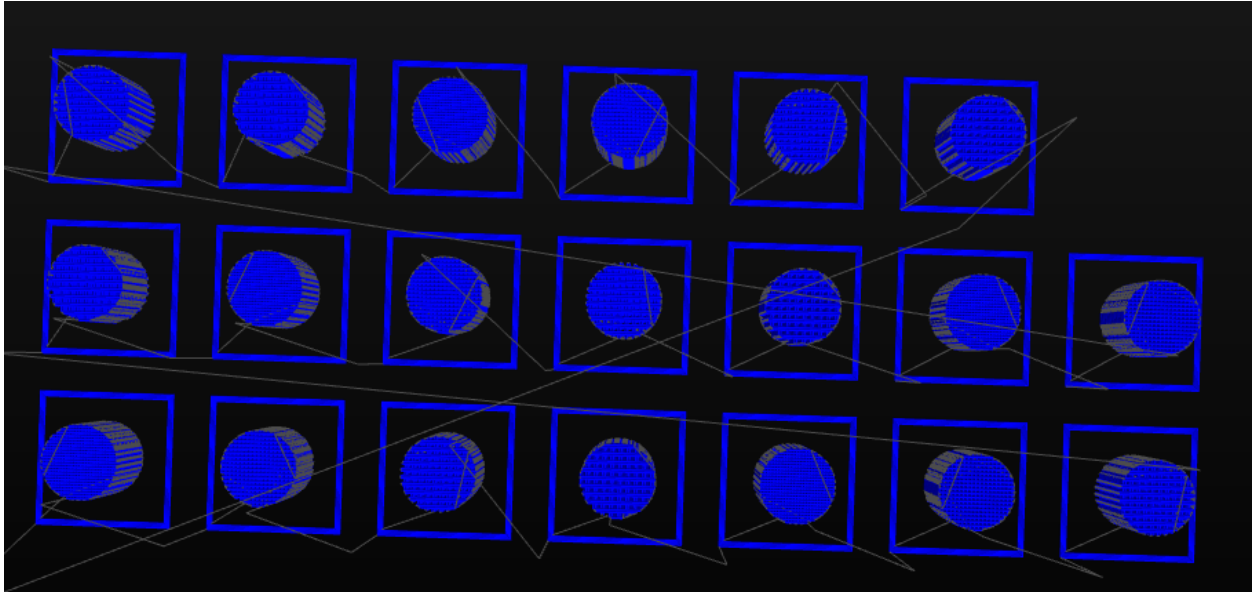
Figure A-1: Example of Output GCODE Visualized in Repetier
There are four scaffold designs (Pore sizes). These designs are repeated in sequence from left to right starting at the origin in the bottom left corner. Each repetition of the sequence uses an increased print speed.

```
clearvars
addpath('sub functions')

%% Make a Cylinder Shape
ix=200;iy=200;
r=85;
cx=100;cy=100;
he = ix;
[x,y]=meshgrid(-(cx-1):(ix-cx),-(cy-1):(iy-cy));
c_mask=((x.^2+y.^2)<=r^2);
V = repmat(c_mask, [1 1 he]);
V(:,:, he-4:he)=0;
V = double(V);

%% Prepare the GCODE as file
fileID = fopen(fullfile('gcode','header_abs.txt'),'r');
gstart = textscan(fileID,'%s','delimiter','\n');
gstart = string(gstart{1});
fclose(fileID);
fileID = fopen(fullfile('gcode','footer.txt'),'r');
gend = textscan(fileID,'%s','delimiter','\n');
gend = string(gend{1});
fclose(fileID);
```

```matlab
% Read GCODE lines into output file
fileID = fopen(fullfile('Output','Figure9_Throughput.gcode'),'w');
formatSpec = '%s\n';
fprintf(fileID,formatSpec,gstart);

%% Slicing
VoxelSize = 0.100;
PoreDiameter = [0.200 0.400 0.600 0.800] ;
Porosity = [0.5 0.5 0.5 0.5] ;
XPOS = 30; YPOS = 30;
position = [XPOS YPOS];
printSpeeds = [20 40 80 100 110];
for j = 1:length(printSpeeds)
for i = 1:length(PoreDiameter)

    [glines, toolPaths, preview] = SlicrFn  (   V, ...
        VoxelSize, ...
        PoreDiameter(i)', ...
        Porosity(i), ...
        [XPOS YPOS],...
        'Backtracking', false,...
        'BedTemp', 110,...
        'CreateBrim', true,...
        'ExtruderTemp', 285,...
        'ExtrusionMultiplier', 1.1,...
        'FanHeight', 1,...
        'FanPower', 95,...
        'FilamentDiameter', 2.85,...
        'LayerHeight', 0.200,...
        'NozzleDiameter', 0.500,...
        'PauseTime', 200,...
        'PrintSpeed', printSpeeds(j),...
        'SupportPoreDiam', 0.95...
        );

    glines(glines == '')=[]; %remove empty dimensions
    fprintf(fileID,formatSpec,glines');  % Write to file

    if XPOS > 230, XPOS = 30; YPOS = YPOS+40; else, XPOS = XPOS+40; end
%if

end %for pore diameter loop
end %for print speeds loop

fprintf(fileID,formatSpec,gend);
fclose(fileID);
```

scafSLICR Source Code

```matlab
function [varargout] = SlicrFn (V, VoxelSize, PoreDiameter, Porosity,
Position, varargin)


% V           Volume to be sliced
% VoxelSize   Dimension of a voxel in mm
% PoreDiameter Array of diameters in mm
% Porosity    Array of diameters in mm
% position    [ x_pos   y_pos ]


%%% SlicrFn is a function that generates support structure for a desired
%%% 3D volume, slices the volume into a porous scaffold according to input
%%% patterns, generates a 3D preview of the sliced volume, and writes gcode
%%% for the sliced volume and support

%%% SlicrFn does not return any values, instead it saves the following
%%% files to the output directory:
% glines    gcode for the nozzle movements for a single scaffold
% G matrix  (GraphicMatrix) -- binary matrix showing the sliced 3D
% volume    Sliced volume without support structure


%% Section 1: Inputs and Defaults
V                  =   V;
[a,b,c]            =   size(V);
supportPoreDiam    =   1.5;  % mm
bedTemp            =   110;    % Deg Celsius, Default ABS
extruderTemp       =   285;    % Deg Celsius, Default ABS
printSpeed         =   2100;   % mm / min, Default ABS
createBrim         =   true;   % Default to create brim
pauseTime          =   50;     % ms on each strut end, default in ABS
% If zero, then pauseBoolean = False
pauseBoolean       =   true;
backtrackingBoolean =   true;   % Back track or not
fanOnHeight        =   0.2;    % mm height where fan is turned on
fanPower           =   100;    % 0 - 100 percent of fan power
NozzleDiameter     =   0.500;  % in mm
ExtrusionMult      =   1.01;   % Amount of over/under material flow
rate
LayerHeight        =   0.200;  % in mm, between each z-change
FilamentDiameter   =   2.85;   % mm
```

```matlab
if size(varargin,2)>1
    for i2=1:2:size(varargin,2) % Must be in ('Name', Value) pairs
        switch varargin{i2}
            case 'FanPower'
                if varargin{i2+1} < 100.1
                    fanPower = varargin{i2+1};
                end
            case 'FanHeight'
                fanOnHeight = varargin{i2+1};
            case 'Backtracking' % Input as boolean
                backtrackingBoolean = varargin{i2+1};
            case 'PauseTime'
                pauseTime = varargin{i2+1};
                if pauseTime == 0, pauseBoolean = false; end
            case 'CreateBrim'    % Input as boolean
                createBrim = varargin{i2+1};
            case 'PrintSpeed'
                printSpeed = varargin{i2+1};
            case 'ExtruderTemp'
                extruderTemp = varargin{i2+1};
            case 'BedTemp'
                bedTemp = varargin{i2+1};
            case 'SupportPoreDiam'
                supportPoreDiam = varargin{i2+1};
            case 'NozzleDiameter'
                NozzleDiameter = varargin{i2+1};
            case 'ExtrusionMultiplier'
                ExtrusionMult = varargin{i2+1};
            case 'LayerHeight'
                LayerHeight = varargin{i2+1};
            case 'FilamentDiameter'
                FilamentDiameter = varargin{i2+1};
        end % switch
    end %for
end %if


% Find the smallest feature and common multiple of the nozzle diameter so
% that the strut widths are integer multiples of the nozzle diameter.
features = [PoreDiameter' LayerHeight NozzleDiameter];
features(features==0)=[]; % Do not include features that are 0 (solid
material)
small_Feature = min(features);
if small_Feature < VoxelSize
    if mod(NozzleDiameter, small_Feature) ~= 0
        g = gcd(NozzleDiameter*1000, small_Feature*1000);
        small_Feature = g / 1000;
    end
    scale = VoxelSize / small_Feature;
    V = imresize3(V, scale, 'nearest');
    VoxelSize = small_Feature;
    [a,b,c]           =   size(V);
elseif mod(NozzleDiameter, VoxelSize) ~= 0
    g = gcd(NozzleDiameter*1000, VoxelSize*1000);
    small_Feature = g / 1000;
    scale = VoxelSize / small_Feature;
    V = imresize3(V, scale, 'nearest');
    VoxelSize = small_Feature;
```

```matlab
    [a,b,c]                 =   size(V);
end


SliceThickness = ceil(PoreDiameter./VoxelSize);  %in voxels
LayersPerSlice = ceil(PoreDiameter./LayerHeight);

% For solid sections (pore = 0 or porosity = 0) make SliceThickness
equal
% to Layer Height in Voxels
SliceThickness(SliceThickness==0) = ceil(LayerHeight / VoxelSize);
LayersPerSlice(LayersPerSlice==0) = 1;

%% Section 2: Support Shape
% 1. Creates a volume of 1s the same size as the input volume.
% 2. Subtract the input shape.
% 3. Remove any whole columns--support from top to bottom.
% 4. Remove the parts of any columns attached to the top.

V_s = (ones(size(V)) - (V~=0));      % Same size at V, less V
Z=size(V_s,3);
Tops = V_s(:,:,Z);
[iT, jT] = ind2sub(size(Tops),find(Tops));
for i3=1:size(iT,1)
    if sum(V_s(iT(i3),jT(i3),:))==Z
        V_s(iT(i3),jT(i3),:)=0;
    else
        A = find(~V_s(iT(i3),jT(i3),:));
        % Create a gap between the support and the actual print to make
        % easier to remove the support...one voxel or ~0.1mm?
        if A(1)>1, A(1) = A(1)-1; end
        V_s(iT(i3),jT(i3),A(1):end)=0;
    end
end


%% Section 3: Voxels as Design Input
% Input a volume V, where each voxel corresponds to a pore size and
% porosity ordered the same way unique(V) is ordered.

% 3.1 Begin by finding the number of tool paths to make a strut in each
design
patternIDs = unique(V); patternIDs = patternIDs(2:end);
numPatterns = size(patternIDs,1);
strutNums = ceil((PoreDiameter ./ NozzleDiameter).*((1./Porosity')-1));
strutNums(strutNums==0) = 1;
strutNums(strutNums~=strutNums)=1; % NaN catch for pore of 0
strutWidths = strutNums*NozzleDiameter./VoxelSize;

% 3.2 Create a template for each design. templateX and templateY are
for 3D volume vs. linesX and linesY are 2D-toolpaths
templateX = zeros(a,b,numPatterns+1); templateY=templateX;
linesX=zeros(a,b,numPatterns); linesY=linesX;
for q1=1:numPatterns
    [templateX(:,:,q1), templateY(:,:,q1), linesX(:,:,q1),
linesY(:,:,q1)] ...
        = templateFUNC(strutNums(q1), strutWidths(q1),
PoreDiameter(q1));
end
```

```matlab
% Make template support, append to the other templates
PoreDiameter(end+1) = supportPoreDiam; % Support Pore Diameter
numPatterns=numPatterns+1;

[templateX(:,:,numPatterns), templateY(:,:,numPatterns  ),...
    linesX(:,:,numPatterns), linesY(:,:,numPatterns     )] ...
    = templateFUNC(1, ceil(NozzleDiameter/VoxelSize),
PoreDiameter(end));

% Combine the object volume and the support volume with the object
support_voxel = rand*10;
V = V + V_s.*support_voxel;
patternIDs(end+1)=support_voxel;

% 3.3 For each layer, for each density, convolve that range with the
% appropriate template, resulting in a series of tool paths for each
level.
T = zeros(a,b,c); G = T;
LayersPerSlice(end+1)=LayersPerSlice(end);
SliceThickness(end+1)=SliceThickness(end);
endpointlist = cell([c 1 1]);

% z-index levels where print is happening
print_levels = (LayerHeight/VoxelSize):(LayerHeight/VoxelSize):c;

xdir_all = zeros(numPatterns, c);
for k1=1:numPatterns
    xdir_temp = [ones(SliceThickness(k1),1)'
zeros(SliceThickness(k1),1)']';
    xdir_temp = repmat(xdir_temp,ceil(c/(SliceThickness(k1)*2)),1);
    xdir_all(k1,:) = xdir_temp(1:c);
    for q=1:c % for each z-level of V...
        if k1==numPatterns % Support Design
            H = (V(:,:,q)==patternIDs(end)).*linesX(:,:,end);
            T(:,:,q) =  T(:,:,q)+2*H;
            if ismember(q, print_levels)
            endpointlist{q} = findpoints(H, endpointlist{q}, 'X'); end
        elseif xdir_all(k1,q) %other designs if their x-direction
            H = (V(:,:,q)==patternIDs(k1)).*linesX(:,:,k1);
            T(:,:,q) =  T(:,:,q)+H;
            G(:,:,q) =
G(:,:,q)+((V(:,:,q)==patternIDs(k1)).*templateX(:,:,k1));
            if ismember(q, print_levels)
            endpointlist{q} = findpoints(H, endpointlist{q}, 'X'); end
        else
            H = (V(:,:,q)==patternIDs(k1)).*linesY(:,:,k1);
            T(:,:,q) =  T(:,:,q)+H;
            G(:,:,q) =
G(:,:,q)+((V(:,:,q)==patternIDs(k1)).*templateY(:,:,k1));
            if ismember(q, print_levels)
            endpointlist{q} = findpoints(H, endpointlist{q}, 'Y'); end
        end
    end
end % for num patterns
```

```matlab
%% Section 4: Translate toolpaths into endpoints then into GCODE
X=Position(1); Y=Position(2); Z=0.2; % Initial Position of the toolhead
bot = 1;
tiptop = c;
top = bot+SliceThickness-1;
glines = [];
% Holder for each line of gcode. Will be dynamically updated.

% Add any extruder and bed temperature adjustments
glines = [glines [ 'M190 S' num2str(bedTemp) ' ;Adjust Bed Temp from
Header Setting']];
glines = [glines [ 'M109 S' num2str(extruderTemp) ' ;Adjust Extruder
Temp from Header Setting']];

if createBrim, glines = [glines makeBrim(V,0,0)]; end
% writes gocde for initial skirt at Z = 0.2

numSlice = 1;        o=1;        fanOn = true;
Zz = zeros(ceil(c/(LayerHeight/VoxelSize)), 1);
Tt = zeros(a, b, ceil(c/(LayerHeight/VoxelSize)));
for i6 = print_levels
    % Turn fan on
    if (fanOnHeight > 1+i6*2*(LayerHeight/VoxelSize)) && fanOn
        glines = [glines ['M106 S' num2str(round(fanPower*2.55)) '; fan
power']];
        fanOn = false; % only add to code one time
    end %if fanOnHeight

    if (top>tiptop), top=tiptop; end
    if (bot>=top), bot = top-1; end
    if ~mod(o,LayersPerSlice), numSlice = numSlice+1; end

    [code,X,Y] = writeCode3(endpointlist{i6},X,Y); % get commands for
one print layer
    if ~isempty(code), glines = [glines code]; end

    % update z height
    %   Pause when going up a layer
    glines = [glines ['G0 Z' num2str(Z+LayerHeight) ';']];
    if pauseBoolean
        glines = [glines ['G4 P' num2str(pauseTime)]];
    end

    Zz(o) = Z; % Output for path preview
    Tt(:,:,o) = T(:,:,i6);
    Z = Z+LayerHeight;

    bot = bot+SliceThickness;
    top = top+SliceThickness;
    o=o+1;
end
glines = [glines ['G0 X' n2sX(X) ' Y' n2sY(Y) ' Z' num2str(Z+15) ';
Move away from scaffold']];
% Move print head away from print
glines(glines == '')=[]; %remove empty dimensions
```

```matlab
%% Section 5: Save Variables
if nargout>2 % Scaffold Preview Output
    graphics.scaffold = G;
    graphics.support = V_s;
    varargout{3} = graphics;
end
if nargout>1 % Tool Paths Output
    preview.Z_heights = Zz;
    preview.ToolPaths = Tt;
    varargout{2} = preview;
end
if nargout>0
    varargout{1} = glines;
else
    savefile = fullfile('Output', 'Graphic_Matrix.mat');
    save(savefile, 'G', 'V_s','-v7.3','-nocompression')
    savefile2 = fullfile('Output','glines.mat');
    save(savefile2,'glines');
    savefile3 = fullfile('Output','preview.mat');
    save(savefile3,'Zz', 'Tt','-v7.3','-nocompression');
end


    function C = findpoints(slice, endpointlist, dir)
        if isempty(endpointlist)
            index = 0;
        else
            index = endpointlist(end, end, end);
        end

        if dir=='X'
            [slice, num] = bwlabel(slice,8);
        else
            [slice, num] = bwlabel(slice',8);
            slice = slice';
        end

        M = zeros(num*2,3);
%matrix to collect each (x,y) endpoint and the corresponding path
%number

        for k=1:2:(num*2)
%find all of the end points for all paths in this slice
            M(k:k+1,3) = k+index;
            points = bwmorph((slice == ((k+1)/2)),'endpoints');
            [xt,yt] = find(points);
            if size(xt)==1, continue, end
            M(k,1) = xt(1); M(k,2) = yt(1);
            M(k+1,1) = xt(2); M(k+1,2) = yt(2);
        end

        C = [endpointlist; M];

    end % findpoints function
```

```matlab
    function [glines] = makeBrim(V,X,Y)
%%% making code for the brim (currently makes 2 squares/rings)
%%% also this is hard coded to make a square...in the future we may
want it to trace the first layer of the print
        X = X-50; Y = Y-50; % Displace in Voxels
        fildiam = 1.2*FilamentDiameter;
        xmax = size(V,1)*1.2; ymax = size(V,2)*1.2;
        numRings = 4;
        ring  = numRings-1;
        glines = strings(1,4*numRings+2);

        glines(1) = ['G1 X' n2sX(X-ring*(fildiam)) ' Y' n2sY(Y-
ring*(fildiam)) ';'];
        glines(2) = ['G1 Z' num2str(0.2) ';'];

        for i = 3:4:4*numRings+1
            glines(i) = ['G1 X' n2sX(xmax+ring*(fildiam)) ' Y' n2sY(Y-
ring*(fildiam)) ' E' extrude(distance(X-ring*(fildiam),Y-
ring*(fildiam),xmax+ring*(fildiam),Y-ring*(fildiam))) ';'];
            glines(i+1) = ['G1 X' n2sX(xmax+ring*(fildiam)) ' Y'
n2sY(ymax+ring*(fildiam)) ' E' extrude(distance(xmax+ring*(fildiam),Y-
ring*(fildiam),xmax+ring*(fildiam),ymax+ring*(fildiam))) ';'];
            glines(i+2) = ['G1 X' n2sX(X-ring*(fildiam)) ' Y'
n2sY(ymax+ring*(fildiam)) ' E'
extrude(distance(xmax+ring*(fildiam),ymax+ring*(fildiam),X-
ring*(fildiam),ymax+ring*(fildiam))) ';'];
            glines(i+3) = ['G1 X' n2sX(X-ring*(fildiam)) ' Y' n2sY(Y-
(ring-1)*(fildiam)) ' E' extrude(distance(X-(fildiam),ymax+(fildiam),X-
(fildiam),Y-(ring-1)*(fildiam))) ';'];
            ring = ring-1;
        end % for i:numRings
    end % makeBrim Function
```

```matlab
function [templateX, templateY, linesX, linesY] = templateFUNC(...
        strutNum, strutWidth, PoreDiameter)
    %%%%%%%%%%%%%%  IN X %%%%%%%%%%%%%%%%%%%%%%%%%%%
    %% Create Template Base Units
    poreX = zeros(a,ceil(PoreDiameter/VoxelSize)); %pore template
    strutX = ones(a,strutWidth); %strut template

    % Tool Path Template
    lineX = zeros(size(strutX,1),ceil(NozzleDiameter/VoxelSize));
% Start with a single toolpath
    lineX(:,ceil(size(lineX,2)/2))=1;
%Add a line of ones in the middle for the toolpath
    lineX=repmat(lineX,[1 strutNum 1]);
% Repeat the lines enough to create the single strut
    linesX = cat(2, poreX, lineX);
% pore and toolpaths for one unit (pore + strut)
    linesX = repmat(linesX, [1 ceil(b/size(linesX,2))]);
% Repeat the unit template for the width of the volume
    linesX = linesX(1:a,1:b);
% Crop the template to the exact size of the volume (Volume might not
equal exact multiples of unit template)

    % 3D Volume Template for Modeling and Visualization
    templateX = cat(2, poreX, strutX);
% pore and strut for one unit template
    templateX = repmat(templateX, [1 ceil(b/size(templateX,2))]);
    templateX=templateX(1:a, 1:b);

    %%%%%%%%%%%%%%% IN Y %%%%%%%%%%%%%%%%%%%%%%%%%%%
    %% Create Template Base Units
    poreY = zeros(b,ceil(PoreDiameter/VoxelSize)); %pore template
    strutY = ones(b,strutWidth); %strut template

    % Tool Path Template
    lineY = zeros(size(strutY,1),ceil(NozzleDiameter/VoxelSize));
    lineY(:,ceil(size(lineY,2)/2))=1;
    lineY=repmat(lineY,[1 strutNum 1]);
    linesY = cat(2, poreY, lineY);
    linesY = repmat(linesY, [1 ceil(a/size(linesY,2))]);
    linesY = linesY(1:b,1:a);
    linesY = linesY';

    % 3D Volume Template for Modeling and Visualization
    templateY = cat(2, poreY, strutY);
    templateY = repmat(templateY, [1 ceil(a/size(templateY,2))]);
    templateY=templateY';
    templateY=templateY(1:a, 1:b);

end % Template Func
```

```matlab
function [gcode, finX, finY] = writeCode3(M, prevX, prevY)
        % for slice of volume V, and previous pixel positions prevX, prevY
        % writeCode creates gcode instructions for each XY-slice of toolpaths
        % M is the list of points
        % X and Y are the current positions.
        d_thresh = 0.9*PoreDiameter(1)/VoxelSize;
        num = size(M,1)/2;
        gcode = strings(num*7,1);

%%% calculate distance from current position to each point in M for
first loop of k. It is recalculated at the end of the loop.
        d = zeros(size(M,1),1);
        for j = 1:size(M,1)
            d(j) = distance(M(j,1),M(j,2),prevX,prevY);
        end
        [~,index] = min(d); % nearest point

        %% writing code
        %%% one movement along a line repeated for each tool path
        for k=1:num
            % 1. Check that nearest extrude move is long enough to do.
            % 2. Move to closest (x,y) end of that move
            % 3. Extrude along that move
            % 4. Remove the entries from M

            if mod(index,2) == 0 %index is even number so corresponding
row is before
                dist = distance(M(index,1),M(index,2),M(index-
1,1),M(index-1,2));
                prevX2 = M(index,1); prevY2 = M(index,2); %save for
backtracking
                if dist > 2*NozzleDiameter/VoxelSize

                    gcode((k*7)-6) = ['G1 X' n2sX(M(index,1))...
                        ' Y'  n2sY(M(index,2)) ';']; %go to closest end
                    gcode((k*7)-5) = ['G1 X' n2sX(M(index-1,1)) ' Y'
n2sY(M(index-1,2))...
                        ' E' extrude(dist) ';'];
                    prevX = M(index-1,1); prevY = M(index-1,2);
                end %if dist is great enough
                M = [M(1:index-2,:);M(index+1:end,:)];
            else %index is odd number so corresponding row is after
                dist =
distance(M(index,1),M(index,2),M(index+1,1),M(index+1,2));
                prevX2 = M(index,1); prevY2 = M(index,2);
%save for backtracking
                if dist > 2*NozzleDiameter/VoxelSize
                    %%% move to (x,y) that have smallest distance
                    gcode((k*7)-6) = ['G1 X' n2sX(M(index,1))...
                        ' Y'  n2sY(M(index,2)) ';']; %go to closest end
                    gcode((k*7)-5) = ['G1 X' n2sX(M(index+1,1)) ' Y'
n2sY(M(index+1,2))...
                        ' E' extrude(dist) ';'];
                    prevX = M(index+1,1); prevY = M(index+1,2);
                end %if dist is great enough
                M = [M(1:index-1,:);M(index+2:end,:)];
            end % mod(index)
            d = zeros(size(M,1),1);
```

```matlab
            for j = 1:size(M,1)
                d(j) = distance(M(j,1),M(j,2),prevX,prevY);
            end
            [min_d,index] = min(d); % nearest point
            %% Backtracking %%
    % re-calculate distance from current position to each point in M
            if backtrackingBoolean
                if min_d > d_thresh
                    U = distance(prevX,prevY,prevX2,prevY2);
% vector magnitude
                    if U < 4*PoreDiameter(1)/VoxelSize
%if distance is less than 10 pixels (1mm?) then just use previous XY.
                        backX = prevX2; backY=prevY2;
                    else
                        xu = (prevX-prevX2)/U;
                        yu = (prevY-prevY2)/U; % Normalize the vector
                        backX = prevX -
4*(PoreDiameter(1)/VoxelSize)*xu;
                        backY = prevY -
4*(PoreDiameter(1)/VoxelSize)*yu;
                    end
         % Back track at a speed 30% slow than normal extruder speed
gcode((k*7)-4) = ['G1 F' num2str(0.7*printSpeed) '; slow extruder
speed'];
gcode((k*7)-3) = ['G1 X' n2sX(backX) ' Y'  n2sY(backY) ';'];
if pauseBoolean, gcode((k*7)-2) = ['G4 P'  num2str(pauseTime) ';']; end
gcode((k*7)-1) = [' G1 X' n2sX(prevX) ' Y' n2sY(prevY) ';'];
gcode((k*7)) = ['G1 F' num2str(printSpeed) '; return to normal speed'];
                end % if min_d < thresh
                gcode = gcode';
            end % if backtrackingBoolean
        end % for k=1:num

        if size(gcode,1) ~=1, gcode = gcode'; end
        finX = prevX; finY = prevY;
    end % writeCode3 Nested Function

% Distance creates the sqrt distance between two cartesian points.
    function d = distance(x1, y1, x2, y2), d = sqrt((x1-x2)^2+(y1-
y2)^2); end

% Extrude creates an extrude command scaled to the voxel size
    function e = extrude(dist)
        e = num2str(ExtrusionMult*(LayerHeight / NozzleDiameter)...
            *(VoxelSize*dist)*(NozzleDiameter^2)/(FilamentDiameter^2));
    end % extrude function

% n2s turns numbers of voxels into the equivalent mm distance and
translates it in xy according to the start position input.
    function outString = n2sY(num)
        y = Position(2);
        outString = num2str(y+VoxelSize*num); end % n2sY Function
    function outString = n2sX(num)
        x = Position(1);
        outString = num2str(x+VoxelSize*num); end % n2sX Function
end % SlicrFn2
```

LIST OF REFERENCES

1.   BCC Research, M. E. *Advanced Orthopedic Technologies, Implants and Regenerative Products*. **7215**, (2014).

2.   Kanwisher, N., Mcdermott, J. & Chun, M. M. The Fusiform Face Area : A Module in Human Extrastriate Cortex Specialized for Face Perception. **17**, 4302–4311 (1997).

3.   Wilkinson, N., Paikan, A., Gredeb, G., Rea, F. & Metta, G. Staring us in the face ? An embodied theory of innate face preference. 1–17 (2014). doi:10.1111/desc.12159

4.   Li, J. & Helms, J. A. *20 - Embryology of the craniofacial complex*. *Plastic Surgery* (Elsevier Inc., 2018). doi:10.1016/B978-0-323-35698-5.00020-3

5.   Barbian, L. T. & Sledzik, P. S. Healing Following Cranial Trauma *. **53**, 263–268 (2008).

6.   Johnson, J. V. Gunshot Wounds to the Face. *J. Trauma Inj. Infect. Crit. Care* **62**, S87 (2007).

7.   Broyles, J. M. *et al.* The Fusion of Craniofacial Reconstruction and Microsurgery. *Plast. Reconstr. Surg.* **134**, 760–769 (2014).

8.   Canter, H. I. *et al.* Mandibular reconstruction in Goldenhar syndrome using temporalis muscle osteofascial flap. *J.Craniofac.Surg.* **19**, 165–170 (2008).

9.   Sharma, J. K., Pippal, S. K., Raghuvanshi, S. K. & Shitij, A. Goldenhar-Gorlin's syndrome: A case report. *Indian J. Otolaryngol. Head Neck Surg.* **58**, 97–101 (2006).

10.   Wolford, L. M., Bourland, T. C., Odrigues, D., Perez, D. E. & Limoeiro, E. Successful reconstruction of nongrowing hemifacial microsomia patients with unilateral temporomandibular joint total joint prosthesis and orthognathic surgery. *J. Oral Maxillofac. Surg.* **70**, 2835–2853 (2012).

11.   Fan, W. S., Mulliken, J. B. & Padwa, B. L. An association between hemifacial microsomia and facial clefting. *J. Oral Maxillofac. Surg.* **63**, 330–334 (2005).

12.   Azuma, M. *et al.* Mandibular reconstruction using plates prebent to fit rapid prototyping 3-dimensional printing models ameliorates contour deformity. *Head Face Med.* **10**, 45 (2014).

13.   Chacón-Moya, E., Gallegos-Hernández, J. F., Piña-Cabrales, S., Cohn-Zurita, F. & Goné-Fernández, A. Cranial vault reconstruction using computer-designed polyetheretherketone (PEEK) implant: case report. *Cir. Cir.* **77**, 437–440 (2009).

14. Gillis, R. E., Swenson, W. M. & Laney, W. R. Psychological factors involved in maxillofacial prosthetics. *J. Prosthet. Dent.* **41**, 183–188 (1979).

15. Ridwan-Pramana, A., Wolff, J., Raziei, A., Ashton-James, C. E. & Forouzanfar, T. Porous polyethylene implants in facial reconstruction: Outcome and complications. *J. Cranio-Maxillofacial Surg.* **43**, 1330–1334 (2015).

16. Sbordone, C. *et al.* Volume changes of iliac crest autogenous bone grafts after vertical and horizontal alveolar ridge augmentation of atrophic maxillas and mandibles: A 6-year computerized tomographic follow-up. *J. Oral Maxillofac. Surg.* **70**, 2559–2565 (2012).

17. Delloye, C., Cornu, O., Druez, V. & Barbier, O. Bone allografts: What they can offer and what they cannot. *J. Bone Joint Surg. Br.* **89**, 574–9 (2007).

18. Shen, W. Cost comparison of femoral head banking versus bone substitutes. *J. Orthop. Surg. (Hong Kong)* **18**, 258; author reply 258-9 (2010).

19. Berryhill, W. E., Rimell, F. L., Ness, J., Marentette, L. & Haines, S. J. Fate of rigid fixation in pediatric craniofacial surgery. 1–5 (1999).

20. Gosain, A. K., Chim, H. & Arneja, J. S. Application-Specific Selection of Biomaterials for Pediatric Craniofacial Reconstruction: Developing a Rational Approach to Guide Clinical Use. *Plast. Reconstr. Surg.* **123**, 319–330 (2009).

21. Giannoudis, P. V, Dinopoulos, H. & Tsiridis, E. Bone substitutes: an update. *Injury* **36 Suppl 3**, S20-7 (2005).

22. Stock, U. A. & Vacanti, J. P. T ISSUE E NGINEERING : Current State and Prospects. (2001).

23. Liu, Y., de Groot, K. & Hunziker, E. B. BMP-2 liberated from biomimetic implant coatings induces and sustains direct ossification in an ectopic rat model. *Bone* **36**, 745–57 (2005).

24. Grayson, W. L. *et al.* Stromal cells and stem cells in clinical bone regeneration. *Nat. Rev. Endocrinol.* **11**, 140–150 (2015).

25. Hutton, D. L. & Grayson, W. L. Stem cell-based approaches to engineering vascularized bone. *Curr. Opin. Chem. Eng.* **3**, 75–82 (2014).

26. Temple, J. P. *et al.* Engineering anatomically shaped vascularized bone grafts with hASCs and 3D-printed PCL scaffolds. *J. Biomed. Mater. Res. A* 1–9 (2014). doi:10.1002/jbm.a.35107

27. Hung, B. P. *et al.* Three-dimensional printing of bone extracellular matrix for craniofacial regeneration. *ACS Biomater. Sci. Eng.* acsbiomaterials.6b00101 (2016). doi:10.1021/acsbiomaterials.6b00101

28. Fisher, M., Dorafshar, A., Bojovic, B., Manson, P. N. & Rodriguez, E. D. The Evolution of Critical Concepts in Aesthetic Craniofacial Microsurgical Reconstruction. *Plast. Reconstr. Surg.* 1 (2012). doi:10.1097/PRS.0b013e3182589e12

29. Dorafshar, A. H. *et al.* Total face, double jaw, and tongue transplantation: an evolutionary concept. *Plast. Reconstr. Surg.* **131**, 241–51 (2013).

30. Obregon, F., Vaquette, C., Ivanovski, S., Hutmacher, D. W. & Bertassoni, L. E. Three-Dimensional Bioprinting for Regenerative Dentistry and Craniofacial Tissue Engineering. **XX**, 1–10 (2015).

31. Mandrycky, C., Wang, Z., Kim, K. & Kim, D.-H. 3D bioprinting for engineering complex tissues. *Biotechnol. Adv.* 1–13 (2015). doi:10.1016/j.biotechadv.2015.12.011

32. Zuo, K. J. & Wilkes, G. H. Clinical Outcomes of Osseointegrated Prosthetic Auricular Reconstruction in Patients With a Compromised Ipsilateral Temporoparietal Fascial Flap. *J. Craniofac. Surg.* **27**, 44–50 (2016).

33. Ariani, N. *et al.* Current state of craniofacial prosthetic rehabilitation. *Int. J. Prosthodont.* **26**, 57–67 (2012).

34. Visser, A., Raghoebar, G. M., van Oort, R. P. & Vissink, A. Fate of implant-retained craniofacial prostheses: life span and aftercare. *Int. J. Oral Maxillofac. Implants* **23**, 89–98 (2007).

35. McKinstry, R. E. *Fundamentals of facial prosthetics*. (ABI Professional publications, 1995).

36. Thomas, K. F. *The art of clinical anaplastology*. (2006).

37. Tanner, P. B. & Mobley, S. R. External auricular and facial prosthetics: a collaborative effort of the reconstructive surgeon and anaplastologist. *Facial Plast. Surg. Clin. North Am.* **14**, 137–145 (2006).

38. He, Y., Xue, G. & Fu, J. Fabrication of low cost soft tissue prostheses with the desktop 3D printer. *Sci. Rep.* **4**, (2014).

39. Struct3D. Available at: http://www.structur3d.io/.

40. Lazarus3D. Available at: http://www.laz3d.com/.

41. Picsima. Available at: http://www.picsima.com/.

42. Zhang, Y., Yin, C., Zheng, C. & Zhou, K. Computational hydrographic printing. *ACM Trans. Graph.* **34**, 131:1-131:11 (2015).

43. Levine, J. P., Patel, A., Saadeh, P. B. & Hirsch, D. L. Computer-Aided Design and Manufacturing in Craniomaxillofacial Surgery. *J. Craniofac. Surg.* **23**, 288–293 (2012).

44. D'Urso, P. S. *et al.* Stereolithographic (SL) biomodelling in craniofacial surgery. *Br. J. Plast. Surg.* **51**, 522–530 (1998).

45. Navarro, M., Michiardi, a, Castaño, O. & Planell, J. a. Biomaterials in orthopaedics. *J. R. Soc. Interface* **5**, 1137–1158 (2008).

46. Farias, T. P. *et al.* Prototyping: Major Advance in Surgical Planning and Customizing Prostheses in Patients with Bone Tumors of the Head and Neck. *Int. J. Clin. Med.* **04**, 1–7 (2013).

47. Rodby, K. A. *et al.* Advances in oncologic head and neck reconstruction: Systematic review and future considerations of virtual surgical planning and computer aided design/computer aided modeling. *J. Plast. Reconstr. Aesthetic Surg.* **67**, 1171–1185 (2014).

48. Seruya, M. *et al.* Computer-aided design and manufacturing in craniosynostosis surgery. *J. Craniofac. Surg.* **24**, 1100–5 (2013).

49. Peled, M., El-Naaj, I. A., Lipin, Y. & Ardekian, L. The use of free fibular flap for functional mandibular reconstruction. *J. Oral Maxillofac. Surg.* **63**, 220–224 (2005).

50. Brown, E. N. *et al.* Total face, double jaw, and tongue transplant simulation: a cadaveric study using computer-assisted techniques. *Plast. Reconstr. Surg.* **130**, 815–23 (2012).

51. Gougoutas, A. J., Bastidas, N., Bartlett, S. P. & Jackson, O. The use of computer-aided design/manufacturing (CAD/CAM) technology to aid in the reconstruction of congenitally deficient pediatric mandibles: A case series. *Int. J. Pediatr. Otorhinolaryngol.* **79**, 2332–2342 (2015).

52. Fernandes da Silva, A. L. *et al.* Customized polymethyl methacrylate implants for the reconstruction of craniofacial osseous defects. *Case Rep. Surg.* **2014**, 358569 (2014).

53. Podolsky, D. J., Mainprize, J. G., Edwards, G. P. & Antonyshyn, O. M. Patient-Specific Orbital Implants: Development and Implementation of Technology for More Accurate Orbital Reconstruction. *J. Craniofac. Surg.* **27**, 131–133 (2016).

54. Parthasarathy, J. 3D modeling, custom implants and its future perspectives in craniofacial surgery. *Ann. Maxillofac. Surg.* **4**, 9 (2014).

55. Jalbert, F. *et al.* One-step primary reconstruction for complex craniofacial resection with PEEK custom-made implants. *J. Cranio-Maxillofacial Surg.* **42**, 141–148 (2014).

56. Shan, X.-F., Chen, H.-M., Liang, J., Huang, J.-W. & Cai, Z.-G. Surgical Reconstruction of Maxillary and Mandibular Defects Using a Printed Titanium Mesh. *J. Oral Maxillofac. Surg.* **73**, 1437.e1-1437.e9 (2015).

57. Van Gestel, N. A. P. *et al.* Clinical Applications of S53P4 Bioactive Glass in Bone Healing and Osteomyelitic Treatment: A Literature Review. *Biomed Res. Int.* **2015**, (2015).

58. Aitasalo, K. M. J., Piitulainen, J. M., Rekola, J. & Vallittu, P. K. Craniofacial bone reconstruction with bioactive fiber-reinforced composite implant. *Head Neck* **36**, 722–728 (2014).

59. Fu, Q., Saiz, E. & Tomsia, A. P. Direct Ink Writing of Highly Pourous and Strong Glass Scaffolds for Load-bearing Bone Defects Repair and Regeneration. *Acta Biomater.* **7**, 3547–3554 (2011).

60. Huang, T. S. *et al.* Freeze extrusion fabrication of 13-93 bioactive glass scaffolds for repair and regeneration of load-bearing bones. *Ceram. Trans.* **228**, 45–55 (2011).

61. Kolan, K. C. R., Leu, M. C., Hilmas, G. E., Brown, R. F. & Velez, M. Fabrication of 13-93 bioactive glass scaffolds for bone tissue engineering using indirect selective laser sintering. *Biofabrication* **3**, 025004 (2011).

62. Brie, J. *et al.* A new custom made bioceramic implant for the repair of large and complex craniofacial bone defects. *J. Cranio-Maxillofacial Surg.* **41**, 403–407 (2013).

63. Gibson, I., Rosen, D. W. & Stucker, B. Additive Manufacturing Technologies. in *Additive Manufacturing Technologies* 17–40 (2010). doi:10.1007/978-1-4419-1120-9

64. e-Nable. Available at: http://enablingthefuture.org/.

65. Dunham, S. Surgeon's Helper: 3D Printing Is Revolutionizing Health Care (Op-Ed). *Live Science* (2015).

66. Ashok Khanna, Sukhdev Balaji, Thanga Jawahar, A. D. *3D Printing: New Opportunities for the Medical Devices Industry*. (2015).

67. Roohani-Esfahani, S.-I., Newman, P. & Zreiqat, H. Design and Fabrication of 3D printed Scaffolds with a Mechanical Strength Comparable to Cortical Bone to Repair Large Bone Defects. *Sci. Rep.* **6**, 19468 (2016).

68.	Yuan, H. *et al.* Osteoinductive ceramics as a synthetic alternative to autologous bone grafting. *Proc. Natl. Acad. Sci. U. S. A.* **107**, 13614–13619 (2010).

69.	Eshraghi, S. & Das, S. Mechanical and microstructural properties of polycaprolactone scaffolds oriented porous architectures produced by selective laser sintering. *Acta Biomater.* **6**, 2467–2476 (2010).

70.	Loh, Q. L. & Choong, C. Three-dimensional scaffolds for tissue engineering applications: role of porosity and pore size. *Tissue Eng. Part B. Rev.* **19**, 485–502 (2013).

71.	Hutmacher, D. W., Schantz, J. T., Lam, C. X. F., Tan, K. C. & Lim, T. C. State of the art and future directions of scaffold-based bone engineering from a biomaterials perspective. *J. Tissue Eng. Regen. Med.* **1**, 245–260 (2007).

72.	Melchels, F. P. W. *et al.* Effects of the architecture of tissue engineering scaffolds on cell seeding and culturing. *Acta Biomater.* **6**, 4208–4217 (2010).

73.	Perez, R. A. & Mestres, G. Role of pore size and morphology in musculo-skeletal tissue regeneration. *Mater. Sci. Eng. C Mater. Biol. Appl.* **61**, 922–939 (2016).

74.	Chiu, Y. C. *et al.* The role of pore size on vascularization and tissue remodeling in PEG hydrogels. *Biomaterials* **32**, 6045–6051 (2011).

75.	Artel, A., Mehdizadeh, H., Chiu, Y.-C., Brey, E. M. & Cinar, A. An agent-based model for the investigation of neovascularization within porous scaffolds. *Tissue Eng. Part A* **17**, 2133–41 (2011).

76.	Murphy, C. M., Haugh, M. G. & O'Brien, F. J. The effect of mean pore size on cell attachment, proliferation and migration in collagen–glycosaminoglycan scaffolds for bone tissue engineering. *Biomaterials* **31**, 461–466 (2010).

77.	Temple, J. P. *et al.* Engineering anatomically shaped vascularized bone grafts with hASCs and 3D-printed PCL scaffolds. *J. Biomed. Mater. Res. A* **102**, 4317–25 (2014).

78.	Inzana, J. A. *et al.* 3D printing of composite calcium phosphate and collagen scaffolds for bone regeneration. *Biomaterials* **35**, 4026–34 (2014).

79.	Azami, M., Samadikuchaksaraei, A. & Ali Poursamar, S. Synthesis and characterization of a laminated hydroxyapatite/gelatin nanocomposite scaffold with controlled pore structure for bone tissue engineering. *Int. J. Artif. Organs* **33**, 86 (2010).

80.	Sawyer, A. A. *et al.* The stimulation of healing within a rat calvarial defect by mPCL–TCP/collagen scaffolds loaded with rhBMP-2. *Biomaterials* **30**, 2479–2488 (2009).

81.   Suwanprateeb, J., Sanngam, R., Suvannapruk, W. & Panyathanmaporn, T. Mechanical and in vitro performance of apatite–wollastonite glass ceramic reinforced hydroxyapatite composite fabricated by 3D-printing. *J. Mater. Sci. Mater. Med.* **20**, 1281–1289 (2009).

82.   Hollister, S. J. *et al.* Engineering craniofacial scaffolds. *Orthod. Craniofac. Res.* **8**, 162–73 (2005).

83.   Zhou, Y., Hutmacher, D. W., Varawan, S. & Lim, T. M. In vitro bone engineering based on polycaprolactone and polycaprolactone – tricalcium phosphate composites. *Polym. Int.* **342**, 333–342 (2007).

84.   Hutmacher, D. W. *et al.* Mechanical properties and cell cultural response of polycaprolactone scaffolds designed and fabricated via fused deposition modeling. *J. Biomed. Mater. Res.* **55**, 203–16 (2001).

85.   Eshraghi, S. & Das, S. Mechanical and microstructural properties of polycaprolactone scaffolds with one-dimensional, two-dimensional, and three-dimensional orthogonally oriented porous architectures produced by selective laser sintering. *Acta Biomater.* **6**, 2467–2476 (2010).

86.   Rasperini, G. *et al.* 3D-printed bioresorbable scaffold for periodontal repair. *J. Dent. Res.* **94**, 153S-157S (2015).

87.   Graham, S. *et al.* Investigating the role of PDGF as a potential drug therapy in bone formation and fracture healing. *Expert Opin Investig Drugs* **18**, 1633–1654 (2009).

88.   Hung, B. P. *et al.* Platelet-derived growth factor BB enhances osteogenesis of adipose-derived but not bone marrow-derived mesenchymal stromal/stem cells. *Stem Cells* (2015).

89.   Osteopore. Available at: http://www.osteopore.com.sg/index.html.

90.   Lohfeld, S. *et al.* Fabrication, mechanical and in vivo performance of polycaprolactone/ tricalcium phosphate composite scaffolds. *Acta Biomater.* **8**, 3446–3456 (2012).

91.   Wang, S. *et al.* Gradient lithography of engineered proteins to fabricate 2D and 3D cell culture microenvironments. *Biomed. Microdevices* **11**, 1127–34 (2009).

92.   Cai, K. *et al.* Inkjet printing of laminin gradient to investigate endothelial cellular alignment. *Colloids Surf. B. Biointerfaces* **72**, 230–5 (2009).

93.   Di Luca, A. *et al.* Influencing chondrogenic differentiation of human mesenchymal stromal cells in scaffolds displaying a structural gradient in pore size. *Acta Biomater.* (2016). doi:10.1016/j.actbio.2016.03.014

94. Di Luca, A. *et al.* Gradients in pore size enhance the osteogenic differentiation of human mesenchymal stromal cells in three-dimensional scaffolds. *Sci. Rep.* **6**, 22898 (2016).

95. Gao, G. & Cui, X. Three-dimensional bioprinting in tissue engineering and regenerative medicine. *Biotechnol. Lett.* 1–9 (2015). doi:10.1007/s10529-015-1975-1

96. Kim, R. Y., Fasi, A. C. & Feinberg, S. E. Soft tissue engineering in craniomaxillofacial surgery. *Annals of Maxillofacial Surgery* **4**, 4–8 (2014).

97. Kolesky, D. B. *et al.* 3D bioprinting of vascularized, heterogeneous cell-laden tissue constructs. *Adv. Mater.* **26**, 3124–3130 (2014).

98. Catelas, I. *et al.* Human mesenchymal stem cell proliferation and osteogenic differentiation in fibrin gels in vitro. *Tissue Eng.* **12**, 2385–2396 (2006).

99. Gao, G. *et al.* Improved properties of bone and cartilage tissue from 3D inkjet-bioprinted human mesenchymal stem cells by simultaneous deposition and photocrosslinking in PEG-GelMA. *Biotechnol. Lett.* **37**, 2349–2355 (2015).

100. Gao, G. *et al.* Bioactive nanoparticles stimulate bone tissue formation in bioprinted three-dimensional scaffold and human mesenchymal stem cells. *Biotechnol. J.* **9**, 1304–11 (2014).

101. Merceron, T. K. *et al.* A 3D bioprinted complex structure for engineering the muscle–tendon unit. *Biofabrication* **7**, 035003 (2015).

102. Kang, H.-W. *et al.* A 3D bioprinting system to produce human-scale tissue constructs with structural integrity. *Nat Biotech* **34**, 312–319 (2016).

103. Yanez, M. *et al.* In Vivo Assessment of Printed Microvasculature in a Bilayer Skin Graft to Treat Full-Thickness Wounds. *Tissue Eng. Part A* **00**, 1–10 (2014).

104. Wilkins, L. M., Watson, S. R., Prosky, S. J., Meunier, S. F. & Parenteau, N. L. Development of a bilayered living skin construct for clinical applications. *Biotechnol. Bioeng.* **43**, 747–756 (1994).

105. Binder, K. In situ bioprinting of the skin. (Wake Forest University, 2011).

106. Keriquel, V. *et al.* In vivo bioprinting for computer- and robotic-assisted medical intervention: preliminary study in mice. *Biofabrication* **2**, 014101 (2010).

107. Cui, X., Breitenkamp, K., Finn, M. G., Lotz, M. & D'Lima, D. D. Direct Human Cartilage Repair Using Three-Dimensional Bioprinting Technology. *Tissue Eng. Part A* **18**, 1304–1312 (2012).

108. Pati, F. *et al.* Ornamenting 3D printed scaffolds with cell-laid extracellular matrix for bone tissue regeneration. *Biomaterials* **37**, 230–241 (2015).

109. O'Keefe, R. J. & Mao, J. Bone tissue engineering and regeneration: from discovery to the clinic--an overview. *Tissue Eng. Part B* **17**, 389–92 (2011).

110. Khan, S. N. *et al.* The biology of bone grafting. *J Am Acad Orthop Surg* **1**, 77–86 (2005).

111. Luginbuehl, V. *et al.* Impact of IGF-I release kinetics on bone healing: a preliminary study in sheep. *Eur. J. Pharm. Biopharm.* **85**, 99–106 (2013).

112. Chen, G., Deng, C. & Li, Y.-P. TGF-β and BMP signaling in osteoblast differentiation and bone formation. *Int. J. Biol. Sci.* **8**, 272–88 (2012).

113. Schipani, E., Maes, C., Carmeliet, G. & Semenza, G. L. Regulation of osteogenesis-angiogenesis coupling by HIFs and VEGF. *J. Bone Miner. Res.* **24**, 1347–53 (2009).

114. Mckibbin, B. The biology of fracture healing in long bones. *J Bone Jt. Surg* **60**-**B**, 150–162 (1978).

115. Caplan, A. I. & Correa, D. PDGF in bone formation and regeneration: new insights into a novel mechanism involving MSCs. *J. Orthop. Res.* **29**, 1795–803 (2011).

116. Marie, P. J., Miraoui, H. & Sévère, N. FGF/FGFR signaling in bone formation: progress and perspectives. *Growth Factors* **30**, 117–23 (2012).

117. Kleinheinz, J., Jung, S., Wermker, K., Fischer, C. & Joos, U. Release kinetics of VEGF165 from a collagen matrix and structural matrix changes in a circulation model. *Head Face Med.* **6**, 17 (2010).

118. Ruhé, P. Q. *et al.* In vivo release of rhBMP-2 loaded porous calcium phosphate cement pretreated with albumin. *J. Mater. Sci. Mater. Med.* **17**, 919–27 (2006).

119. Urist, M. Bone: Formation by Autoinduction. *Science (80-.).* **150**, 893–899 (1965).

120. Kisiel, M. *et al.* Improving the osteogenic potential of BMP-2 with hyaluronic acid hydrogel modified with integrin-specific fibronectin fragment. *Biomaterials* **34**, 704–12 (2013).

121. Rahman, C. *et al.* Controlled release of BMP-2 from a sintered polymer scaffold enhances bone repair in a mouse calvarial defect model. *J. Tissue Eng. Regen. Med.* **8**, 59–66 (2014).

122. Yazici, C. *et al.* Self-complementary AAV2.5-BMP2-coated femoral allografts mediated superior bone healing versus live autografts in mice with equivalent biomechanics to unfractured femur. *Mol. Ther.* **19**, 1416–25 (2011).

123. Bessa, P. C., Casal, M. & Reis, R. L. Bone morphogenetic proteins in tissue engineering: The road from laboratory to clinic, part II (BMP delivery). *Journal of Tissue Engineering and Regenerative Medicine* **2**, 81–96 (2008).

124. Yilgor, P., Tuzlakoglu, K., Reis, R. L., Hasirci, N. & Hasirci, V. Incorporation of a sequential BMP-2/BMP-7 delivery system into chitosan-based scaffolds for bone tissue engineering. *Biomaterials* **30**, 3551–9 (2009).

125. Ebara, S. & Nakayama, K. Mechanism for the action of bone morphogenetic proteins and regulation of their activity. *Spine (Phila. Pa. 1976).* **27**, 10–15 (2002).

126. Silva, E. A. & Mooney, D. J. Effects of VEGF temporal and spatial presentation on angiogenesis. *Biomaterials* **31**, 1235–41 (2010).

127. Lenze, U. *et al.* Influence of osteogenic stimulation and VEGF treatment on in vivo bone formation in hMSC-seeded cancellous bone scaffolds. *BMC Musculoskelet. Disord.* **15**, 350 (2014).

128. MacGabhann, F., Ji, J. W. & Popel, A. S. VEGF gradients, receptor activation, and sprout guidance in resting and exercising skeletal muscle. *J. Appl. Physiol.* **102**, 722–734 (2007).

129. Kaigler, D., Wang, Z., Horger, K., Mooney, D. J. & Krebsbach, P. H. VEGF scaffolds enhance angiogenesis and bone regeneration in irradiated osseous defects. *J. Bone Miner. Res.* **21**, 735–44 (2006).

130. Ferrara, N., Gerber, H.-P. & LeCouter, J. The biology of VEGF and its receptors. *Nat. Med.* **9**, 669–76 (2003).

131. Hutton, D. L., Moore, E. M., Gimble, J. M. & Grayson, W. L. Platelet-derived growth factor and spatiotemporal cues induce development of vascularized bone tissue by adipose-derived stem cells. *Tissue Eng. Part A* **19**, 2076–86 (2013).

132. Amos, P. J. *et al.* Hypoxic culture and in vivo inflammatory environments affect the assumption of pericyte characteristics by human adipose and bone marrow progenitor cells. *AJP Cell Physiol.* **301**, C1378–C1388 (2011).

133. Takechi, M., Tatehara, S., Satomura, K., Fujisawa, K. & Nagayama, M. Effect of FGF-2 and melatonin on implant bone healing: a histomorphometric study. *J. Mater. Sci. Mater. Med.* **19**, 2949–52 (2008).

134. Aspenberg, P. & Lohmander, L. S. Fibroblast growth factor stimulates bone formation Bone induction studied in rats. *Acta Orthop.* **60**, 473–476 (1989).

135. Dyondi, D., Webster, T. J. & Banerjee, R. A nanoparticulate injectable hydrogel as a tissue engineering scaffold for multiple growth factor delivery for bone regeneration. *Int. J. Nanomedicine* **8**, 47–59 (2012).

136. Clark, R. A. F. Synergistic signaling from extracellular matrix-growth factor complexes. *J. Invest. Dermatol.* **128**, 1354–5 (2008).

137. Kang, H. *et al.* Insulin-like growth factor 2 promotes osteogenic cell differentiation in the parthenogenetic murine embryonic stem cells. *Tissue Eng. Part A* **18**, 331–41 (2012).

138. Srouji, S., Rachmiel, A., Blumenfeld, I. & Livne, E. Mandibular defect repair by TGF-beta and IGF-1 released from a biodegradable osteoconductive hydrogel. *J. Craniomaxillofac. Surg.* **33**, 79–84 (2005).

139. Xian, L. *et al.* Matrix IGF-1 maintains bone mass by activation of mTOR in mesenchymal stem cells. *Nat. Med.* **18**, 1095–101 (2012).

140. Crane, J. L. & Cao, X. Function of matrix IGF-1 in coupling bone resorption and formation. *J. Mol. Med. (Berl).* **92**, 107–15 (2014).

141. Lin, C.-Y. *et al.* The use of ASCs engineered to express BMP2 or TGF-β3 within scaffold constructs to promote calvarial bone repair. *Biomaterials* **34**, 9401–12 (2013).

142. Malafaya, P. B., Silva, G. A. & Reis, R. L. Natural-origin polymers as carriers and scaffolds for biomolecules and cell delivery in tissue engineering applications. *Adv. Drug Deliv. Rev.* **59**, 207–33 (2007).

143. Gunatillake, P. A., Adhikari, R. & Gadegaard, N. Biodegradable synthetic polymers for tissue engineering. *European Cells and Materials* **5**, 1–16 (2003).

144. Tessmar, J. K. & Göpferich, A. M. Matrices and scaffolds for protein delivery in tissue engineering. *Adv. Drug Deliv. Rev.* **59**, 274–91 (2007).

145. Raiche, A. . & Puleo, D. . In vitro effects of combined and sequential delivery of two bone growth factors. *Biomaterials* **25**, 677–685 (2004).

146. Geuze, R. E. *et al.* A differential effect of bone morphogenetic protein-2 and vascular endothelial growth factor release timing on osteogenesis at ectopic and orthotopic sites in a large-animal model. *Tissue Eng. Part A* **18**, 2052–62 (2012).

147. Uludag, H. *et al.* Implantation of recombinant human bone morphogenetic proteins with biomaterial carriers: A correlation between protein pharmacokinetics and osteoinduction in the rat ectopic model. *J. Biomed. Mater. Res.* **50**, 227–38 (2000).

148. Brown, K. V *et al.* Improving bone formation in a rat femur segmental defect by controlling bone morphogenetic protein-2 release. *Tissue Eng. Part A* **17**, 1735–46 (2011).

149. Shields, L. B. E. *et al.* Adverse effects associated with high-dose recombinant human bone morphogenetic protein-2 use in anterior cervical spine fusion. *Spine (Phila. Pa. 1976).* **31**, 542–547 (2006).

150. Cahill, K. S., Chi, J. H., Day, A. & Claus, E. B. Prevalence, complications, and hospital charges associated with use of bone-morphogenetic proteins in spinal fusion procedures. *JAMA* **302**, 58–66 (2009).

151. Border, W. A. & Ruoslahti, E. Transforming growth factor-beta in disease: the dark side of tissue repair. *J. Clin. Invest.* **90**, 1–7 (1992).

152. Saltzman, W. M. Growth-factor Delivery in Tissue Engineering. *MRS Bull.* **21**, 62–65 (1996).

153. Zieris, A. *et al.* FGF-2 and VEGF functionalization of starPEG–heparin hydrogels to modulate biomolecular and physical cues of angiogenesis. *Biomaterials* **31**, 7985–7994 (2010).

154. Lopac, S. K., Torres, M. P., Wilson-Welder, J. H., Wannemuehler, M. J. & Narasimhan, B. Effect of polymer chemistry and fabrication method on protein release and stability from polyanhydride microspheres. *J. Biomed. Mater. Res. - Part B Appl. Biomater.* **91**, 938–947 (2009).

155. Madurantakam, P. a., Rodriguez, I. a., Beckman, M. J., Simpson, D. G. & Bowlin, G. L. Evaluation of biological activity of bone morphogenetic proteins on exposure to commonly used electrospinning solvents. *J. Bioact. Compat. Polym.* **26**, 578–589 (2011).

156. Determan, A. S., Wilson, J. H., Kipper, M. J., Wannemuehler, M. J. & Narasimhan, B. Protein stability in the presence of polymer degradation products: Consequences for controlled release formulations. *Biomaterials* **27**, 3312–3320 (2006).

157. Jeon, O., Song, S. J., Kang, S.-W., Putnam, A. J. & Kim, B.-S. Enhancement of ectopic bone formation by bone morphogenetic protein-2 released from a heparin-conjugated poly(L-lactic-co-glycolic acid) scaffold. *Biomaterials* **28**, 2763–71 (2007).

158. Zhao, B. *et al.* Heparin potentiates the in Vivo ectopic bone formation induced by bone morphogenetic protein-2. *J. Biol. Chem.* **281**, 23246–23253 (2006).

159. Bhang, S. H., Ph, D. & Jeon, J. Heparin-Conjugated Fibrin as an Injectable System. *Tissue Eng. Part A* **16**, 1–10 (2010).

160. Whang, K., Goldstick, T. K. & Healy, K. E. A biodegradable polymer scaffold for delivery of osteotropic factors. *Biomaterials* **21**, 2545–51 (2000).

161. Nam, Y. S., Yoon, J. J. & Park, T. G. A novel fabrication method of macroporous biodegradable polymer scaffolds using gas foaming salt as a porogen additive. *J. Biomed. Mater. Res.* **53**, 1–7 (2000).

162. Schliephake, H., Weich, H. A., Schulz, J. & Gruber, R. In vitro characterization of a slow release system of polylactic acid and rhBMP2. *J. Biomed. Mater. Res. A* **83**, 455–62 (2007).

163. Gruber, R., Weich, H. A., Dullin, C. & Schliephake, H. Ectopic bone formation after implantation of a slow release system of polylactic acid and rhBMP-2. *Clin. Oral Implants Res.* **20**, 24–30 (2009).

164. Srouji, S. *et al.* Slow-release human recombinant bone morphogenetic protein-2 embedded within electrospun scaffolds for regeneration of bone defect: in vitro and in vivo evaluation. *Tissue Eng. Part A* **17**, 269–77 (2011).

165. Fu, Y.-C., Nie, H., Ho, M.-L., Wang, C.-K. & Wang, C.-H. Optimized bone regeneration based on sustained release from three-dimensional fibrous PLGA/HAp composite scaffolds loaded with BMP-2. *Biotechnol. Bioeng.* **99**, 996–1006 (2008).

166. Kim, B.-R., Nguyen, T. B. L., Min, Y.-K. & Lee, B.-T. In Vitro and In Vivo Studies of BMP-2-Loaded PCL-Gelatin-BCP Electrospun Scaffolds. *Tissue Eng. Part A* **20**, 3279–89 (2014).

167. Schofer, M. D. *et al.* Electrospun PLLA nanofiber scaffolds and their use in combination with BMP-2 for reconstruction of bone defects. *PLoS One* **6**, e25462 (2011).

168. Li, C., Vepari, C., Jin, H.-J., Kim, H. J. & Kaplan, D. L. Electrospun silk-BMP-2 scaffolds for bone tissue engineering. *Biomaterials* **27**, 3115–24 (2006).

169. Kim, S.-H., Turnbull, J. & Guimond, S. Extracellular matrix and cell signalling: the dynamic cooperation of integrin, proteoglycan and growth factor receptor. *J. Endocrinol.* **209**, 139–51 (2011).

170. Ruppert, R., Hoffmann, E. & Sebald, W. Human bone morphogenetic protein 2 contains a heparin-binding site which modifies its biological activity. *Eur. J. Biochem.* **237**, 295–302 (1996).

171. Rider, C. C. Heparin/heparan sulphate binding in the TGF-beta cytokine superfamily. *Biochem. Soc. Trans.* **34**, 458–60 (2006).

172. Bhakta, G. *et al.* Hyaluronic acid-based hydrogels functionalized with heparin that support controlled release of bioactive BMP-2. *Biomaterials* **33**, 6113–22 (2012).

173. Martino, M. M. & Hubbell, J. A. The 12th-14th type III repeats of fibronectin function as a highly promiscuous growth factor-binding domain. *FASEB J.* **24**, 4711–21 (2010).

174. Martino, M. M. *et al.* Engineering the growth factor microenvironment with fibronectin domains to promote wound and bone tissue healing. *Sci. Transl. Med.* **3**, 100ra89 (2011).

175. Hamilton, P. T. *et al.* Improved bone morphogenetic protein-2 retention in an injectable collagen matrix using bifunctional peptides. *PLoS One* **8**, e70715 (2013).

176. Haynes, C. A. & Norde, W. Globular proteins at solid/liquid interfaces. *Colloids Surfaces B Biointerfaces* **2**, 517–566 (1994).

177. King, W. J. & Krebsbach, P. H. Growth factor delivery: how surface interactions modulate release in vitro and in vivo. *Adv. Drug Deliv. Rev.* **64**, 1239–56 (2012).

178. De Geest, B. G., Sanders, N. N., Sukhorukov, G. B., Demeester, J. & De Smedt, S. C. Release mechanisms for polyelectrolyte capsules. *Chem. Soc. Rev.* **36**, 636–49 (2007).

179. Decher, G., Hong, J. D. & Schmitt, J. Buildup of ultrathin multilayer films by a self-assembly process: III. Consecutively alternating adsorption of anionic and cationic polyelectrolytes on charged surfaces. *Thin Solid Films* **210**–**211**, 831–835 (1992).

180. Benkirane-Jessel, N. *et al.* Short-time tuning of the biological activity of functionalized polyelectrolyte multilayers. *Adv. Funct. Mater.* **15**, 648–654 (2005).

181. Jessel, N. *et al.* Multiple and time-scheduled in situ DNA delivery mediated by beta-cyclodextrin embedded in a polyelectrolyte multilayer. *Proc. Natl. Acad. Sci. U. S. A.* **103**, 8618–21 (2006).

182. Lvov, Y., Ariga, K., Ichinose, I. & Kunitake, T. Assembly of Multicomponent Protein Films by Means of Electrostatic Layer-by-Layer Adsorption. *J. Am. Chem. Soc.* **117**, 6117–6123 (1995).

183. Holmes, C., Daoud, J., Bagnaninchi, P. O. & Tabrizian, M. Polyelectrolyte multilayer coating of 3D scaffolds enhances tissue growth and gene delivery: non-invasive and label-free assessment. *Adv. Healthc. Mater.* **3**, 572–80 (2014).

184. Macdonald, M. L. *et al.* Tissue integration of growth factor-eluting layer-by-layer polyelectrolyte multilayer coated implants. *Biomaterials* **32**, 1446–53 (2011).

185. Sakai, S., Yamada, Y., Yamaguchi, T., Ciach, T. & Kawakami, K. Surface immobilization of poly(ethyleneimine) and plasmid DNA on electrospun poly(L-lactic acid) fibrous mats using a layer-by-layer approach for gene delivery. *J. Biomed. Mater. Res. A* **88**, 281–7 (2009).

186. Yu, X., Khalil, A., Dang, P. N., Alsberg, E. & Murphy, W. L. Multilayered Inorganic Microparticles for Tunable Dual Growth Factor Delivery. *Adv. Funct. Mater.* **24**, 3082–3093 (2014).

187. Xu, X., Jha, A. K., Duncan, R. L. & Jia, X. Heparin-decorated, hyaluronic acid-based hydrogel particles for the controlled release of bone morphogenetic protein 2. *Acta Biomater.* **7**, 3050–9 (2011).

188. Luz, G. M., Boesel, L., del Campo, A. & Mano, J. F. Micropatterning of bioactive glass nanoparticles on chitosan membranes for spatial controlled biomineralization. *Langmuir* **28**, 6970–7 (2012).

189. Sheyn, D. *et al.* Gene-modified adult stem cells regenerate vertebral bone defect in a rat model. *Mol. Pharm.* **8**, 1592–601 (2011).

190. Li, Y. *et al.* The promotion of bone regeneration through positive regulation of angiogenic-osteogenic coupling using microRNA-26a. *Biomaterials* **34**, 5048–58 (2013).

191. Ishihara, A., Zekas, L. J., Litsky, A. S., Weisbrode, S. E. & Bertone, A. L. Dermal fibroblast-mediated BMP2 therapy to accelerate bone healing in an equine osteotomy model. *J. Orthop. Res.* **28**, 403–11 (2010).

192. Elangovan, S. *et al.* The enhancement of bone regeneration by gene activated matrix encoding for platelet derived growth factor. *Biomaterials* **35**, 737–47 (2014).

193. Park, J. *et al.* The effect on bone regeneration of a liposomal vector to deliver BMP-2 gene to bone grafts in peri-implant bone defects. *Biomaterials* **28**, 2772–82 (2007).

194. Kretlow, J. D. & Mikos, A. G. Review: mineralization of synthetic polymer scaffolds for bone tissue engineering. *Tissue Eng.* **13**, 927–38 (2007).

195. Kokubo, T. *et al.* Ca,P-rich layer formed on high-strength bioactive glass-ceramic A-W. *J. Biomed. Mater. Res.* **24**, 331–43 (1990).

196. Barrère, F. *et al.* Osteointegration of biomimetic apatite coating applied onto dense and porous metal implants in femurs of goats. *J. Biomed. Mater. Res. B. Appl. Biomater.* **67**, 655–65 (2003).

197. Park, S.-B., Hasegawa, U., van der Vlies, A. J., Sung, M.-H. & Uyama, H. Preparation of poly(γ-glutamic acid)/hydroxyapatite monolith via biomineralization for bone tissue engineering. *J. Biomater. Sci. Polym. Ed.* **25**, 1875–90 (2014).

198. Davis, H. E., Case, E. M., Miller, S. L., Genetos, D. C. & Leach, J. K. Osteogenic response to BMP-2 of hMSCs grown on apatite-coated scaffolds. *Biotechnol. Bioeng.* **108**, 2727–35 (2011).

199. Deplaine, H. *et al.* Biomimetic hydroxyapatite coating on pore walls improves osteointegration of poly(L-lactic acid) scaffolds. *J. Biomed. Mater. Res. B. Appl. Biomater.* **101**, 173–86 (2013).

200. Liu, Y., Hunziker, E. B., Layrolle, P., De Bruijn, J. D. & De Groot, K. Bone morphogenetic protein 2 incorporated into biomimetic coatings retains its biological activity. *Tissue Eng.* **10**, 101–8 (2004).

201. Szentivanyi, A., Chakradeo, T., Zernetsch, H. & Glasmacher, B. Electrospun cellular microenvironments: Understanding controlled release and scaffold structure. *Adv. Drug Deliv. Rev.* **63**, 209–20 (2011).

202. Bajpai, A. K., Shukla, S. K., Bhanu, S. & Kankane, S. Responsive polymers in controlled drug delivery. *Prog. Polym. Sci.* **33**, 1088–1118 (2008).

203. Holloway, J. L., Ma, H., Rai, R. & Burdick, J. A. Modulating hydrogel crosslink density and degradation to control bone morphogenetic protein delivery and in vivo bone formation. *J. Control. Release* **191**, 63–70 (2014).

204. He, X., Ma, J. & Jabbari, E. Effect of grafting RGD and BMP-2 protein-derived peptides to a hydrogel substrate on osteogenic differentiation of marrow stromal cells. *Langmuir* **24**, 12508–12516 (2008).

205. Patel, N. *et al.* Spatially controlled cell engineering on biodegradable polymer surfaces. *FASEB J.* **12**, 1447–54 (1998).

206. Segura, T., Chung, P. H. & Shea, L. D. DNA delivery from hyaluronic acid-collagen hydrogels via a substrate-mediated approach. *Biomaterials* **26**, 1575–84 (2005).

207. Zhang, H., Migneco, F., Lin, C.-Y. & Hollister, S. J. Chemically-conjugated bone morphogenetic protein-2 on three-dimensional polycaprolactone scaffolds stimulates osteogenic activity in bone marrow stromal cells. *Tissue Eng. Part A* **16**, 3441–8 (2010).

208. Shah, N. J. *et al.* Adaptive growth factor delivery from a polyelectrolyte coating promotes synergistic bone tissue repair and reconstruction. *Proc. Natl. Acad. Sci. U. S. A.* **111**, 12847–52 (2014).

209. Sant, S., Hancock, M. J., Donnelly, J. P., Iyer, D. & Khademhosseini, A. Biomimetic gradient hydrogels for tissue engineering. *Can. J. Chem. Eng.* **88**, 899–911 (2010).

210. Kapur, T. A. & Shoichet, M. S. Immobilized concentration gradients of nerve growth factor guide neurite outgrowth. *J. Biomed. Mater. Res. A* **68**, 235–43 (2004).

211. De Long, S. A., Gobin, A. S. & West, J. L. Covalent immobilization of RGDS on hydrogel surfaces to direct cell alignment and migration. *J. Control. Release* **109**, 139–148 (2005).

212. Chen, R. R., Silva, E. A., Yuen, W. W. & Mooney, D. J. Spatio-temporal VEGF and PDGF delivery patterns blood vessel formation and maturation. *Pharm. Res.* **24**, 258–64 (2007).

213. Simmons, C. A., Alsberg, E., Hsiong, S., Kim, W. J. & Mooney, D. J. Dual growth factor delivery and controlled scaffold degradation enhance in vivo bone formation by transplanted bone marrow stromal cells. *Bone* **35**, 562–9 (2004).

214. Huang, Y.-C., Kaigler, D., Rice, K. G., Krebsbach, P. H. & Mooney, D. J. Combined angiogenic and osteogenic factor delivery enhances bone marrow stromal cell-driven bone regeneration. *J. Bone Miner. Res.* **20**, 848–57 (2005).

215. He, X., Yang, X. & Jabbari, E. Combined effect of osteopontin and BMP-2 derived peptides grafted to an adhesive hydrogel on osteogenic and vasculogenic differentiation of marrow stromal cells. *Langmuir* **28**, 5387–97 (2012).

216. Yilgor, P., Hasirci, N. & Hasirci, V. Sequential BMP-2/BMP-7 delivery from polyester nanocapsules. *J. Biomed. Mater. Res. A* **93**, 528–36 (2009).

217. Wilson, C. G., Martín-Saavedra, F. M., Vilaboa, N. & Franceschi, R. T. Advanced BMP gene therapies for temporal and spatial control of bone regeneration. *J. Dent. Res.* **92**, 409–17 (2013).

218. Epstein, N. E. Complications due to the use of BMP/INFUSE in spine surgery: The evidence continues to mount. *Surg. Neurol. Int.* **4**, S343-52 (2013).

219. Mroz, T. E., Wang, J. C., Hashimoto, R. & Norvell, D. C. Complications related to osteobiologics use in spine surgery: a systematic review. *Spine (Phila. Pa. 1976).* **35**, S86-104 (2010).

220. Vacanti, J. P. & Langer, R. Tissue engineering: the design and fabrication of living replacement devices for surgical reconstruction and transplantation. *Lancet* **354**, 32–34 (1999).

221. Lanza, R., Langer, R. & Vacanti, J. *Principles of tissue engineering*. (Academic Press, 2011).

222. Beachley, V. Z. *et al.* Tissue matrix arrays for high-throughput screening and systems analysis of cell function. *Nat. Methods* 7–9 (2015). doi:10.1038/nmeth.3619

223. Fang, F. & Kevin Chung. An Evolutionary Perspective on the History of Flap Reconstruction in the Upper Extremity. *Hand Clin.* **30**, 1–21 (2014).

224. Shah, A. M., Jung, H. & Skirboll, S. Materials used in cranioplasty: a history and analysis. *Neurosurg. Focus* **36**, 1–7 (2014).

225. Urist, M. R. & Strates, B. S. Bone morphogenetic protein. *J. Dent. Res.* **50**, 1392–406 (2009).

226. Zara, J. N. *et al.* High Doses of Bone Morphogenetic Protein 2 Induce Structurally Abnormal Bone and Inflammation In Vivo. **17**, (2011).

227. Jensen, T., Schou, S., Stavropoulos, A., Terheyden, H. & Holmstrup, P. Maxillary sinus floor augmentation\with Bio-Oss or Bio-Oss mixed with autogenous bone as graft: A systematic review. *Clin. Oral Implants Res.* **23**, 263–273 (2012).

228. Orsini, G. *et al.* Maxillary Sinus Augmentation with Bio-Oss ○π Particles : A Light , Scanning , and Transmission Electron Microscopy Study in Man. 448–457 (2005). doi:10.1002/jbm.b.30196

229. PENEL, G., DELFOSSE, C., DESCAMPS, M. & LEROY, G. Composition of bone and apatitic biomaterials as revealed by intravital Raman microspectroscopy. *Bone* **36**, 893–901 (2005).

230. Benders, K. E. M. *et al.* Extracellular matrix scaffolds for cartilage and bone regeneration. *Trends Biotechnol.* **31**, 169–176 (2013).

231. Datta, N., Holtorf, H. L., Sikavitsas, V. I., Jansen, J. A. & Mikos, A. G. Effect of bone extracellular matrix synthesized in vitro on the osteoblastic differentiation of marrow stromal cells. *Biomaterials* **26**, 971–977 (2005).

232. Nyberg, E. L., Rindone, A., Dorafshar, A. & Grayson, W. L. Comparison of 3D-Printed Poly-ε-caprolactone Scaffolds Functionalized with Tricalcium Phosphate, Hydroxyapatite, Bio-Oss, or Decellularized Bone Matrix. *Tissue Eng. Part A* (2016). doi:10.1089/ten.TEA.2016.0418

233. Más Estellés, J., Vidaurre, A., Meseguer Dueñas, J. M. & Castilla Cortázar, I. Physical characterization of polycaprolactone scaffolds. *J. Mater. Sci. Mater. Med.* **19**, 189–195 (2008).

234. Phillipson, K. Ageing and Crystallisation of Polycaprolactone Doctor of Philosophy. (2014).

235. Bezwada, R. S. *et al.* Monocryl?? suture, a new ultra-pliable absorbable monofilament suture. *Biomaterials* **16**, 1141–1148 (1995).

236. Williams, J. M. *et al.* Bone tissue engineering using polycaprolactone scaffolds fabricated via selective laser sintering. *Biomaterials* **26**, 4817–4827 (2005).

237. Shor, L., Güçeri, S., Wen, X., Gandhi, M. & Sun, W. Fabrication of three-dimensional polycaprolactone/hydroxyapatite tissue scaffolds and osteoblast-scaffold interactions in vitro. *Biomaterials* **28**, 5291–5297 (2007).

238. Sun, H., Mei, L., Song, C., Cui, X. & Wang, P. The in vivo degradation, absorption and excretion of PCL-based implant. *Biomaterials* **27**, 1735–1740 (2006).

239. Hernández, A. R., Contreras, O. C., Acevedo, J. C. & Moreno, L. G. N. Poly(ε-caprolactone) Degradation Under Acidic and Alkaline Conditions. *Am. J. Polym. Sci.* **3**, 70–75 (2013).

240. Yeo, A., Wong, W. J. & Teoh, S. Surface modification of PCL-TCP scaffolds in rabbit calvaria defects : Evaluation of scaffold degradation profile , biomechanical properties and bone healing patterns. (2009). doi:10.1002/jbm.a.32633

241. Woodruff, M. A. & Hutmacher, D. W. The return of a forgotten polymer—Polycaprolactone in the 21st century. *Prog. Polym. Sci.* **35**, 1217–1256 (2010).

242. Long, J., Gholizadeh, H., Lu, J., Bunt, C. & Seyfoddin, A. Application of Fused Deposition Modelling (FDM) Method of 3D Printing in Drug Delivery. 433–439 (2017). doi:10.2174/1381612822666161026.1

243. Hung, B. P. *et al.* Platelet-Derived Growth Factor BB Enhances Osteogenesis of Adipose-Derived but Not Bone Marrow-Derived Mesenchymal Stromal/Stem Cells. *Stem Cells* **33**, 2773–2784 (2015).

244. Vetsch, J. R., Paulsen, S. J., Müller, R. & Hofmann, S. Effect of fetal bovine serum on mineralization in silk fibroin scaffolds. *Acta Biomater.* **13**, 277–285 (2015).

245. Hutton, D. L. *et al.* Vascular morphogenesis of adipose-derived stem cells is mediated by heterotypic cell-cell interactions. *Tissue Eng. Part A* **18**, 1729–40 (2012).

246. Hutton, D. L. & Grayson, W. L. Hypoxia Inhibits De Novo Vascular Assembly of Adipose-derived Stromal/Stem Cell Populations but Promotes Growth Of Pre-Formed Vessels. *Tissue Eng. Part A* **22**, 1–26 (2015).

247. Allori, A. C., Sailon, A. M. & Warren, S. M. Biological basis of bone formation, remodeling, and repair-part II: extracellular matrix. *Tissue Eng. Part B. Rev.* **14**, 275–283 (2008).

248. Mendez, A. *et al.* Phenotyping the Microvasculature in Critical-Sized Calvarial Defects via Multimodal Optical Imaging. *Tissue Eng. Part C MethodsTissue Eng* **24**, 430–440 (2018).

249. Castro, F. P. *et al.* A Cost Analysis of Two Anterior Cervical Fusion Procedures. *J. Spinal Disord.* **13**, 511–514 (2000).

250. Goulet, J. A., Senunas, L. E., Desilva, G. L., Lou, M. & Greenfield, K. H. Autogenous Iliac Crest Bone Graft Complications and Functional Assessment. *Clin. Orthop. Relat. Res.* 76–81 (1997).

251. Younger, E. M. & Chapman, M. W. Morbidity at Bone Graft Donor Sites. *J. Orthop. Trauma* **3**, 192–195 (1989).

252. Banwart, J. C., Asher, M. A. & Hassanein, R. S. Iliac Crest Bone Graft Harvest Donor Site Morbidity: A Statistical Evaluation. *Spine (Phila. Pa. 1976).* **20**, 1055–1060 (1995).

253. Chen, Q. & Thouas, G. A. Metallic implant biomaterials. *Mater. Sci. Eng. R* **87**, 1–57 (2015).

254. Grayson, W. L., Martens, T. P., Eng, G. M., Radisic, M. & Vunjak-Novakovic, G. Biomimetic approach to tissue engineering. *Semin. Cell Dev. Biol.* **20**, 665–73 (2009).

255. Inzana, J. a. *et al.* 3D printing of composite calcium phosphate and collagen scaffolds for bone regeneration. *Biomaterials* **35**, 4026–4034 (2014).

256. Cox, S. C., Thornby, J. A., Gibbons, G. J., Williams, M. A. & Mallick, K. K. 3D printing of porous hydroxyapatite scaffolds intended for use in bone tissue engineering applications. *Mater. Sci. Eng. C. Mater. Biol. Appl.* **47**, 237–47 (2015).

257. Trombetta, R., Inzana, J. A., Schwarz, E. M., Kates, S. L. & Awad, H. A. 3D Printing of Calcium Phosphate Ceramics for Bone Tissue Engineering and Drug Delivery. *Ann. Biomed. Eng.* 1–22 (2016). doi:10.1007/s10439-016-1678-3

258. Le Blanc, K. *et al.* Fetal mesenchymal stem-cell engraftment in bone after in utero transplantation in a patient with severe osteogenesis imperfecta. *Transplantation* **79**, 1607–1614 (2005).

259. Mott, E. J. *et al.* Digital micromirror device (DMD) -based 3D printing of poly (propylene fumarate) scaffolds. *Mater. Sci. Eng. C* **61**, 301–311 (2016).

260. Sun, Q., Rizvi, G. M., Bellehumeur, C. T. & Gu, P. Effect of processing conditions on the bonding quality of FDM polymer filaments. *Rapid Prototyp. J.* **15**, 72–80 (2008).

261. Kruth, J.-P., Mercelis, P., Vaerenbergh, J. Van, Froyen, L. & Rombouts, M. Binding mechanisms in selective laser sintering and selective laser melting. *Rapid Prototyp. J.* **11**, 26–36 (2013).

262. Ifkovits, J. L. & Burdick, J. A. Review: Photopolymerizable and Degradable. *Tissue Eng.* **13**, 2369–2385 (2007).

263. Gibson, I., Rosen, D. & Stucker, B. The Impact of Low-Cost AM Systems. in *Additive Manufacturing Technologies* 293–301 (Springer, 2015). doi:10.1007/978-1-4939-2113-3

264. Seyednejad, H. *et al.* Preparation and characterization of a three-dimensional printed scaffold based on a functionalized polyester for bone tissue engineering applications. *Acta Biomater.* **7**, 1999–2006 (2011).

265. He, H., Zhang, J., Mi, X., Hu, Y. & Gu, X. Rapid prototyping for tissue-engineered bone scaffold by 3D printing and biocompatibility study. *Int. J. Clin. Exp. Med.* **8**, 11777–11785 (2015).

266. Pitt, C. G. *et al.* Aliphatic Polyesters . I . The Degradation of Poly (e- caprolactone) In Vivo. *J. Appl. Polym. Sci.* **26**, 3779–3787 (1981).

267. Calvert, J. W. *et al.* Characterization of osteoblast-like behavior of cultured bone marrow stromal cells on various polymer surfaces. *J. Biomed. Mater. Res.* **52**, 279–284 (2000).

268. Yoon, E., Dhar, S., Chun, D. E., Gharibjanian, N. a & Evans, G. R. D. In vivo osteogenic potential of human adipose-derived stem cells/poly lactide-co-glycolic acid constructs for bone regeneration in a rat critical-sized calvarial defect model. *Tissue Eng.* **13**, 619–27 (2007).

269. Suwandi, J. S., Toes, R. E. M., Nikolic, T. & Roep, B. O. Inducing tissue specific tolerance in autoimmune disease with tolerogenic dendritic cells. *J. Biomed. Mater. Res. - Part A* **33**, 97–103 (2015).

270. Rai, B. *et al.* Biomaterials Differences between in vitro viability and differentiation and in vivo bone-forming ef fi cacy of human mesenchymal stem cells cultured on PCL e TCP scaffolds. *Biomaterials* **31**, 7960–7970 (2010).

271. Polini, A., Pisignano, D., Parodi, M., Quarto, R. & Scaglione, S. Osteoinduction of human mesenchymal stem cells by bioactive composite scaffolds without supplemental osteogenic growth factors. *PLoS One* **6**, 1–8 (2011).

272. Park, S. A., Lee, S. H. & Kim, W. D. Fabrication of porous polycaprolactone/hydroxyapatite (PCL/HA) blend scaffolds using a 3D plotting system for bone tissue engineering. *Bioprocess Biosyst. Eng.* **34**, 505–513 (2011).

273. Guarino, V. *et al.* The role of hydroxyapatite as solid signal on performance of PCL porous scaffolds for bone tissue regeneration. *J. Biomed. Mater. Res. - Part B Appl. Biomater.* **86**, 548–557 (2008).

274. Causa, F. *et al.* Poly-??-caprolactone/hydroxyapatite composites for bone regeneration: In vitro characterization and human osteoblast response. *J. Biomed. Mater. Res. - Part A* **76**, 151–162 (2006).

275. Vorndran, E. *et al.* 3D Powder Printing of β-Tricalcium Phosphate Ceramics Using Different Strategies. *Adv. Eng. Mater.* **10**, B67–B71 (2008).

276. Wang, L. *et al.* Osteogenesis and angiogenesis of tissue-engineered bone constructed by prevascularized β-tricalcium phosphate scaffold and mesenchymal stem cells. *Biomaterials* **31**, 9452–61 (2010).

277. Detsch, R. *et al.* In vitro -Osteoclastic Activity Studies on Surfaces of 3D Printed Calcium Phosphate Scaffolds. *J. Biomater. Appl.* **26**, 359–380 (2011).

278. von Doernberg, M. C. *et al.* In vivo behavior of calcium phosphate scaffolds with four different pore sizes. *Biomaterials* **27**, 5186–5198 (2006).

279. Sathyavathi, R. *et al.* Raman spectroscopic sensing of carbonate intercalation in breast microcalcifications at stereotactic biopsy. *Sci Rep* **5**, 9907 (2015).

280. Chuenjitkuntaworn, B. *et al.* Polycaprolactone/hydroxyapatite composite scaffolds: Preparation, characterization, and in vitro and in vivo biological responses of human primary bone cells. *J. Biomed. Mater. Res. - Part A* **94**, 241–251 (2010).

281. Asa 'ad, F. *et al.* 3D-Printed Scaffolds and Biomaterials: Review of Alveolar Bone Augmentation and Periodontal Regeneration Applications. **2016**, (2016).

282. Warnke, P. H. *et al.* Ceramic scaffolds produced by computer-assisted 3D printing and sintering: Characterization and biocompatibility investigations. *J. Biomed. Mater. Res. - Part B Appl. Biomater.* **93**, 212–217 (2010).

283. Huri, P. Y., Ozilgen, B. A., Hutton, D. L. & Grayson, W. L. Scaffold pore size modulates in vitro osteogenesis of human adipose-derived stem/stromal cells. *Biomed. Mater.* **9**, 045003 (2014).

284. Wesełucha-Birczyńska, A. *et al.* Raman spectroscopy and the material study of nanocomposite membranes from poly(ε-caprolactone) with biocompatibility testing in osteoblast-like cells. *Analyst* 2311–2320 (2015). doi:10.1039/c4an02284j

285. Goldstein, S. A. The mechanical properties of trabecular bone: Dependence on anatomic location and function. *J. Biomech.* **20**, 1055–1061 (1987).

286. Zein, I., Hutmacher, D. W., Tan, K. C. & Teoh, S. H. Fused deposition modeling of novel scaffold architectures for tissue engineering applications. *Biomaterials* **23**, 1169–1185 (2002).

287. Shor, L. *et al.* Precision extruding deposition (PED) fabrication of polycaprolactone (PCL) scaffolds for bone tissue engineering. *Biofabrication* **1**, 015003 (2009).

288. Kim, J. Y. *et al.* Cell adhesion and proliferation evaluation of SFF-based biodegradable scaffolds fabricated using a multi-head deposition system. *Biofabrication* **1**, 015002 (2009).

289. Azevedo, M. C., Reis, R. L., Claase, M. B., Grijpma, D. W. & Feijen, J. Development and properties of polycaprolactone/hydroxyapatite composite biomaterials. *J. Mater. Sci. Mater. Med.* **14**, 103–107 (2003).

290. Eosoly, S., Lohfeld, S. & Brabazon, D. Effect of Hydroxyapatite on Biodegradable Scaffolds Fabricated by SLS. *Key Eng. Mater.* **396**–**398**, 659–662 (2009).

291. Morris, M. D. & Mandair, G. S. Raman assessment of bone quality. *Clin. Orthop. Relat. Res.* **469**, 2160–2169 (2011).

292. Hoppe, A., Güldal, N. S. & Boccaccini, A. R. A review of the biological response to ionic dissolution products from bioactive glasses and glass-ceramics. *Biomaterials* **32**, 2757–2774 (2011).

293. Woodruff, M. A. & Hutmacher, D. W. The return of a forgotten polymer - Polycaprolactone in the 21st century. *Prog. Polym. Sci.* **35**, 1217–1256 (2010).

294. Rumpel, E. *et al.* The biodegradation of hydroxyapatite bone graft substitutes in vivo. *Folia Morphol. (Warsz).* **65**, 43–48 (2006).

295. Arinzeh, T. L., Tran, T., Mcalary, J. & Daculsi, G. A comparative study of biphasic calcium phosphate ceramics for human mesenchymal stem-cell-induced bone formation. *Biomaterials* **26**, 3631–3638 (2005).

296. Albrecht, L. D., Sawyer, S. W. & Soman, P. Developing 3D Scaffolds in the Field of Tissue Engineering to Treat Complex Bone Defects. *3D Print. Addit. Manuf.* **3**, 106–112 (2016).

297. Castro, N., Goldstein, P. & Cooke, M. N. Synthesis and manufacture of photocrosslinkable poly(caprolactone)-based three-dimensional scaffolds for tissue engineering applications. *Adv. Biosci. Biotechnol.* **02**, 167–173 (2011).

298. Laurencin, C. T., Ambrosio, A. M. A., Borden, M. D. & Cooper, J. A. Tissue engineering: orthopedic applications. *Annu. Rev. Biomed. Eng.* **1**, 19–46 (1999).

299. Rouwkema, J. & Khademhosseini, A. Vascularization and Angiogenesis in Tissue Engineering: Beyond Creating Static Networks. *Trends Biotechnol.* **34**, 733–745 (2016).

300. Novosel, E. C., Kleinhans, C. & Kluger, P. J. Vascularization is the key challenge in tissue engineering. *Adv. Drug Deliv. Rev.* **63**, 300–311 (2011).

301. Zawicki, D. F., Jain, R. K., Schmid-Schoenbein, G. W. & Chien, S. Dynamics of neovascularization in normal tissue. *Microvasc. Res.* **21**, 27–47 (1981).

302. Helmlinger, G., Yuan, F., Dellian, M. & Rakesh Jain. Interstitial pH and pO2 gradients in solid tumors in vivo: High-resolution measurments reveal a lack of correlation. *Nat. Med.* **3**, 177–182 (1997).

303. Miller, J. S. *et al.* Rapid casting of patterned vascular networks for perfusable engineered three-dimensional tissues. *Nat. Mater.* **11**, 768–774 (2012).

304. Fan, H., Zeng, X., Wang, X., Zhu, R. & Pei, G. Efficacy of prevascularization for segmental bone defect repair using beta-tricalcium phosphate scaffold in rhesus monkey. *Biomaterials* **35**, 7407–7415 (2014).

305. Laschke, M. W. & Menger, M. D. Prevascularization in tissue engineering: Current concepts and future directions. *Biotechnol. Adv.* **34**, 112–121 (2016).

306. Lesman, A. *et al.* Biomaterials Engineering vessel-like networks within multicellular fi brin-based constructs. **32**, 7856–7869 (2011).

307. Tsigkou, O. *et al.* Engineered vascularized bone grafts. *Proc. Natl. Acad. Sci.* **107**, 3311–3316 (2010).

308. Correia, C. *et al.* In vitro model of vascularized bone: Synergizing vascular development and osteogenesis. *PLoS One* **6**, 1–9 (2011).

309. Waters, J. P. *et al.* In vitro self-Assembly of human pericyte-supported endothelial microvessels in three-dimensional coculture: A simple model for interrogating endothelial-pericyte interactions. *J. Vasc. Res.* **50**, 324–331 (2013).

310. Hutton, D. L. D. *et al.* Vascular morphogenesis of adipose-derived stem cells is mediated by heterotypic cell-cell interactions. *Tissue Eng. Part A* **18**, 1729–40 (2012).

311. Mitchell, J. B. *et al.* Immunophenotype of Human Adipose-Derived Cells: Temporal Changes in Stromal-Associated and Stem Cell-Associated Markers. *Stem Cells* **24**, 376–385 (2006).

312. Boquest, A. C., Noer, A., Sørensen, A. L., Vekterud, K. & Collas, P. CpG methylation profiles of endothelial cell-specific gene promoter regions in adipose tissue stem cells suggest limited differentiation potential toward the endothelial cell lineage. *Stem Cells* **25**, 852–61 (2007).

313. Fischer, L. J. *et al.* Endothelial Differentiation of Adipose-Derived Stem Cells: Effects of Endothelial Cell Growth Supplement and Shear Force. *J. Surg. Res.* **152**, 157–166 (2009).

314. Amos, P. J. *et al.* IFATS collection: The role of human adipose-derived stromal cells in inflammatory microvascular remodeling and evidence of a perivascular phenotype. *Stem Cells* **26**, 2682–90 (2008).

315. Kelly-Goss, M. R., Sweat, R. S., Stapor, P. C., Peirce, S. M. & Murfee, W. L. Targeting pericytes for angiogenic therapies. *Microcirculation* **21**, 345–357 (2014).

316. Hutton, D. L. *et al.* Tumor necrosis factor improves vascularization in osteogenic grafts engineered with human adipose-derived stem/stromal cells. *PLoS One* **9**, 1–9 (2014).

317. Gawlitta, D. *et al.* Hypoxia Impedes Vasculogenesis of In Vitro Engineered Bone. *Tissue Eng. Part A* **18**, 208–218 (2012).

318. Griffith, C. K. & George, S. C. The effect of hypoxia on in vitro prevascularization of a thick soft tissue. *Tissue Eng. Part A* **15**, 2423–2434 (2009).

319. Dubois, S. G. *et al.* Isolation of human adipose-derived stem cells from biopsies and liposuction specimens. in *Methods in molecular biology (Clifton, N.J.)* **449**, 69–79 (2008).

320. Niemistö, A., Dunmire, V., Yli-Harja, O., Zhang, W. & Shmulevich, I. Robust quantification of in vitro angiogenesis through image analysis. *IEEE Trans. Med. Imaging* **24**, 549–553 (2005).

321. Ozerdem, U. & Stallcup, W. B. Early contribution of pericytes to angiogenic sprouting and tube formation. *Angiogenesis* **6**, 241–249 (2003).

322. Stratman, A. N., Malotte, K. M., Mahan, R. D., Davis, M. J. & Davis, G. E. Pericyte recruitment during vasculogenic tube assembly stimulates endothelial basement membrane matrix formation. *Blood* **114**, 5091–101 (2009).

323. Ribatti, D., Nico, B. & Crivellato, E. The role of pericytes in angiogenesis. *Int. J. Dev. Biol.* **55**, 261–268 (2011).

324. Phng, L.-K. & Gerhardt, H. Angiogenesis: a team effort coordinated by notch. *Dev. Cell* **16**, 196–208 (2009).

325. Bergers, G. & Song, S. The role of pericytes in blood-vessel formation and maintenance. *Neuro. Oncol.* **7**, 452–64 (2005).

326. Newman, a. C., Nakatsu, M. N., Chou, W., Gershon, P. D. & Hughes, C. C. W. The requirement for fibroblasts in angiogenesis: fibroblast-derived matrix proteins are essential for endothelial cell lumen formation. *Mol. Biol. Cell* **22**, 3791–3800 (2011).

327. Franco, M. *et al.* Pericytes promote endothelial cell survival through induction of autocrine VEGF-A signaling and Bcl-w expression. *Blood* **118**, 2906–2917 (2012).

328. Isik, F. F., Gibran, N. S., Jang, Y. C., Sandell, L. & Schwartz, S. M. Vitronectin decreases microvascular endothelial cell apoptosis. *J. Cell. Physiol.* **175**, 149–155 (1998).

329. Fraisl, P., Mazzone, M., Schmidt, T. & Carmeliet, P. Regulation of Angiogenesis by Oxygen and Metabolism. *Dev. Cell* **16**, 167–179 (2009).

330. Zhang, J., Tan, Z. & Tran, N. D. Chemical hypoxia-ischemia induces apoptosis in cerebromicrovascular endothelial cells. *Brain Res.* **877**, 134–140 (2000).

331. Ezhilarasan, R., Mohanam, I., Govindarajan, K. & Mohanam, S. Glioma cells suppress hypoxia-induced endothelial cell apoptosis and promote the angiogenic process. *Int. J. Oncol.* **30**, 701–707 (2007).

332. Parenti, A., Brogelli, L., Filippi, S., Donnini, S. & Ledda, F. Effect of hypoxia and endothelial loss on vascular smooth muscle cell responsiveness to VEGF-A: role of flt -1 / VEGF-receptor-1. *Cardiovasc. Res.* **55**, 201–212 (2002).

333. Farris, A., Rindone, A. & Grayson, W. Oxygen Delivering Biomaterials for Tissue Engineering. *J. Mater. Chem. B* **4**, (2016).

334. Cook, C. A., Hahn, K. C., Morrissette-McAlmon, J. B. F. & Grayson, W. L. Oxygen delivery from hyperbarically loaded microtanks extends cell viability in anoxic environments. *Biomaterials* **52**, 376–384 (2015).

335. Nakatsu, M. N. *et al.* Angiogenic sprouting and capillary lumen formation modeled by human umbilical vein endothelial cells (HUVEC) in fibrin gels: The role of fibroblasts and Angiopoietin-1. *Microvasc. Res.* **66**, 102–112 (2003).

336. Chen, X. *et al.* Prevascularization of a fibrin-based tissue construct accelerates the formation of functional anastomosis with host vasculature. *Tissue Eng. Part A* **15**, 1363–1371 (2009).

337. Carmeliet, P. Angiogenesis in health and disease. *Nat. Med.* **9**, 653–660 (2003).

338. Guimarães-Camboa, N. *et al.* Pericytes of Multiple Organs Do Not Behave as Mesenchymal Stem Cells In Vivo. *Cell Stem Cell* 1–15 (2017). doi:10.1016/j.stem.2016.12.006

339. Snippert, H. J. & Clevers, H. Tracking adult stem cells. *EMBO Rep* **12**, 113–122 (2011).

340. Topper, J. N. & Gimbrone, M. a. Blood flow and vascular gene expression: fluid shear stress as a modulator of endothelial phenotype. *Mol. Med. Today* **5**, 40–46 (1999).

341. Jain, R. K. Molecular regulation of vessel maturation. *Nat Med* **9**, 685–693 (2003).

342. Hashambhoy, Y. L., Chappell, J. C., Peirce, S. M., Bautch, V. L. & Mac Gabhann, F. Computational modeling of interacting VEGF and soluble VEGF receptor concentration gradients. *Front. Physiol.* **2**, 62 (2011).

343. Peirce, S. M., Mac Gabhann, F. & Bautch, V. L. Integration of experimental and computational approaches to sprouting angiogenesis. *Curr. Opin. Hematol.* **19**, 184–91 (2012).

344. Nör, J. E., Christensen, J., Mooney, D. J. & Polverini, P. J. Vascular endothelial growth factor (VEGF)-mediated angiogenesis is associated with enhanced endothelial cell survival and induction of Bcl-2 expression. *Am. J. Pathol.* **154**, 375–384 (1999).

345. Schemitsch, E. H. Size Matters: Defining Critical in Bone Defect Size! *J. Orthop. Trauma* **31**, S20–S22 (2017).

346. Marbacher, S., Andres, R. H., Fathi, A.-R. & Fandino, J. Primary Reconstruction of Open Depressed Skull Fractures With Titanium Mesh. *J. Craniofac. Surg.* **19**, 490–495 (2008).

347. Webb, K., Hlady, V. & Tresco, P. A. Relationships among cell attachment, spreading, cytoskeletal organization, and migration rate for anchorage-dependent cells on model surfaces. *J. Biomed. Mater. Res.* **49**, 362–368 (2000).

348. Morrish, R. B. *et al.* Osteonecrosis in patients irradiated for head and neck carcinoma. *Cancer* **47**, 1980–1983 (1981).

349. Asatrian, G., Pham, D., Hardy, W. R., James, A. W. & Peault, B. Stem cell technology for bone regeneration: Current status and potential applications. *Stem Cells Cloning Adv. Appl.* **8**, 39–48 (2015).

350. Brocher, J. *et al.* Inferior ectopic bone formation of mesenchymal stromal cells from adipose tissue compared to bone marrow: Rescue by chondrogenic pre-induction. *Stem Cell Res.* **11**, 1393–1406 (2013).

351. Brennan, M. A. *et al.* Inferior In Vivo Osteogenesis and Superior Angiogeneis of Human Adipose Tissue: A Comparison with Bone Marrow-Derived Stromal Stem Cells Cultured in Xeno-Free Conditions. *Stem Cells Transl. Med.* **6**, 2160–2172 (2017).

352. Chan, C. K. F. *et al.* Identification of the Human Skeletal Stem Cell. *Cell* **175**, 43-56.e21 (2018).

353. Bourin, P. *et al.* Stromal cells from the adipose tissue-derived stromal vascular fraction and culture expanded adipose tissue-derived stromal / stem cells : a joint statement of the International Federation for Adipose Therapeutics and Science (IFATS) and the Internation. *J. Cytotherapy* **15**, 641–648 (2013).

354. Cornejo, A. *et al.* Effect of Adipose Tissue-Derived Osteogenic and Endothelial Cells on Bone Allograft Osteogenesis and Vascularization in Critical-Sized Calvarial Defects. *Tissue Eng. Part A* **18**, 1552–1561 (2012).

355. Unger, R. E. *et al.* Tissue-like self-assembly in cocultures of endothelial cells and osteoblasts and the formation of microcapillary-like structures on three-dimensional porous biomaterials. *Biomaterials* **28**, 3965–3976 (2007).

356. Müller, A. M. *et al.* Towards an intraoperative engineering of osteogenic and vasculogenic grafts from the stromal vascular fraction of human adipose tissue. *Eur. Cells Mater.* **19**, 127–135 (2010).

357. Mehrkens, A. *et al.* Intraoperative engineering of osteogenic grafts combining freshly harvested, human adipose-derived cells and physiological doses of bone morphogenetic protein-2. *Eur. Cells Mater.* **24**, 308–319 (2012).

358. Zhang, Y., Husch, J. F. A. & van den Beucken, J. J. J. P. Intraoperative Construct Preparation: A Practical Route for Cell-Based Bone Regeneration. *Tissue Eng. Part B Rev.* **00**, ten.teb.2018.0010 (2018).

359. Güven, S. *et al.* Engineering of large osteogenic grafts with rapid engraftment capacity using mesenchymal and endothelial progenitors from human adipose tissue. *Biomaterials* **32**, 5801–5809 (2011).

360. Rhee, S. C. *et al.* In vivo evaluation of mixtures of uncultured freshly isolated adipose-derived stem cells and demineralized bone matrix for bone regeneration in a rat critically sized calvarial defect model. *Stem Cells Dev.* **20**, 233–242 (2011).

361. Prins, H.-J., Schulten, E. A. J. M., ten Bruggenkate, C. M., Klein-Nulend, J. & Helder, M. N. Bone Regeneration Using the Freshly Isolated Autologous Stromal Vascular Fraction of Adipose Tissue in Combination With Calcium Phosphate Ceramics. *Stem Cells Transl. Med.* **1**, 98–107 (2016).

362. Lendeckel, S. *et al.* Autologous stem cells (adipose) and fibrin glue used to treat widespread traumatic calvarial defects: case report. *J. Craniomaxillofac. Surg.* **32**, 370–3 (2004).

363. Mesimäki, K. *et al.* Novel maxillary reconstruction with ectopic bone formation by GMP adipose stem cells. *Int. J. Oral Maxillofac. Surg.* **38**, 201–209 (2009).

364. Sándor, G. K. *et al.* Adipose stem cells used to reconstruct 13 cases with cranio-maxillofacial hard-tissue defects. *Stem Cells Transl. Med.* **3**, 530–540 (2014).

365. Thesleff, T. *et al.* Cranioplasty with Adipose-Derived Stem Cells , Beta- Tricalcium Phosphate Granules and Supporting Mesh: Six-year Clinical Follow-up Results. *Stem Cells Transl. Med.* **6**, 1576–1582 (2017).

366. Rindone, A., Nyberg, E. & Grayson, W. 3D-Printing Composite Polycaprolactone-Decellularized Bone Matrix Scaffolds for Bone Tissue Engineering Applications. *Methods Mol. Biol.* 257–284 (2017). doi:10.1007/7651_2017_37

367. Cowan, C. M. *et al.* Adipose-derived adult stromal cells heal critical-size mouse calvarial defects. *Nat. Biotechnol.* **22**, 560–567 (2004).

368. Levi, B. *et al.* Human adipose derived stromal cells heal critical size mouse calvarial defects. *PLoS One* **5**, e11177 (2010).

369. Asatrian, G., Chang, L. & James, A. W. Muscle Pouch Implantation: An Ectopic Bone Formation Model. in *Animal Models for Stem Cell Therapy* **1213**, 185–191 (Springer Science, 2014).

370. Ghanavati, S., Yu, L. X., Lerch, J. P. & Sled, J. G. A perfusion procedure for imaging of the mouse cerebral vasculature by X-ray micro-CT. *J. Neurosci. Methods* **221**, 70–77 (2014).

371. Preibisch, S., Saalfeld, S. & Tomancak, P. Globally optimal stitching of tiled 3D microscopic image acquisitions. *Bioinformatics* **25**, 1463–1465 (2009).

372. McIntosh, K. *et al.* The Immunogenicity of Human Adipose-Derived Cells: Temporal Changes In Vitro. *Stem Cells* **24**, 1246–1253 (2006).

373. Ruetze, M. & Richter, W. Adipose-derived stromal cells for osteoarticular repair: trophic function versus stem cell activity. *Expert Rev Mol Med* **16**, e9 (2014).

374. Murphy, M. B., Moncivais, K. & Caplan, A. I. Mesenchymal stem cells: Environmentally responsive therapeutics for regenerative medicine. *Exp. Mol. Med.* **45**, e54-16 (2013).

375. Caplan, A. I. & Correa, D. The MSC: An injury drugstore. *Cell Stem Cell* **9**, 11–15 (2011).

376. Nyberg, E. L. *et al.* 3D-Printing Technologies for Craniofacial Rehabilitation, Reconstruction, and Regeneration. *Ann. Biomed. Eng.* 1–13 (2016). doi:10.1007/s10439-016-1668-5

377. Mantripragada, V. P., Lecka-Czernik, B., Ebraheim, N. A. & Jayasuriya, A. C. An overview of recent advances in designing orthopedic and craniofacial implants. *J. Biomed. Mater. Res. - Part A* **101**, 3349–3364 (2013).

378. Huang, G. J. *et al.* Craniofacial reconstruction with poly(methyl methacrylate) customized cranial implants. *J. Craniofac. Surg.* **26**, 64–70 (2015).

379. Bhumiratana, S. *et al.* Tissue-engineered autologous grafts for facial bone reconstruction. **8**, 1–13 (2016).

380. Gu, H. *et al.* Bone regeneration in a rabbit ulna defect model: use of allogeneic adipose-derivedstem cells with low immunogenicity. *Cell Tissue Res.* **358**, 453–64 (2014).

381. Kolambkar, Y. M. *et al.* Spatiotemporal delivery of bone morphogenetic protein enhances functional repair of segmental bone defects. *Bone* **49**, 485–92 (2011).

382. James, A. W. *et al.* A Review of the Clinical Side Effects of Bone Morphogenetic Protein-2. *Tissue Eng. Part B Rev.* **22**, 284–297 (2016).

383. Cawthorn, W. P., Scheller, E. L. & MacDougald, O. a. Adipose tissue stem cells: the great WAT hope. *Trends Endocrinol. Metab.* **23**, 270–277 (2012).

384. Sears, N. A., Seshadri, D. R., Dhavalikar, P. S. & Cosgriff-hernandez, E. A Review of Three-Dimensional Printing in Tissue Engineering. **22**, 298–310 (2016).

385. Kelly, C. N., Miller, A. T., Hollister, S. J., Guldberg, R. E. & Gall, K. Design and Structure–Function Characterization of 3D Printed Synthetic Porous Biomaterials for Tissue Engineering. *Adv. Healthc. Mater.* **7**, 1–16 (2018).

386. Jammalamadaka, U. & Tappa, K. Recent Advances in Biomaterials for 3D Printing and Tissue Engineering. *J. Funct. Biomater.* **9**, 22 (2018).

387. Bandyopadhyay, A., Bose, S. & Das, S. 3D printing of biomaterials. *MRS Bull.* **40**, 108–115 (2015).

388. Chia, H. N. & Wu, B. M. Recent advances in 3D printing of biomaterials. *J. Biol. Eng.* **9**, 4 (2015).

389. Zeltinger, J., Sherwood, J. K., Graham, D. A., Müeller, R. & Griffith, L. G. Effect of Pore Size and Void Fraction on Cellular Adhesion , Proliferation , and Matrix Deposition. *Tissue Eng.* **7**, 557–572 (2001).

390. Lee, M., Wu, B. M. & Dunn, J. C. Y. Effect of scaffold architecture and pore size on smooth muscle cell growth. *J. Biomed. Mater. Res. - Part A* **87**, 1010–1016 (2008).

391. Sobral, J. M., Caridade, S. G., Sousa, R. A., Mano, J. F. & Reis, R. L. Three-dimensional plotted scaffolds with controlled pore size gradients: Effect of scaffold geometry on mechanical performance and cell seeding efficiency. *Acta Biomater.* **7**, 1009–1018 (2011).

392. Woodfield, T. B. F. *et al.* Polymer scaffolds fabricated with pore-size gradients as a model for studying the zonal organization within tissue-engineered cartilage constructs. *Tissue Eng.* **11**, 1297–1311 (2005).

393. Di Luca, A. *et al.* Influencing chondrogenic differentiation of human mesenchymal stromal cells in scaffolds displaying a structural gradient in pore size. *Acta Biomater.* **36**, 210–219 (2016).

394. Di Luca, A. *et al.* Tuning Cell Differentiation into a 3D Scaffold Presenting a Pore Shape Gradient for Osteochondral Regeneration. *Adv. Healthc. Mater.* **5**, 1753–1763 (2016).

395. Luca, A. Di *et al.* Surface energy and stiffness discrete gradients in additive manufactured scaffolds for osteochondral regeneration Surface energy and stiffness discrete gradients in additive manufactured scaffolds for osteochondral regeneration. *Biofabrication* **8**, (2016).

396. Moroni, L., De Wijn, J. R. & Van Blitterswijk, C. A. 3D fiber-deposited scaffolds for tissue engineering: Influence of pores geometry and architecture on dynamic mechanical properties. *Biomaterials* **27**, 974–985 (2006).

397. Xu, S. *et al.* Bone regeneration in 3D printing bioactive ceramic scaffolds with improved tissue/material interface pore architecture in thin-wall bone defect. *Biofabrication* **9**, 025003 (2017).

398. Ranellucci, A. & Lenox, J. Slic3r. (2011). Available at: https://slic3r.org/about/. (Accessed: 1st July 2018)

399. Braam, D. Cura. *Git Hub* (2016).

400. Wang, M. O. *et al.* Evaluating 3D-Printed Biomaterials as Scaffolds for Vascularized Bone Tissue Engineering. *Adv. Mater.* **27**, 138–144 (2015).

401. Trachtenberg, J. E. *et al.* Open-source three-dimensional printing of biodegradable polymer scaffolds for tissue engineering. *J. Biomed. Mater. Res. Part A* n/a-n/a (2014). doi:10.1002/jbm.a.35108

402. Zalm., E. van der. Rep Rap Marlin. *Git Hub* (2011). Available at: https://github.com/MarlinFirmware.

403. Liu, K. & Tovar, A. MATLAB 3D-Plot. *Git Hub* (2016). Available at: https://github.com/coolzai/top3d_doMovie.

404. Aitkenhead, A. H. MATLAB STL Import. *Mathworks* (2013). Available at: https://www.mathworks.com/matlabcentral/fileexchange/27390-mesh-voxelisation. (Accessed: 1st July 2018)

405. Hotaling, N. A., Bharti, K., Kriel, H. & Simon, C. G. DiameterJ: A validated open source nanofiber diameter measurement tool. *Biomaterials* **61**, 327–338 (2015).

406. Schindelin, J. *et al.* Fiji : an open-source platform for biological-image analysis. *Nat. Methods* **9**, 676–682 (2012).

407. Szojka, A. *et al.* Biomimetic 3D printed scaffolds for meniscus tissue engineering. *Bioprinting* **8**, 1–7 (2017).

408. Karageorgiou, V. & Kaplan, D. Porosity of 3D biomaterial scaffolds and osteogenesis. *Biomaterials* **26**, 5474–5491 (2005).

409. Kasten, P. *et al.* Porosity and pore size of ??-tricalcium phosphate scaffold can influence protein production and osteogenic differentiation of human mesenchymal stem cells: An in vitro and in vivo study. *Acta Biomater.* **4**, 1904–1915 (2008).

410. Gauthier, O., Bouler, J. M., Aguado, E., Pilet, P. & Daculsi, G. Macroporous biphasic calcium phosphate ceramics: Influence of macropore diameter and macroporosity percentage on bone ingrowth. *Biomaterials* **19**, 133–139 (1998).

411. Amini, A. R., Laurencin, C. T. & Nukavarapu, S. P. Bone Tissue Engineering: Recent Advances and Challenges. *NIH Public Access* **42**, 157–162 (2008).

412. Barui, S., Chatterjee, S., Mandal, S., Kumar, A. & Basu, B. Microstructure and compression properties of 3D powder printed Ti-6Al-4V scaffolds with designed porosity: Experimental and computational analysis. *Mater. Sci. Eng. C* **70**, 812–823 (2017).

413. Gleadall, A., Visscher, D., Yang, J., Thomas, D. & Segal, J. Review of additive manufactured tissue engineering scaffolds : relationship between geometry and performance. *Burn. Trauma* 1–16 (2018).

414. Hung, B. P., Hutton, D. L. & Grayson, W. L. Mechanical control of tissue-engineered bone. *Stem Cell Res. Ther.* **4**, 10 (2013).

415. Lethaus, B. *et al.* A treatment algorithm for patients with large skull bone defects and first results. *J. Cranio-Maxillofacial Surg.* **39**, 435–440 (2011).

416. Mohan, K. *et al.* Treatment of Infected Facial Implants. *Semin. Plast. Surg.* **30**, 78–82 (2016).

417. Challis, V. J., Guest, J. K., Grotowski, J. F. & Roberts, A. P. Computationally generated cross-property bounds for stiffness and fluid permeability using topology optimization. *Int. J. Solids Struct.* **49**, 3397–3408 (2012).

418. Chen, Y., Zhou, S. & Li, Q. Microstructure design of biodegradable scaffold and its effect on tissue regeneration. *Biomaterials* **32**, 5003–5014 (2011).

419. Sridharan, R., Cameron, A. R., Kelly, D. J., Kearney, C. J. & O'Brien, F. J. Biomaterial based modulation of macrophage polarization: A review and suggested design principles. *Mater. Today* **18**, 313–325 (2015).

420. Paris, J. L., Román, J., Manzano, M., Cabañas, M. V. & Vallet-Regí, M. Tuning dual-drug release from composite scaffolds for bone regeneration. *Int. J. Pharm.* **486**, 30–37 (2015).

421. Nyberg, E., Farris, A., O'Sullivan, A., Rodriguez, R. & Grayson, W. Comparison of SVF and Passaged ASCs as Point-of-Care Agents for Bone Regeneration. *Tissue Eng. Part A* **ja**, (2018).

422. Rodriguez, E. D., Bluebond-Langner, R., Park, J. E. & Manson, P. N. Preservation of Contour in Periorbital and Midfacial Craniofacial Microsurgery: Reconstruction of the Soft-Tissue Elements and Skeletal Buttresses. *Plast. Reconstr. Surg.* **121**, 1738–1747 (2008).

423. Bose, S., Roy, M. & Bandyopadhyay, A. Recent advances in bone tissue engineering scaffolds. *Trends Biotechnol.* **30**, 546–554 (2012).

424. Loh, Q. L. & Choong, C. Three-dimensional scaffolds for tissue engineering applications: role of porosity and pore size. *Tissue Eng. Part B. Rev.* **19**, 485–502 (2013).

425. Sutradhar, A., Paulino, G. H., Miller, M. J. & Nguyen, T. H. Topological optimization for designing patient-specific large craniofacial segmental bone replacements. *Proc. Natl. Acad. Sci.* **107**, 13222–13227 (2010).

426. Sutradhar, A. *et al.* Designing patient-specific 3D printed craniofacial implants using a novel topology optimization method. *Med. Biol. Eng. Comput.* **54**, 1123–1135 (2016).

427. Kang, H., Lin, C. Y. & Hollister, S. J. Topology optimization of three dimensional tissue engineering scaffold architectures for prescribed bulk modulus and diffusivity. *Struct. Multidiscip. Optim.* **42**, 633–644 (2010).

428. Hollister, S. J. *et al.* Integrating Image-Based Design and 3D Biomaterial Printing To Create Patient Specific Devices within a Design Control Framework for Clinical Translation. *ACS Biomater. Sci. Eng.* acsbiomaterials.6b00332 (2016). doi:10.1021/acsbiomaterials.6b00332

429. SHIMADA, A. *et al.* Measurement of dynamic bite force during mastication. *J. Oral Rehabil.* **39**, 349–356 (2012).

430. Sigmund, O. & Maute, K. Topology optimization approaches: A comparative review. *Struct. Multidiscip. Optim.* **48**, 1031–1055 (2013).

431. Sigmund, O. & Petersson, J. Numerical instabilities in topology optimization: A survey on procedures dealing with checkerboards, mesh-dependencies and local minima. *Struct. Optim.* **16**, 68–75 (1998).

432. Liu, K. & Tovar, A. An efficient 3D topology optimization code written in Matlab. *Struct. Multidiscip. Optim.* **50**, 1175–1196 (2014).

433. Zuo, W. & Saitou, K. Multi-material topology optimization using ordered SIMP interpolation. *Struct. Multidiscip. Optim.* **55**, 477–491 (2017).

434. Liao, Y. *et al.* Using three-dimensional multigrid-based snake and multiresolution image registration for reconstruction of cranial defect. *Med. Biol. Eng. Comput.* **51**, 89–101 (2013).

435. Guest, J. K. & Prévost, J. H. Optimizing multifunctional materials: Design of microstructures for maximized stiffness and fluid permeability. *Int. J. Solids Struct.* **43**, 7028–7047 (2006).

436. Stricker-Krongrad, A., Shoemake, C. R. & Bouchard, G. F. The Miniature Swine as a Model in Experimental and Translational Medicine. *Toxicol. Pathol.* **44**, 612–623 (2016).

437. Vapniarsky, N. *et al.* The Yucatan Minipig Temporomandibular Joint Disc Structure–Function Relationships Support Its Suitability for Human Comparative Studies. *Tissue Eng. Part C Methods* **00**, ten.tec.2017.0149 (2017).

438. Gutierrez, K., Dicks, N., Glanzner, W. G., Agellon, L. B. & Bordignon, V. Efficacy of the porcine species in biomedical research. *Front. Genet.* **6**, 1–9 (2015).

439. Swindle, M. M., Makin, A., Herron, A. J., Clubb, F. J. & Frazier, K. S. Swine as Models in Biomedical Research and Toxicology Testing. *Vet. Pathol.* **49**, 344–356 (2012).

VITA

Ethan Nyberg was born to Lori and Karl Nyberg in Fairfax, Virginia. He was raised in Northern Virginia, where his parents homeschooled him and his three younger sisters. Throughout his youth, Ethan enjoyed reading science fiction and is thrilled with the ways that those ideas are becoming reality. In particular, he was captivated with the idea of nanorobots controlled to rebuild the body.

Throughout high-school and college, Ethan spent large portion of his life at the natatorium, with a successful career as an athlete, lifeguard, and coach. He also had a passion for the outdoors and adventure and was deeply involved with the Boy Scouts, with membership in the Order of the Arrow, and attained the rank of Eagle Scout.

For the past 15 years, Ethan has been a student of martial arts, particularly Shotokan karate, teaching locally and competing on the national and international stage. Training with martial arts has imparted mental focus, a deep understanding of biomechanics, and has provided an enduring avenue of stress relief.

Preparing to go to the University of Virginia, Ethan was going to major in a combination of literature and business, but thought last minute to give engineering a try instead. He took the first entry Biomedical Engineering class in physiology and fell in love with it. He realized that there are already nanorobots in the body—cells—that we can engineer to heal and regenerate the body.

Ethan's research at UVA in the Botchwey and Peirce-Cottler Labs granted him valuable experience with stem cells and vascular regeneration, and extensive training in rodent biomethodology. This experience gave him the idea of using a rapidly vascularized network as a platform for regeneration of different tissues. His first contact with 3D-printing cells occurred in 2013, and the experience left him painfully aware of the complications and barriers to directly printing cells. Those difficulties (e.g. oozing gel into a petri dish) made him doubt that the cells really benefit from spatial manufacturing. Ethan graduated with high distinction from the University of Virginia in May, 2014 with a Bachelor's of Science in Biomedical Engineering and a minor in business. Ethan was the Outstanding Student of the School of Engineering and Applied Science that year. He took the Fundamentals of Engineering exam that summer and is registered as EIT in the state of Virginia.

In the fall of 2014, Ethan started the Johns Hopkins School of Medicine Biomedical Engineering PhD program. At JHU, Ethan worked at length with stem cells for vascularization and bone regeneration. The first year of medical school courses were some of the most worthwhile education since the intro to biomedical engineering physiology course at UVA. He added 3D-printing as a dominating research focus in his third year of graduate school, and saw opportunities to redevelop and scale the 3D-printing systems in the Grayson Lab. Combining that 3D-printing system with the stem cell and vasculature approach resulted in the work in his doctoral dissertation.

As a result of working for years to scale those technologies from the petri dish to the human craniofacial skeleton, Ethan developed an interest in regulatory science and affairs, particularly as applied to patient-specific design and manufacturing.

Ethan has authored or coauthored 6 peer reviewed journal articles, a book chapter. He has given or been an author of 18 oral and poster presentations. He an inventor on one patent pertaining to 3D-printing bone ECM. During his academic training, Ethan taught undergraduate courses on Earth Systems Engineering Management, Nanoscience, Business and Ethics of Regenerative Medicine, and Engineering Design Principles for Implants. He has mentored eight undergraduate students in lab experiences.

Education

Johns Hopkins University, Baltimore, MD   ***Anticipated*** **July 2019**
PhD Candidate, Biomedical Engineering
Topic: 3D-Printed Tissue Engineered Bone Scaffolds for Craniofacial Skeletal Regeneration

University of Virginia, Charlottesville, VA   **May 2014**
B.S., Biomedical Engineering, Engineering Business Minor, with **High Distinction**
Theses: (1) Adipose-derived Stem Cells in Vascular Constructs: Pericyte-like Function
          (2) Societal, Ethical, and Technological Contributions to Organ Transplant Policy

Research Activities

Graduate Research Assistant
The Grayson Laboratory for Craniofacial and Orthopedic Tissue Engineering
Department of Biomedical Engineering, Translational Tissue Engineering Center

The Peirce-Cottler Laboratory: Vascular and Tissue Systems Bioengineering
Independent Research, *Advisor: Shayn Pierce-Cottler, Ph.D.*
Murine Adipose Stem Cell Implant Study: Interaction between Putative mASC Pericyte and Endogenous Pericyte Population in Angiogenesis

The Botchwey Laboratory: Biomaterials, Regenerative Medicine, Stem Cells
Independent Research, *Advisors: Ed Botchwey, Ph.D. and Cynthia Huang, M.S.*
Cranial Defect Study: The Effects of Local, Sustained Delivery of FTY720 on Bone Graft Integration

Publications

1. **Nyberg, E.L.**, Farris, A.L., O'Sullivan, A., Rodriguez, R.L., Grayson, W.L. Differences between SVF and P2 ASCs in forming bone *in vitro* and *vitro*. *Tissue Engineering Part A* (2019)

2. **Nyberg, E.L**., Osanov, M., Chartrain, N., Farris, A.L., Aggarwal, S., Williams, C., Guest, J., Grayson, W.L. Topology Optimized Design of Unit Cells for Graded Bone Tissue Engineering Scaffolds. (**In Preparation,** 2019)

3. **Nyberg, E.L**., Guest, J., Grayson, W.L. Optimized Pore structure of 3D-Printed implants in response to physiologic load (**In Preparation,** 2019)

4. **Nyberg, E.L**., Bart, Dorafshar, A.H., Grayson, W.L. Feasibility of 3 D-printed scaffolds in different craniofacial defects: a retrospective patient study (**In Preparation**, 2019)

5. **Nyberg, E.L.**, & O'Sullivan, A., Grayson, W.L. scafSLICR: a MATLAB-based Slicing Algorithm to Enable 3D-Printing of Tissue Engineering Scaffolds with Heterogenous Porous Microarchitecture (**Submitted**, 2019)

6. **Nyberg, E.L**. and Grayson W.L. Assessing the Minimum Time-Period of Normoxic Preincubation for Stable Adipose Stromal Cell-Derived Vascular Networks. *Cell. and Mol. Bioengineering.* (2018)

7. **Nyberg, E.L**., Rindone A., Dorafshar, A.H., and Grayson, W.L. Comparison of 3D-Printed Poly-ε-caprolactone Scaffolds Functionalized with Tricalcium Phosphate, Hydroxyapatite, Bio-Oss, or Decellularized Bone Matrix. *Tissue Engineering Part A.* (2016).
** Most Read *Tissue Engineering* Article of 2017 **

8. **Nyberg, E. L**., Rindone, A., & Grayson, W. L. 3D-Printing Composite Polycaprolactone-Decellularized Bone Matrix Scaffolds for Bone Tissue Engineering Applications. *Methods in Molecular Biology.* (2017).

9. **Nyberg, E.L**., Farris, A.L., Hung, B.P., Dias, M., Garcia, J.R., Dorafshar, A.H., and Grayson, W.L. 3D-Printing Technologies for Craniofacial Rehabilitation, Reconstruction, and Regeneration. *Annals of Biomedical Engineering*. (2016).

10. Hung, B.P., Naved, B.A., **Nyberg, E.L**., Dias, M., Holmes, C.A., Elisseeff, J.H., Dorafshar, A.H., and Grayson, W.L. Three-dimensional printing of bone extracellular matrix for craniofacial regeneration. *ACS Biomaterials Science & Engineering*. (2016).

11. **Nyberg, E.L**., Holmes, C., Witham, T., & Grayson, W. L. Growth Factor-eluting Technologies for Bone Tissue Engineering. *Drug Delivery and Translational Research*. (2015).

1. Ashley L. Farris, Dennis Lambrechts, Nicholas Zhang, Alexandra Rindone, **Ethan L. Nyberg,** Aine O'Sullivan, S. J. Burris, Kendall Free, and Warren L. Grayson. *Tunable Oxygen-Releasing, 3D-printed Scaffolds Improve In Vivo Osteogenesis.* (Oral Presentation, 2019) Society for Biomaterials Conference

2. **E. Nyberg,** A. Farris, A. O'Sullivan, M. Grant, and W. Grayson (2019). *3D-Printed Craniofacial Bone Grafts with Autologous Cells for Bone Regeneration.* Military Health System Research Symposium (Submitted)

3. **E. Nyberg,** A. Farris, A. O'Sullivan, and W. Grayson (2018). *Assessing the Osteogenic Potential of Adipose-derived Stromal Vascular Fraction Cells.* Johns Hopkins DOM Retreat **** Student Research Finalist ****

4. **E. Nyberg,** A. Farris, A. O'Sullivan, and W. Grayson (2018). *scafSLICR: A MATLAB Tool for Designing 3D-printed Tissue Engineered Scaffolds with Heterogeneous Features*. Poster at the Symposium on Advanced Biomanufacturing. Charlottesville, Virginia. November 5, 2018

5. **Nyberg, E. L.,** O'Sullivan, A., and Grayson, W. "Design and manufacture of 3D-printed scaffolds for regeneration of massive craniomaxillofacial bone loss". *World Congress of Biomechanics* Dublin, Ireland. July 2018.

6. O'Sullivan, A., **Nyberg, E.,** Grayson, W. *3D Printing Heterogeneous Porous Patterns in Tissue Engineered Bone Scaffolds.* Presentation at Northeast Bioengineering Conference. Philadelphia, Pennsylvania. March 2018. (Oral Presentation)

7. Aggarwal, S., **Nyberg, E.,** Osanov, M., Guest, J., & Grayson, W. *Design of 3D-Printed Craniofacial Bone Scaffolds for Physiologic Loading.* Poster Presented at Institute for Nano Biotechnology Innovation through Engineering Symposium. Baltimore, Maryland. May 2018.

8. **E. L. Nyberg**, A. Farris, W. Grayson. *Assessing the Osteogenic Potential of Adipose-derived Stromal Vascular Fraction Cells.* Poster at the Tissue Engineering and Regenerative Medicine Society Annual Conference. Charlotte, North Carolina. (2017) **** Winner, Student and Young Investigator Section ****

9. O'Sullivan, A., **Nyberg, E.,** Grayson, W. *Design, Manufacturing, and Analysis of 3D Anatomic Bone Scaffolds* **2nd Place** Poster Presented at Institute for Nano Biotechnology Innovation through Engineering Symposium. Baltimore, Maryland. November 2017.

10. Aggarwal, S., **Nyberg, E.,** Osanov, M., Chartrain, N., Farris, A., Guest, J., & Grayson, W. *Validating Bio-Scaffolds Optimized for Mechanical Strength and*

Permeability. Poster Presented at Institute for Nano Biotechnology Innovation through Engineering Symposium. Baltimore, Maryland. November 2017.

11. O'Sullivan, A., **Nyberg, E.,** Grayson, W. *Design, Manufacturing, and Analysis of 3D Anatomic Bone Scaffolds* Presentation at Johns Hopkins University Undergraduate Research Symposium. Baltimore, Maryland. October 2017. (Oral Presentation).

12. Aggarwal, S., **Nyberg, E.,** Osanov, M., Chartrain, N., Farris, A., Guest, J., & Grayson, W. *Validating Bio-Scaffolds Optimized for Mechanical Strength and Permeability* Presentation at Johns Hopkins University Undergraduate Research Symposium. Baltimore, Maryland. October 2017. (Oral Presentation).

13. **E. L. Nyberg,** A. Rindone, A. O'Sullivan, W. Grayson. *Manufacturing of 3D-Printed Polycaptolactone Scaffolds Functionalized with Tricalcium Phosphate, Hydroxyapatite, Bio-Oss, or Decellularized Bone Matrix.* Poster at the Symposium on Advanced Biomanufacturing. Charlottesville, Virginia. November 6, 2017

14. **Nyberg E.L.**, Hutton D.L., Grayson W.L. ASC Vascular Assembly in Hypoxia is Mediated by the Extent of Normoxic Preassembly. *Tissue Engineering Part A, Vol 21 p176* (2015)

15. D.T. Bowers, L. A. Langman, **E. L. Nyberg**, B. J. Kane, D. A. Griggs, D. R. Dart, J. K. Bagwell, D. D. Johnson, B. L. Allen, P. Chhabra, A. Toumadje, C. A. Campbell, S. M. Peirce, K. L. Brayman *Bioartificial Pancreas Engineering Using 3D Bioprinting* Presentation to the Department of Surgery, University of Virginia. Charlottesville, Virginia. April 15, 2014.

16. **E.L. Nyberg** *Biofabrication of Microvascular Components of Organs.* American Society for Artificial Internal Organs Design Competition, Washington D.C. June 6, 2014.

17. S. M. Cronk, T.A. Mendel, **E. L. Nyberg**, A. R. Sheets, A. C. Bruce, I. M. Herman, P. A. Yates, and S. M. Peirce *Adipose-derived Stem Cells from Healthy and Diabetic Mice have Differential Effects on the Retinal Microvasculature* Presentation to the Tissue Engineering and Regenerative Medicine Society Annual Conference. Atlanta, Georgia. November 12, 2013

18. **E. L. Nyberg**, S. Seaman, and S. M. Peirce *Evaluating Pericyte-like Behaviors of Adipose-derived Stem Cells on Excised Microvessels* Presentation to the Biomedical Engineering Society Annual Meeting. Seattle, Washington, September 27, 2013

19. S. M. Cronk, T.A. Mendel, **E. L. Nyberg**, A. R. Sheets, A. C. Bruce, I. M. Herman, P. A. Yates, and S. M. Peirce *Hyperglycemia Suppresses Revascularization potential of Adipose-derived Stem Cells in the Treatment of Diabetic Retinopathy* Presentation to NHLBI Symposium on Cardiovascular Regenerative Medicine. Bethesda, Maryland. September 26, 2013

20. C. S. Huang, **E. L. Nyberg**, R. C. Ogle, and E. A. Botchwey *Local Sustained Delivery of FTY720 Accelerates Bone Growth and Enhances Bone Graft Integration* Presentation to the Biomedical Engineering Society Annual Meeting. Atlanta, Georgia, October 27, 2012.

Teaching Experience

Lecturer   **2016-2018**
- **The Ethics and Business of Regenerative Medicine**
- **Engineering Design Process for Craniofacial Orthopedics**

Designed and taught one course on the interweavings of business, ethics, and societal dimensions as relevant to recent advances and failures of regenerative medicine; similarly created and taught a course using craniofacial implants to teach the engineering design process.

Graduate Teaching Assistant,   **2017**
- **Biomedical Engineering Modeling and Design**

Taught 12 sections the principles of modeling human systems and the design of medical devices. Provided feedback on writing technical reports, creating and giving presentations, and career advice.

Teaching Academy, Johns Hopkins Center for Teaching and Learning   **2016**
Completed a three-day course to develop teaching skills including: active learning, flipped classrooms, course design, and student assessment.

Senior Teaching Assistant   **2013-2015**
- **Earth Systems Engineering Management**
- **Societal Dimensions of Nanotechnology**

Led discussions, lectured, redesigned course content, graded assignments, moderated forums, managed team of TAs, ran writing workshops, managed online course content and distance learners, and held office hours.

Awards and Fellowships

Outstanding Student Award, School of Engineering, UVA   **2014**
To honor a (graduating) student who has exhibited service before self, integrity, and excellence and demonstrated outstanding academic performance, leadership, and service.

Harrison Award   **2013-2014**
A competitive grant to enable original undergraduate research at UVA. *Research Topic:* The ability to engineer organic biological replacements or repairs for failed or diseased tissues such as bones, blood vessels and organs by leveraging emerging stem cell technology.

Kinnier Fellowship   **2012-2013**
A competitive fellowship for engineering students interested in academia; combining discussions with distinguished faculty from across the University of Virginia, focused on the nature of academia and teaching engineering, as well as a focused student-run outreach program on the opportunities of secondary education in engineering to local underprivileged high schools.

Honors and Awards

Travel Award, Symposium on Advanced Biomanufacturing, University of Virginia	2018
Finalist, Research Symposium, Johns Hopkins Dept. of Medicine	2018
Winner, Student and Young Investigator Section, TERMIS-Americas	2017
Travel Award, Graduate Student Association, Johns Hopkins	2016
Medical Hackathon, 2nd Place Winner, Johns Hopkins	2015
Phi Eta Sigma National Honor Society; University of Virginia	2011-2014
National Residence Hall Honorary Association	2011-2013
Dean's List; University of Virginia	2010-2011
Dean's List; Northern Virginia Community College	2008-2010
Eagle Scout / Order of the Arrow, Boy Scouts of America	2007

Certifications and Training

Regulatory Affairs Professional Society, Training Fellow, Certificate   2018
EIT Designation, registered in Virginia   2014
Human Subjects Research   2014
Training and Practice of Clinical Staff   2016
Conflict of Interest and Commitment   2016
Research Ethics I, II   2014, 2016
Title IX Workplace and Harassment Prevention for Supervisors   2015, 2017

Extracurricular Activities

Biomedical Engineering PhD Program Student Council   2014-2017
- Managed recruitment and social activities
- Chairperson for annual program retreat

Research Experience for Intercity Students, Summer Employer   2015
Mentored and employed students from local inner-city high-schools as lab technicians.

Peer-Mentoring Program, Univ. Virginia. Co-founder, Mentor.   2012-2014
Helped to conceive and design a peer-mentoring program to address the needs of students struggling academically, socially, mentally, or emotionally as they pursue an engineering degree. Organized and facilitated events and mentor training.

Hobbies: Woodworking, open-water swimming, running, beach volleyball, karate, backpacking